IDO-17081

295
9/13

MASTER

NUCLEAR TECHNOLOGY BRANCHES QUARTERLY REPORT

October 1-December 31, 1964

PHILLIPS PETROLEUM COMPANY

ATOMIC ENERGY DIVISION

NATIONAL REACTOR TESTING STATION

US ATOMIC ENERGY COMMISSION

DISCLAIMER

PRINTED IN USA. PRICE $4.00. AVAILABLE FROM THE CLEARINGHOUSE FOR FEDERAL SCIENTIFIC AND TECHNICAL INFORMATION, NATIONAL BUREAU OF STANDARDS, U. S. DEPARTMENT OF COMMERCE, SPRINGFIELD, VIRGINIA

PRINTED IN USA

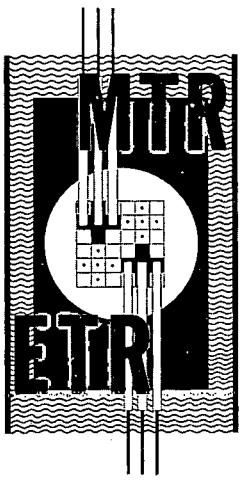

IDO-17081
AEC Research and Development Report
Reactor Technology
TID-4500 (42nd Ed.)
Issued: July 1965

NUCLEAR TECHNOLOGY BRANCHES QUARTERLY REPORT

FORMERLY -- MATERIALS TESTING REACTOR-ENGINEERING TEST REACTOR TECHNICAL BRANCHES QUARTERLY REPORT

OCTOBER 1 - DECEMBER 31, 1964

D. R. deBoisblanc
ASSISTANT MANAGER
ATOMIC ENERGY DIVISION

W. C. Francis
MANAGER,
REACTOR ENGINEERING

R. G. Fluharty
MANAGER,
NUCLEAR TECHNOLOGY

M. E. Thomas
MANAGER,
INSTRUMENT DEVELOPMENT &
TECHNICAL SERVICES

L. A. Schmittroth
MANAGER,
MATHEMATICAL ANALYSIS &
MACHINE COMPUTATIONS

PHILLIPS
PETROLEUM
COMPANY

Atomic Energy Division
Contract AT(10-1)-205
Idaho Operations Office

U. S. ATOMIC ENERGY COMMISSION

Previous Quarterly Reports in the MTR-ETR Series

Quarter	Number
1959	
1	IDO-16543
2	IDO-16561
3	IDO-16580
4	IDO-16620
1960	
1	IDO-16633
2	IDO-16648
3	IDO-16658
4	IDO-16665
1961	
1	IDO-16695
2	IDO-16710
3	IDO-16733
4	IDO-16760
1962	
1	IDO-16781
2	IDO-16805
3	IDO-16827
4	IDO-16857
1963	
1	IDO-16898
2	IDO-16917
3	IDO-16932
4	IDO-16977
1964	
1	IDO-16994
2	IDO-17042
3	IDO-17052
4	IDO-17081

SUMMARY

The reactivity effects of the experiment mock-ups in the ATRC have been measured. Experimental and calculated distributions of excess reactivity for the ATR are compared. The reactivity effect of a possible radial shift of fuel elements in the ATR due to hydraulic stresses has been measured to be less than 0.1$.

A diagram shows the measured power distribution in the ATRC core. The hot-spot power density normalized to full-power (250 MW) in the ATR is 27,000 W/g U-235. The effects on the core hot spot due to venting or slotting the fuel element side plates are depicted graphically in radial, axial, and azimuthal profiles.

The shutdown reactivity in the ATRC safety rods is greater than 7$ in all cases measured. Interaction effects between the shims and safety rods were investigated.

An experimental program has been conducted to determine the reactivity effect of displacing different volumes of water at various locations in the ARMF-I central experimental hole.

Initial operation of a once-through loop in the ETR core was executed in support of ATR fuel materials development.

A computer code has been written to calculate axial wall and bulk coolant temperatures for fuel elements of the ATR design.

Analyses of the pressure and thermally induced stresses and deflections of the ATR fuel element generating the maximum power density have been executed and are reported. It is shown that axial thermal stresses may exceed the yield strength of the fuel plates in some areas under maximum peak power (hot spot) conditions.

The microprobe has been applied successfully to the identification of fission products in two highly irradiated MTR fuel materials. One of these materials consisted of UO_2 particles in an aluminum matrix and had undergone a burnup of 83 percent. The fission products, cerium and barium, were found in the UO_2 fuel particles and in the aluminum matrix immediately adjacent to them. No indication of chemical reaction between the UO_2 and aluminum matrix was found.

The other fuel material, a uranium-aluminum alloy, consisting of uranium aluminide particles suspended in an aluminum matrix had been irradiated to 24 percent burnup. In this material, cerium was found within the fuel particles and in the immediately adjacent aluminum matrix. Barium was not detected.

Two ATR-type fuel elements which had been previously tested in the Hydraulic Facility and one MTR-type fuel element in which uranium-bearing Fiberglas was used as the fuel material were examined during the quarter. The results of these examinations are reported.

The beta decay of Pt-199 to Au-199 was studied using lithium-drifted germanium, NaI(Tl), permanent-field spectrographs, and γ-γ and β-γ coincidence techniques. The half-life of Pt-199 was measured to be 31.4 ± 0.5

minutes. The energies of the prominent transitions (and their photon intensities relative to the 543-keV gamma ray) are 54.9, 74.6, 185.6 (401), 219 (22), 226(30), 246.5(163), 316.9(358), 417(14), 425(23), 467(133), 474.2(99), 493.6(379), 542.8 (1000), 644(6), 665(12), 715(122), 791(76), 836(1), 889(2), 967(63) keV. Conversion electrons were observed for the 55-, 75-, 186-, 246-, 317-, and 543-keV transitions. No photons were observed corresponding to the 55-keV transition. On the basis of the experimental results, tentative levels were placed in Au-199 at 74.6, 316.9, 321.1, 540.2, 542.8, 728.4, 733.8, 788.1, 790.6, 930, and 967 keV. Evidence was found for an isomeric state in Au-199 with a half-life greater than 200 msec and less than 1 sec.

The total neutron cross section of U-232 was measured for neutrons of energies between 0.01 and 10000 eV. From the data, preliminary values of resonance parameters were obtained for five resonances below 28 eV. A small, 1 mg, sample of the Th-228 daughter of U-232 was chemically separated from the latter and used for positive identification of the 2 eV resonance which grows into U-232 after initial purification.

Measurements were made of the relative yield of high total kinetic energy fragments of the fission of U-235 induced by neutrons of energy between 0.1 and 10 eV.

Alpha spectra of Th-229 and its daughters were obtained. A new chemistry isolation box was built and installed in the MTR Hot Alpha Cave. The box is capable of processing several different radioactive nuclides prepared for Fast Chopper cross section measurements and replaces the original box designed only for Pa-233 chemistry.

A sample of irradiated Tl was discharged from the ETR, processed through the Alpha Cave, and the material prepared for Fast Chopper measurement of the cross section of Tl-204.

Slow neutron scattering calculations were made for ethane and n-butane using improved averaging methods for molecular orientations. As a result, better agreement between experimentally measured and theoretically calculated data was obtained. Further theoretical computations were completed on a model formulated to describe the scattering of slow neutrons by methane.

Using the ARMF-II, infinitely dilute resonance absorption integrals were measured for Tb, Ho, Er, Tm, and Yb in their natural isotopic ratios.

A recently developed eddy current proximity detector and its associated circuitry; a special purpose nuclear pulse amplifier with a field effect transistor (FET) input stage; an electrochemical fast data logger, which interrogates a chemical cell and provides a digital readout; an automatic ultrasonic flaw detector, which is designed to test the curved ATR fuel plates; special input and output stages, designed for an operational amplifier employed in conjunction with an electroanalytical potentiostat; and circuit modifications to constant air monitors are reported.

The transient behavior of the Power Burst Facility (PBF) was studied on the analog computer in order to estimate the rod motion required for shaping the power burst under various operating conditons. Adiabatic and

nonadiabatic thermal models of the reactor core were investigated. Reactor shutdown transients by means of the scram rods were also investigated.

Analog studies of the effects of a rupture in the ETR vessel as well as the effects of a power failure in the ETR primary coolant pumps were performed.

Progress continued on Phillips' Monte Carlo program. The input program is now essentially complete. The output includes a complete statistical analysis of the flux in each region. The efficiency of the program for use in reactor physics calculations is being studied.

An IBM 7040 program has been written to produce a radiation dose report for TRA maintenance.

A program has been written and checked out to calculate the real and complex roots of a polynomial with real coefficients using a combination of Newton and Bairstow formulas.

An IBM 7040 program has been developed for calculating the pulse-height response of a sodium iodide scintillation detector.

Reactor physics calculations were made on single-, two-, and three-region Westinghouse critical experiments described in WCAP-1433 for support of LOFT and PBF design calculations.

CONTENTS

FIGURES

TABLES

NUCLEAR TECHNOLOGY BRANCHES QUARTERLY REPORT
1964 QUARTER 4
OCTOBER 1 - DECEMBER 31, 1964

I. REACTOR ENGINEERING

1. CRITICAL FACILITIES
(E. E. Burdick)

1.1 Reactivity Measurements in the ATRC (N. C. Kaufman, J. W. Henscheid)

In January 1964, the Babcock and Wilcox Company completed an extensive computational study on the Advanced Test Reactor with a 39-kg loading of fuel [1]. This study was carried out using a two-dimensional depletion code, TURBO, with a one-quarter core mock-up of the ATR. To compare experimental results with the results of this study, sufficient changes were made in the core of the ATRC to simulate the loading used in the TURBO study. The only significant but unavoidable exception was the use of a 35-kg core loading rather than the 39-kg loading assumed in the TURBO study and subsequently prescribed for the ATR. The required core loading additions to go from the second ATRC start-up core configuration [2] to the configuration used in the TURBO study and the reactivity worths of these changes are summarized in Table I-1.

These reactivity measurements showed that the total reactivity worth for the nine experiments specified by the Navy (two A-1's, one A-3, and six A-5's) was 5.75$ which agrees well with an estimate of 6.0$ based on preliminary U-235 and aluminum statistical weights reported earlier [3]. The reactivity worth of the four hafnium rods in the H-hole positions is somewhat less than it will be in the ATR, due to these rods having a smaller diameter than those to be used in the ATR.

1.2 Experimental and Calculated Reactivity Distribution for the ATR (N. C. Kaufman)

Some differences between the ATRC measured excess reactivities and the values reported in the TURBO study [1] have been observed. With particular reference to the ATR beginning-of-cycle reactivity distribution, the present best estimates for a TURBO-type core configuration with 39 kg of fuel are presented in Table I-2 and are compared with the values reported in the TURBO study. These estimates are extrapolations to a 39-kg core of the most recent experimental values from the ATRC 35-kg core.

1.3 Reactivity Effect of a Fuel Element Radial Shift in the ATRC (N. C. Kaufman)

An experiment was performed in the ATRC to assess the reactivity effect of a 0.020-inch radial bowing of the plates within ATR elements due to hydraulic stresses [4]. Six entire elements were shifted radially an average distance of 0.018 inch toward the center of the flux trap which they partially surrounded. A reactivity change of $-0.016 \pm 0.003$$ was observed. The shift of an entire element produces a larger reactivity change than the bowing would, since in the latter case only the midplane of the plates is displaced the full amount. However, even if all 40 elements were shifted, rather than bowed, the reactivity change would be only 0.1$. All indicated errors represent one standard deviation.

TABLE I-1

SUMMARY OF CORE CHANGES AND RESULTING
REACTIVITY WORTHS FOR "TURBO" LOADING IN THE ATRC

Core Position[a]	Experiment Added	Average Reactivity Worth ($)	Average Reactivity Worth (percent Δk/k)[b]
NW or SE Flux Traps	A-1 Experiment (26.8 g U-235 in sixty-four 0.187-inch-diameter Al rods)	+0.43	+0.32
SW or NE Flux Traps	A-5 Experiment (80.3 g U-235 in sixty-four 0.187-inch-diameter Al rods)	+0.80	+0.60
Center Flux Trap	A-3 Experiment (53.6 g U-235 in sixty-four 0.187-inch-diameter Al rods)	+0.55	+0.41
E, N, S, or W Flux Traps	A-5 Experiment (80.3 g U-235 in sixty-four 0.187-inch-diameter Al rods)	+0.70	+0.52
B-Holes 1 to 8	5/8-inch-OD 304 SS rods	-0.15/rod	-0.11/rod
A-Holes 1 to 8	1/2-inch-OD 304 SS rods	-0.038/rod	-0.03/rod
A-Holes 9 to 12	1/2-inch-OD 304 SS rods	-0.04/rod	-0.03/rod
H-Holes 3 and 11	1/2-inch-OD Al tube with 0.083-inch wall	+0.025/rod	+0.02/rod
H-Holes 1, 5, 9, and 13	1/4-inch-OD Hf rods	-0.15/rod	-0.11/rod

[a] For reference to ATRC core, see Figure I-1.

[b] While not strictly correct, all reactivity values in percent were obtained using $ = 0.75% Δk/k.

The radial shift of the elements was achieved by placing shims on first one side of the T-shaped support bar and then on the other side, making a critical run each time. The thickness of the required shims provided an accurate measure of the extent of the radial shift. The reactivity reproducibility for the removal and insertion of the six assemblies was established as ± 0.003$.

1.4 ATRC Power Calibration (L. C. Richardson, J. W. Henscheid)

One of the more significant features of the ATR is the ability to adjust the neutron flux level in a given in-pile loop without adversely affecting the other loops in the core. This is accomplished using primarily the outer shims to adjust the power density in the eight fuel elements surrounding the flux trap and in-pile tube. The experiment loading, flux trap composition, and power split of the TURBO study discussed above is an example of an operational core in the ATR. For this reason, the ATRC was loaded accordingly and the shims positioned to give a power split approximately proportional to the 40-50-60 MW split in the TURBO study. (The actual power split in the ATRC was proportional to 39 MW in the NE and SW lobes, 54 MW in the center lobe,

TABLE I-2

EXCESS REACTIVITY DISTRIBUTION FOR THE ATR:
A COMPARISON OF EXPERIMENTAL AND CALCULATED VALUES

	ATRC (percent Δk/k)[a]	TURBO (percent Δk/k)
Reactivity held in 165 g natural boron	8.6	7.4
Reactivity held in shims, cold and clean	12.3	9.6
Temperature effect from ambient to 250 MW	0.6[c]	0.6
Reactivity held in shims, hot and clean	12.9	10.2
Reactivity held in shims at the beginning of 40-50-60 MW operation[b]	11.0	10.2
Total excess reactivity, cold and clean	20.9	17.0
Total excess reactivity, hot and clean	21.5	17.6
Total excess reactivity at the beginning of 40-50-60 MW operation[b]	19.6	17.6
Total movable shim reactivity worth	13.6	13.9

[a] Assuming $ = 0.75% Δk/k.

[b] It is estimated that the shim configuration required for a 40-50-60 MW power split will not be attained until after 6 hours of operation at 250 MW.

[c] Not measured.

and 59 MW in the NW and SE lobes.) The shim positions required to attain this power split in the ATRC were as follows: Outer shims N1-2, E3-4, S1-2, and W3-4 (see Figure I-1) at approximately 100°, all other outer shims at 0°; neck shims 5 and 6 in each neck fully withdrawn, and all other neck shims in their inner limits.

For the zero-time step in the TURBO study, the shim positions for the 40-50-60 MW power split were not much different. The outer shim positions in the TURBO study were the same as those in the ATRC; but in the TURBO study, all neck shims were in their inner limits except the No. 4 shims in the NE and SW necks that were fully withdrawn. Since the ATRC neck shims are somewhat more effective than the ATR neck shims [5], the difference with like neck shims would be even less. In fact, the difference between excess reactivity in the TURBO study and in the ATRC is only about 1$ in spite of the fact that the U-235 content of the two cores differs by 4 kg as noted in Section I-1. Based upon U-235 weighting factors measured in the ATRC, a 4-kg increase in the U-235 content would increase the excess reactivity by approximately 5.0$.

The cross-sectional core diagram of Figure I-2 shows the power generated in each fuel element normalized to a total core power of 250 MW. Nearly all of the detailed fission-rate measurements were made in the quarter-core comprising elements 6 through 15 inclusive. However, since each quarter of the core is a mirror image of the adjacent quarter (referred to as "quarter-core symmetry"), the power-generation values are duplicated in each quarter to obtain a complete

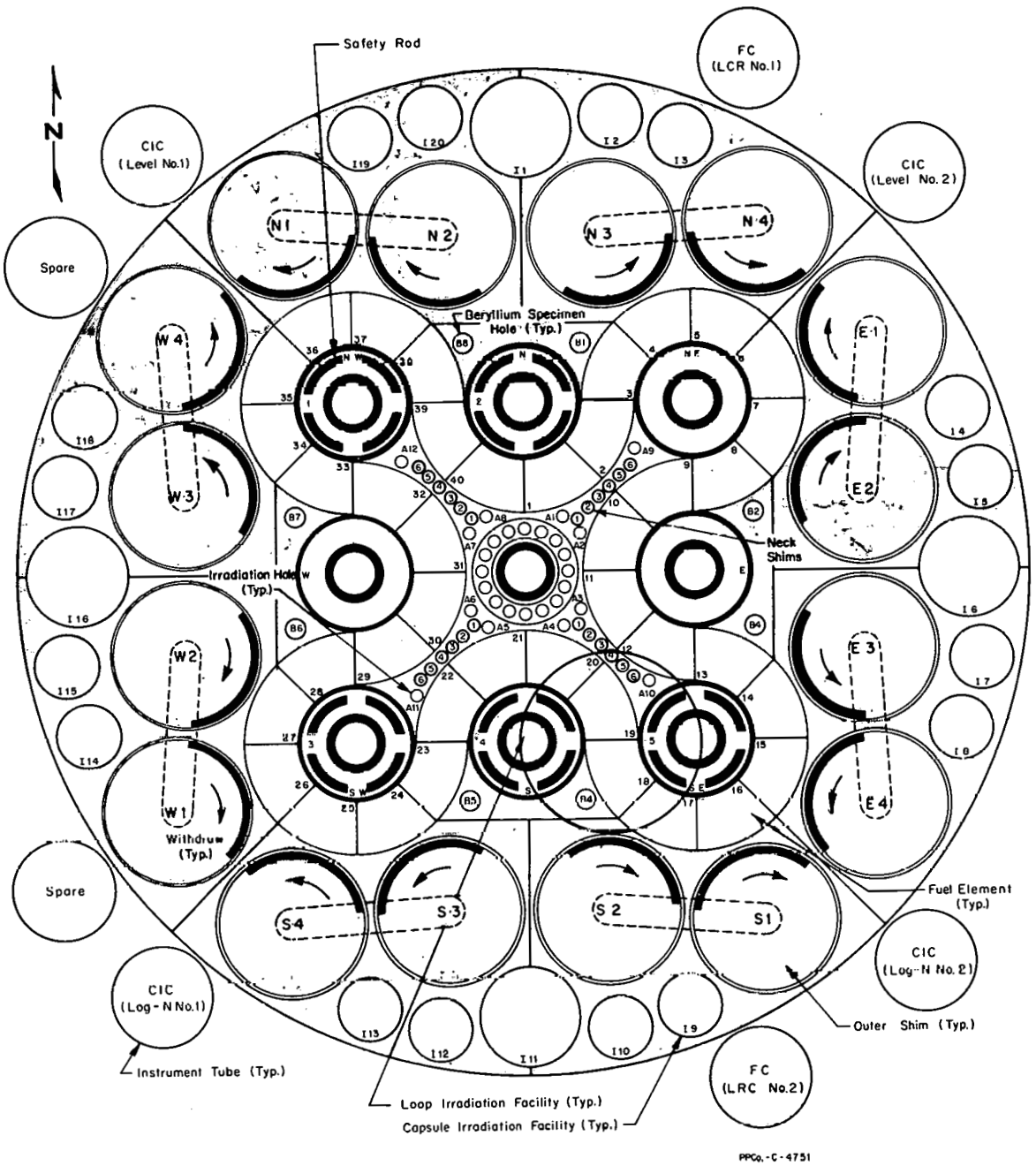

Fig. I-1 ATRC core midplane cross section.

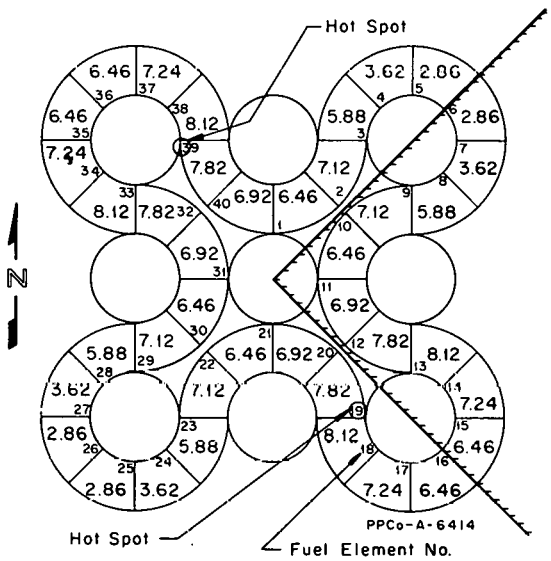

Fig. I-2 ATRC core diagram showing lines of "quarter-core symmetry" and the power generated in each fuel element (in MW) normalized to a total core power of 250 MW.

power map of the core. The detailed data provided the following additional information:

(1) The maximum fission rate in the core at 250 MW is approximately 27,000 watts per gram and occurs in each of the two high-power lobes in fuel positions 19 and 39. Due to a slight asymmetry in the ATRC core near the outboard A-holes in the neck regions (see Figure I-1), there is somewhat less power peaking in core positions 12 and 32, the mirror images of positions 19 and 39.

(2) The axial fission-rate profile in the core has a very symmetrical cosine shape about the radial midplane of the reactor with a peak-to-average ratio of 1.42.

(3) The ratio of peak-to-average fission rate in the radial midplane is 2.66, and for the entire core is 3.80.

(4) As expected, the radial fission-rate gradients in individual fuel elements are quite pronounced and vary considerably from one element to another. For example, the ratio of maximum-to-minimum fission rate in the radial midplane of fuel position 9 is 1.9, compared to 3.6 in position 6.

The power distribution in the ATRC core was determined using quarter-inch wires of U-235 in aluminum as fission-rate monitors. Experience to date indicates that this is the most practical way to measure power distributions in the ATRC since it does not require cadmium ratio measurements to account for variations in the epithermal fission rate. The power calibration measurements described above required approximately one thousand U-235 monitors in five separate runs.

1.5 Effects of Venting ATR Fuel Element Side Plates (N. C. Kaufman)

A detailed mapping of the fission-rate density within a pair of ATRC fuel elements was done to determine the effect of a proposed side plate venting. The two elements used were mapped both with and without vents in the region of the expected hot spot in a TURBO core configuration.

Although the proposed venting is to be done near the top, bottom, and midplane of the side plates, the vents near the midplane will be most influential on the heat generation. Thus, only these vents were actually machined in the test elements. The actual placement and dimensions of the vents in the side plates are shown in Figure I-3.

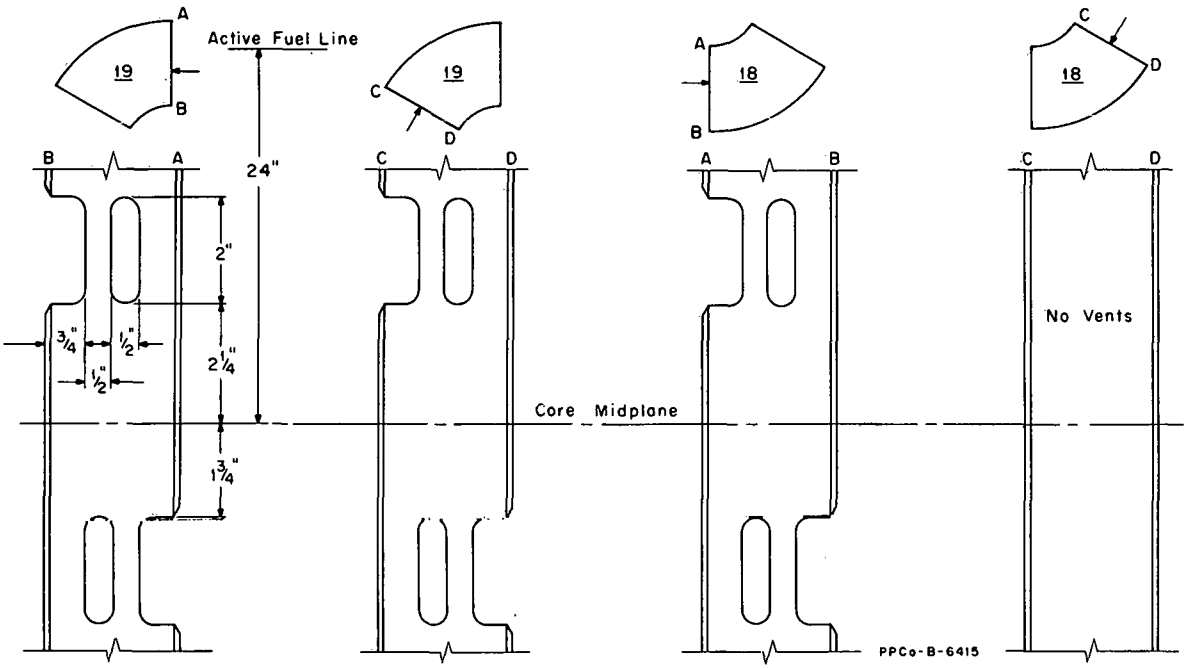

Fig. I-3 Location and dimensions of the venting pattern used in elements in positions 18 and 19.

The hot spot was expected near the interface of fuel positions 19 and 18 on the side of the fuel annulus adjacent to the SE flux trap. This region is circled in the core diagram presented in Figure I-1. Thus, elements in both positions 19 and 18 were studied; and the vents were placed at their interface.

The outer shims and neck shims were positioned to simulate a nominal 40-50-60 MW power split in the ATR, with the 60 MW lobe containing the SE flux trap. Thus, in summary, the measurements were made in the hot-spot region, in the high-power lobe, and with the vents at core midplane.

Profiles of the relative fission rates, both with and without vents, are shown in Figures I-4, I-5, and I-7. The orientation and nomenclature used in these profiles are described in Figure I-6. Comparison of Figures I-4a and I-4b shows that the perturbations due to the vents are rather pronounced at the position 19-18 interface, but are no longer evident at the azimuthal center. Figure I-5 shows the axial perturbation in channel 19, in position 19, near the 19-18 interface. Additionally, with the exception of the normalization, Figures I-7a, -b, -c, and -d may be compared with the calculated, zero-time profiles in the TURBO report, and indicate that the measured fission rate in position 19 diminishes more rapidly than calculated as one moves away from the position 19-18 interface in channels 19 or 18.

All fission rates were calculated from the activation of 1/4-inch, uranium-aluminum wires. This activation was converted to fission rate using constants obtained by the MTR counting room. An overall pointwise standard deviation of $\pm$ 4 percent was calculated from errors in weight grouping and counting statistics. Wire locations were known to within $\pm$ 1/16 inch.

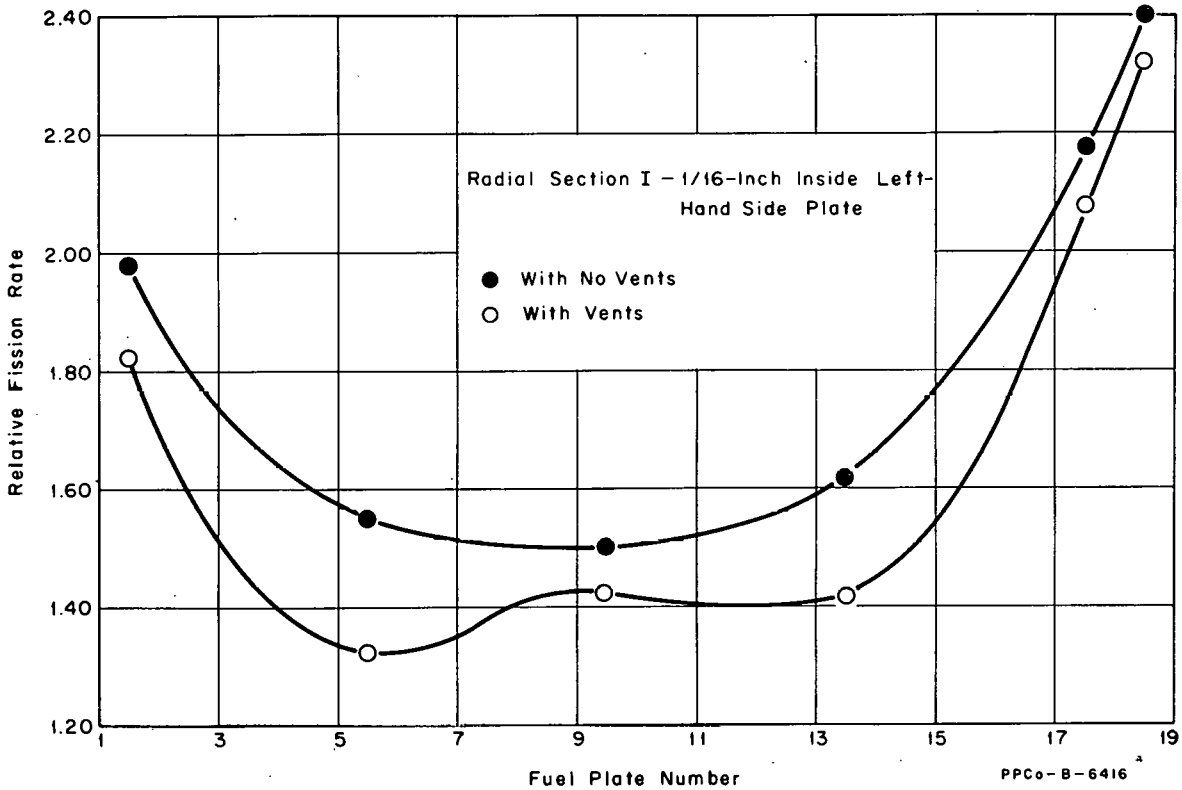

A

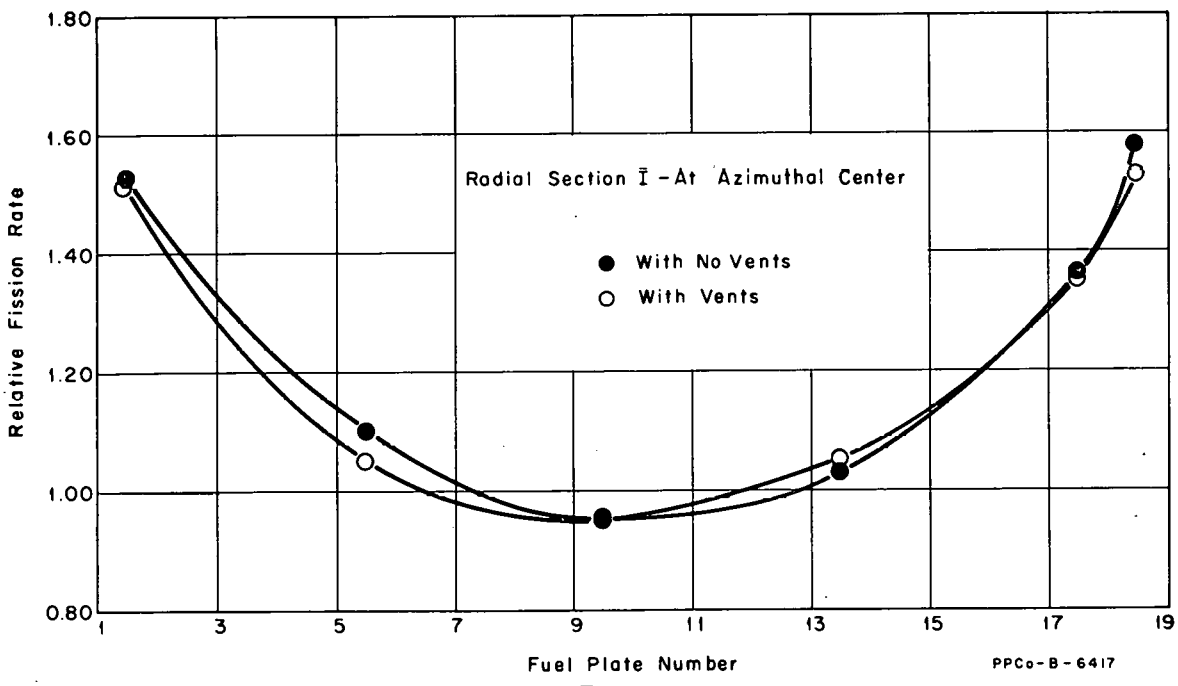

B

Fig. I-4 Midplane radial fission-rate profiles in element 19.

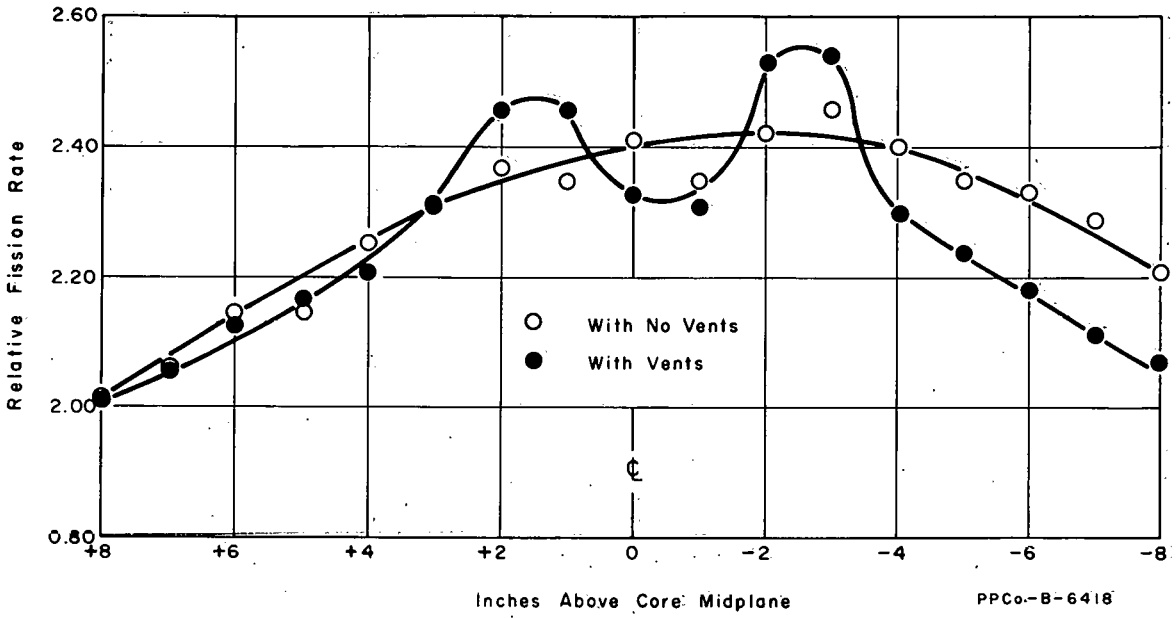

Fig. I-5 Vertical fission-rate profiles in channel 19 of element 19, 1/16-inch-inside, left-hand side plate.

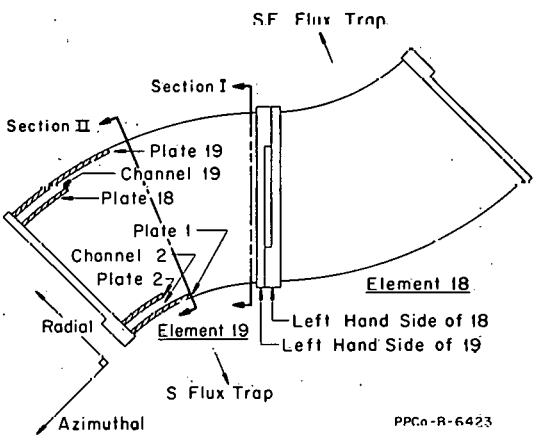

Fig. I-6 Location of the radial sections and nomenclature used in Figures I-4 and I-5.

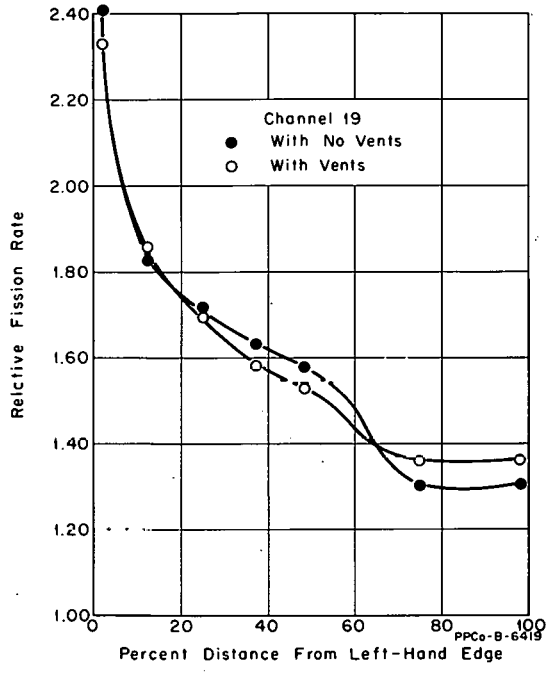

A

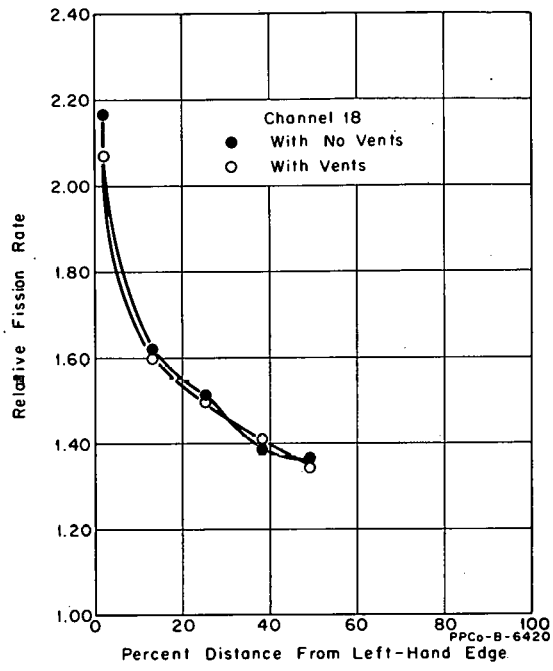

B

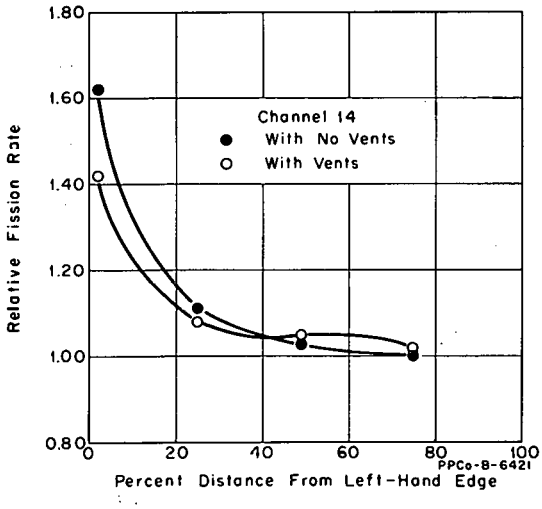

C

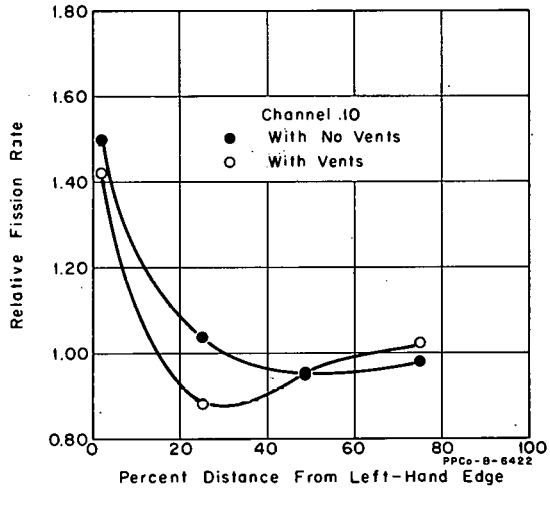

D

Fig. I-7 Azimuthal fission-rate profiles at midplane in element 19.

1.6 ATRC Safety Rod Calibrations (W. L. Schrader, J. L. Durney)

The safety rods in the ATRC have been calibrated using asymptotic periods. These measurements were used to partially evaluate the effects on safety rod worths due to changes in shim configurations, changes in flux trap and experiment composition, and safety rod interactions. The measurements were made with the ATRC core in the TURBO mock-up configuration described above. A typical calibration curve is shown in Figure I-8, and the safety rod worths are summarized in Table I-3. Only one of the five safety rods in the ATRC (rod 4, see Figure I-1) was calibrated over its entire range of 36 inches [a]. Rods 1 and 3 were calibrated from 19 to 36 inches, and the ganged pairs (1,5 and 3,4) were calibrated from 23 to 36 inches. The calibration curve of rod 4, shown in Figure I-8, was used to extrapolate the partial calibration curves of the other rods in order to obtain the total worths listed in Table I-3. All the partial calibration curves as well as the entire calibration curve of rod 4 have the same shape as the safety rod calibration curve measured in the ATR Critical Experiment [6], within ± 1/2 inch of rod position.

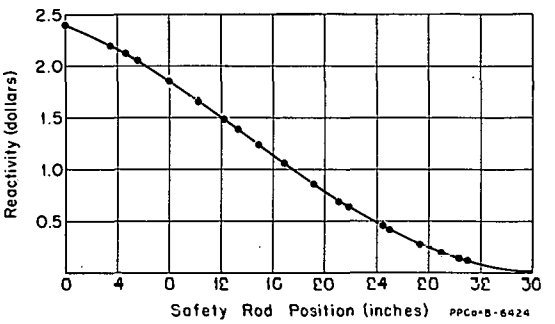

Fig. I-8 Reactivity calibration curve of safety rod No. 4 in the ATRC.

Three different shim configurations were used in the calibration to determine their effect on the safety rod worths. The shutdown reactivity in the safety rods was found to be greater than 7$ in each shim configuration. Also, the worth of the safety rods increased as the outer shims were withdrawn and as the neck shims were inserted. The core power distributions in each of the balanced shim configurations were not known except that the four lobes were at approximately the same power level; whereas the unbalanced shim configuration was the same as that for the 40-50-60 power split.

Preliminary information indicates that the worth of the ganged set of five safety rods may be approximately equal to the sum of the individual rod worths. Comparisons were made from two extreme cases, assuming maximum rod interaction to occur between adjacent rods (3 and 4) and minimum interaction between widely separated rods (1 and 5). Comparison of the ganged worth to the sum of the individual worths in both cases indicated only a small interaction between rods.

A safety rod in an outer flux trap (rod 4) was worth more than either of the two inner-flux-trap rods measured (rods 1 and 3). Also, the worths of the rods in the inner flux traps were affected more than those in the outer flux traps as the shim configuration was changed. The worths of the safety rods were also affected by the difference in U-235 content of the flux trap. The rod worths increased with increased U-235 content. This effect was more

---

[a] The poison section of an ATRC (as well as an ATR) safety rod is only 36 inches long; whereas the core height is 48 inches. In the scrammed position, the bottom of the safety rod poison section is 9 inches above the bottom of the core. When the rod is raised 36 inches to its upper limit, the bottom of the poison section is 3 inches below the top of the core.

TABLE I-3

ATRC SAFETY ROD WORTHS FROM PERIOD MEASUREMENTS

Safety Rod Number	40-50-60 Power Split	Balanced Core	
	Shim Configuration No. 1[a] ($)	Shim Configuration No. 2[a] ($)	Shim Configuration No. 3 [a] ($)
1	1.9	1.3	1.0
2	2.4[b]	2.2[b]	2.1[b]
3	1.4	2.1	1.4
4	2.4	2.2	2.1
5	1.9[c]	1.3[c]	1.0[c]
Ganged set of 5 rods[d]	10.0	9.1	7.6
1 and 5 ganged	3.9		
1 and 5 summed	3.8		
3 and 4 ganged	3.6		
3 and 4 summed	3.8		

[a] Shim Configurations:

No. 1 Outer shims N12, W34, S12, and E34 were at 100°; all other outer shims were in; neck shims 5 and 6 were out in each neck; and all other neck shims were initially in.

No. 2 All outer shims were at 80°, and all neck shims were in.

No. 3 All outer shims were in; neck shims 1, 2, 3, and 4 were out in each neck; and all other neck shims were initially in.

[b] Inferred from rod 4 measurements.

[c] Inferred from rod 1 measurements.

[d] The worths of the ganged sets of 5 rods were obtained by summing the individual rod worths.

pronounced with the outer shims withdrawn and the neck shims inserted than with the outer shims inserted and the neck shims withdrawn.

It should be noted that the safety rods in the ATR will have hafnium poison sections rather than cadmium as in the ATRC. Consequently, it is expected that the reactivity worth of the safety rods in the ATR will be somewhat greater than the ATRC values reported here.

1.7 COREMAP: A Computer Program for Reduction of ETRC Flux Data (S. R. Reyes)

Hand calculations of ETRC flux data are tedious and time consuming. Because of the time involved, there are occasions when ETR or ETRC operating time is lost; for example: generally, ETR operation may not resume after a scheduled shutdown until ETRC mock-up data have been evaluated. Frequently, ETRC data are obtained in a series of flux runs with each run dependent on the results of the previous one. In order to best utilize reactor and personnel time and to reduce calculational errors, the analysis of ETRC flux data has been programmed for the 7040.

The ETRC-ETR core map program is based on a (10 x 10) array with each point corresponding to a core position. The program has been designed so that the only core positions having a definite assignment are the 16 control rod positions. All other positions can be assigned as either fuel elements or experiments. Thus, a new program need not be written for each core configuration.

The ETRC activation data are measured on the MTR Automatic Foil Counting Facility which punches the results on paper tape. Computer input is obtained by putting the paper tape in the automatic tape-to-card converter. Data are obtained only in the fuel element positions; therefore dummy cards must be inserted in all other positions. The program provides for the calculation of ETRC thermal neutron flux, ETRC power, ETR thermal neutron flux at 175 MW, total [a] fuel element flux, total [a] control rod flux, and percent of total core power. The results are printed in an array corresponding to the core configuration. Each cell contains the ETRC flux, ETR flux, and the percent of total core power generated in the cell.

The program will be expanded in the future to perform other calculations. The primary addition to the program will be an operation which will calculate the percent change in the flux and power distribution from that of any previously calculated core map.

1.8 Water Displacement Coefficient of Reactivity for ARMF-I Central Experimental Hole (J. W. Rogers)

An experimental program has been conducted to determine the reactivity effect of displacing different volumes of water at various locations in the ARMF-I central experimental hole.

The ARMF-I central experimental hole is a water column, 6.583 inches square, extending through the center of the core (Figure I-9). A universal capsule holder made of perforated aluminum occupies approximately one-quarter inch of the space around the perimeter of the experimental hole [7]. If an object composed of a material with a low absorption cross section (such as aluminum) should fall into this hole, the net effect of displacing part of the water would be the algebraic sum of (a) a negative reactivity caused by displacing moderator and (b) a positive reactivity due to the difference between the cross sections of the object and the water. Since the purpose of the experiment was to measure the net effect of displacing water, no attempt was made to separate the effects.

The experimental program was divided into two main parts: (a) determining the vertical and horizontal displacement coefficients using a small object and (b) measuring the reactivity effects of relatively large displacements at only a few positions in the water hole. Aluminum was chosen to make all the displacement measurements because it has a cross section smaller than water and because it is used extensively around the reactors. The vertical and horizontal coefficients were measured using a solid aluminum sample, 0.5

---

[a] Total flux is obtained by summing the flux values in each cell over the number of fuel element or control rod positions.

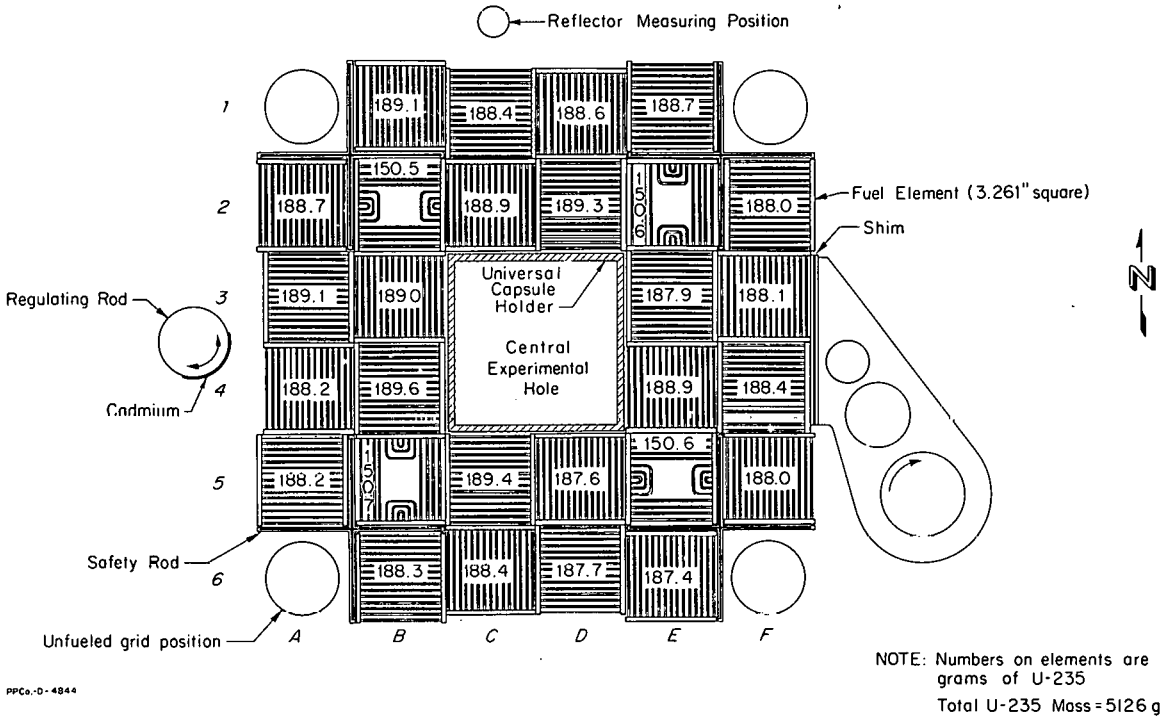

Fig. I-9 ARMF-I core loading diagram.

inch in diameter and 2.0 inches long. The reactivity effects of larger aluminum samples with volumes ranging between 127 and 1054 cm^3 (3 by 3 by 6 inches) were measured to determine the nonlinear effects by comparing their reactivity effects to values obtained from the integral,

$$\int^{V} S(r,h)\, dV'$$

where S is the measured coefficients to displacement and V is the sample volume.

Figure I-10 is a plot of the measured vertical and radial coefficients. Polynomial expressions were found by a computer fitting process to fit the displacement coefficient curves. The expression for the coefficient along the horizontal midplane as a function of the distance, r, in centimeters, from the center of the experimental hole is

$$S(r) = 2.879 + 0.2660\ r - 0.1351\ r^2 + 0.03121\ r^3 - 0.0019\ r^4 \quad .$$

A similar expression for the coefficient at the center of the experimental hole as a function of vertical distance, h, in centimeters, from the horizontal midplane is

$$S(h) = 2.826 + 0.253\ h - 0.0076\ h^2 + 0.00013\ h^3$$

where S(r) and S(h) are in units of $\mu k/cm^3$.

Coefficients were measured for only the part of the central experimental hole that is inside the universal capsule holder. It was found from the experiment

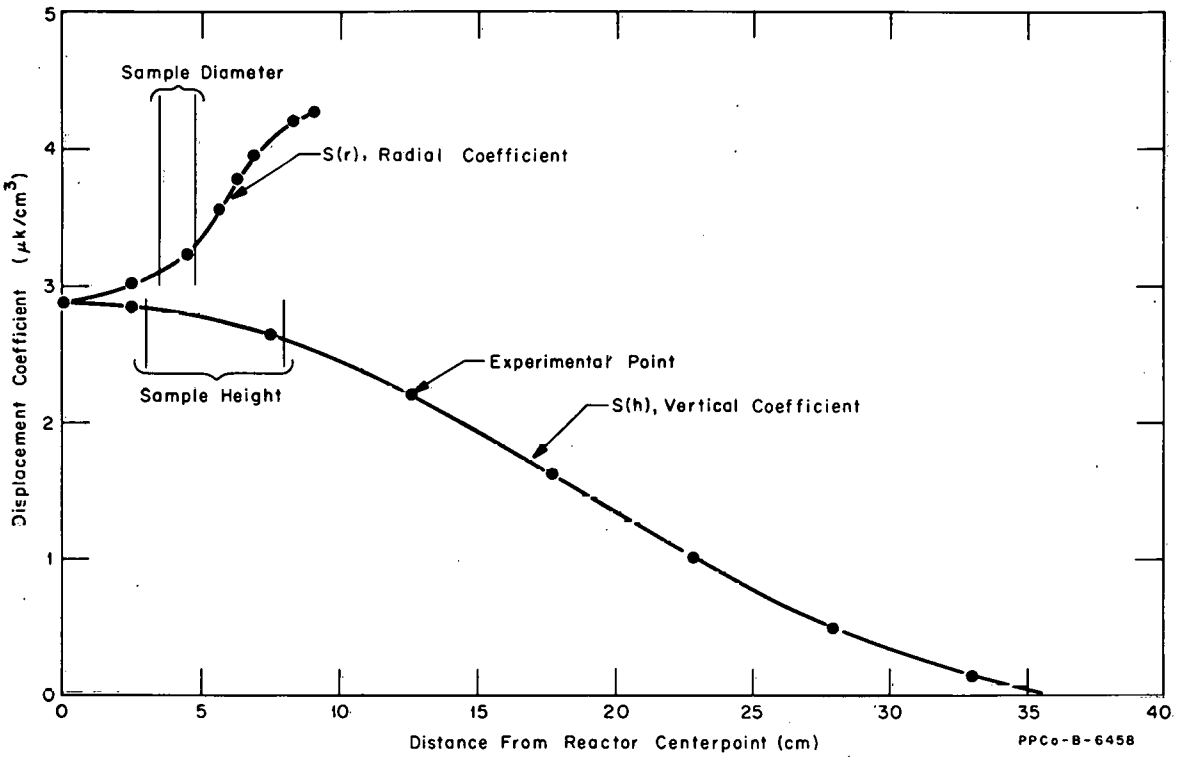

Fig. I-10 ARMF-I radial and vertical water displacement coefficients.

that all of the displacement coefficients within the universal holder were positive (ie, if the water is displaced by aluminum, a positive reactivity results). Previous experiments have shown, as would be expected, that the displacement coefficient of part of the water occupied by the perforated universal holder and the water between the universal holder and the fuel is negative.

The comparison of the measured and the integral prediction of reactivities for the larger aluminum samples is shown in Table I-4. As can be seen in Table I-4, the reactivity effects of aluminum volumes in the experimental hole up to nearly 500 cm^3 can be predicted by this method with good accuracy. However, at the larger volume of 1054 cm^3, the technique underestimates the reactivity effect by about 11 percent. Even though the technique becomes less accurate for large volumes, it has proven useful in estimating water displacement effects.

TABLE I-4

PREDICTED AND MEASURED WATER DISPLACEMENT COEFFICIENTS

Sample Volume (cm^3)	Measured [ρ (μk)]	$\int^V S(r,h)dv^1$ [ρ (μk)]
1054	3858	3425
443	1548	1552
325	1135	1140
214	704	710
127[a]	396	398
127[a]	453	456

[a] Measured at different positions.

A reactivity coefficient due to a void is of interest but is difficult to determine for large volumes other than by calculational techniques. However, measurements made on a 46 cm^3 void and a 46 cm^3 aluminum sample show that the reactivity difference is approximately + 1 μk/cm^3. The validity of applying a correction based on these measurements to calculate the effect of large voids is questionable because of nonlinear effects.

2. ENGINEERING EXPERIMENTS
(V. A. Walker)

2.1 PAED G-12 ETR Water Loop (E. H. Porter, V. A. Walker)

A loop facility in which irradiations may be performed on fuel materials of possible use in high performance test reactors has been constructed. Operation of this facility began during ETR Cycle 68. The loop employs the once-through concept in that a side stream of ETR primary coolant is pressurized, pumped through the sample train, and returned to the ETR primary coolant system. The 2.5-inch-diameter, Zircalloy 2, in-pile tube occupies ETR core position G-12. Through flux trapping and selective ETR fuel core loading, the sample fission rate may be varied up to an equivalent maximum heat flux of about 2.5×10^6 Btu/hr-ft^2.

The initial experiment was directed toward proof testing of fuel materials that may be used in the ATR or HFIR. The calculated conditions for this experiment together with the fuels tested are shown in Table I-5. The experiment operated successfully for 2050 MWd, with about nine days at full

TABLE I-5

OPERATING CHARACTERISTICS OF ATR
FUEL MATERIALS EXPERIMENTS -- ETR CYCLE 68

Fuel Material	Maximum Nominal Heat Flux (10^6 Btu/hr-ft^2)	Maximum Nominal Wall Temperature (°F)	Fission Density (10^{20} f/cc)
50 wt% UAl_3 with 0.19 wt% B_4C	2.15	340	8.0
55 wt% UAl_3 with 0.19 wt% B_4C	1.8	295	6.6
41 wt% U_3O_8 with 0.19 wt% B_4C	2.15	340	8.0
35 wt% U_3O_8 with 0.19 wt% B_4C	2.3	350	8.5
41 wt% U_3O_8	1.5	310	5.0

power. Visual inspection of the plates in the ETR canal indicated the formation of a light brown coating upon those plates operating near the maximum wall temperature. Five of these plates will be replaced with unirradiated plates, and the assembly will be returned to the G-12 position for additional irradiation.

2.2 ATR Fuel Element Thermal-Hydraulic and Structural Performance (M. L. Griebenow, C. A. Moore, D. C. Weddle)

2.21 Thermal-Hydraulic Analysis. The previously reported [8] ATR isothermal hydraulic computer program that has been experimentally verified has been expanded to allow heat transfer. In addition to solving the hydraulic balances of continuity and energy with the stipulation that, at a vent, all channels in communication with the vent must be at the same pressure, the program now solves the matrix generated by the conduction and convection equations

with the required boundary conditions. The program iterates on flow until all of the requirements of pressure drop and heat removal are met simultaneously. The program still allows nonuniform channels, and it also allows a vertical and radial variation in the heat generation. The Dittus-Boelter correlation is used to compute the film coefficient. There are sufficient multipliers inserted into the thermal and hydraulic equations to permit hot spot-hot channel analysis. The program has been verified by hand calculations.

It is planned that an instrumented fuel element with a fuel plate containing twice the normal fuel loading will be inserted in the first ATR power run. This element should provide data to check the nonisothermal calculations.

2.22 ATR Fuel Element Stress Analysis. A theoretical analysis of ATR fuel elements was made to determine fuel plate stresses and deflections caused by temperature gradients at reactor operating conditions. These thermal gradients produce stresses not present in the isothermal static and hydraulic tests. For several channel configurations, azimuthal pressure and thermal stress and vertical plate deflection were calculated for Plates 18 and 19. Axial thermal stresses were calculated for Plates 18 and 19 in two cases: (a) the element with the highest peak power, (b) the element with the highest peak power including hot spot-hot track factors.

(1) Pressure-Thermal Azimuthal Stress and Vertical Plate Deflection. Only Plates 18 and 19 were analyzed, since these are potentially the weakest plates in the ATR element. Items calculated included:

(1) Plate 19 center-span azimuthal pressure stress

(2) Plate 19 center-span, azimuthal thermal stress

(3) Plate 19 vertical pressure deflection

(4) Plate 19 vertical thermal deflection

(5) Plate 18 center-span total azimuthal stress (due to pressure differential across Plate 19 and induced by Plate 19)

(6) Plate 18 vertical deflection induced by Plate 19.

Stresses and deflections were calculated by a method developed for the ATR plate geometry and reported in the literature [4]. The method was modified to include a fixed end moment for Plate 19. For the range of differential pressures and temperatures involved, the calculations hold for both roll-swaged and welded joint elements. Temperatures and pressure differentials were obtained from IBM computer program MACBRE, 40.0041, which was written for the ATR fuel element.

The following assumptions made were:

(1) Fuel plate material is homogeneous 6061-0 aluminum

(2) The elastic limit is not exceeded

(3) All joints are completely fixed against rotation, except that the maximum end moment for Plate 19 is equal to 0.4 of the fully developed plastic moment.

(4) The side plate temperature is 140°F for all calculations

(5) The average temperature of plates 1-18 is 350°F for determining the modulus of elasticity, E, for high peak power elements.

(6) The average temperature of plates 1-18 is 475°F for determining E for the hot spot, hot tract, peak power elements.

(7) Azimuthal stress at the azimuthal plate centerline is the critical stress.

Calculations were made for the following problems:

(1) Problem 1 -- peak power element. Channel 20 -- 0.063 inch; channels 1 to 19 -- 0.078 inch.

(2) Problem 2 -- hot spot, hot track, peak power element. Channel 20 -- 0.063 inch; channels 1 to 19 -- 0.078 inch.

(3) Problem 3 -- peak power element. Channel 20 -- 0.113 inch; channels 1 to 19 -- 0.078 inch.

(4) Problem 4 -- hot spot, hot track, peak power element. Channel 20 -- 0.113 inch; channels 1 to 19 -- 0.078 inch.

(5) Problem 5 -- peak power element. Channel 20 -- 0.175 inch; channels 1 to 19 -- 0.078 inch.

(6) Problem 6 -- hot spot, hot track, peak power element. Channel 20 -- 0.175 inch; channels 1 to 19 -- 0.078 inch.

(7) Problem 7 -- peak power element. Channel 20 -- 0.063 inch; channels 18 and 19 -- 0.072 inch; channel 1 to 17 -- 0.078 inch.

(8) Problem 8 -- hot spot, hot track, peak power element. Channel 20 -- 0.063 inch; channels 18 and 19 -- 0.072 inch; channels 1 to 17 -- 0.078 inch.

(9) Problem 9 -- hot spot, hot track, peak power element. Channel 20 -- 0.175 inch; channel 19 -- 0.083 inch; channel 18 -- 0.073 inch; channel 19 has a 0.006-inch dimple at 28.75 inches below the top of the fuel plates.

Complete results of the calculations are listed in Table I-6. The maximum stress was 3180 psi in Plate 18 at a plate surface temperature of 427°F; the yield strength of 6061-0 aluminum is 5600 psi at 427°F. The maximum stress in Plate 19 was 2750 psi at 369°F; the yield strength is 7400 psi at 369°F.

The deflection of Plate 19 due to differential pressure acting across the plate was found to be only slightly larger than the induced deflection of Plate

TABLE I-6

THERMAL AND PRESSURE AZIMUTHAL STRESS AND PLATE DEFLECTION

Problem Number	ΔP Channel 19 to 20 (psi)	ΔP Channel 18 to 19 (psi)	ΔT Plate 19 to Rest (°F)	Center-Span Plate 19 Pressure Stress Outside/Inside (psi)	Center-Span Plate 19 Thermal Stress Outside/Inside (psi)	Center-Span Plate 19 Combined Stress Outside/Inside (psi)	Center-Span Plate 18 Total Stress Outside/Inside (psi)	Yield Stress 6061-0 Al at Plate Temperature (psi)	Vertical Pressure Deflection Plate 19 to Channel 20+ (in. x 10^3)	Vertical Thermal Deflection Plate 19 to Channel 20+ (in. x 10^3)	Combined Vertical Deflection Plate 19 to Channel 20+ (in. x 10^3)	Vertical Deflection Plate 18 Due to ΔP_{19} to Channel 20+ (in. x 10^3)	Location Below Top of Plate (in.)
1	-1.24	+0.25	68	330 C 312 T	990 T 1213 C	660 T 901 C	134 C 163 T	7900	-0.55	+2.51	+1.96	-0.51	44.5
2	-1.54	+0.38	89	408 C 371 T	1353 T 1670 C	945 T 1299 C	157 C 193 T	6900	-0.69	+3.72	+3.03	-0.64	44.5
3	-2.18	+0.17	27	530 C 532 T	393 T 482 C	187 C 50 T	252 C 301 T	7900	-0.96	+0.96	0	-0.90	44.5
4	-2.41	+0.27	47	638 C 551 T	715 T 882 C	77 T 301 C	265 C 318 T	7000	-1.07	+1.97	+0.90	-1.00	44.5
5	+4.05	0	57	1075 T 988 C	830 T 1016 C	1905 T 2004 C	496 T 575 C	8000	+1.78	+2.10	+3.88	+1.66	14
6	+4.47	0	89	1184 T 1077 C	1353 T 1670 C	2537 T 2747 C	522 T 617 C	7400	+1.99	+3.72	+5.71	+1.86	14
7	-0.93	+0.24	77	247 C 227 T	1120 T 1374 C	873 T 1147 C	98 C 120 T	8000	-0.41	+2.84	+2.43	-0.87	44.5
8	-1.25	+0.37	96	331 C 301 T	1460 T 1804 C	1129 T 1503 C	123 C 154 T	6500	-0.56	+4.02	+3.46	-1.17	44.5
9	0	+5.15	77	0 0	1170 T 1445 C	1170 T 1445 C	3180 T 2650 C	5600	0	+3.22	-3.22	0	28.75

18; and since the difference in Plates 18 and 19 temperatures is small, it is postulated that the differential deflection between Plates 18 and 19 will be negligible for all reactor operating conditions. A similar argument is used for the remaining channels.

(2) Axial Thermal Stress Calculations. Plates 18 and 19 were analyzed for axial thermal stress for two conditions: (a) the nominal peak power element; and (b) the maximum peak power element, hot spot, hot track factors included. Each plate was considered to be integral with its proportional part of the side plate; the resulting unit being free to expand axially, but with the ends restrained against rotation. Plate temperatures were calculated from IBM computer program MACBRE, 40.0041, and PDQ, 40.0018; side plate temperatures were taken as 140°F. Stresses were calculated from the equation:

$$\sigma(x) = \frac{1}{A} \sum_{i=1}^{14} \left[\Delta T(y)_i\right] \left[E_i\right] \left[\alpha_i\right] - E_x \alpha_x \Delta T(y)_x$$

where $\sigma(x)$ = axial plate or side plate stress at any point in psi

A = area of fuel plate and side plate in $in.^2$

i = integration regions as shown in Figure I-11

$\Delta T(y)_i$ = average temperature increase in regions i in °F

E_i = modulus of elasticity of region in i in psi

α_i = coefficient of thermal expansion in region i in in./in.-°F

E_x = modulus of elasticity at point of stress calculation in psi

α_x = coefficient of thermal expansion at point of stress calculation in in./in.-°F

$\Delta T(y)_x$ = increase in temperature at point of stress calculation in °F.

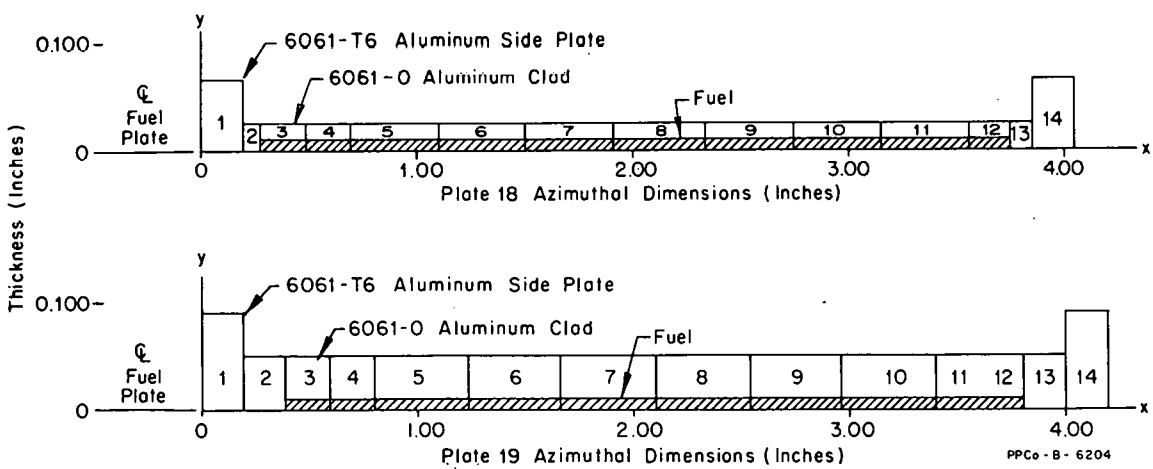

Fig. I-11 Fuel plate thermal stress integration regions.

The following assumptions were made in the analysis:

(1) There is no slippage of the swaged attachment of fuel plates to side plates.

(2) The fuel plate material is homogenous 6061-0 aluminum

(3) The elastic limit is not exceeded

(4) The side plate temperature is 140°F

(5) The initial temperature of fuel plates and side plates is 70°F.

Maximum stresses for the peak power element were: (a) 16,960 psi tension in the side plate adjacent to Plate 19, (b) 14,450 psi compression at the center of the fuel in plate 19, (c) 11,450 psi tension at the surface of Plate 19, and (d) 7300 psi compression at the surface of Plate 19. Maximum stresses for the peak power element, hot spot, hot track factors included were: (a) 22,500 psi tension in the side plate adjacent to Plate 19, (b) 18,800 psi compression at the center of the fuel in Plate 19, (c) 16,800 psi tension at the surface of Plate 19, and (d) 10,200 psi compression at the surface of Plate 18. Table I-7 lists plate temperatures and stresses for each region of Plate 19.

(3) Discussion of Results. The theoretical analysis shows that the azimuthal fuel plate stresses developed by hydraulic pressure differentials and thermal differentials will be much less than the yield strength of 6061-0 aluminum at all reactor operating conditions for elements meeting design specifications. The analysis indicates, however, that axial thermal stresses will exceed the yield strength of the fuel plates at some points across the plates, particularly near the center of the fuel.

Four factors have influenced the conclusion that axial yielding will not affect the operation of the fuel element:

(1) Axial thermal stresses are not additive with azimuthal stresses and will not contribute to plate deflections

(2) Regions where the axial yield stress is exceeded are small

(3) Yielding reduces thermal stresses

(4) Thermal distortion tests [9] showed no significant plate rippling.

TABLE I-7

AXIAL THERMAL STRESS DISTRIBUTION PLATE 19
PEAK POWER ELEMENT AT 25 INCHES BELOW TOP OF PLATES
(Channel 20 -- 0.113 inch,
Channel 1 -- 0.108 inch, Channel 2 to 19 -- 0.078 inch)

Region i[a]	Average Clad Surface Temperature $T(y)_i$ (°F)	$E_i \times 10^6$ (psi)	$\alpha_i \times 10^{-6}$ in./in./°F	$\Delta T(y)_i$ (°F)	$E_i.\alpha_i.\Delta T(y)_i$ (psi)	$\sigma(x)_t$[b] (psi)	$\sigma(x)$[c] Stress at Outside Clad (psi)
1	140	9.85	13.9	70	8,890	25,850	+16,960 T
2	208	9.6	13.2	138	17,500		+ 8,350 T
3	327	9.1	13.35	257	31,200		- 5,350 C
4	348	8.9	13.4	278	33,100		- 7,300 C
5	338	9.0	13.35	268	32,200		- 6,350 C
6	321	9.1	13.35	251	30,500		- 4,650 C
7	301	9.2	13.3	231	28,300		- 2,450 C
8	281	9.3	13.25	211	26,000		- 150 C
9	267	9.3	13.2	197	24,200		+ 1,650 T
10	256	9.4	13.2	186	23,100		+ 2,750 T
11	249	9.4	13.2	179	22,200		+ 3,650 T
12	234	9.5	13.15	167	20,900		+ 4,950 T
13	183	9.7	13.1	113	14,400		+11,450 T
14	140	9.85	12.9	70	8,890		+16,960 T

[a] See Figure I-11 for region locations.

[b] $\sigma(x)_t = \frac{1}{A} \sum_{i=1}^{14} \left[\Delta T(y)_i\right] \left[E_i\right] \left[\alpha_i\right]$.

[c] $\sigma(x) = \sigma(x)_t - E_x \alpha_x \Delta T(y)_x$.

3. MATERIALS RESEARCH
(J. M. Beeston)

3.1 Microprobe Examination of Irradiated UO_2-Al and U-Al Alloy Nuclear Fuel Materials (W. F. Zelezny)

Application of the microprobe to the study of two irradiated MTR fuel materials is described. The presence of two of the fission products (cerium and barium) in the two fuel materials which had undergone different burnups were qualitatively determined. Both of these fission products were found in the fuel which had undergone the higher burnup (the UO_2-Al fuel). Only cerium was found in the fuel with the lower burnup (the U-Al alloy fuel).

3.11 Materials. Two specimens, designated by the numbers 28-3 and 79-3, were examined. These were taken from sample MTR fuel plates of the compositions given in Table I-8. The radiation exposure histories, radioactivities, and other pertinent data concerning these specimens are also given.

TABLE I-8

COMPOSITIONS, RADIATION HISTORIES, AND RADIOACTIVITES OF FUEL SPECIMENS

Composition	Specimen 28-3	Specimen 79-3
Core	52 wt% UO_2, 30 percent enriched, Al matrix	50 wt% U, fully enriched, 3 wt% Sn, Al matrix
Cladding	1100 Al	APM 583 Al alloy
Radiation History	**Specimen 28-3**	**Specimen 79-3**
Number of cycles in MTR	25	4
MWd	15,775	2,652
nvt	25.77×10^{20}	3.85×10^{20}
Burnup	83 percent	24 percent
Temperature during irradiation	65°C	65°C
Time since removal from reactor	32 months	35 months
Radioactivity	**Specimen 28-3**	**Specimen 79-3**
At "contact"	> 5r/hr	> 5r/hr
Beta-to-gamma ratio	≈ 5/1	≈ 5/1

Preparation of the specimens was accomplished entirely by remote control in the MTR Hot Cell. By the use of a micro-cutoff wheel, wafers 10 mils thick were made by cuts across the fuel sample, giving a cross-section of the core and its cladding as shown in the sketch in Figure I-12. The wafers of fuel plates were held upright during the mounting process by brass specimen supports formed from pieces of brass sheet. The fuel plate wafer and its support were mounted in a standard 1-1/4 inch diameter metallurgical mount by embedding in a mixture of 50 volume percent Fisher Quickmount (a liquid epoxy) and 50 volume percent lead powder. The lead provided shielding against the radioactivity of the specimen.

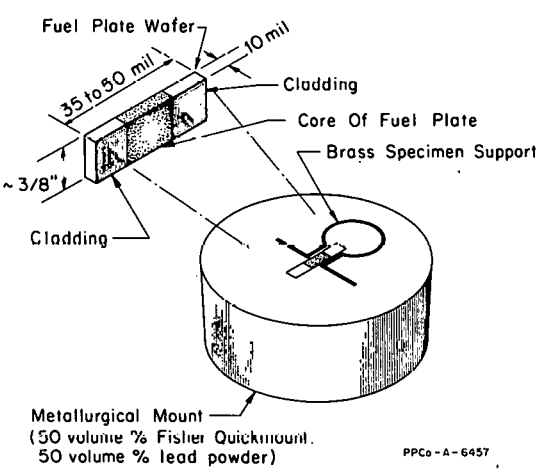

Fig. I-12 Specimen mounts used in preparing irradiated specimens for microprobe examination.

3.12 Microprobe Examination. A Model 400 MAC electron probe microanalyzer was employed in this investigation. No shielding was used other than the lead powder incorporated in the specimen mount. Exposures appreciably

greater than those due to the normal background level were avoided by handling specimens with tongs and tweezers as rapidly as possible to minimize exposure of personnel to radiation.

Techniques in the use of the microprobe included: (a) motor driven scans across the sample accompanied by the simultaneous recording on strip charts of the resultant X-ray intensities, (b) counting for fixed times at points on the sample of both peak and background intensities for quantitative determinations, and (c) counting "over-the-peak" for the detection of the fission products, cerium and barium.

A KAP crystal was used in one of the spectrometers for the selection of Al Kα radiation, while an ADP crystal was used for all the other elements mentioned in this report. Pulse height analyzers were employed in the counting circuits at all times with the X-ray line peaks carefully centered in the window, and the window widths were made as narrow as possible to minimize the high background from the radioactivity of the specimens.

3.13 Results and Conclusions. The U-Al alloy fuel in Specimen 79-3 consisted of an alloy of 50 weight percent uranium in aluminum, and had been irradiated to a burnup of 24 percent. The uranium was segregated in the form of uranium aluminide particles shown in the photomicrograph reproduced in Figure I-13. One-dimensional scans with the probe showed the uranium to be confined within these particles, with no uranium detectable outside the boundaries of the particles.

A search was made for the fission products, barium and cerium, by counting over the Ba Lα and Ce Lα X-ray line peaks. Before looking for these elements, however, it was considered desirable to verify that variations did not occur in the X-ray backgrounds from excitation of aluminum and uranium by the electron beam of the microprobe or in the background due to the radioactivity of the specimen which would give false indications of the presence of either barium or cerium. This was accomplished by making counts over-the-peak on 1100 aluminum and on depleted uranium while being excited with the electron beam and on the background due to the radioactivity of the specimen during which time the electron beam was turned off. No spurious indications of barium or cerium were found in any of these tests. Figure I-13 shows the result of counting over the cerium peak on 1100 aluminum, while Figure I-16, page 27, shows the same type of count on a depleted UO_2 particle.

Cerium was found in the fuel particles and, to a slightly lesser extent, in the aluminum matrix immediately adjacent to the fuel particles. No cerium was found in the aluminum matrix at distances greater than approximately 10 microns from the fuel particles. No definite indications of barium have been found as yet in the fuel particles of Specimen 79-3, or in the aluminum matrix immediately surrounding them.

The UO_2-Al fuel material, designated as Specimen 28-3, contained UO_2 of 30 percent enrichment and had been irradiated to the very high burnup of 83 percent. The 30 percent enrichment was attained by mixing particles of fully enriched UO_2 with the appropriate quantity of depleted UO_2. The fact that the fuel particles are mixed is revealed in a most interesting manner in Figure I-14 which shows that the enriched UO_2 particles have changed drastically in appearance in comparison with the depleted particles. This figure also

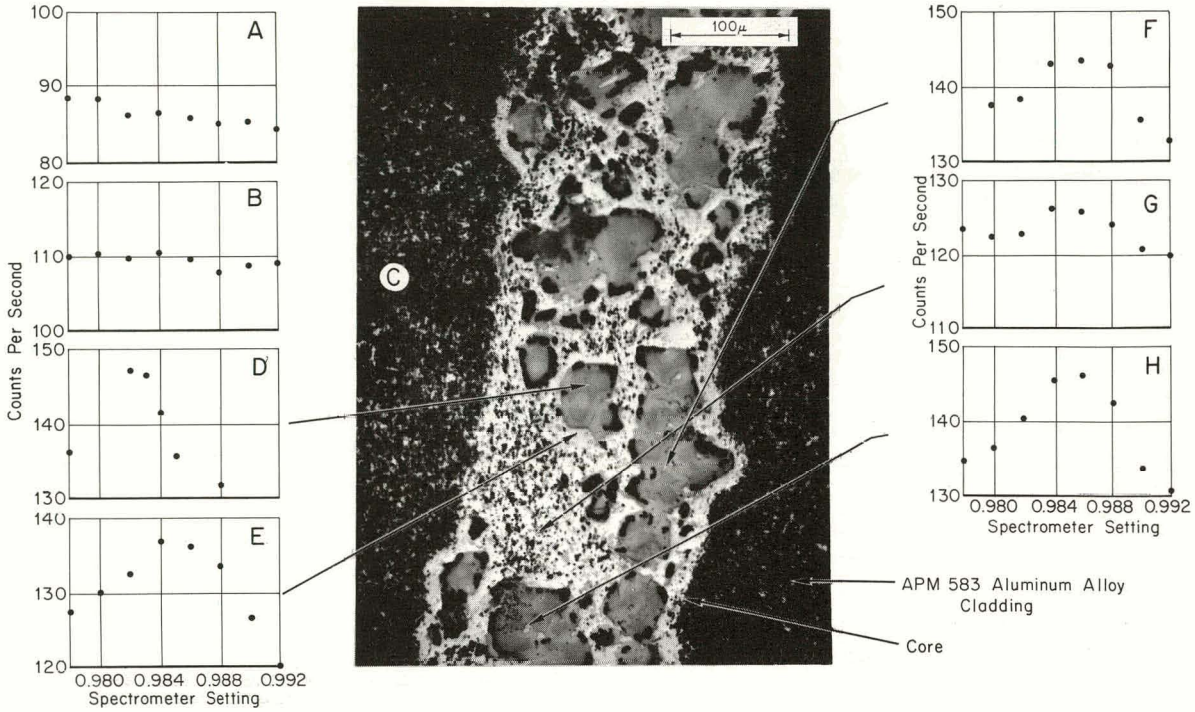

Fig. I-13 Photomicrograph and cerium Lα X-ray counts of 50 weight percent U-Al fuel material.

A. Over-the-peak count on 1100 Al
B. Over-the-peak count from background due to radioactivity of specimen, microprobe beam off
C. Photomicrograph; polished; unetched
D. Over-the-peak Ce Lα count on fuel particles
E. Over-the-peak Ce Lα count on aluminum matrix adjacent to fuel particles
F. Over-the-peak Ce Lα count on fuel particle
G. Over-the-peak Ce Lα count on aluminum matrix away from fuel particle
H. Over-the-peak Ce Lα count on fuel particle.

shows an altered zone in the aluminum matrix surrounding the enriched, but not the depleted, UO_2 particles. The altered zone polished to a characteristic appearance much lighter than that of the aluminum surrounding the depleted particles and at larger distances from the enriched particles. With Figure I-14 is a key which points out these aforementioned characteristic regions shown in the photomicrograph. The portion of this photomicrograph which is enclosed within the small rectangle is reproduced on an enlarged scale in Figure I-15. The entire photomicrograph is again reproduced in Figure I-16 to show the distribution of the fission products.

The difference between the enriched and depleted particles is demonstrated further in Figure I-15 which shows the U $M\beta_1$, Al $K\alpha$, and Ce $L\alpha_1$ X-ray intensities obtained during a probe scan which crosses in succession (a) an enriched particle with its zone of altered aluminum matrix, (b) a depleted particle, and (c) another enriched particle and accompanying altered zone. The depleted particle produced a considerably higher U $M\beta_1$ X-ray intensity which would be expected since it would have undergone no appreciable burnup.

The Al $K\alpha$ trace (Figure I-15) shows no aluminum at the centers of the particles (this was verified also by quantitative point counts) and possible no aluminum in any place within the boundaries of the particles. The only region about which there is any doubt regarding the presence of aluminum within the

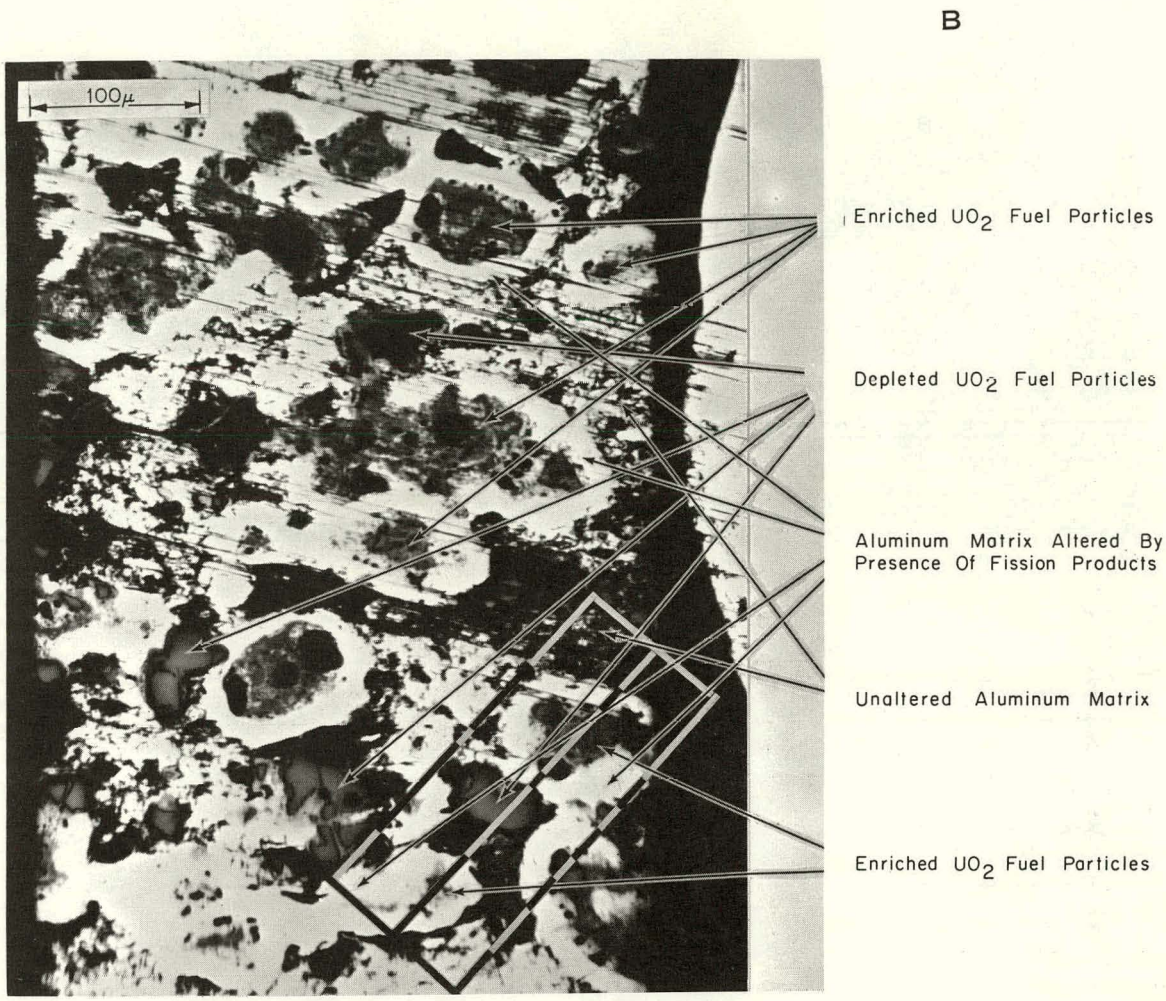

Fig. I-14 Photomicrograph of specimen 28-3, together with key indicating characteristic regions shown in photomicrograph.

A. Photomicrograph; unetched. Area within small rectangle shows region chosen for probe scan shown in Figure I-15.
B. Key to photomicrograph.

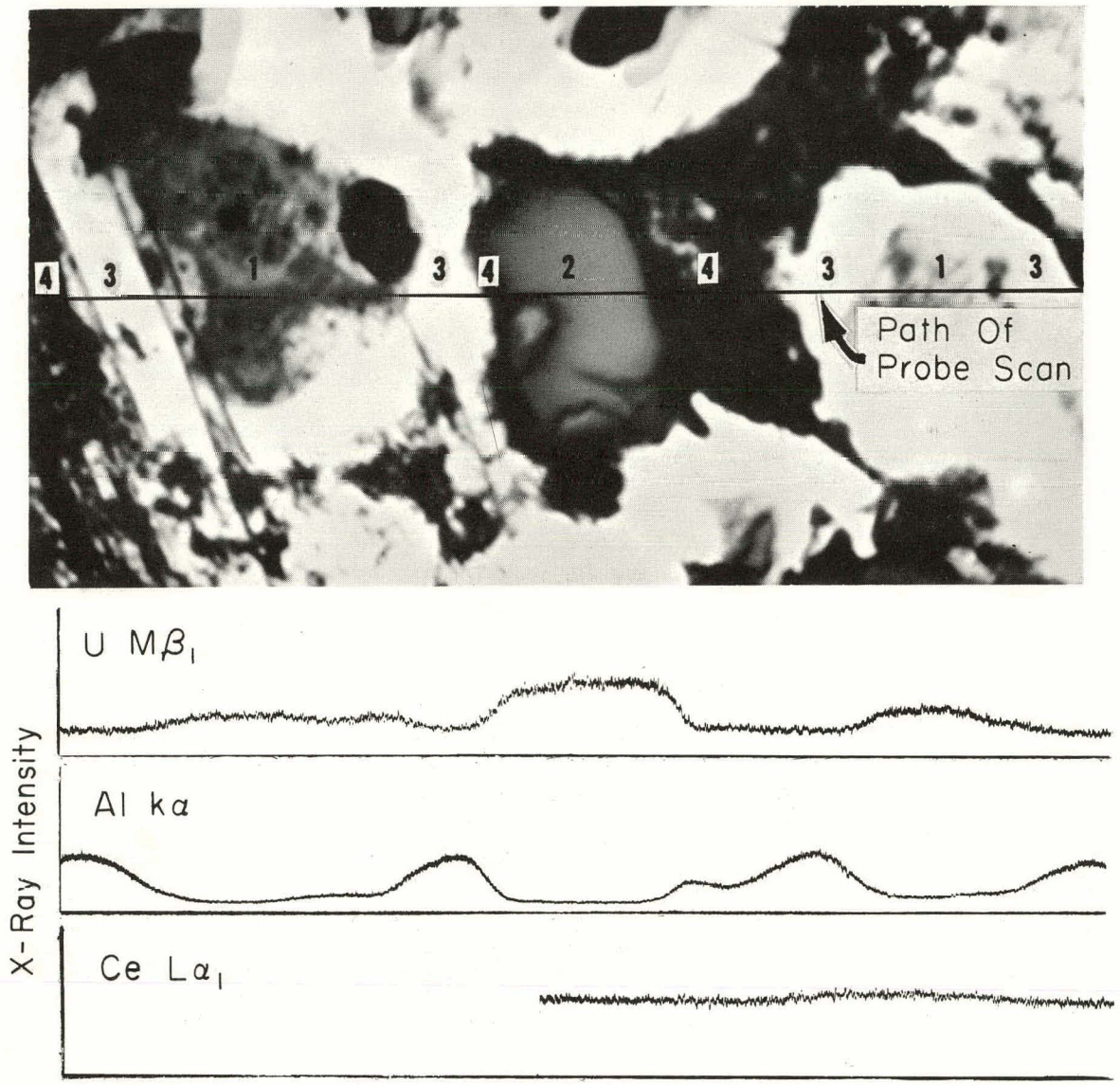

Fig. I-15 Results of one-dimensional probe scan across region enclosed in small rectangle in Figure I-14.

(1) ENRICHED UO_2 PARTICLES

(2) DEPLETED UO_2 PARTICLES

(3) "ALTERED" ALUMINUM MATRIX

(4) UNALTERED ALUMINUM MATRIX

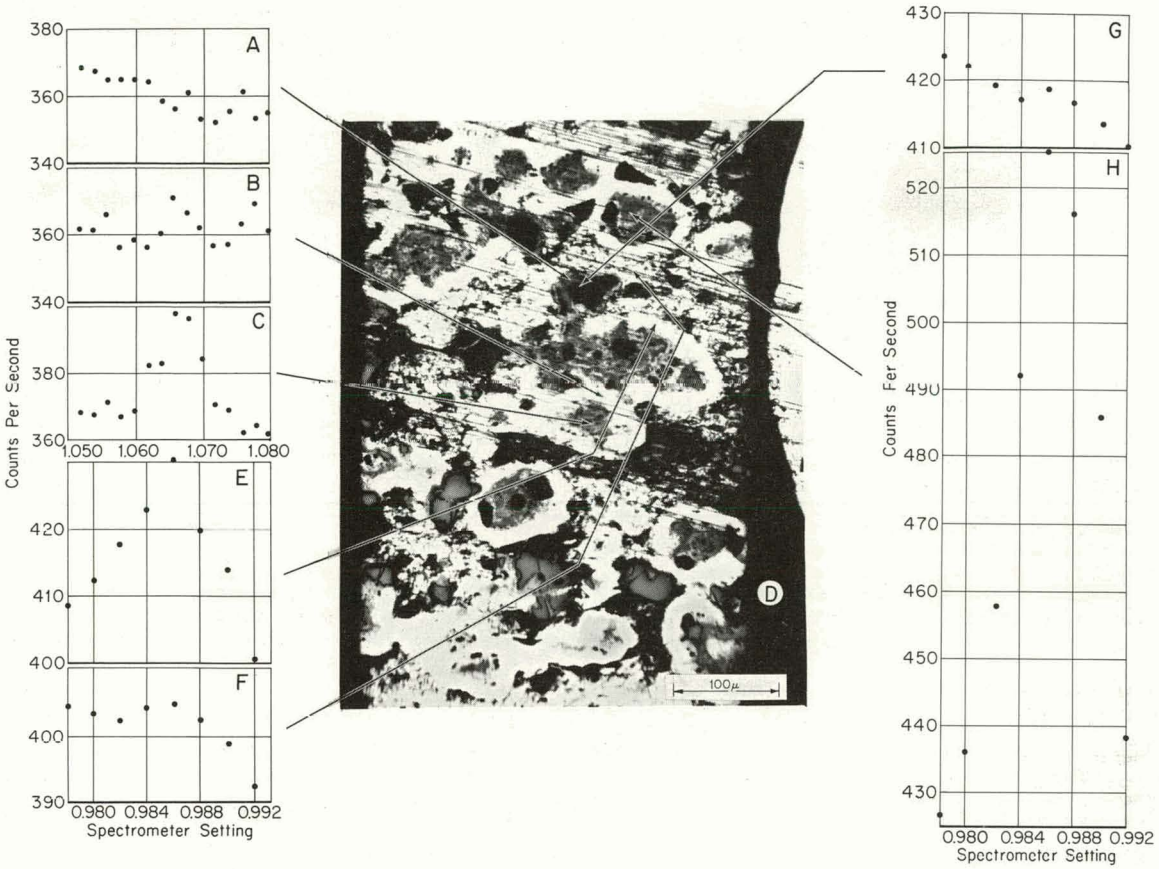

Fig. I-16 Photomicrograph of UO_2-Al fuel material, and over-the-peak counts of Ba Lα and Ce Lα X-rays at various points on the specimen.

A. Over-the-peak Ba Lα count on depleted UO_2 particle
B. Over-the-peak Ba Lα count on aluminum matrix adjacent to enriched UO_2 particle
C. Over-the-peak Ba Lα count on enriched UO_2 particle
D. Photomicrograph; polished; unetched
E. Over-the-peak Ce Lα count on aluminum matrix adjacent to enriched UO_2 particle
F. Over-the-peak Ce Lα count on aluminum matrix adjacent to depleted UO_2 particle
G. Over-the-peak Ce Lα count on depleted UO_2 particle
H. Over-the-peak Ce Lα count on enriched UO_2 particle.

particles is in the immediate vicinity of the boundary in a region no wider than the limitation imposed on resolution by the finite diameter of the probe. From this, it is concluded that no indication of chemical reaction between the aluminum and the UO_2 has been demonstrated by this investigation. If any such reaction has taken place, it is limited to a region around the periphery of the particle and no wider than the resolution of the probe. Under similar conditions, appreciable reaction has been reported [10] between UO_2 and Al. Apparently a number of variables, including the stoichiometry of the UO_2, influence the rate with which this reaction approaches completion.

The fission product, cerium, was barely detectable on the strip chart recording (Figure I-15). This recording indicated the presence of cerium only in the enriched particles and possibly in the altered zone of the aluminum

matrix immediately adjacent to the enriched particles. This is exactly the distribution which would be expected since no fissioning would occur [a] in the depleted particle.

In order to establish more definitely the distribution of fission products in the fuel core, and intensive series of over-the-peak counts for barium and for cerium was made in the various regions of the core. Neither barium nor cerium was detected in the depleted fuel particles (Figure I-16). Barium was found in the enriched fuel particles. Counts made in the aluminum matrix near an enriched particle were suggestive of the presence of barium, but this indication is not considered conclusive at the time of this writing.

Strong cerium peaks were found in the enriched fuel particles while slightly less strong, but definite, peaks were obtained from the altered matrix near these particles. This is suggestive of concentration gradients of fission products from the fuel particles to the aluminum matrix. No cerium was found in or near the depleted particles.

The detection of both cerium and barium in the fuel material of Specimen 28-3 which had received a very high burnup (83 percent) and the detection of only cerium in Specimen 79-3 which had received a lesser (24 percent) burnup is consistent with the following observations. The specimen undergoing high burnup showed pronounced cerium peaks and less strong barium peaks even though cerium and barium are reported to be formed in almost identical quantities [11] by the fission process. Apparently, cerium is more readily detectable under the experimental conditions which were employed. The specimen receiving the lower burnup and, hence, giving a less strong cerium peak would show a proportionately still weaker barium peak which could well be below the limit of detectability.

3.2 Corrosion of Aluminum by Mercury (R. A. Moen)

An Advanced Test Reactor (ATR) fuel element was found to be severely corroded after only 48 hours of testing in the Hydraulic Test Facility. The failure occurred by corrosion as the result of mercury contamination in the loop. The most severe corrosion occurred on the leading edges of the fuel plates, as shown in Figures I-17 and -18. The relatively short duration of the test prohibited the corrosion from penetrating to the cores of the fuel plates and exposing the fuel.

The probable sequence of events in the corrosion problem occurred as follows:

(1) Mercury entered the hydraulic test loop from an overpressured manometer and was constantly circulated throughout the loop.

(2) The mercury being transported in the constantly recirculating system came in contact with the leading edges of the fuel element and penetrated the protective oxide coating on the aluminum.

---

[a] Strictly speaking, conversion of some of the U-238 in the depleted particle to Pu-239 would occur; and part of the Pu would then undergo fission, thus producing its fission products. The extent of this conversion and fissioning may be considered negligible as far as the present investigation is concerned.

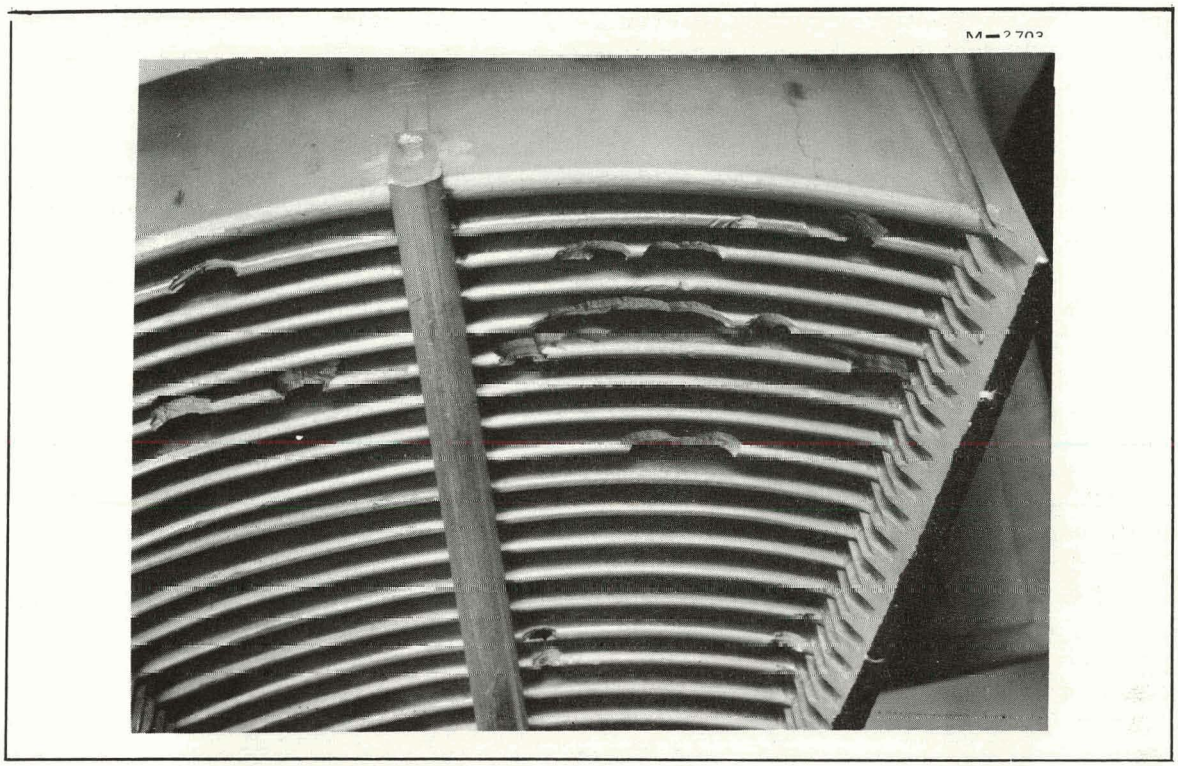

Fig. I-17 View of the leading edge of the fuel element after removal of the upper end box.

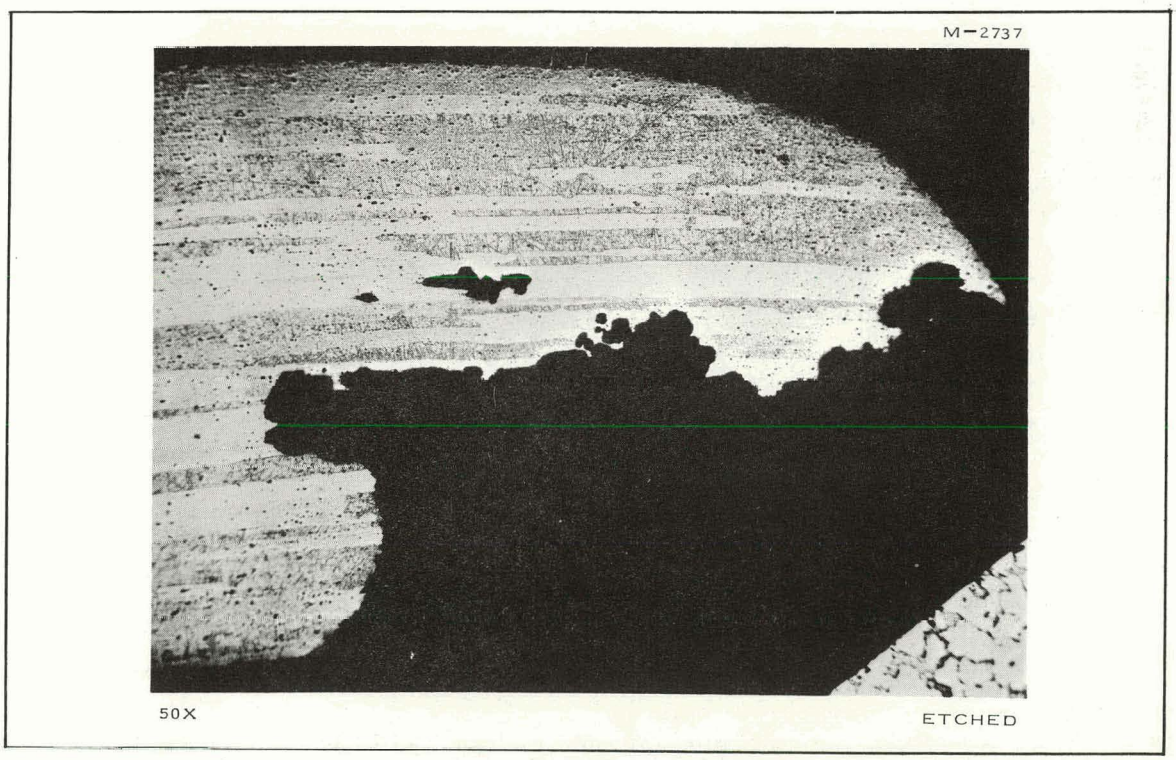

Fig. I-18 Cross section at the leading edge of a damaged fuel plate (50X -- etched).

(3) An amalgam was formed between the mercury and aluminum and was swept away by the flowing water. As the amalgam was swept away, fresh mercury impinged upon the exposed aluminum surfaces and the corrosion process continued.

The 6061 aluminum fuel plate and side plate material corroded to a greater extent than the cast 356 aluminum end boxes. The results found were in general agreement with those found by Alcoa [12].

3.3 Recent Advances in Replicating Techniques for Electron Microscopy (R. A. Moen)

A recent innovation has permitted the adoption of a new replicating procedure for use on highly radioactive samples.

It has been known for some time that the modified polyvinyl alcohol(PVA) replication process [13] would be superior over the Faxfilm procedure used previously. The main problem encountered in the use of the modified PVA procedure was the separation of the Formvar positive replica from the PVA negative. The separation of the two replicating materials is facilitated by placing a thin film of vacuum grease around the periphery of the PVA replica prior to application of the Formvar. The grease is not allowed to touch the replicated area. Once the Formvar replica is dry, it can be easily dry-stripped by first separating the PVA and Formvar at the greased edges and then dry-stripping them the remainder of the way. Since the master PVA replica is retained intact, additional replicas can be obtained from the master replica rather than reverting back to the original radioactive sample.

4. METALLURGICAL DEVELOPMENT (G. W. Gibson)

4.1 Destructive Examination of ATR-Type Fuel Elements (E. C. Norman, G. W. Gibson, J. C. Read, B. G. Carlson, M. J. Laird)

Two ATR fuel elements which had been previously tested in the Hydraulic Facility [8] were destructively examined in the Metallurgy Laboratory this quarter. One of these, element No. DA1B, a welded element manufactured by the Babcock and Wilcox Company, was examined to evaluate the concept of welded side plates used in its fabrication. In this element, side plates were produced and attached to the nineteen fuel plates by a welding procedure and were subsequently machined to meet ATR element dimensional specifications. The second element examined, No. DA6A, manufactured by the Westinghouse Corporation, was fabricated using the roll-swaging procedure developed by the Oak Ridge National Laboratory (ORNL). This element had failed during the hydraulic tests and was destructively examined to determine the reason for failure.

The two elements were evaluated against and/or compared to the roll-swaging assembly procedure developed by ORNL for the manufacture of ATR fuel elements. The roll-swaging assembly procedure is described in ORNL-3643, "Development of the Assembly Method for Fuel Elements for the Advanced Test Reactor". Figure I-19 is a photomicrograph of a typical roll-

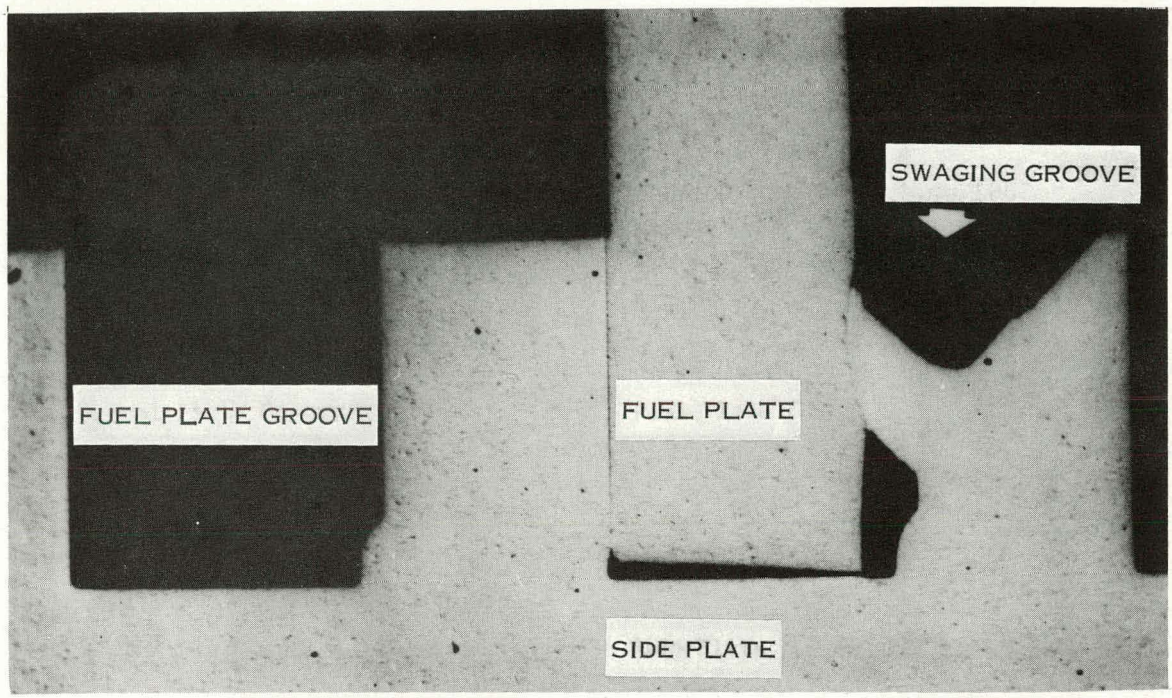

Fig. I-19 Photomicrograph of a roll-swaged joint showing the terminology used.

swaged joint and is labeled to define some of the terminology used in this report.

4.11 Macro-Examinations. Figure I-20 shows photographs of the roll-swaged element and shows details of a typical fuel plate-side plate joint failure as visible from the outside of the element. In the picture, part of the swaging groove which should hold plate No. 19 (the widest of the 19 fuel plates) secure has "peeled" away. Similar failures of the roll-swaging groove were noted throughout the element.

Although not photographed, the welded element was also visually examined; and it was noted that plate No. 1 was not joined to the side plate material along about 18 inches of element length.

Photographs of cross sections obtained by sectioning the two elements are shown in Figure I-21. The welded element is shown at the top, and the roll-swaged element is shown at the bottom.

Two problems were noted in the case of the welded element: (a) Cracking at all four side-plate corners at various points along the element length was common. This was the reason for the non-joined length along fuel plate No. 1 noted previously. (b) Sideplate thickness varied from a minimum of 0.125 inch to a maximum of 0.193 inch. ATR specifications call for a side plate thickness of $0.187\ ^{+0.000}_{-0.005}$ inch. In this regard, it was of early concern that the welded side plate material might possibly overlap the fuel plate cores at various points along the element length. This problem proved to be nonexistent. However, it appears that B and W made the minimum ATR fuel plate core widths nominal to avoid covering cores with weld metal.

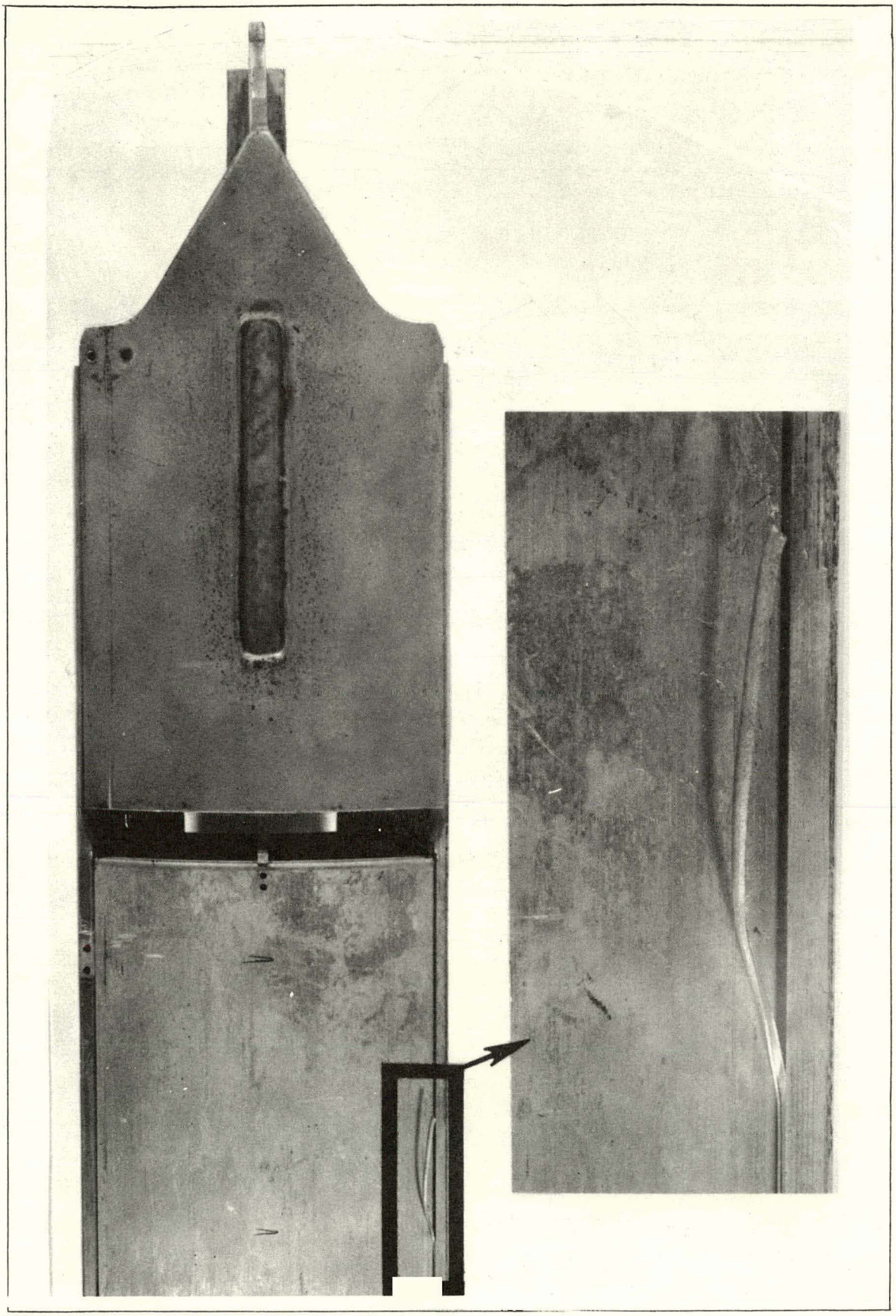

Fig. I-20 Convex side of a roll-swaged element showing swaging groove failure on plate 19.

M-2666

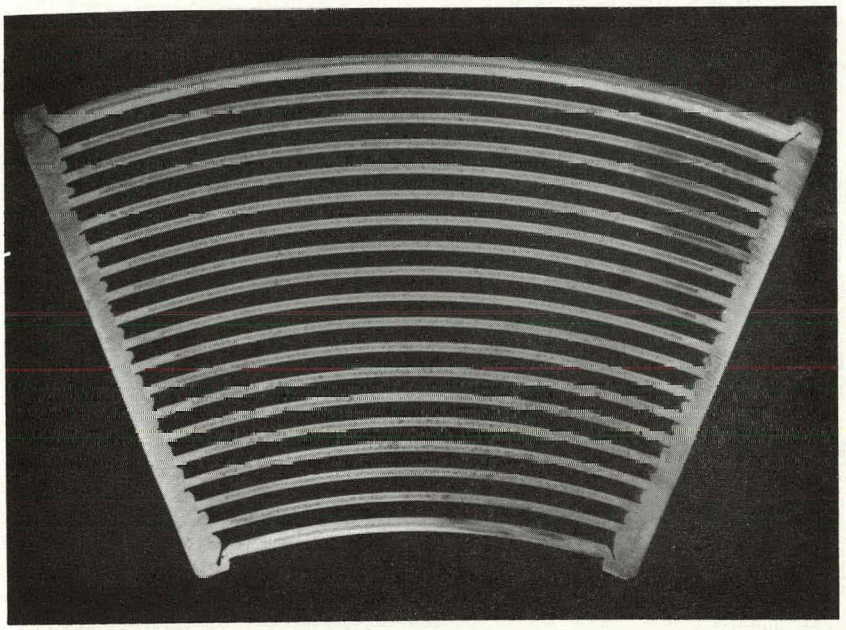

1X AS POLISHED

WELDED ELEMENT NO. DA1B

M-2804

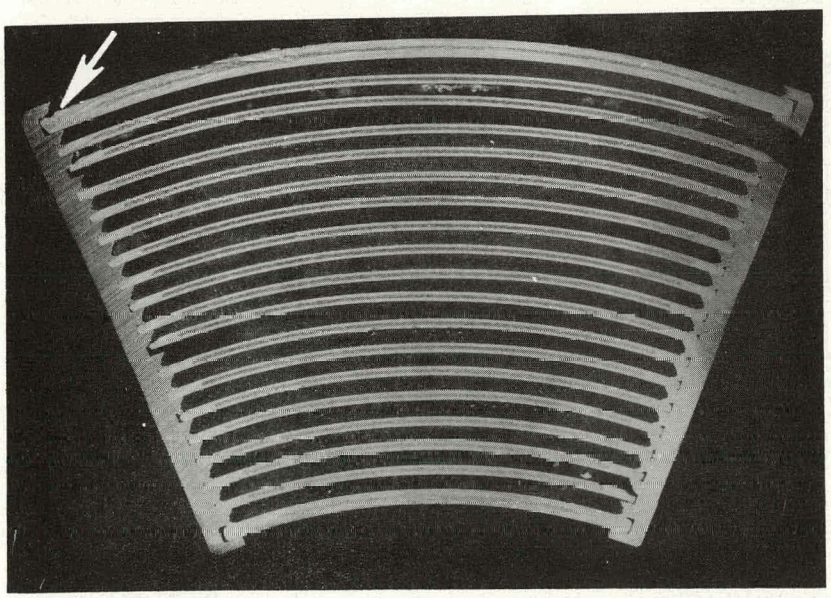

1X AS POLISHED

ROLL-SWAGED ELEMENT NO. DA6A (ARROW SHOWS "PEELED" AWAY PORTION OF SWAGING GROOVE SHOWN IN FIGURE I-20)

Fig. I-21 Cross sections of ATR fuel elements.

4.12 Metallographic Examinations. The point where the swaging groove "peeled" away from plate No. 19 on the roll-swaged element is indicated by the arrow on the photograph of the lower cross section, as shown in Figure I-21. Several joint failures in addition to this one were noted. In all cases, the shearing off of the swaging groove was the cause of failure.

A comparison of the two cross sections indicates the welded element to be more uniform in fuel plate spacing. In addition, the fuel plate-side plate joints appear to be stronger in the welded element. This observation is further borne out by comparing Figures I-22 and -23. Figure I-22 is a 40X photomicrograph of a welded fuel plate-side plate joint and Figure I-23 is a 50X photomicrograph of one of the roll-swaged joints that was still "intact" on the Westinghouse element. The photomicrograph of the welded joint shows that the bond is definitely metallurgical in nature and, thus, would be stronger than the mechanical bond produced by the roll swaging procedure. The roll-swaged joint shown in Figure I-23, is, however, not properly constructed and is, therefore, abnormally weak. It can be seen that even though the joint was still intact, the swaging groove had begun to yield. Failure by shear is indicated. There are two situations that could have led to this condition: (a) the stress applied to the swaging groove was excessive, or (b) the material from which the side plate was constructed was not stong enough. In the first case, an excessive force could have resulted from one of the following situations: (a) the pressure applied to the swaging tool was too great; (b) the swaging tool was of smaller dimensions than specified and acted as a stress concentrator; or (c) the resisting force due to the fuel plate was too small because the wrong materials were used for cladding and/or picture frame, or the materials used were in the wrong temper.

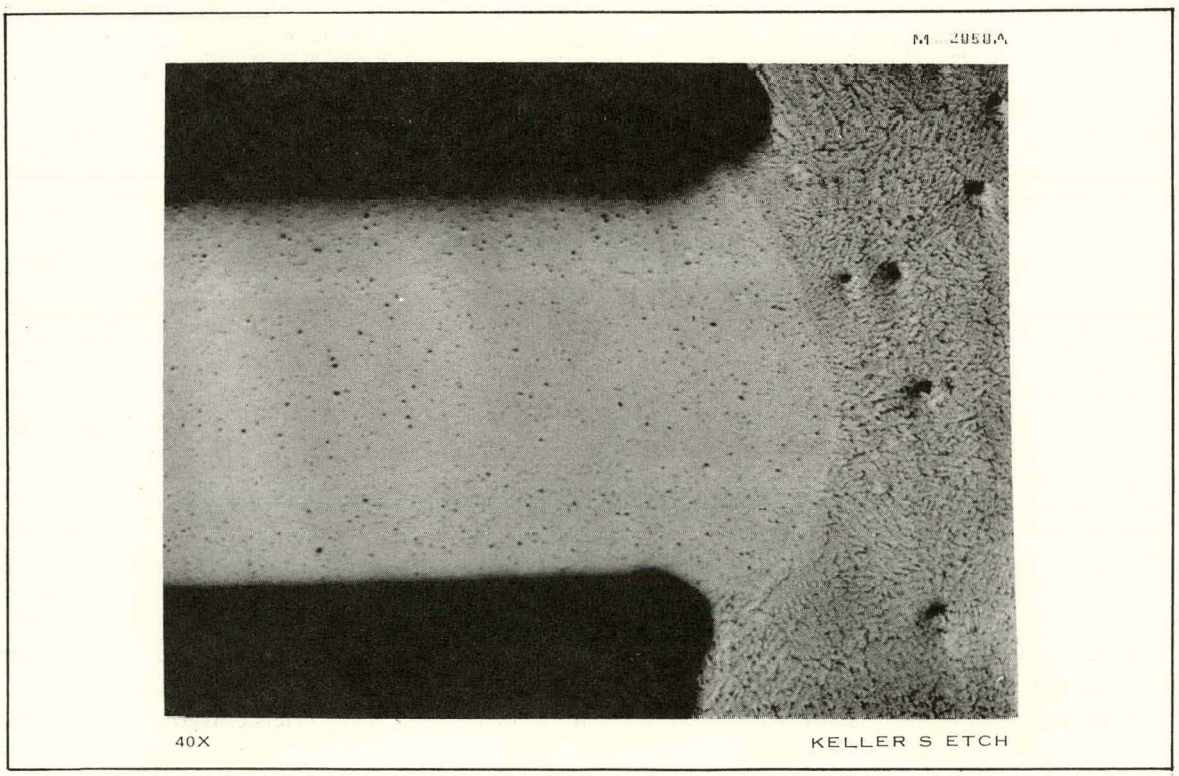

Fig. I-22 Welded fuel plate-side plate joint.

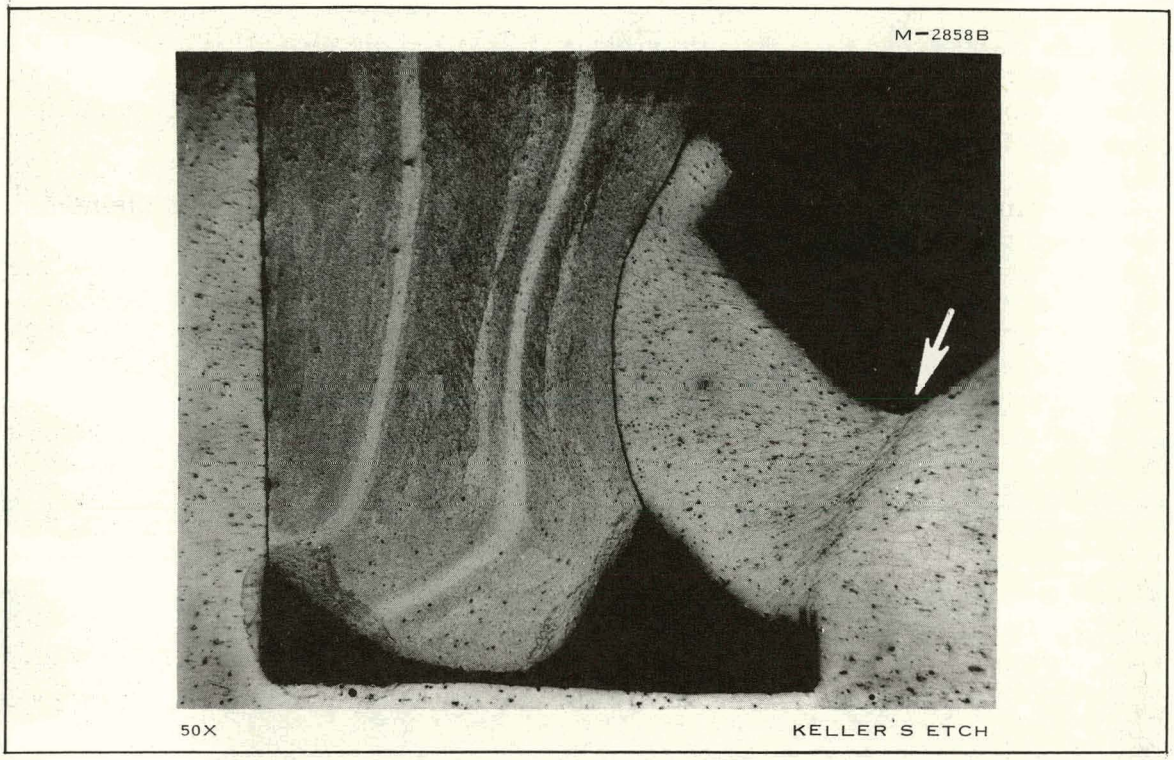

Fig. I-23 Roll-swaged fuel plate-side plate joint. Arrow indicates point where failure by shear has begun; note the shear flow lines.

ORNL 3643 specifies that the radius of the swaging wheel be 3/8 inch and that the width of the swaging wheel tip be 0.028 inch. Measurement of the depression produced in the swaging groove by the swaging wheel, as shown in Figure I-23, yields a width of 0.03 inch. This indicates that the swaging tool used by Westinghouse had the correct width. Although it was impossible to determine the radius of the swaging wheel accurately, an estimate was obtained from Figure I-24. This is a 6X macrophotograph looking down the grooves of the element after the end box was removed. It can be seen that the swaging wheel cut out an arc in the swaging grooves as it was removed after each joint was finished. At 6X, the wheel radius prescribed by ORNL becomes 18/8 or 2-1/4 inches. An arc of this radius is shown superimposed on one of the arcs cut out by the swaging wheel. The two arcs seem to match, indicating that the Westinghouse swaging wheel was of the correct radius.

4.13 Mechanical Property Checks. The mechanical properties (ultimate strength, percent elongation, and hardness) of the side plate materials from the two fuel elements were measured for comparison with the mechanical properties of the specified ATR alloys. Hardness checks were also made on the roll-swaged element fuel plate cladding and picture frame materials. ATR specifications call for 6061 aluminum to be used for side plates as well as cladding and picture frames. However, the side plates are to be in the "T6" temper (age-hardened condition). The fuel plates are heat treated according to an ORNL specified procedure. This procedure does not put the alloy into a standard temper. 6061 aluminum, heat-treated by the ORNL procedure, has the Mg_2Si particles partially agglomerated rather than fully agglomerated as in the fully annealed temper (6061-0). The weld metal used in fabrication of the side plates of element No. DAlB was essentially 4043 aluminum, a casting alloy. The data from these tests are summarized in Table I-9.

M-2901

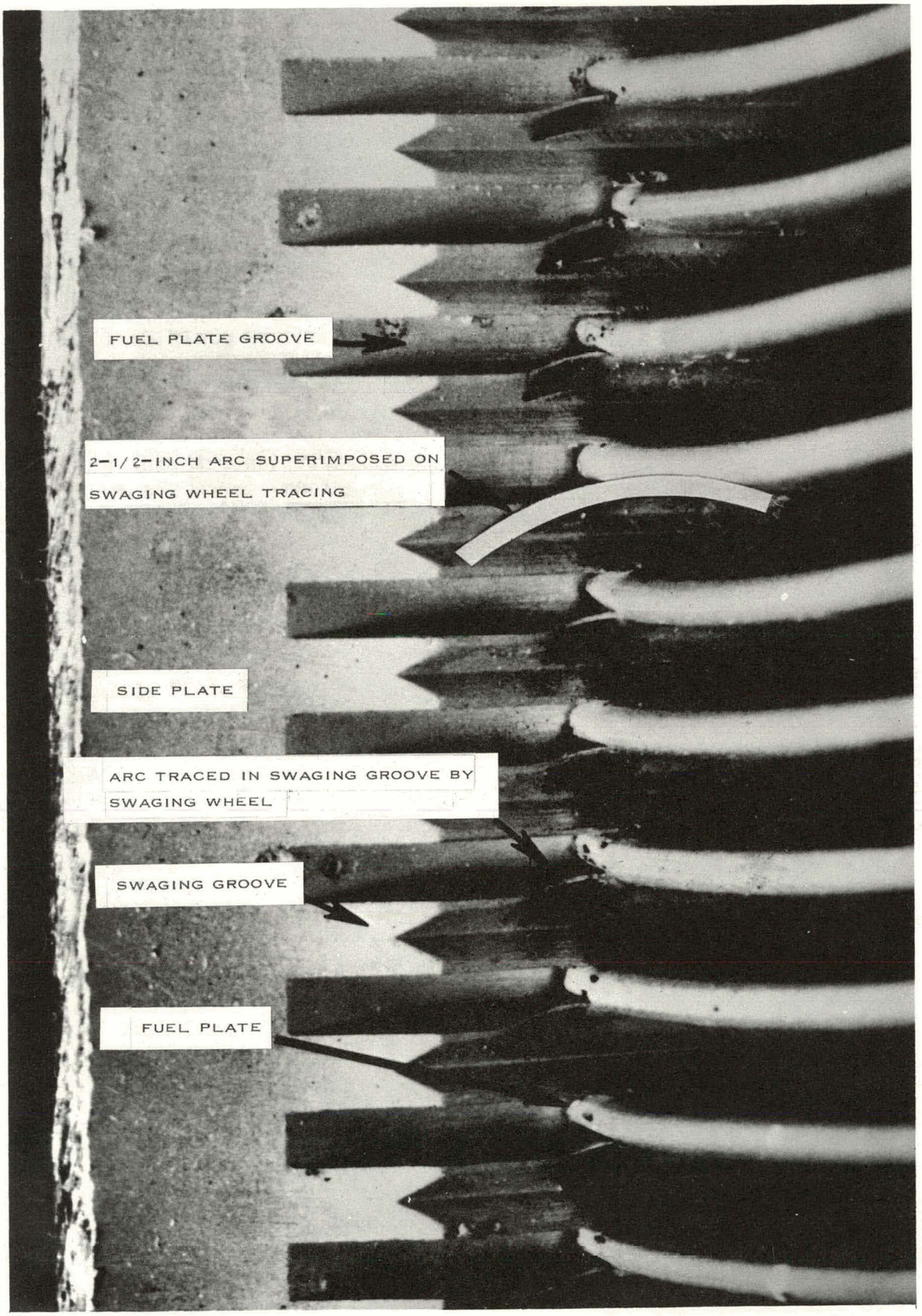

Fig. I-24 Photograph taken through roll-swaged element coolant channels after removal of end box.

TABLE I-9

COMPARISON OF PROPERTIES OF MATERIALS USED IN ATR FUEL ELEMENTS

Material	Ultimate Strength (psi)	Elongation[a] (percent)	Hardness	
			Brinell[b]	Rockwell 15-T Superficial
6061-T6[c]	45,000	12	95	81
6061-0[c]	18,000	25	30	44
4043[c]	23,000	10	45	--
Welded Side Plate	23,800	14[d]	31	
6061-ORNL Heat Treat	------	--	--	43 to 45
Roll-Swaged Fuel Plates	------	--	--	59
Roll-Swaged Side Plates	45,250	13	--	80

[a] Two-inch gauge length except as noted.

[b] 500 kg load -- 10 mm ball.

[c] Values for standard alloys were taken from the literature: either "Aluminum Heat Treating", Reynolds Metals Company (1957), or "ALCOA Aluminum Handbook", Aluminum Company of America (1957).

[d] One-inch gauge length.

The data indicate that the mechanical properties of the welded side plate material are inferior to 6061-T6. However, as noted previously, the integrity of the metallurgical bond produced by the welded method is much greater than the mechanical bond produced by the roll-swaging method.

Regarding the roll-swaged element, the data show the side plate material to be in the correct temper. In addition, the DA6A fuel plate cladding and picture frame materials were at or near the prescribed ORNL temper and certainly not too soft.

4.14 Conclusions. It was concluded that the welded assembly certainly offers promise as an ATR element fabrication method. However, several problems are indicated:

(1) Better control of side plate thickness is needed

(2) The cracking at the four side plate corners where the side plate is joined to plates 1 and 19 and the lack of joint along plate 1 need to be corrected

(3) The "roughness" of the weld metal on the inside of the element may have undesirable effects on the hydraulic characteristics. Final analysis of this question will, however, be dependent on the results of the hydraulic tests.

Regarding the roll-swaged element (No. DA6A) the following conclusions were reached:

(1) The DA6A side plate material had the mechanical properties of 6061-T6 aluminum as specified. Therefore, the swaging grooves did not shear off because of insufficient strength.

(2) The Westinghouse swaging tool was of the correct dimensions and, therefore, did not act as a stress concentrator.

(3) The DA6A fuel plate cladding and picture frame material had the mechanical properties of 6061 aluminum in the ORNL specified heat treated condition and, therefore, provided sufficient resisting force to the swaging forces.

(4) The plausible cause of joint failures was, then, the application of excessive pressure to the swaging tool during the swaging operation.

4.2 MTR-Type Fuel Element Containing Fuel Bearing Fiberglas (E.C. Norman, G. W. Gibson, J. C. Read, B. G. Carlson)

One MTR-type fuel element in which the fuel was in the form of a uranium-bearing Fiberglas was delivered to the NRTS for irradiation testing. This element, number CX-1, had been fabricated by the Clevite Corporation using aluminum-coated, uranium-bearing Fiberglas developed by the Owens Corning Fiberglas Corporation [14]. Irradiation tests on miniature fuel plates containing this type of Fiberglas have been performed, and the results evaluated by Battelle Memorial Institute [15].

As previously reported [11], it was believed that this element could not be safely irradiated in the MTR because of the brittleness of the Fiberglas fuel plate cores. In order to verify this belief, the side plates were removed from the fuel plates; and the fuel plates were examined. The results of this examination are discussed below.

4.21 Ultrasonic Examination. Each of the 19 fuel plates was given an ultrasonic inspection using the through-transmission technique. The ultrasonic inspection of a fuel plate depends on the principle of sound transmission. Areas of the fuel plate where there is lack of integral bonding between core and cladding have poorer sound transmission properties than do plate areas where a good bond exists. Thus, if a suitable standard is available, the ultrasonic instrumentation can be connected to a strip chart recorder and adjusted so that the recorder "draws" a picture of the plate showing the nonbonded areas as the fuel plate is scanned by the sound beam.

The instrumentation used in the scanning of the CX-1 plates was a commercial ultrasonic instrument, a Model 424 A "Immerscope", manufactured by Curtis-Wright and a fuel plate scanner designed and built by Phillips' Instrument Development Branch personnel especially for inspecting curved fuel plates. The fuel plate holder rotates through a small arc after each pass of the transmitting-receiving crystal pair along the plate. This procedure keeps the surface of the plate always perpendicular to the sound beam. The use of this scanner eliminated some of the errors inherent in the earlier inspection of the one extra Clevite plate (B-273). This plate was delivered to Phillips Petroleum Company along with the element CX-1. It was inspected on the basis of it being representative of the nineteen plates in the element assembly. On

the basis of the suspicions that were aroused after its examination, it was decided to examine each of the CX-1 plates individually. The earlier test, however, did not take into consideration the curvature of the plate: that is, the extra plate was tested as though it were flat. The transducers used for both transmitting and receiving in the scanning procedure were 10 megacycle, Li_2SO_4 crystals with 0.558-inch focal lengths. Figure I-25 shows the ultransonic scanning tank together with the transducer crystals and the holder for inspection of curved plates.

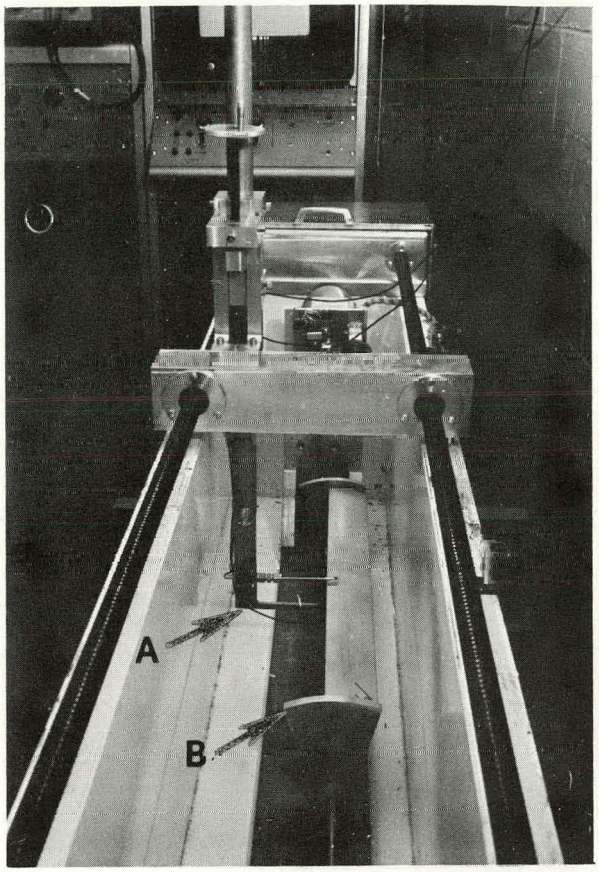

Fig. I-25 Ultrasonic scanner.

A. Scanner transducers
B. Scanner plate holder.

The standard used for simulation of flaws in the plates was a pair of lead washers, one laid on the plate at each end. Each washer was approximately 3/8 inch in outside diameter, 3/16 inch in inside diameter, and 0.030 inch thick. The scans of each of the CX-1 fuel plates are shown in Figures I-26 through -29. The flaws simulated by the presence of the lead washers are circled at the ends of the plates.

The electrical linkage between the crystals scanning the plate and the recorder pen "drawing" the plate is not in a 1:1 ratio. Thus the scale factor for the longitudinal dimension of Figures I-26 through -29 is 5.4, while the transverse scale factor is 1.9. That is, the longitudinal dimension of the scans from the figures represents the 25.125-inch length of a MTR fuel plate, while the transverse dimension of the scans from the figures represents a 2.75-inch width of a MTR fuel plate. As can be seen by examination of the scans, large nonbonded areas are indicated in most of the plates.

Plate number three which seemed to have a particularly large nonbonded area was chosen for metallographic examination.

4.22 Metallographic Examination. An enlargement of the ultrasonic scan of plate number three is shown in Figure I-30. This enlargment represents a scale factor of 2.9 in the longitudinal direction and 1.05 across the plate width. Sections A and B were cut from the largest nonbonded area indicated on the plate. This nonbond represents an actual area of approximately 2.3 inches across the plate width by approximately 2.9 inches maximum along the plate length. A composite photomicrograph from Section A is shown in Figure I-31. As can be seen, there is a pronounced separation between core and cladding. This crack occurred on the convex side of the fuel plate. The portion of the crack shown in the photomicrograph represents only approximately 0.014 inch of the indicated 2.3-inch wide crack. A similar photomicrograph from Section B is

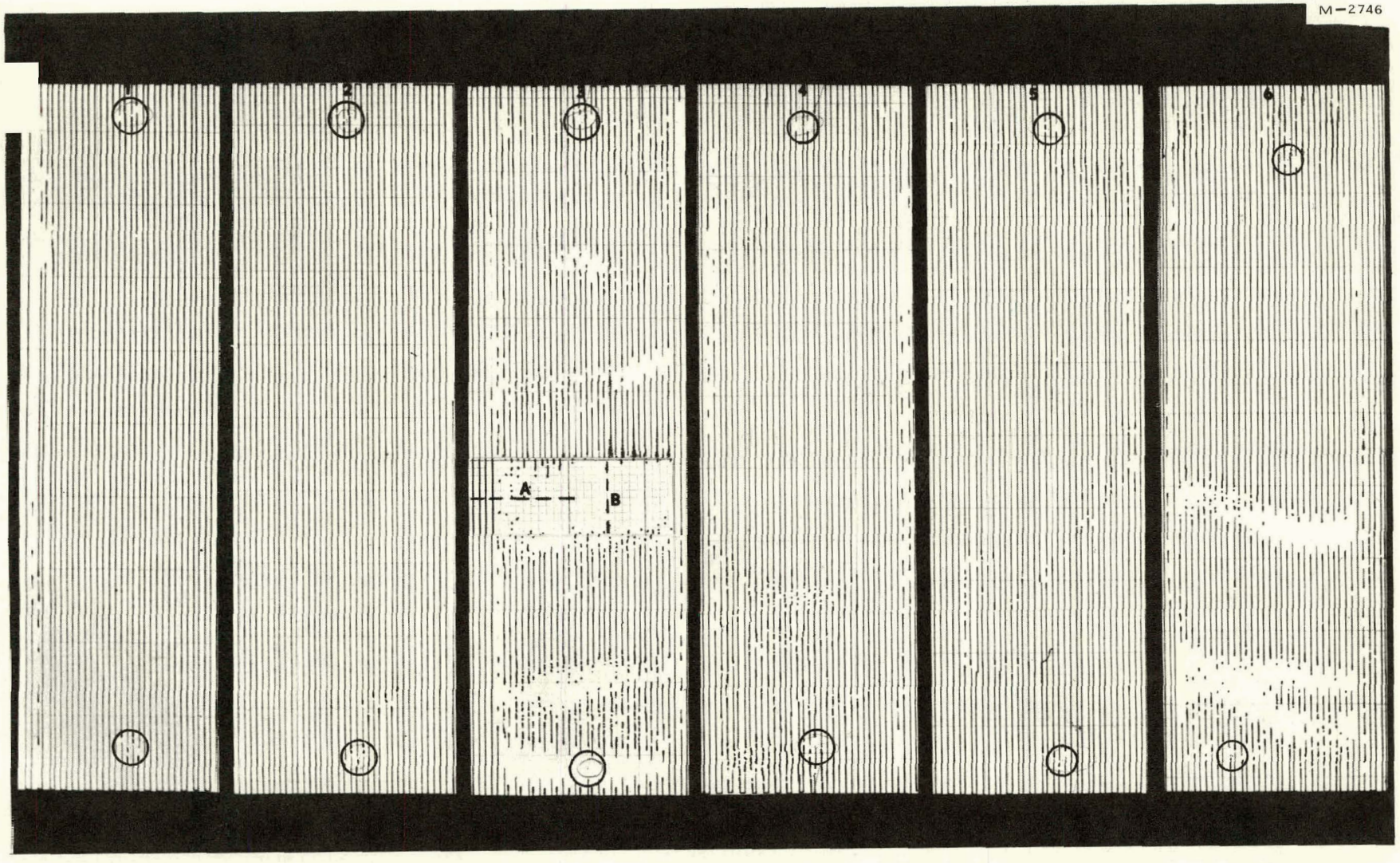

Fig. I-26 Ultrasonic scans of plates 1 through 6.

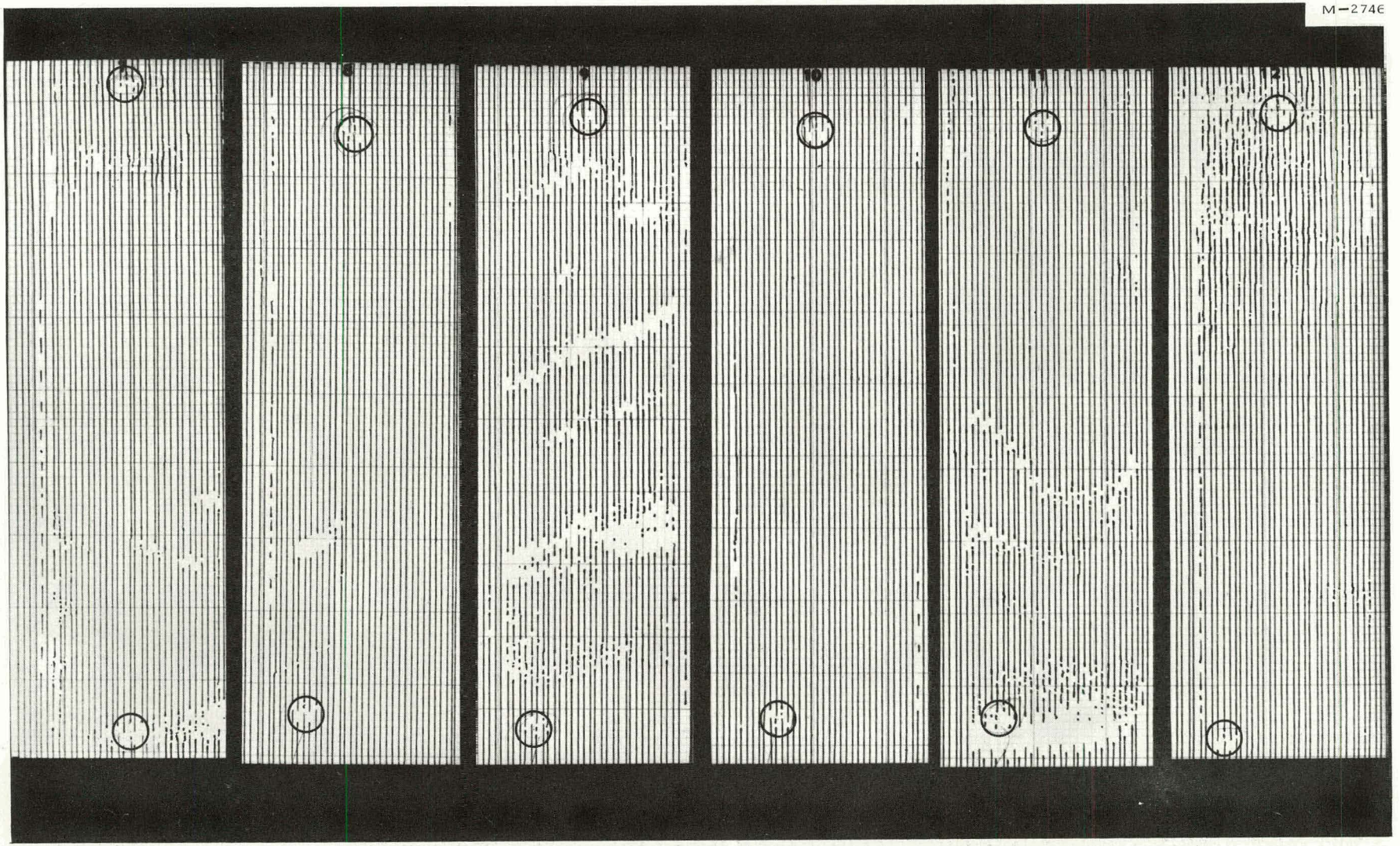

Fig. I-27 Ultrasonic scans of plates 7 through 12.

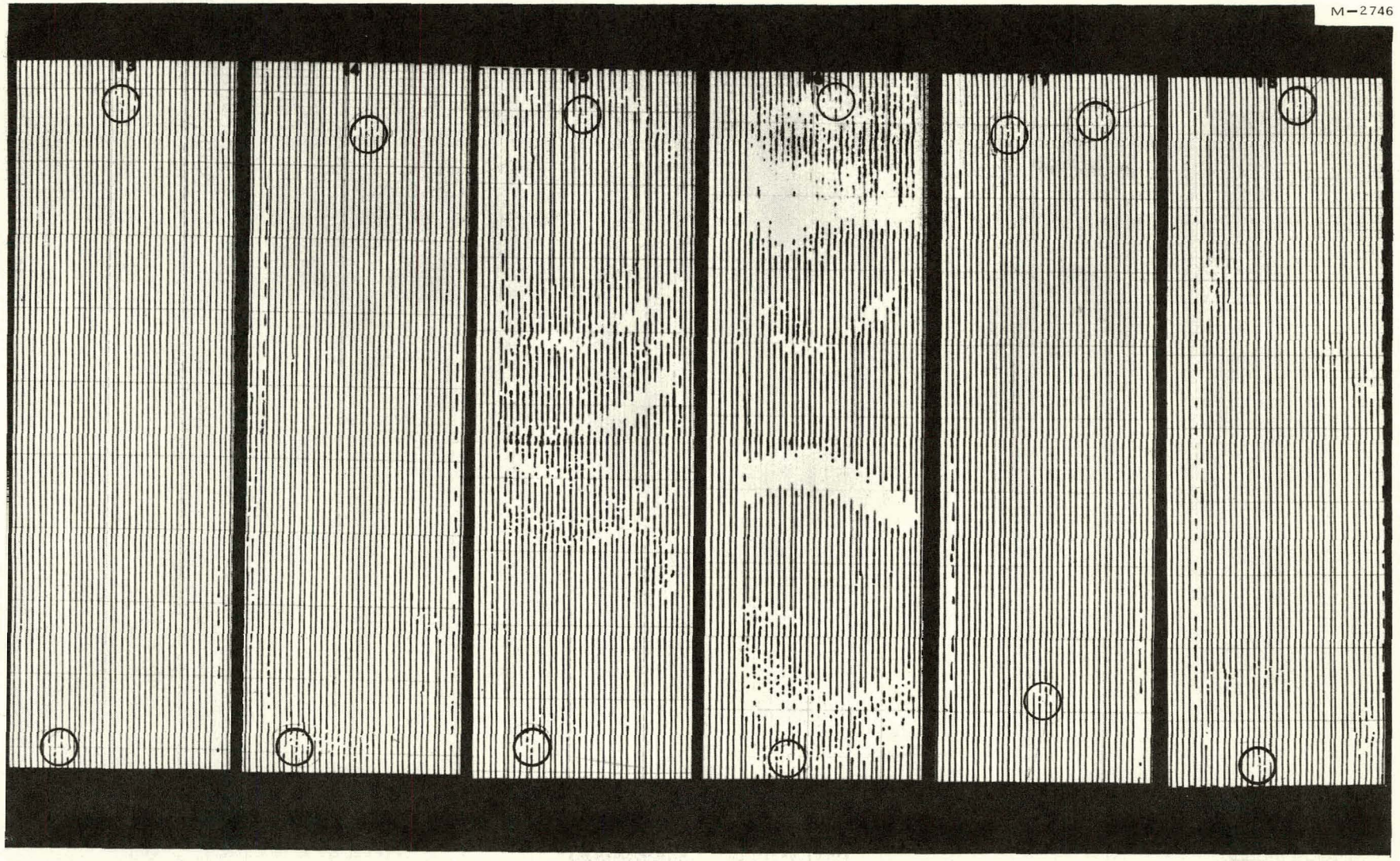

Fig. I-28 Ultrasonic scans of plates 13 through 18.

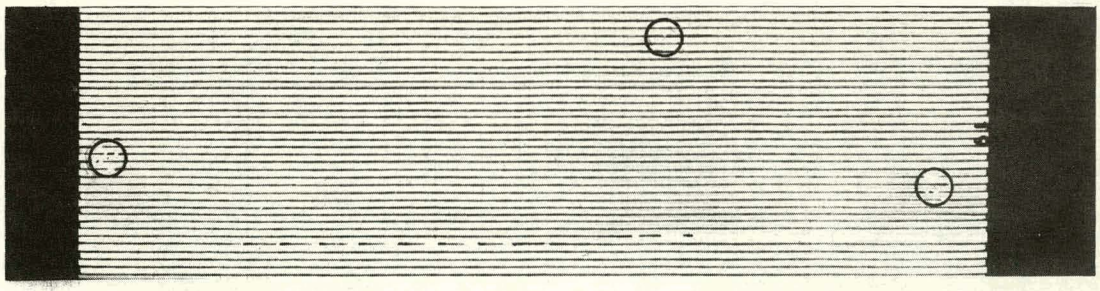

Fig. I-29 Ultrasonic scan of plate 19.

shown in Figure I-32. This picture represents only about 0.014 inch of the indicated 2.9-inch-long crack. It will be noted that cracking is shown on both the convex and concave sides of the core in Section B (Figure I-32).

Because of the extremely brittle nature of the Fiberglas material, it was deemed desirable to show that the separation between core and cladding was not produced in the sectioning of the material for metallographic specimens and the subsequent polishing of the specimens. Figure I-33 shows a photomicrograph taken from an area of plate number three that was indicated to be "sound" by the ultrasonic scan. As can be seen, there is no separation between core and cladding in this area. This shows that the cracking was not put in during the metallographic preparation but was present before as indicated by the ultrasonic examination.

Measurements taken from the photomicrographs indicate that the plate, core, and cladding thicknesses are within dimensional specifications (50 ± 3 mils plate, nominal 15 mils cladding, and nominal 20 mils core). However, the core thickness does seem to be on the low side (approximately 17 mils) rather than on the high side. Thicker cores would undoubtedly have been more ductile.

4.23 Radiographic Examination. Individual radiographs of the nineteen plates of element CX-1 were taken after the disassembly of the element and, thus, after the curvature was put into the plates. Normally, radiographs of MTR fuel plates are taken before they are curved but there is no reason to assume that the radiographing of the plates after the forming operation would affect the results of the examination in any way. Densitometer measurements of the CX-1 radiographs indicate that the Fiberglas cores are more uniform than the fuel plate cores from normal MTR production elements. MTR production elements normally have percentage differences between corrected low readings (thickest core areas) and average readings, as determined from densitometer measurements, of 20 to 30 percent on over half of the plates. The densitometer measurements from the radiographs of the plates from the Fiberglas element are given in Table I-10.

Noting the measurements for plates 16, 17, and 19, it can be seen that the "corrected" low readings are higher than the "average" readings. This is probably due to the fact that errors in the densitometer readings accumulated to a greater value than the actual difference in readings for these three plates which are very uniform and for which the actual differences are very slight.

MTR production elements normally have the thickest portion of the core located near the ends of the core. However, the lowest densitometer

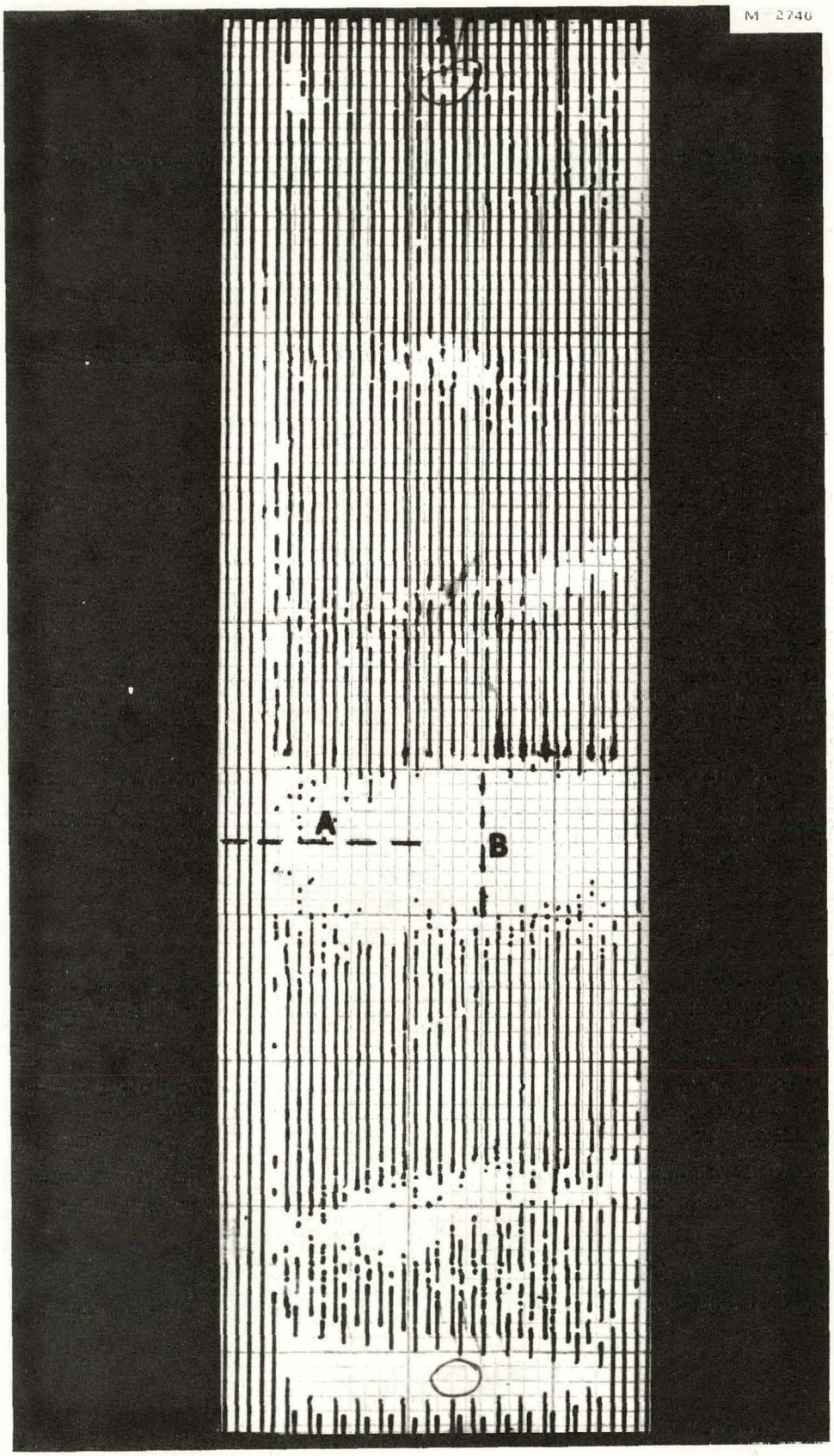

Fig. I-30 Ultrasonic scan of plate 3.

M-2743

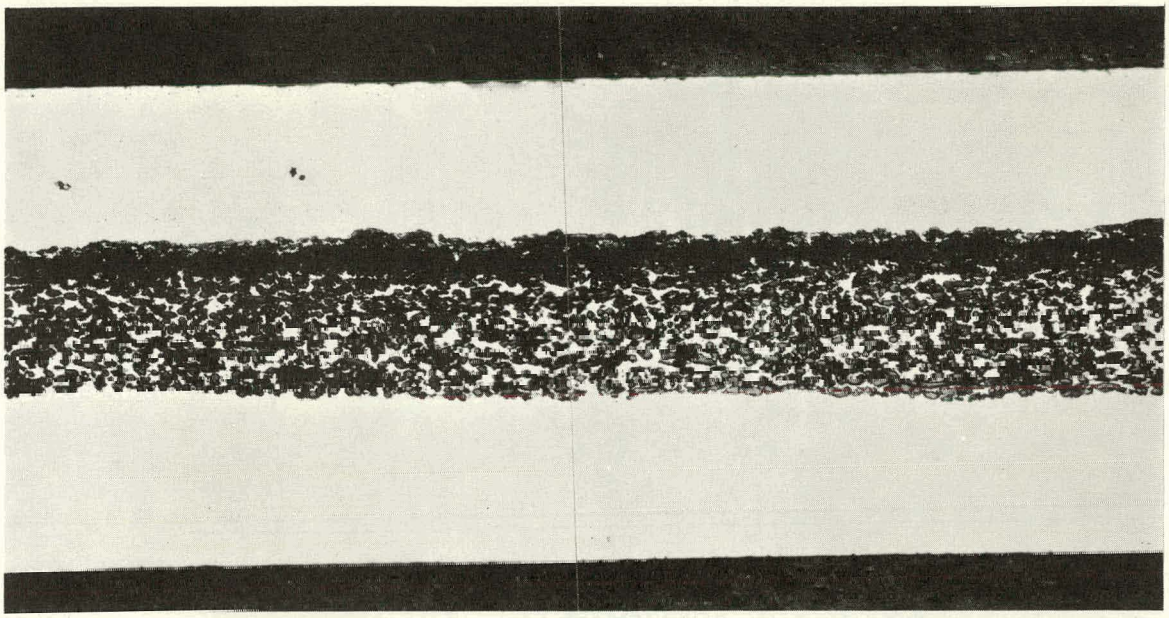

AS POLISHED 50X

Fig. I-31 Cross section through section A of plate 3.

M-2755

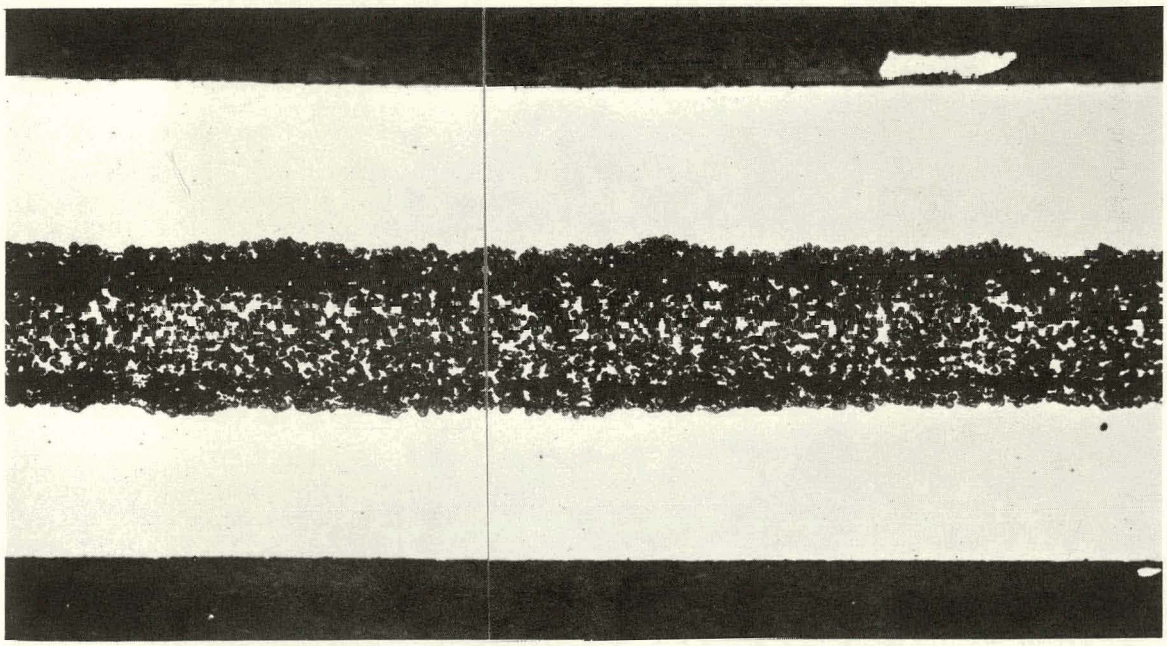

AS POLISHED 50X

Fig. I-32 Cross section through section B of plate 3.

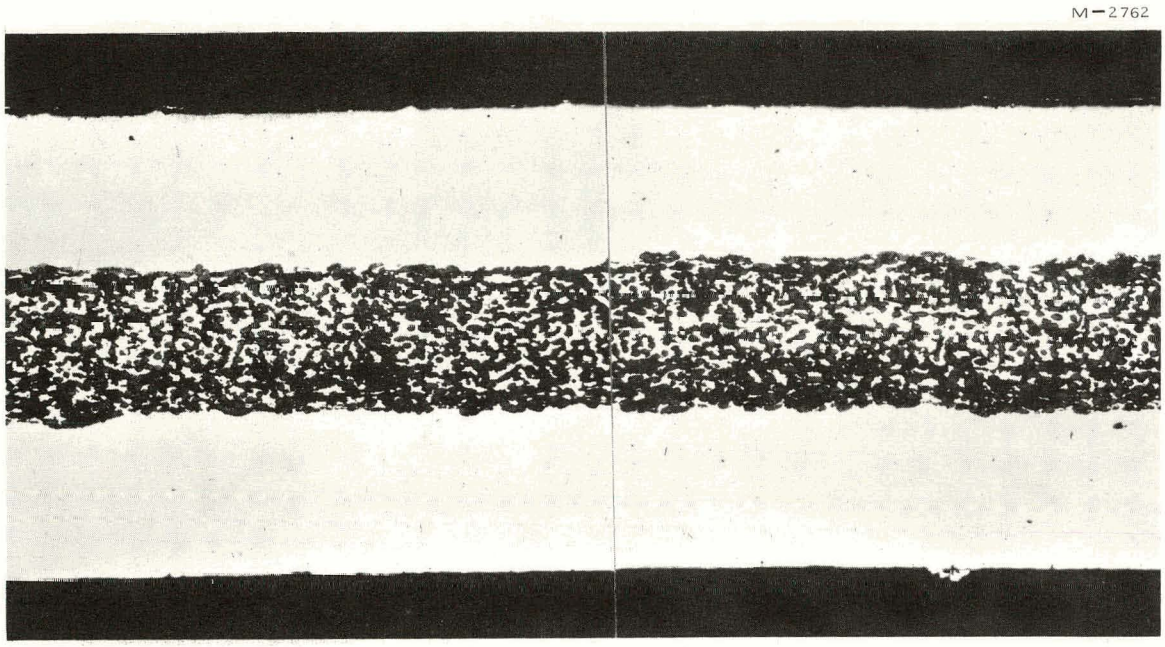

Fig. I-33 Cross section through sound area of plate 3.

TABLE I-10

DENSITOMETER DATA OF FUEL PLATES FROM MTR ELEMENT CX-1

Plate Number	Average Reading	Corrected Low Reading	Difference (percent)
1	0.74	0.74	0
2	0.85	0.84	2
3	0.85	0.77	27
4	0.85	0.82	9
5	0.85	0.80	18
6	0.84	0.76	28
7	0.81	0.79	6
8	0.85	0.85	0
9	0.83	0.81	7
10	0.87	0.87	0
11	0.85	0.85	0
12	0.82	0.82	0
13	0.88	0.87	2
14	0.74	0.72	9
15	0.78	0.78	0
16	0.77	0.79	7
17	0.75	0.76	2
18	0.75	0.74	2
19	0.70	0.71	3

measurements of the radiographs from some of the Fiberglas plates were obtained in the main part of the core, indicating the maximum core thickness to be in the middle portion of the core and not at the ends.

4.24 Conclusions. The results of the examination of element CX-1 bear out the suspicions aroused by the examination of the extra Clevite plate. Large nonbonded areas are indicated on most of the plates. It seems obvious that the separations occurred when the required curvature was put in the plates. These defects seemingly were not detected because all inspection and testing were done before the forming operation.

5. REFERENCES

1. R. A. Turner, Advanced Test Reactor TURBO Report, IDO-24459 (January 1964).

2. J. W. Henscheid and W. L. Schrader, "ATRC Start-up with Permanent Neck Shim Housing", Nuclear Technology Branches Quarterly Report July 1-September 30, 1964, IDO-17052 (February 1965) pp 12-13.

3. N. C. Kaufman and J. W. Henscheid, "Initial ATRC Experiments", Nuclear Technology Branches Quarterly Report April 1-June 30, 1964, IDO-17042 (November 1964) pp 7-10.

4. V. A. Walker et al, "Engineering Development for the ATR", MTR-ETR Technical Branches Quarterly Report January 1-March 31, 1964, IDO-16994 (August 1964) pp 1-10.

5. J. L. Durney and J. W. Henscheid, "Comparison of ATR and ATRC Neck Shims", Nuclear Technology Branches Quarterly Report July 1-September 30, 1964, IDO-17052 (February 1965) pp 14-15.

6. A. L. MacKinney et al, Advanced Test Reactor Critical Experiments Final Report, TID-19421 (August 1963) Fig. 5-1.

7. E. E. Burdick et al, The Advanced Reactivity Measurement Facilities -- A Description and Performance Evaluation, IDO-17005 (October 1964).

8. V. A. Walker et al, "Hydraulic and Structural Studies Upon ATR Fuel Elements", Nuclear Technology Branches Quarterly Report April 1-June 30, 1964 (November 1964) p 2.

9. R. E. Deville, Differential Thermal Expansion Tests on Advanced Test Reactor Fuel Plates, IDO-24461 (October 1963).

10. G. W. Gibson et al, Annual Progress Report on Reactor Fuels and Materials Development for FY 1964, IDO-17037 (November 1964).

11. I. Kaplan, Nuclear Physics, Reading: Addison-Wesley Publishing Company, Inc., 1955, p 498.

12. R. C. Plumb et al, "A Radiochemical Tracer Investigation of the Role of Mercury in the Corrosion of Aluminum", Corrosion, 12 (June 1956) pp 277t-285t.

13. J. D. Fleming et al, Materials for High-Temperature Nuclear Engineering Applications. Quarterly Report No. 6, October 1, 1963-January 1, 1964, TID-20589.

14. R. H. Baskey, Fuel Bearing Fiberglas in Aluminum-Base Fuel Elements, TID-16847 (June 1962).

15. R. J. Burian et al, Radiation Stability of Compacts of Aluminum and Fuel-Bearing Glass Fibers, BMI-1573 (March 1962).

THIS PAGE

WAS INTENTIONALLY

LEFT BLANK

II. NUCLEAR TECHNOLOGY

1. CROSS SECTIONS
(M. S. Moore)

1.1 U-232 Total Neutron Cross Section (O. D. Simpson et al)

The total cross section of U-232, which has a 72-year half-life, has been measured on the MTR fast chopper from 0.01 to 10,000 eV. Three samples, having inverse thicknesses of 287, 565, and 2205 were used. These samples were prepared from approximately 1 g of U-232, which was extracted at Oak Ridge National Laboratory from irradiated Pa-231, and were repurified in the hot alpha cave at the MTR. The data shown in Figure II-1 have been corrected for the presence of an unknown contaminant which was assumed to be oxygen, resulting from anomalous oxidation induced by the high level of radioactivity of the sample. The thermal cross section, after this correction is made, agrees well with the independent measurement of Halperin et al [1].

Analysis of the data has been carried out using multilevel techniques. Since the levels are widely separated, the effects of interference in fission among neighboring resonances is small. The data indicate, however, that interference in fission exists and can be adequately treated as a single-channel process. The analysis of the data was carried out independently of the fission cross-section measurements of James [2]. Preliminary parameters of resonances below 30 eV are given in Table II-1.

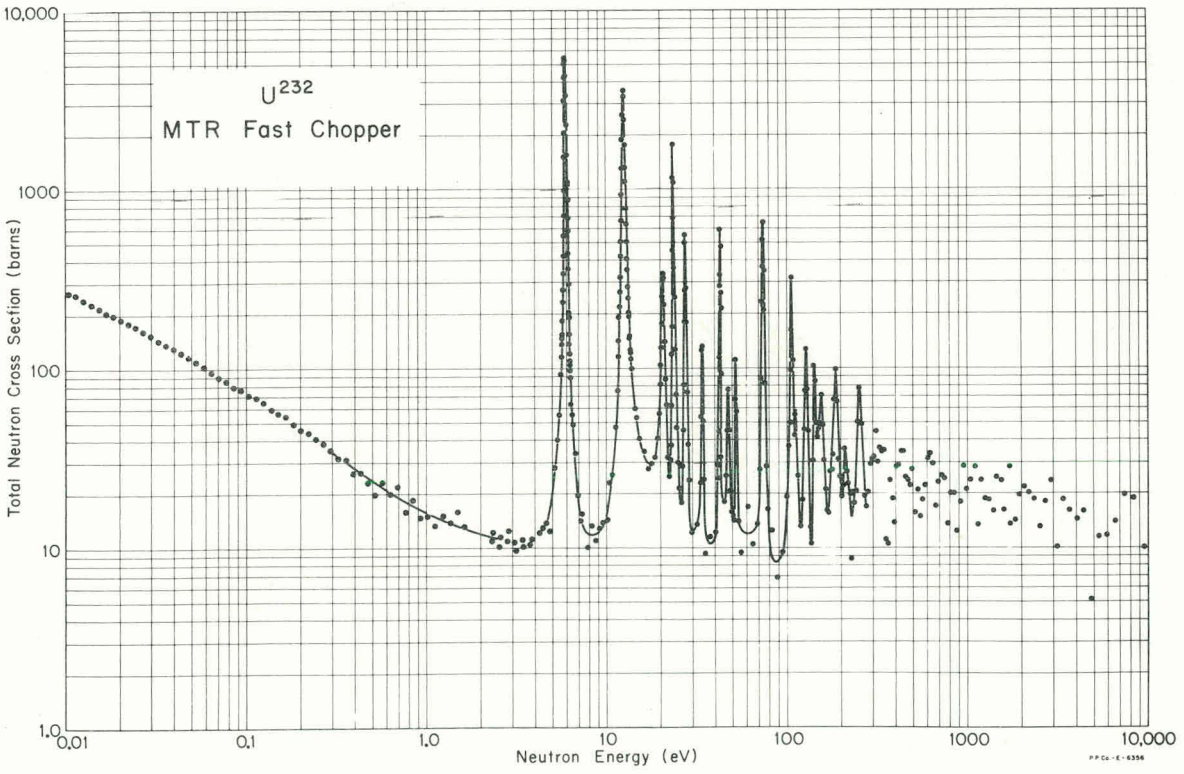

Fig. II-1 The total neutron cross section of U-232 from 0.02 to 10,000 eV.

TABLE II-1

PRELIMINARY U-232
RESONANCE PARAMETERS

E_o (eV)	Γ_n^o (mV)	Γ_γ[a] (mV)	Γ_f (mV)
5.945	0.61	47	23
12.656	1.75	47	253
20.95	0.55	47	753
23.71	1.20	47	93
27.65	0.75	47	453

[a] Assumed values

1.2 Th-228 Total Neutron Cross Section (O. D. Simpson et al)

During the course of the measurements taken on U-232, reported above, a narrow resonance appeared at 2 eV which had not been observed with fresh U-232 samples. Repurification of the U-232 sample and preparation of a 1 mg Th-228 sample gave positive identification that the 2 eV resonance belongs to Th-228. The Th-228 data shown in Figure II-2 were analyzed, with the use of the single-level, Breit-Wigner formula. The resonance parameters are as follows: $\Gamma_n^o = 0.57 \pm 0.04$ MeV, $\Gamma_\gamma = 36 \pm 2$ MeV, and $E_o = 1.896 \pm 0.002$ eV. Other small resonances were observed at higher neutron energies in old U-232 samples, but have not yet been positively identified as being due to Th-228.

1.3 Variation of the Relative Yield of High Total Kinetic Energy Fragments of U-235 (M. S. Moore, L. G. Miller)

Measurements of the relative yield of high total kinetic energy fragments of the fission of U-235 induced by neutrons of energy from 0.1 to 10 eV have been made on the MTR crystal spectrometer. The data, obtained with both the $10\bar{1}1$ and $10\bar{1}3$ planes of beryllium with high intensity (poor resolution) collimation, are shown in Figure II-3(a). Shown in Figure II-3(b) is the fission cross section of U-235 as measured in the same experiment, which shows the resolution conditions which existed.

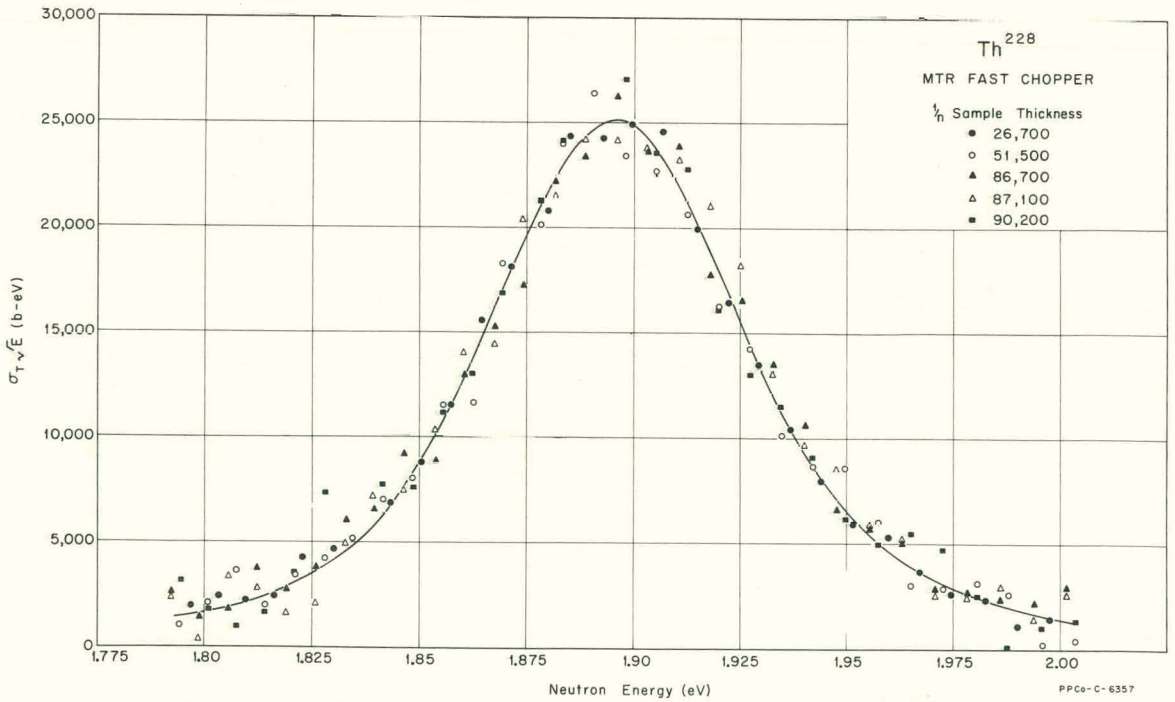

Fig. II-2 The total neutron cross section of Th-228 in the region of 2 eV. The solid line is a single-level Breit-Wigner fit to the data.

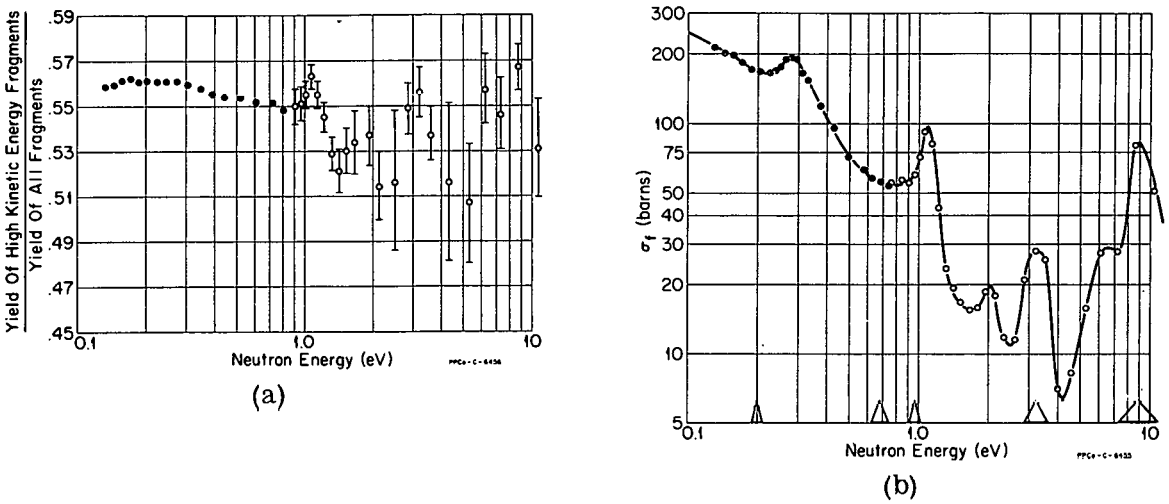

Fig. II-3 (a) Ratio of the yield of high kinetic energy fragments to the yield of all fragments for U-235.

(b) Measured fission cross section of U-235 showing resolution conditions under which the above data were obtained.

2. NUCLEAR CHEMISTRY
(W. H. Burgus)

2.1 Beryllium Gases Experiment (R. L. Tromp)

Heating and swelling measurements of beryllium samples cut from the midplane of MTR lattice piece LB-15 (average He-4 content of 32 cc/cc Be, equivalent to 1.6 x 10^{22} n/cm^2 fast nvt) were continued. Various samples were heated at temperatures of 500, 550, 600, 700, and 800°C for times up to at least 20 hours for each sample. Both the density versus heating time plot (Figure II-4) and the comparison of He-4 evolution (Figure II-5) confirm that the swelling threshold is approximately 550°C as reported earlier [3].

An unexpected phenomenon was encountered in heating one of these samples at 800°C. This same unexpected behavior was observed in heating a piece of Be from MTR permanent Be piece F-2, which had received only slightly less fast neutron dosage (approximately 1.3 x 10^{22} n/cm^2). Previously, expansion to densities as low as 1.18 and 1.11 had been observed with the high-purity, ETR-irradiated Be containing only 2 cc He/cc Be. It was assumed that the LB-15 and F-2 pieces containing considerably more reaction gas would, at comparable temperatures, decrease to even lower densities. Instead, it was found that after the large initial density decrease at 800°C, the LB-15 Be density remained nearly constant between 1.4 and 1.5 over the next several hours, followed by a gradual increase. This was accompanied by marked visual structural cracking and striating.

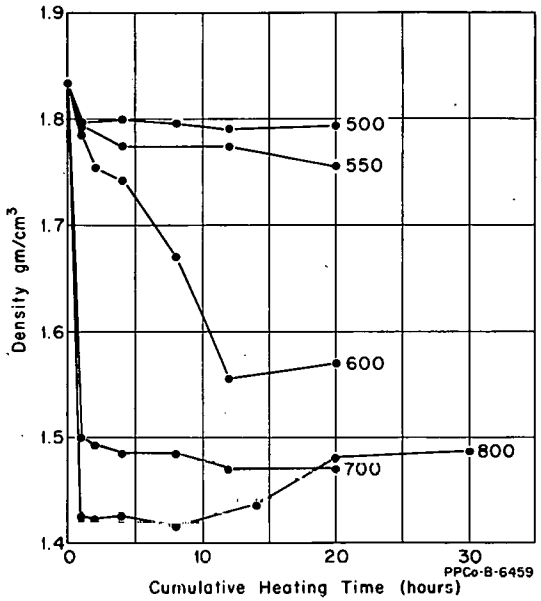

Fig. II-4 Swelling of LB-15 Be samples at various heating temperatures.

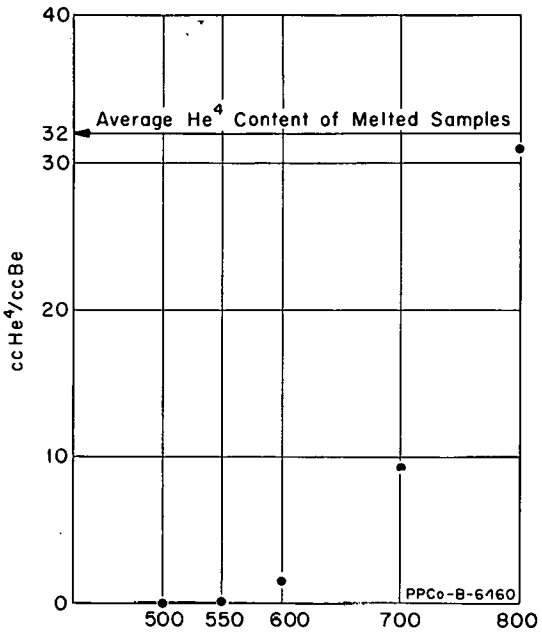

Fig. II-5 Helium evolution from heated LB-15 samples for 20 hours of heating.

2.2 Compilation of an Alpha-Spectrum Catalogue (R. N. Chanda, R. A. Deal, R. P. Schuman)

A new effort, the preparation of an alpha-spectrum catalogue, has been initiated in collaboration with the Decay Schemes Group. The object of this work is to produce a complete and up-to-date complication of standard spectra of alpha emitters -- both naturally occurring and artifically produced. These alpha spectra will be taken with semiconductor silicon detectors, and the data will be published graphically as well as in digital form for computer use.

To obtain the best spectra possible, effort is being expended in examining detectors and electronics equipment with a view toward realizing maximum resolution. In search for a very stable low-noise amplifier system, exhaustive tests were made this quarter on the "ORTEC" 101-201 and 103-203 preamplifier-amplifier systems. The 101-201 unit is superior to the 103-203 and, indeed, is comparable to any unit available at this time. In addition to the electronic components, studies were also begun on other alpha-counting parameters in order to optimize counting conditions. These have included source-to-crystal distance, chamber size, and methods of sample preparation. In connection with sample preparation, a procedure for isolating Ac-227 from Pa-231 was developed. The Ac isotope was isolated by TTA extraction into benzene from pH 2.3 solution. It was then back extracted into 1N HCl and purified by ion exchange using Dowex 1, after which the α spectrum was taken.

2.3 Cadmium Shield Burn-Through (K. T. Faler)

The purpose and methods of experimentally verifying Cd shield burn-through have been given in detail previously [4]. Following a second cycle of neutron irradiation on a cadmium test shield, as previously described, the "unperturbed" integrated flux was found to have reached a total value of 1.24×10^{21} thermal neutrons/cm^2. After allowing the shield to "cool" by decay, the transmission was again checked and found to be 0.46 percent. This value again

falls above the calculated value [4] based on an assumed flux depression due to the cadmium, and by the same amount as found for the value previously determined at an nvt of 4.8×10^{20} n/cm^2. This gives added evidence to the idea that the estimated flux depression value was too high.

The cadmium test shield was reevaluated and is being irradiated for another cycle.

2.4 Design of Chemistry Isolation Box for the MTR Hot Alpha Cave (J. W. Codding)

A new chemistry isolation box for the MTR Hot Alpha Cave has been completed and is nearly ready for installation. This box replaces the recently discarded Pa-233 processing box, and it will be installed adjacent to the mechanical isolation box. Because of the requirements of the Pa-233 work, the previously used chemical box was designed to handle only the recovery and purification of Pa-233 and, thus, contained specialized equipment directed toward that end. The new chemistry box is of a more versatile design, so arranged that a variety of operations can be carried out.

The basic equipment supplies services necessary for the operation of a miniature chemical processing plant. Permanently installed Pyrex vessels provide the space for chemical reactions and solution storage. These vessels are interconnected with stainless steel fittings and polyethylene tubing and are controlled with manipulator-operated polyethylene valves. The piping is so arranged that maintenance can be done remotely using Model 7 manipulators. A rotary air pump, protected from corrosion by oil and absolute filters and liquid traps, provides controlled air pressure and vacuum for solution transfer, filtration, sparging, or the operation of ion exchange columns. The oil and absolute filters are remotely replaceable, and the liquid traps can likewise be drained and cleaned remotely. Provision is made for other general services such as chemical entry, solution sampling and dilution, waste handling and removal, centrifugation, fume-hood evaporation heating or cooling water, and radiation monitoring.

Unit operations such as dissolution, solvent extraction, or ion exchange will be performed in special equipment which can be plugged into the "service" equipment by using quick disconnect fittings. After use, the special apparatus can be cleaned, unplugged, and either set aside or removed until it is again needed. Thus, the chemical box will supply complete equipment to accommodate many separation and purification processes with the replacement of only a single piece of apparatus for each operation. Ease of such replacement has been enhanced by the recent installation of a shielded transfer drawer leading from the chemistry isolation box inside the cave to a glove box outside the cave. This drawer provides an air and radiation lock between the inside and outside of the cave. Thus, any equipment which can be reasonably decontaminated from gamma emitters can now be removed from the cave without any spread of alpha contamination, easily bagged out of the glove box, and stored for future use. The first use of the new chemical box will be for preparation of chopper samples of Pm-148 and Am-242.

2.5 Alpha Spectra of Th-229 and its Daughters (R. P. Schuman)

About one gram of high purity U-233 was dissolved and purified to make a U-233 stock solution. The thorium daughters of the U-233 were further purified and isolated for the purpose of examining the alpha spectra of Th-229

and its daughters. (This work is a part of a continuing project of measurements of isotopes which are used primarily for cross section measurements but which provide particularly opportune samples for decay studies since they are already on hand.)

The U-233 was purified by absorbing the uranium (as UO_2^{++}) on Dowex 1 from approximately 12N HCl, and then eluting the UO_2^{++} with approximately 0.1N HCl. Thorium passed through the column with the 12N HCl. It was then purified by evaporating the HCl solution nearly to dryness, taking the residue up in 7N HNO_3, and absorbing the Th^{+4} on Dowex 1 from 7N HNO_3. The thorium was then eluted with dil HCl.

The purified thorium contained both Th-228 and Th-229. A sample was electroplated and an alpha spectrum taken (see Figure II-6). Some of the thorium decay daughters in the 7N HNO_3 eluate were also electroplated, and an alpha spectrum was taken after a considerable fraction of the Th-228 daughters had decayed (see Figure II-7). Gamma spectra of the daughters were also taken, the initial spectra showed mainly the Th-228 daughter gamma rays; but after considerable decay, the gamma rays due to Th-229 daughters also became prominent (see Figure II-8).

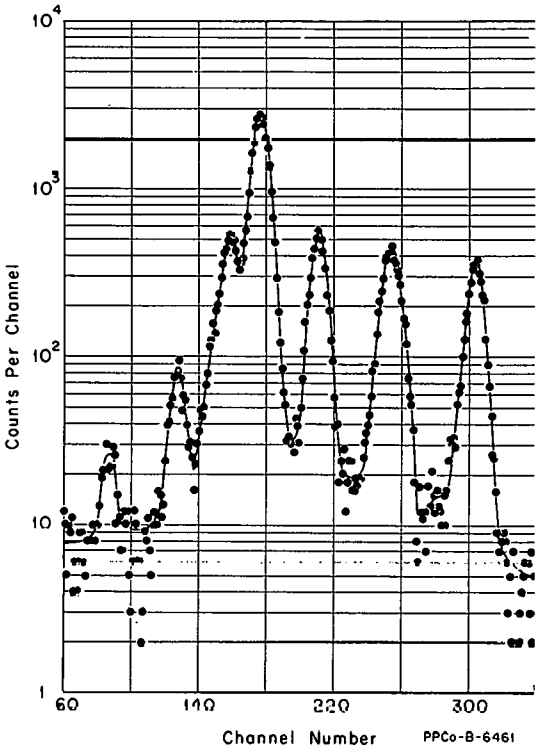

Fig. II-6 Alpha spectrum of Th-229 [a].

[a] L. L. Gol'din et al, "Alpha Decay of Th-229, Interactions of Nuclear Levels", Zhur. Eksptl'. i Teoret. Fiz. XXXVII (October 1959), pp 1155-7. (In Russian).

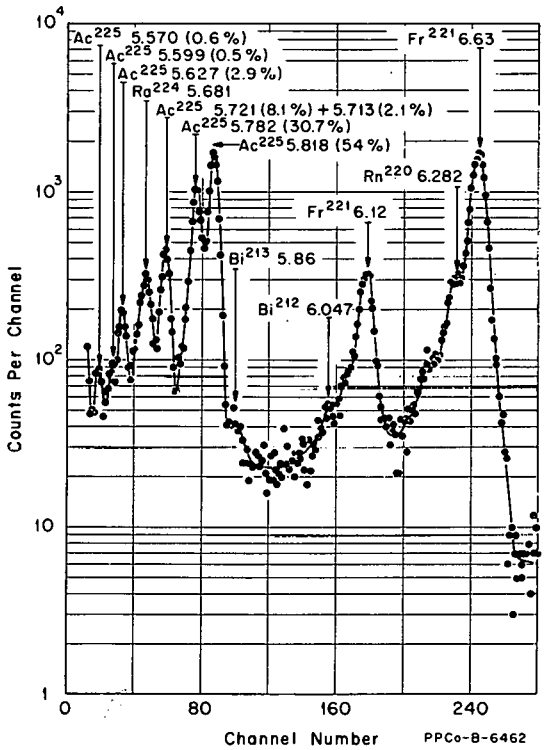

Fig. II-7 Alpha spectrum of Ac-225 and Fr-221 milked from Th-229 (contaminated with Th-228 daughters) [a].

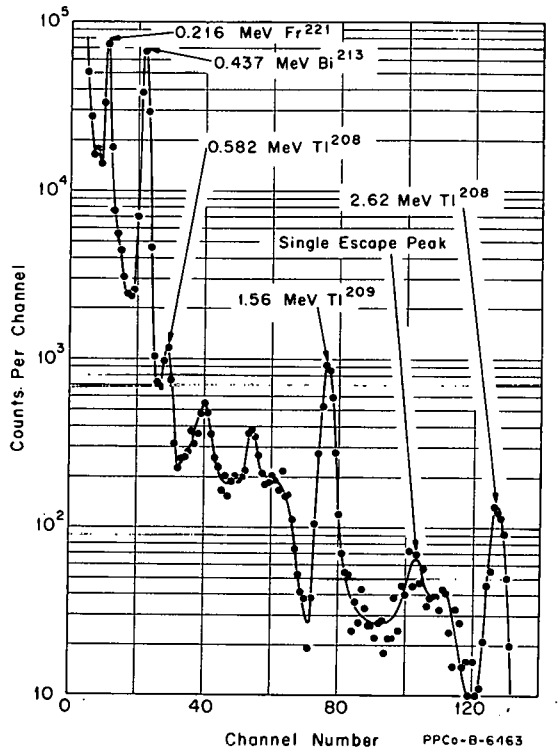

Fig. II-8 Gamma spectrum of daughters of Th-229 plus some Th-228 daughters [b].

2.6 Alpha-Gamma Coincidence Spectra (R. A. Deal, R. P. Schuman, R. N. Chanda)

The alpha-gamma coincidence equipment has been set up and tested with an Am-241 alpha source, using a surface barrier detector for counting alpha rays and a 1-by 1-1/2-inch NaI(Tl) crystal for counting gamma rays. Some gamma-gamma coincidence spectra were also taken using two 3-by 3-inch NaI(Tl) crystals and an Eu-152 source. Thus, equipment will be used in extending studies of the decay scheme of Pa-231 [5].

2.7 Cross Section of Tl-204 (R. P. Schuman, J. R. Berreth)

Two samples of Tl metal have been irradiated in the ETR for this purpose of building in enough Tl-204 for chopper σ measurements. The first of the two irradiated thallium samples was discharged from the ETR and opened. The aluminum sample holders were covered with a white corrosion product. The

---

[a] Ac-225 energies and abundances taken from B. S. Dzhelepov et al, "On α Decay of Ac-225", Zhur. Eksperim. i Teor. Fiz., XLIII (December 1962), pp 2077-9. (In Russian). Other energies from "Table of Isotopes", D. Stromminger et al, Revs. Modern Phys., XXX, p 585 (1958).

[b] Gamma energies from D. Stromminger et al, "Table of Isotopes", Revs. Modern Phys., XXX (April 1958) pp 585-904.

Tl monitor sample was also opened; and either due to corrosion or possibly to melting of Tl, the Al shim cover was stuck to the Tl. The Tl, however, does not appear to be badly distorted, so it is hoped that chopper measurements can be made on the samples without any refabrication. Chopper sample blocks were loaded and measurements started.

2.8 Cross Section of Am-242m (R. P. Schuman, J. W. Codding, R. A. Deal, J. R. Berreth)

The small samples of Am-241, one irradiated in a Cd shield and the other unshielded, have now been mass analyzed. The results of the mass analyses are given in Table II-2.

TABLE II-2

MASS ANALYSIS OF IRRADIATED Am-241

	Am-241 (wt%)	Am-242m (wt%)	Am-243 (wt%)	Burnup of Am-241
Am-241 before irradiation	100	0.0007	---	---
Am irradiated in Cd	98.88	1.082	0.041	5%
Am irradiated unshielded	96.28	1.408	2.315	45%

The mass analyses indicate that a longer Cd-shielded irradiation may give a somewhat higher percentage of Am-242m than the best unshielded irradiation. A new sample of Am-241 is being irradiated inside a Cd shield to about four times the total nvt to see if a larger percentage of Am-242m can be produced. These "pilot" irradiations should provide sufficient data to determine how larger samples of Am-241 should be irradiated to produce optimum Am-242 for chopper measurements.

3. THEORETICAL PHYSICS
(H. L. McMurry)

3.1 Orientation Averaging in Slow Neutron Scattering Calculations (H. L. McMurry)

Slow neutron scattering calculations on ethane and on butane, using the Krieger-Nelkin (K.N.) method of averaging over molecular orientation [6], gave lower intensities at high momentum transfers than are revealed in experimental data from the MTR slow neutron velocity selector.

When the approximations involved in the calculation procedure were examined, it appeared that the one most likely to lead to erroneous results was the K.N. method for averaging over scattering by molecules in different molecular orientations. The calculations approximate this average by replacing functions of Eulerian angle variables which define the molecular orientation by their average values.

The question has been examined by modifying the computational procedure [6] to permit calculations for many molecular orientations. From these, the average is obtained by numerical integration.

Table II-3 compares calculated values for the scattering function $S(\kappa^2,\beta)$ obtained using the exact averaging (E.A.) procedure, and the K.N. procedure

TABLE II-3

COMPARISON OF $S(\kappa^2, \beta)$ CALCULATED USING EXACT AND APPROXIMATE AVERAGING OVER MOLECULAR ORIENTATION

Molecule	κ^2 (A^{-2})	β	$S(\kappa^2, \beta)$ (barns/eV) by ster by molecule		
			Observed	Eulerian Angle	Krieger-Nelkin
C_2H_6	130	0.0	94	90.8	75.2
	130	0.2	100	89.8	74.6
	130	0.4	89	86.7	73.1
	130	0.7	89	79.1	68.9
	130	1.0	69	69.0	63.2
	130	1.5	56	51.6	51.8
	58	1.0	≈ 175	173	178
	58	1.5	≈ 107	102	118
nC_4H_{10}	86.5	0.6	300	265	217

with experimental data from the MTR. The calculations are for the scattering function $S(\kappa^2,\beta)$ which is obtained from the measured partial differential scattering cross section by extracting the detailed balancing factor $(E_o/E)^{1/2} \exp(-\beta/2)$. Here E_o and E are the incident and scattered neutron energies, respectively; and $\beta = (E - E_o)/kT$. The scattering function depends on β and the neutron momentum change κh.

It is seen that every case the E.A. calculation is higher than the K.N. when κ^2 is large ($\kappa^2 = 130$) and agrees better with the data. The calculations on C_2H_6 are sufficient to demonstrate that at this κ^2 the discrepancies are largest for $\beta = 0$.

In C_2H_6 when $\beta = 1.5$ and κ^2 has the intermediate value $\kappa^2 = 58$, the K.N. calculation is higher than both the E.A. result and the observed value. Again the E.A. calculation is closer to the observed value.

The conclusion is that significant errors in calculated partial differential scattering cross sections can arise from not treating the dependence on molecular orientation properly. The errors may not be important for calculating quantities

like spectra, but they can be significant when the detailed dependence of the scattering on energy transfer and scattering angle (or momentum transfer) is studied.

3.2 Scattering of Slow Neutrons by Liquid CH_4 (G. W. Griffing)

Computations have been completed on a model formulated for the scattering of slow neutrons from liquid methane. The model is an extension of the author's work on gaseous methane [7]. The major modification consists of assuming that the positional coordinate R of the center of mass obeys the Langevin Equation:

$$\frac{d^2R}{dt^2} + \frac{dR}{dt} = F(t) \quad .$$

In the computations, the viscous damping coefficient was varied to give a best fit to the experimental data [8]. Upon doing this for one scattering angle and energy, it was found that good agreement at other scattering angles and energies was obtained. Among the interesting points found were: (a) the rotational motion of the methane molecule in the liquid is hindered. (b) The magnitude of the viscous damping coefficient necessary to fit the experimental scattering data is not the measured macroscopic value but is approximately a factor of 4 lower. A paper is being prepared for publication and an oral presentation is planned for the Washington meeting of the APS.

4. REACTOR EXPERIMENTS
(E. Fast)

4.1 Infinitely Dilute Resonance Integrals of Some Rare Earth Elements (J. J. Scoville, J. W. Rogers)

The infinitely dilute resonance absorption integrals of five rare-earth oxides have been determined by reactivity measurements in the ARMF-II cadmium-shielded facility. The methods and procedures used in this determination have been described elsewhere [9], and will not be repeated here.

The materials measured were terbium, holmium, erbium, thulium, and ytterbium, in their natural isotopic abundances. The samples were hollow cylinders, with 0.030-inch walls, 0.860 inch in diameter, and 4.250 inches high, containing the rare-earth oxide in a powder compacted aluminum dispersion. The virgin material was sifted through a 400-mesh sieve to provide negligible particle self-shielding. Disperison was checked chemically and radiographically for uniformity and homogeneity.

Results, together with literature data where available, are shown in Table II-4. Experimental results are based on gold as a standard (assuming the gold resonance integral is 1558 $\pm$ 40 barns, including the 1/v contribution). The four literature values for thulium are from the same source determined by three different experimental techniques and by calculation. The literature value for terbium is calculated from resonance parameters from BNL-325.

TABLE II-4

RARE EARTH RESONANCE INTEGRALS

Element	Atomic Number	Infinitely Dilute Resonance Absorption Integral	
		This Work	Literature
Terbium	65	628 ± 24 barns	393 barns[a]
Holmium	67	860 ± 26 barns	
Erbium	68	1000 ± 200 barns	
Thulium	69	1736 ± 54 barns	1600 ± 500[b] 2210 ± 160 1110 ± 130 1790 ± 200
Ytterbium	70	200 ± 20 barns	

[a] Calculated from published parameters -- Reference 10.

[b] Calculated from published parameters -- Reference 11.

Activation measurements are in progress for holmium and thulium, which will provide a check of the above resonance integral measurements. These results are not yet complete. The resonance integrals of all the above will be calculated in the near future using the best available resonance parameters.

5. DECAY OF Pt-199
(W. W. Black)

Platinum-199 decays by beta emission to Au-199 which similarly decays to stable Hg-199 with a 3.15-day half-life. The beta and gamma radiations of Pt-199 have been studied by means of lithium-drifted germanium and silicon detectors, NaI(Tl), permanent-magnet spectrographs, and β-γ and γ-γ coincidence techniques. Previous investigations of Pt-199 have been carried out by LeBlanc, Cork, and Burson [12] and Joshi, Thosar, and Prasad [13, 14]. These two groups suggested quite different decay schemes. The present work was undertaken in an attempt to derive a unique decay scheme.

5.1 Source Preparation

The Pt-199 activity was produced by neutron irradiation of platinum sponge, isotopically enriched to approximately 60 percent in Pt-198. The sources for the Ge(Li) and NaI(Tl) gamma-ray detectors and the silicon electron detector were obtained by irradiating the sponge in the Materials Testing Reactor in a flux of approximately 1×10^{13} neutrons/cm^2/sec for 1 hour or less. The samples were dissolved in aqua regia and dried. Alcohol was added, and this solution was evaporated on plastic backing for gamma-ray sources and on thin VYNS films for electron sources. Samples for the permanent-magnet spectrographs were irradiated in a flux of approximately 2×10^{14} neutrons/cm^2/sec for 1 hour or less. The radioactive material was then plated onto a 0.006-inch Pt wire.

5.2 Internal Conversion Electron Studies

Several plates were exposed for each of the spectrograph sources. Table II-5 gives the exposure times for each of the plates, where Δt is the exposure duration and t is the time between the irradiation and the start of exposure. Table II-6 summarizes the electron energies measured on each plate. Those

TABLE II-5

PERTINENT TIMES FOR PLATE EXPOSURES

Time (hours)	Source No. 1					Source No. 2			
	Plate 1	Plate 2	Plate 3	Plate 4	Plate 5	Plate 1	Plate 2	Plate 3	Plate 4
t	0.53	1.43	6.12	48.97	120.88	0.57	1.30	5.70	22.65
Δt	0.80	2.12	42.45	27.33	120.97	1.13	4.30	16.83	71.48

TABLE II-6

ELECTRON ENERGIES MEASURED
WITH PERMANENT-MAGNET SPECTROGRAPH
(keV)

Plate 1	Plate 2	Plate 3	Plate 4	Plate 5	Plate 1	Plate 2	Plate 3	Plate 4
				35.08	40.71			
				37.45	43.09			
40.23					51.56			
42.96					54.09			
51.46					60.31			
60.21					62.81			
62.59						62.91	62.99	
	62.07	63.04	62.02		63.70	63.54	63.56	
64.96	65.09				65.33	65.34	65.48	
73.71					73.63	73.84	73.97	
	75.20	75.22	75.01	75.19	75.19	75.26	75.28	
104.85	105.04				76.43	76.28	76.48	
110.64					* 88.19			
*123.37					* 89.90			
	125.17	125.23	124.77	125.10	104.99			
*138.30					110.96	110.43	110.68	
	143.97	144.01	143.60	143.95	125.15	125.13	125.06	125.00
	146.02	145.75	145.53	146.00	*136.04			
	155.12	154.92	154.64	154.76	*136.61			
		157.51	157.65	157.49	144.09	144.09	144.07	144.07
165.75	165.94				145.80	145.86	145.94	145.98
171.78	172.34	171.84			155.30	155.06	155.12	155.16
182.51						157.45	157.55	157.55
			192.95	192.93	*160.56			
		204.56	204.61	204.30	165.47	165.81		
236.20	236.10			207.70	172.02			
267.95	268.84				173.94			
462.09	462.55				183.00			
						193.27	193.29	193.12
							209.91	209.63
								207.54
					236.31	235.96		
					267.88	268.12		
					332.39	332.19		
					462.17			

marked with an asterisk are not well established. Table II-7 gives the adopted electron energies with their estimated uncertainties, the subshell assignments, the transition energies, and their associate . isotopes. Also given are transition energies found by other investigators. The transitions marked with an asterisk are not well established. The precision measurements of the transitions in Hg-199 by Graham et al [15] have been used throughout this investigation as an internal energy calibration.

Figure II-9 shows a typical series of spectra taken with the silicon detector. No new conversion lines were observed in these spectra. However, with this detector, the decay of a source can be followed more easily, permitting a better identification of the lines due to contaminating isotopes.

TABLE II-7

SUMMARY OF TRANSITION ASSIGNMENTS FOR SPECTROGRAPH LINES

Transition In	K	L_1	L_2	L_3	M	N	Previous Measurement	Adopted Value for Transition (keV)
Au-197		62.91	63.60	65.26	73.81		77.345[a]	77.26 ± 0.10
Au-197	110.69							191.41 ± 0.20
Hg-199		35.08		37.45			49.826[b]	49.83 ± 0.10
Hg-199	75.20		143.99	145.87	155.01	157.54	158.366[b]	158.31 ± 0.20
Hg-199	125.08	193.09			204.63	207.62	208.190[b]	208.19 ± 0.30
Pt-197	268.20	332.29					346[c]	346.58 ± 0.40
Au-199		40.47		43.03	51.51			54.89 ± 0.10
Au-199		60.26		62.70				74.62 ± 0.10
Au-199	104.92		172.00		182.76		197[c]	185.56 ± 0.20
Au-199	165.75						246[c]	246.46 ± 0.30
Au-199	236.15						316[c]	316.86 ± 0.40
Au-199	462.13							542.84 ± 0.60
Au-199			88.19	89.90				101.87 ± 0.30*
Au-199		136.04	136.61					150.32 ± 0.50*
Au-199		138.30						219.01 ± 0.50*
Au-199	160.56							241.27 ± 0.50*

[a] Reference 16

[b] Reference 15

[c] Reference 12

5.3 Gamma-Ray Studies Using Ge(Li)

The main contribution of these data was the resolution of transitions with small energy separations and better energy determinations than are possible using NaI(Tl). The depletion depth of the detector used to take this data was 2 mm, and the half width of the photopeaks was approximately 5.4 keV. The apparatus associated with the Ge(Li) detector was a preamplifier, a Tennelec TC-200 amplifier and a 512- or 1024-channel analyzer. Figure II-10 shows a spectrum taken with 1024 channels and a gain of 1.04 keV/channel.

With the aid of a precision linear pulser, it has been determined that the Ge(Li) spectrometer system, including the 1024-channel ramp, has some small nonlinearities. The data shown in Figure II-10 were corrected for this nonlinearity and then the transitions with well-known energies were fit by linear least squares to a line. From the coefficients for this line, the energies corresponding to all other photopeaks were calculated. Table II-8 shows the energies of the transitions in Au-199, Au-197, and Hg-199 observed with Ge(Li) detectors. The values in the second column are those of R. L. Graham et al [15] in the case of the transitions of Hg-199 and the present spectrograph values in the case of the transitions in Au-199. The values marked with an asterisk were obtained from a 5 keV/channel Ge(Li) spectrum, and therefore, do not have the accuracy of the other values.

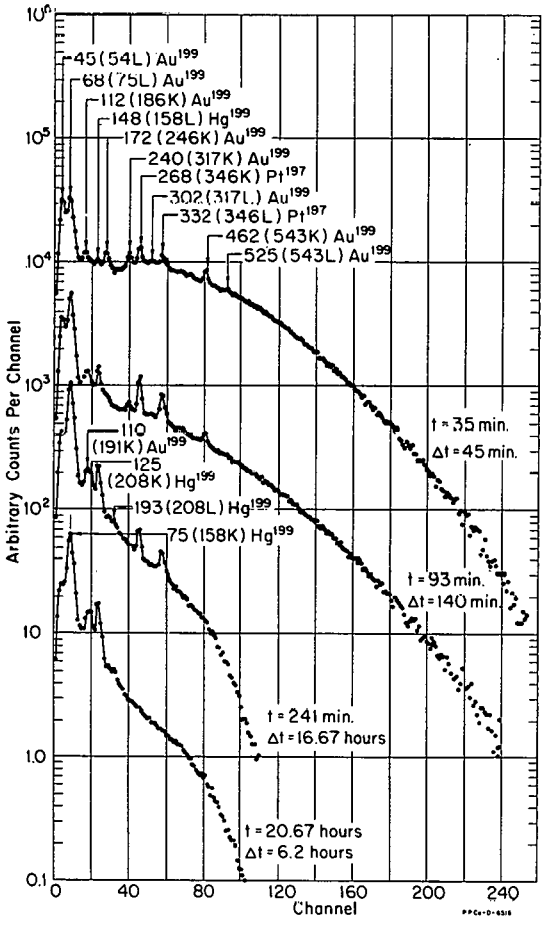

Fig. II-9 Series of electron spectra obtained from a silicon detector. In each case, t represents the time elapsed since the source was removed from the reactor until being placed in the silicon detector. Also, Δt represents the time for which the data were accumulated. The energies are given in keV along with the isotope in which the transition takes place.

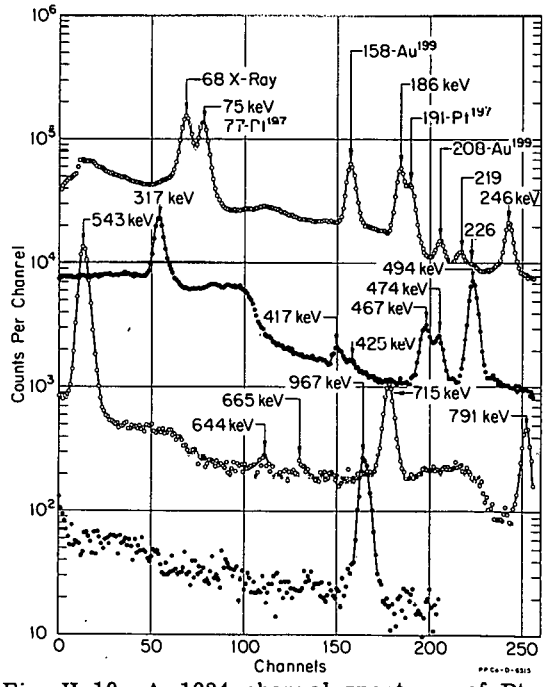

Fig. II-10 A 1024-channel spectrum of Pt-199 taken with a Ge(Li) detector.

TABLE II-8

ENERGIES OF SOME TRANSITIONS IN Au-199, Au-197, AND Hg-199 FROM Ge(Li) DATA

Ge(Li) Energy (keV)	"Correct" Energy (keV)
75 ± 2	74.6
158.3 ± 0.2	158.366
185.6 ± 0.3	185.6
191.43 ± 0.3	
208.2 ± 0.2	208.190
219.1 ± 1.0	
239.7 ± 1.0	
246.4 ± 0.3	246.5
317.0 ± 0.3	316.9
416.9 ± 1.0	
424.8 ± 1.0	
467.0 ± 0.5	
474.2 ± 0.5	
493.6 ± 0.5	
542.8 ± 0.5	542.8
644.3 ± 1.0	
664.7 ± 1.0	
714.9 ± 1.0	
790.6 ± 1.0	
836 ± 5*	
889 ± 5*	
930 ± 5*	
967 ± 1	
1030 ± 10*	
1072 ± 10*	
1103 ± 10*	
1160 ± 10*	
1245 ± 10*	

5.4 Computer Analysis of NaI(Tl) Data

Many gamma-ray spectra were collected during the course of this investigation with a 3- by 3-inch NaI(Tl) gamma-ray scintillation spectrometer. Figure II-11 shows a spectrum taken with the source positioned 10 cm from the crystal. Also shown is a spectrum taken at 0.75 cm from the crystal which enhanced the intensity of coincidence sum peaks. As is noted in the figure, there are definite indications of sum peaks at 320, 734, and 791 keV.

Five gamma-ray spectra from one source were chosen for extensive computer analysis. The computer program that was used is one written by G. A. Jayne [17]. The largest problem in analyzing such a complex spectrum lies in initially identifying the number and

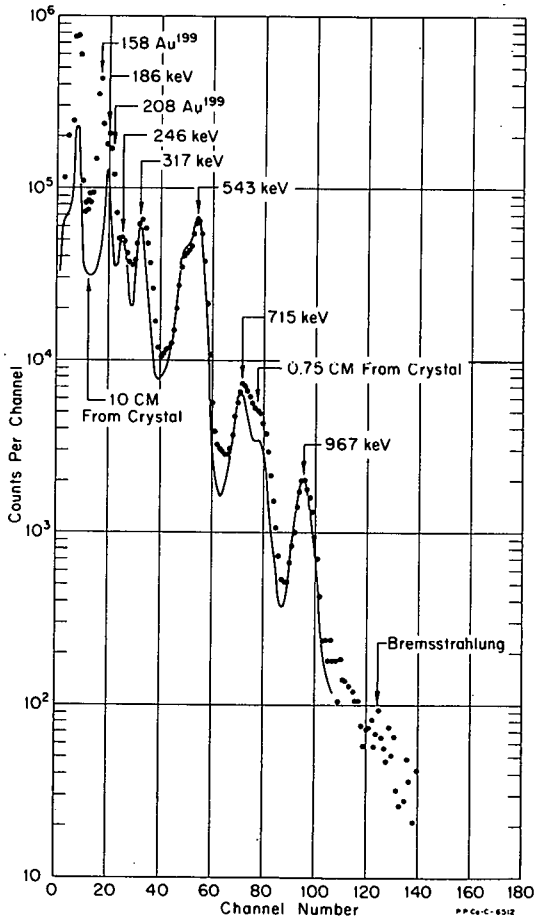

Fig. II-11 Spectra taken with the source 10 and 0.75 cm from the crystal.

approximate energies of the gamma rays that are present. In this case, most of the gamma rays included in the fit were identified from gamma-gamma coincidence data and, to some extent, from data obtained with a Ge(Li) detector. Since an accurate energy measurement was obtained from the spectrographs for the 543-keV transition, this gamma-ray photopeak was used to "gain-shift" the five spectra to correspond to a pulse-height scale on which 661.6 keV falls in channel 132.32. Due to the large amount of computer time needed to analyze a complex spectrum, the results from an extensive analysis of one spectrum were used to aid in the fits of the other four. In the analysis of the first spectrum, photopeak locations and intensities of all the constituent gamma rays were allowed to vary. (The intensities are computed by a linear, least-squares method and the positions by a "direct search" method.) The other four spectra were then fitted with the constituent photopeak locations fixed at these "best" positions and permitting gamma-ray intensities to vary. Table II-9 gives a summary of results for the five spectra. Here t is the time at the beginning of data collection, and Δt is the counting duration. The "goodness-of-fit" number is the sum of the squares of the residuals divided by the number of degrees of freedom. The goodness-of-fit is ideally 1 for a "perfect" fit.

TABLE II-9

TIMES AND COMPUTER-FIT CRITERIA FOR FIVE SPECTRA ANALYZED BY COMPUTER

Spectrum	t (min)	Δt (min)	Goodness of Fit
I	0.0	13.33	1.249
II	19.0	13.33	1.593
III	36.0	16.67	1.556
IV	57.0	16.67	13.33
V	77.0	33.33	1.754

In addition to the individual gamma rays, a Au-199 spectrum, a 1700-keV bremsstrahlung spectrum, and a background spectrum were included as components in these computer fits. Table II-10 gives the photon intensities of the transitions and the bremsstrahlung component relative to that of the 543-keV transition. The intensities of the other components are relative to arbitrary numbers. The last column gives the intensity values adopted and their estimated uncertainties.

Several consistency checks can be applied to these results to determine the quality of the analysis. First, the relative intensities of the major gamma rays agree well from spectrum to spectrum with the exception of the 467- and 474-keV gamma rays. Since the positions of these gamma rays differ by less than 1.5 channels, it is not possible to resolve them. However, the sum of the intensities of these two gamma rays varies only 10 percent. A more sensitive check is to determine the half-life of the Pt-199 decay from the decreasing intensity of the major gamma rays. The results of such a calculation are given in Table II-11. The average of these give a half-life for Pt-199 of 30.6 minutes with a root-mean-square deviation of 0.3 minute. This agrees well with the value of 31.4 $\pm$0.5 minutes found from the $4\pi\beta$-γ coincidence data. Another indication of the quality of analysis is the background intensity. Under normal circumstances, the background intensity given per unit time would be constant. However, the discontinuous change at Spectrum IV (see Table II-10) is of the sign and magnitude actually observed at this time and is probably due to a sudden change in background levels from airborne reactor exhaust gases. Next, the relative intensities of the Au-199 component should follow the usual growth curve. In Figure II-12, the Au-199 intensities of Table II-10 (data points)

TABLE II-10

INTENSITIES OF SOME TRANSITIONS
IN Au-199 AND OTHER SPECTRAL COMPONENTS

Transition or Component	Spectrum I	II	III	IV	V	Adopted Intensity
967	628	628	557	625	647	632 ± 30
930	100	82	126	98	34	102 ± 30
889	23	28	5	13	19	21 ± 10
836	14	23	7	6	19	14 ± 10
791	753	735	770	809	735	760 ± 40
715	1,210	1,270	1,230	1,200	1,210	1,220 ± 30
665	129	120	119	111	137	123 ± 15
644	68	46	41	76	44	55 ± 15
543	10,000	10,000	10,000	10,000	10,000	10,000
494	3,860	3,750	3,740	3,920	3,680	3,790 ± 100
474	795	1,060	1,020	718	1,360	990 ± 250
467	1,410	1,240	1,280	1,390	975	1,330 ± 300
425	192	242	243	232	261	234 ± 100
417	175	135	142	119	110	136 ± 100
317	3,540	3,560	3,660	3,530	3,610	3,580 ± 50
246	1,640	1,640	1,600	1,630	1,660	1,630 ± 30
226	296	266	317	334	269	296 ± 100
219	234	267	207	183	226	223 ± 100
186	4,000	4,000	4,060	4,000	4,010	4,010 ± 40
Bremsstrahlung	255	259	256	270	292	
Background	278	256	262	203	210	
Au-199 Decay	108	132	144	155	158	

are normalized to the proper growth curve (solid lines). Finally, the quality of the computer fit can be judged by how well the components determined by the fit sum up to the original composite spectrum. Figure II-13 is a plot of one of the fits showing the original data (points) and the sum of the calculated components (solid line through points) plus the components. The fit was performed from channel 25 to 230.

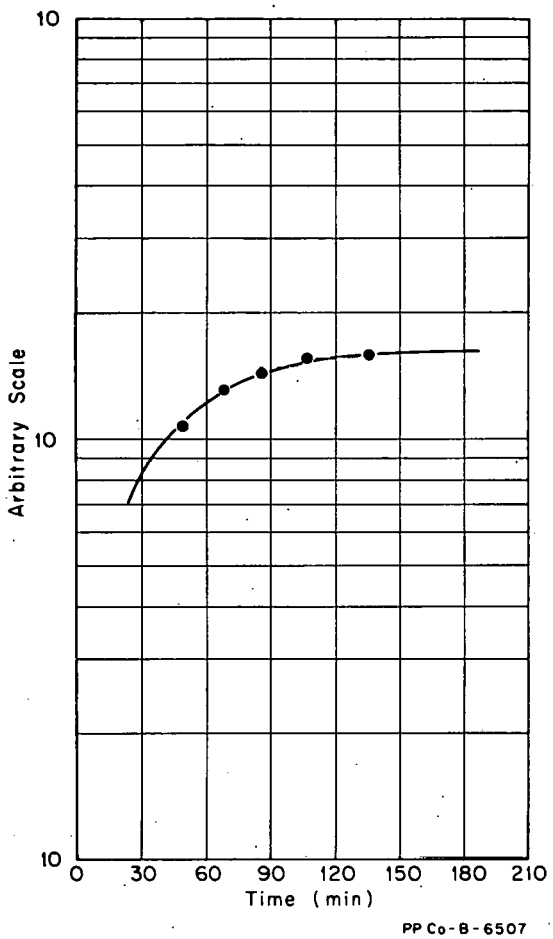

Fig. II-12 Plot of relative Au-199 intensities (data points) from computer analysis normalized to a calculated Au-199 growth curve (solid line).

TABLE II-11

HALF-LIFE OF Pt-199 DECAY FROM THE MAJOR TRANSITIONS

Transition	Half-Life (min)
967	31.2
791	30.8
714	30.0
543	30.6
494	30.2
317	30.6
246	30.8
186	30.6

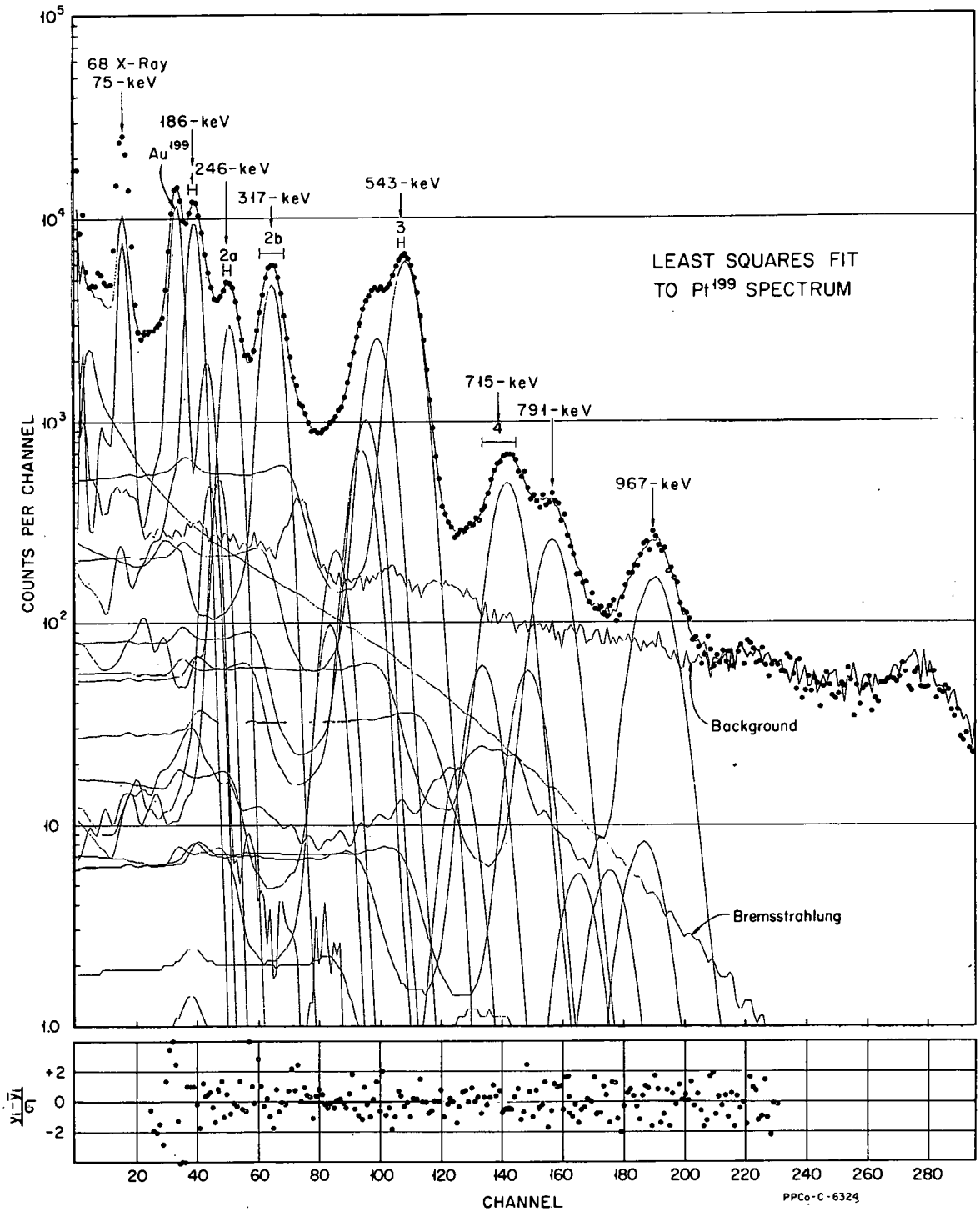

Fig. II-13 Plot showing results of a computer analysis of a Pt-199 spectrum. Original data are shown by points and the sum of the calculated components by the solid line through the points. The gates indicated are those used for the coincidence spectra shown in Figures II-14 through -17. The residuals of the fit are shown along the bottom.

5.5 Gamma-Gamma Coincidence Experiments

Gamma-gamma coincidence measurements were carried out using a 256- x 256-channel, multi-parameter analyzer and two 3- x 3-inch NaI(Tl) detectors. The photomultiplier pulses were fed into conventional A-8 amplifiers which, in turn, were connected to the two ADC's of the analyzer. The resolving time of the fast coincidence circuit (2 τ) was approximately 150 nsec. The two NaI(Tl) detectors were set at an angle of 90° with respect to each other, and a Cd-covered, Pb wedge was placed between them to reduce coincidence events due to Compton scattering. Since Pt-199 has a short half-life, several sources were made; and data were collected for approximately 12 hours during which time approximately 2 x 10^6 coincidence events were recorded.

Figure II-13 shows a spectrum of the gamma rays emitted by Pt-199 and its individual components with the gates for the samples of coincidence spectra shown in Figures II-14 through II-17. Table II-12 is a tabulation of the prominent coincidence observed from analysis of all the coincidence data.

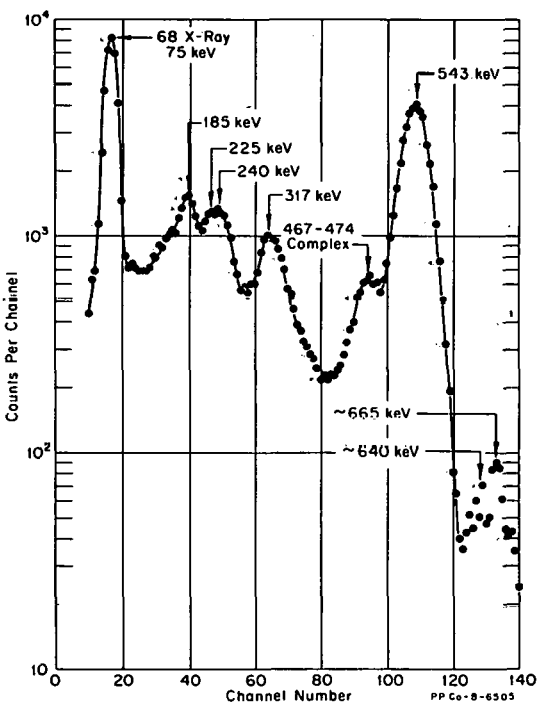

Fig. II-14 Gate 1 of Figure II-13. Coincidences with 186-keV transition.

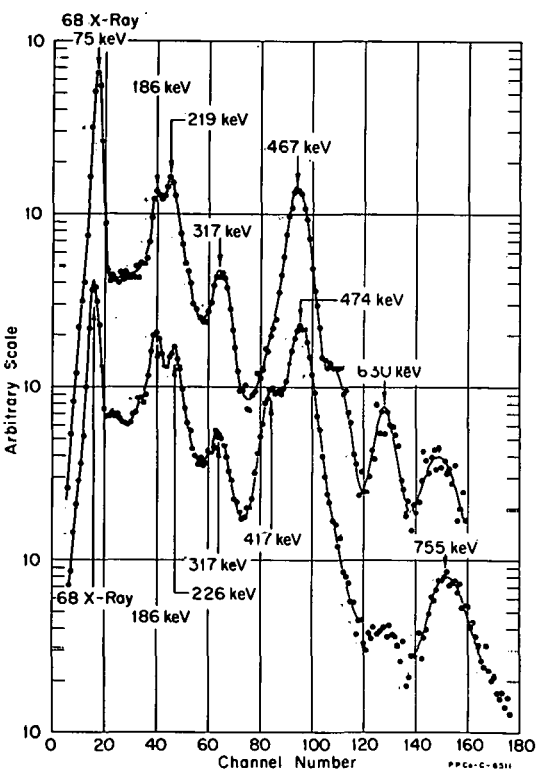

Fig. II-15 Gate 2 of Figure II-13. (a) Coincidences with 246-keV transition. (b) Coincidences with 317-keV transition.

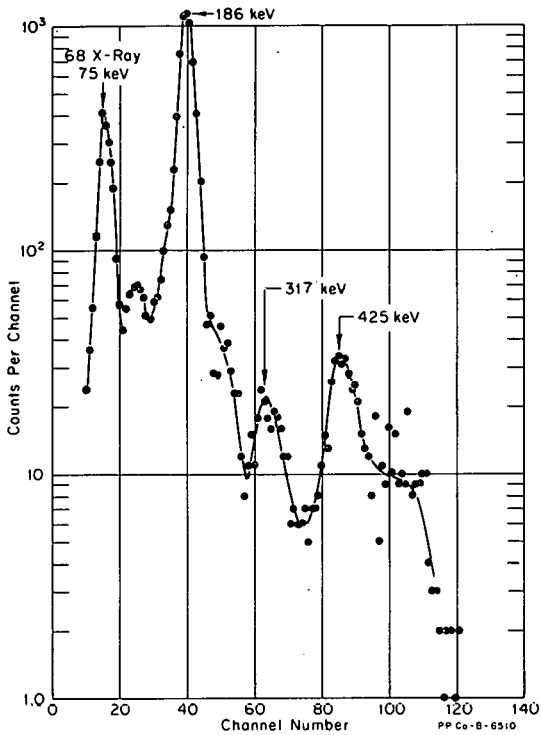

Fig. II-16 Gate 3 of Figure II-13. Coincidences with 543-keV transition.

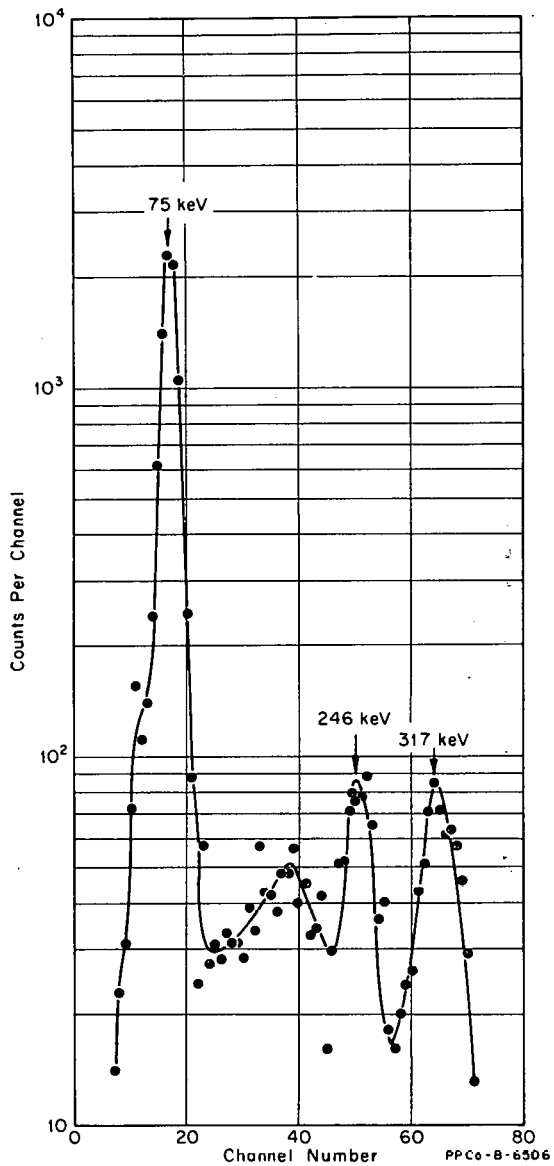

Fig. II-17 Gate 4 of Figure II-13. Coincidences with 714-keV transition.

TABLE II-12

TABULATION OF THE PROMINENT COINCIDENCES
OBSERVED IN THE DECAY OF Pt-199

	75	186	219	226	246	317	417	425	467	474	543	715
75					X				X			X
186											X	
219						X						
226					X							
246	X			X					X			
317			X				X			X		
417						X						
425											X	
467	X				X							
474						X						
543		X						X				
715	X											

5.6 Beta-Gamma Coincidence Experiments

Three distinct types of beta-gamma coincidence experiments were carried out. Two of them used a 4π proportional counter in coincidence with a NaI(Tl) detector which intercepts a solid angle of approximately 2π. In the third experiment, an anthracene detector was used in coincidence with a NaI(Tl) detector. The remainder of the equipment was as described in Section II-5.5.

The first experiment using the proportional counter and NaI(Tl) detector was to determine the half-life of Pt-199. Two sets of data were taken, the first spanning a period of 17 hours and the second a period of 124 hours. The data were analyzed with a nonlinear, least-squares fitting program [a]. In this experiment, the decay curve had three components resulting from the decays of Pt-197, Pt-199, and Au-199. From these data, the adopted values for the half-lives and their estimated errors are: Pt-199, 31.4 ± 0.5 min; Au-199, 3.10 ± 0.09 days; Pt-197, 18.9 ± 2.0 hours. The value for Au-199 measured previously [18] is 3.15 days. Figure II-18 shows a plot of beta counts versus time for the second source.

The proportional counter and NaI(Tl) detector were also used to search for an isomeric state in Au-199. In this experiment, the output of the NaI(Tl) detector was fed into a multichannel analyzer which was gated-off by every β-γ coincidence event. Thus, transitions from any isomeric state should be enhanced in the resultant spectrum relative to those that depopulate prompt states. In Figure II-19, the points represent the spectrum taken in the anticoincidence

[a] Written by D. H. Gipson.

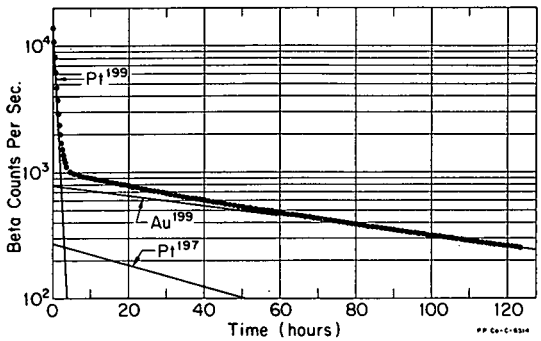

Fig. II-18 Decay curve of Pt-199 + Au-199 + Pt-197 obtained with a 4π proportional counter.

mode, and the solid line represents a singles spectrum. There is some indication of a delayed state at 791 keV; ie, the 791-keV gamma ray appears to be enhanced. The complex around 460- to 540-keV and the 317- and 186-keV transitions also seem to be enhanced, possibly due to cascading from the 791-keV level.

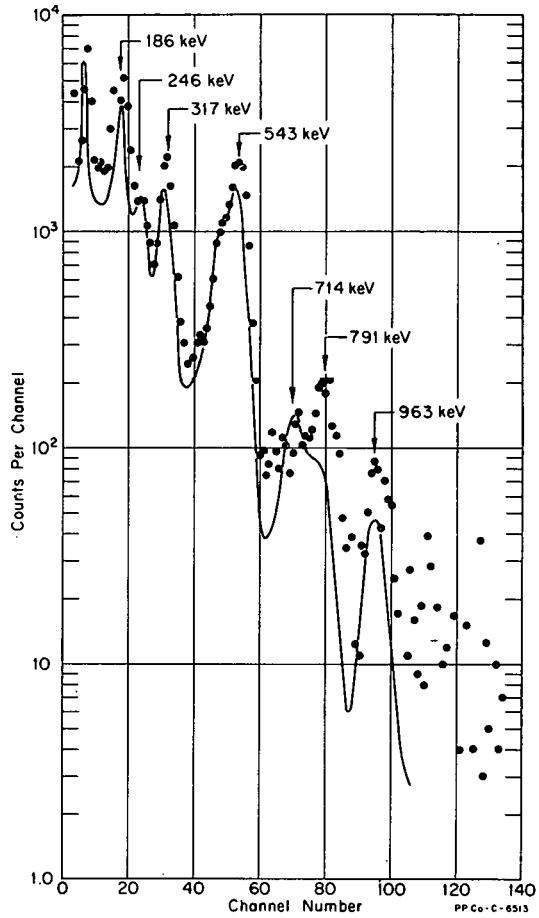

Fig. II-19 Comparison of a spectrum taken in the anti-coincidence mode (points) with a spectrum taken under normal singles conditions (solid line).

From the experiment using the multidimensional analyzer, both gamma spectra coincident with beta energy channels, or beta spectra coincident with beta energy channels, or beta spectra coincident with gamma energy channels can be obtained. Figure II-20 shows spectra of beta rays in coincidence with some of the prominent gamma rays. Figure II-21 shows the gamma rays in coincidence with essentially all beta groups; ie, the gate covered beta energies from approximately 145 keV to approximately 185 keV. This latter spectrum should be the opposite of the spectrum obtained above with the 4π apparatus in the anticoincidence mode. That is, the intensities of all gamma rays depopulating any isomeric state should be depressed. However, care must be taken in analyzing such data to ensure that the observed effects are not a result of exceeding the dynamic range of the coincidence circuit or of the effect of low energy beta groups that are not detected efficiently because of electron absorption in the source and detector system. However, there is no indication of the 494-keV transition in Figure II-21. Also the intensities of the 317- and 543-keV transitions are reduced. The 186-, 715-, and 791-keV transitions appear to be somewhat reduced in intensity; but because of the arguments given above, it cannot be definitely said that this is due to an isomeric state.

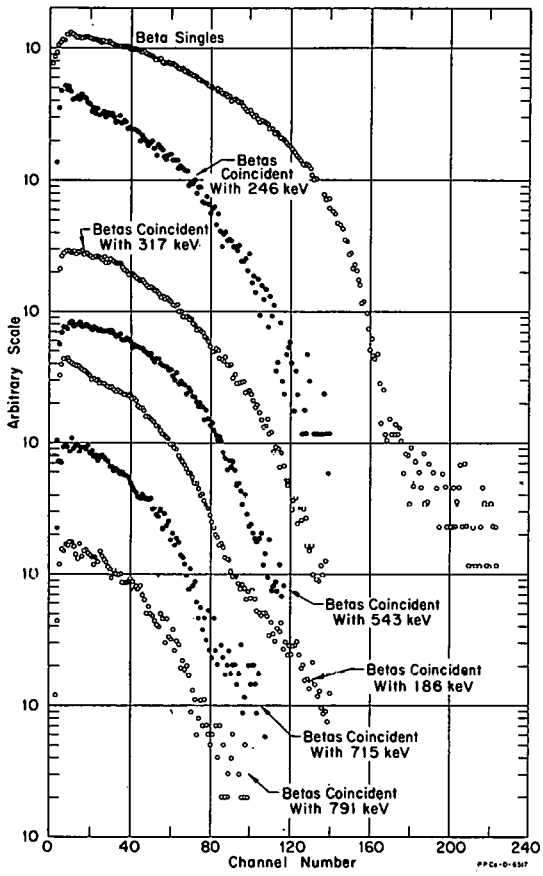

Fig. II-20 Beta-gamma coincidence spectra and a beta singles spectrum.

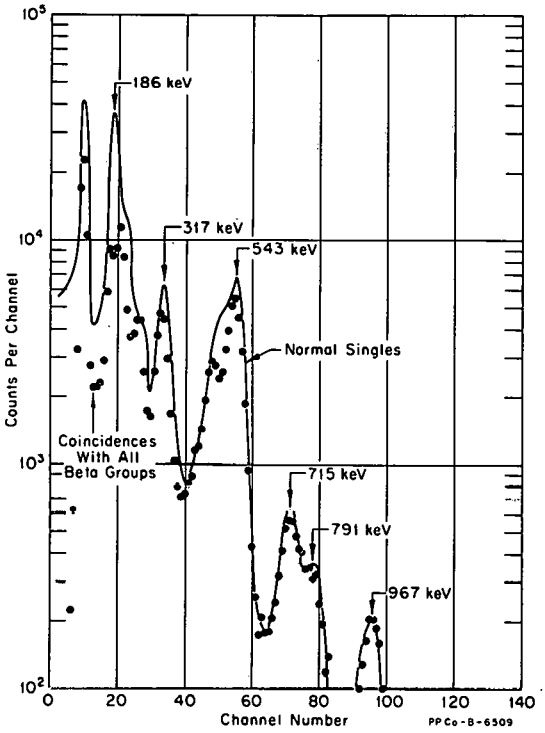

Fig. II-21 Gamma rays in coincidence with essential all beta groups.

5.7 Discussion of Experimental Results

Table II-13 summarizes all the transitions observed in the decay of Pt-199 and the apparatus with which they were detected. The last column lists the adopted value for the energies and their estimated uncertainties. Those marked by an asterisk are not well established.

Figure II-22 gives a tentative decay scheme for Pt-199 based on all the experimental results. The gamma rays shown as dashes have been placed in the scheme strictly on the basis of energy. The experimental evidence does not definitely indicate whether the 715-keV gamma ray comes from the 788- or 791-keV level. Both LeBlanc et al [12] and Joshi et al [13, 14] have the 317- and 246-keV transitions depopulating a common level, the 317-keV transition being the crossover for the 246-75-keV cascade. The results of the present spectrograph measurements show that this is impossible on an energy basis. Previously, Joshi et al [13, 14] reported that both the 317- and 246-keV gamma rays were in coincidence with a 220- and a 475-keV gamma ray; the latter two have been shown to be doublets by this investigation.

Little information was obtained on the 55-keV transition. It has been placed in the scheme of Figure II-22 strictly on the basis of energy. However, some conclusions can be drawn. No photons were observed corresponding to this transition, indicating that it is probably of quadrupole or higher order and possibly depopulates a level with a half-life greater than a few nanoseconds. Since Emery and Sehgal [19] have reported a 53-keV transition in Pt-197m,

TABLE II-13

TRANSITIONS OBSERVED IN THE DECAY OF Pt-199[a]

Ge(Li)	NaI(Tl)	Spectrograph	Silicon Detector	Adopted Value
		54.89 ± 0.1		54.89 ± 0.10
75 ± 2		74.6 ± 0.1	75	74.6 ± 0.1
		101.87 ± 0.30*		101.9 ± 0.3
		150.32 ± 0.50*		150.3 ± 0.5
185.6 ± 0.3		185.56 ± 0.20	186	185.6 ± 0.2
219.1 ± 1.0	213 ± 10			219.0 ± 1.0
225.7 ± 1.0	229 ± 10			226.0 ± 1.0
239.7 ± 1.0*		241.27 ± 0.50		240.0 ± 1.0
246.4 ± 0.3	246 ± 3	246.46 ± 0.3	246	246.5 ± 0.3
317.0 ± 0.3	317 ± 3	316.86 ± 0.3	317	316.9 ± 0.3
416.9 ± 1.0	414 ± 10			417.0 ± 1.0
424.8 ± 1.0	424 ± 10			425.0 ± 1.0
467.0 ± 0.5	467 ± 5			467.0 ± 0.5
474.2 ± 0.5	475 ± 5			474.2 ± 0.5
493.6 ± 0.5	494 ± 5			493.6 ± 0.5
542.8 ± 0.5	542 ± 5	542.84 ± 0.5	543	542.8 ± 0.5
				632.0 ± 10.0
644.3 ± 1.0	632 ± 10			644.0 ± 1.0
664.7 ± 1.0	670 ± 10			665.0 ± 1.0
714.9 ± 1.0	713 ± 5			715.0 ± 1.0
	755 ± 10			755.0 ± 10.0
790.6 ± 1.0	789 ± 5			791.0 ± 1.0
836.0 ± 5.0	831 ± 10			836.0 ± 5.0
889.0 ± 5.0	885 ± 10			889.0 ± 5.0
930.0 ± 5.0	940 ± 10			930.0 ± 20.0
967.0 ± 1.0	964 ± 5			967.0 ± 1.0
1030.0 ± 5.0				1030.0 ± 5.0
1072.0 ± 5.0	1072 ± 10			1072.0 ± 5.0
1103.0 ± 5.0	1100 ± 10			1103.0 ± 5.0
1160.0 ± 5.0				1160.0 ± 5.0
1245.0 ± 5.0				1245.0 ± 5.0

[a] All energies are in keV.

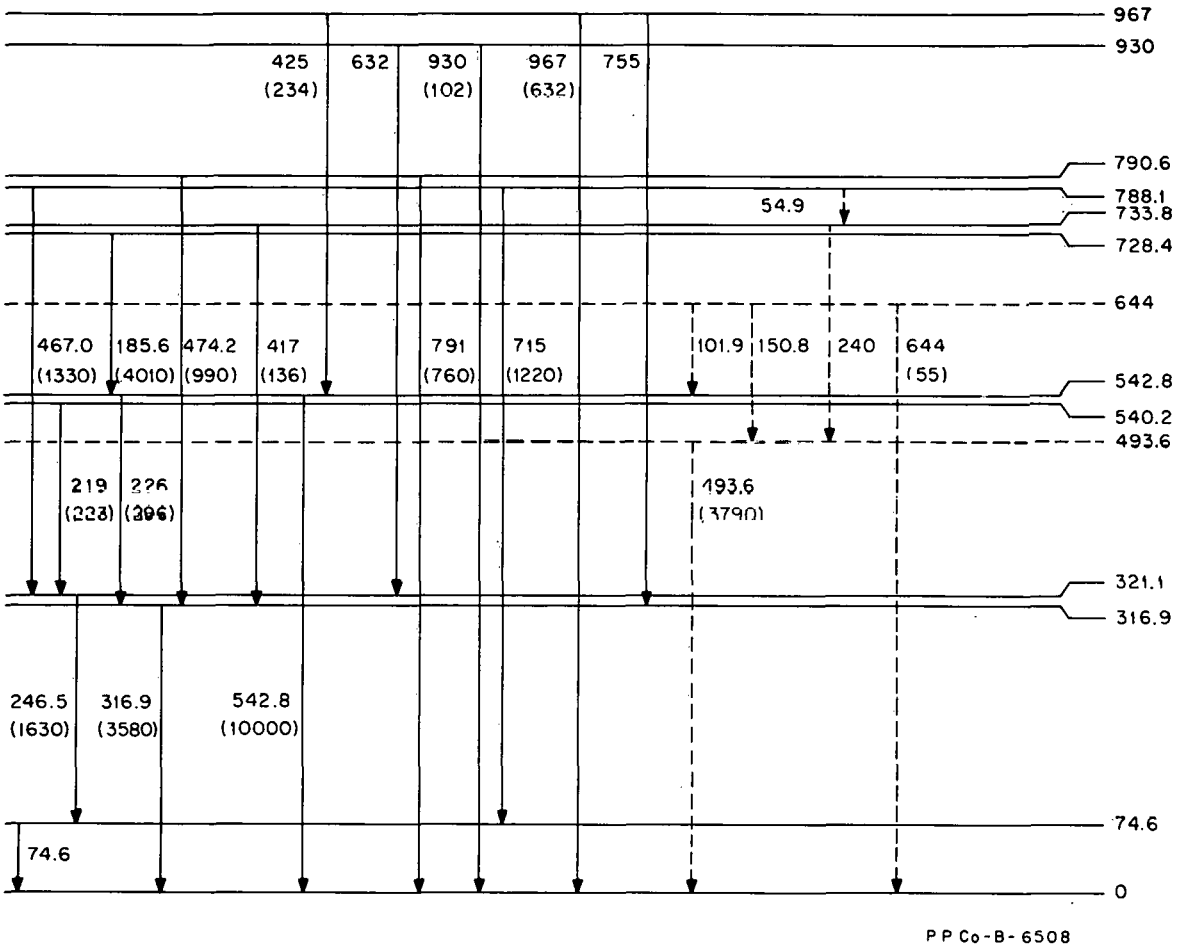

Fig. II-22 Level structure of Au-199 based on present experimental evidence. The numbers in parentheses are gamma-ray intensities relative to the 543-keV gamma ray.

a careful remeasurement of the spectrograph plates was made. These measurements confirmed that the transition reported here is not of the same energy reported for the transition in Pt-197m and, therefore, is still presumed to result from the decay of Pt-199.

Little has been learned about the 494-keV transition. No positive coincidence have been observed in either the γ-γ or β-γ coincidence studies. However, the complete absence of this transition in the spectrum of Figure II-21 indicates that it either depopulates an isomeric level or is in cascade with a gamma ray that does. There is some difficulty with the latter interpretation since coincidence should have been observed unless the 494-keV is in coincidence with a transition that is very highly converted, such as the 55-keV transition. More weight is given to the cascade argument by the fact that the 494-keV transition is not highly converted. It would be expected to be appreciably converted if it resulted from an isomeric state with a half-life much greater than 150 nsec as is the case here. Unfortunately, there is little experimental evidence at present to substantiate these conjectures. As shown in Figure II-22, the 55-keV transition would fit into the tentative level structure; but the 494-keV gamma ray would have to be fed totally by the 240- and 150-keV transitions which would appear not to be of sufficient intensity to match that of the very strong 494-keV transition.

5.8 Future Experiments

Removal of some of the inadequacies of the present decay scheme of Pt-199 are planned in two future experiments. The first will be to perform γ-γ coincidence experiments using one NaI(Tl) and one Ge(Li) detector. In these experiments, the Ge(Li) detector will be adjusted to cover (a) the region from approximately 460 to 500 keV and (b) the region from 210 to 250 keV.

For the second experiment, a very wide-range, time-to-amplitude converter is being built which will be used in an attempt to learn more about any isomeric states in Au-199

6. REFERENCES

1. Oak Ridge National Laboratory, Chemistry Division Annual Progress Report for Period Ending June 20, 1964, ORNL-3679 (September 1964) p 14.

2. G. D. James, "The Fission Cross Section of U-232 From 4 eV to 400 eV", Nucl. Phys., 55 (July 1964) pp 517-22.

3. R. L. Tromp, "Beryllium Gases Experiments", Nuclear Technology Branches Quarterly Report July 1- September 30, 1964, IDO-17052 (February 1965). pp 17-18.

4. K. T. Faler, "Cadmium Neutron Shield Burn-Through", Nuclear Technology Branches Quarterly Report July 1- September 30, 1964, IDO-17052 (February 1965) p 19.

5. R. N. Chanda and R. A. Deal, "Pa-231 Decay Scheme", Nuclear Technology Branches Quarterly Report July 1-September 30, 1964, IDO-17052 (February 1965) p 18.

6. H. L. McMurray and L. J. Gannon, A Machine Program for Calculating Slow Neutron Scattering Cross Sections With Application to Water, IDO-16984 (July 1964).

7. G. W. Griffing, "Influence of the Rotational Levels on the Scattering of Slow Neutrons by Gaseous Methane", Phys. Rev., 124 (December 1961) pp 1489-93.

8. Y. D. Harker and R. M. Brugger, "Slow-Neutron Inelastic Scattering from Low-Temperature Gaseous Methane, Liquid Methane, and Solid Methane", J. Chem. Phys., 42 (January 1965) pp 275-84.

9. J. R. Huffman and D. R. deBoisblanc et al, MTR-ETR Technical Branches Quarterly Report January 1- March 31, 1962, IDO-16781 (June 1962) p 2.

   J. R. Huffman and D. R. deBoisblanc et al, MTR-ETR Technical Branches Quarterly Report July 1- September 30, 1962, IDO-16827 (January 1963) p 3.

   J. R. Huffman and D. R. deBoisblanc et al, MTR-ETR Technical Branches Quarterly Report January 1- March 31, 1963, IDO-16898 (July 1963) p 3.

10. W. H. Walker, Yields and Effective Cross Sections of Fission Products and Pseudo-Fission-Products, CRRP-913 (March 1960).

11. G. Hardie et al, Studies of the Resonance Integrals of Re and Tm, IITRI-578P24-12 (September 1964).

12. J. M. LeBlanc et al, "Decay Scheme of Pt-199", Phys. Rev. 104 (December 1956) pp 1670-73.

13. M. C. Joshi et al, "Nuclear Levels of Au-199", Nucl. Phys., 52 (March 1964) pp 301-14.

14. M. C. Joshi et al, "Low Energy Levels in Au-199", Phys. Letters, 4 (May 1963) pp 354-7.

15. Atomic Energy of Canada Ltd., Physics Division Progress Report, October 1-December 31, 1963, PR-P-60 (1964).

16. I. Marklund and B. Lindstroem, "Precision Determination of Gamma Energies of Nuclei with A = 152-197", Nucl. Phys., 40 (January 1963) pp 329-37.

17. G. A. Jayne, Program for Complex Gamma-Ray Spectrum Decomposition by Direct-Search and Least-Squared Methods.

18. K. Way et al, Nuclear Data Sheets, Printing and Publishing Office, National Academy of Sciences, National Research Council: Washington D. C. NRC-60-2-15.

19. G. T. Emery and M. L. Sehgal, "Decay of Pt-197m", Bull. Am. Phys. Soc., 10 (January 1965) p 83.

III. INSTRUMENT DEVELOPMENT

1. INSTRUMENT COMPONENT AND SYSTEMS DEVELOPMENT
(T. J. Boland)

1.1 Proximity Transducer (T. J. Boland, T. T. Davis, J. B. Colson, J. H. Tormey)

The measurement of fuel plate deflection (bowing or warping) and vibration, under dynamic test conditions and in a rather extreme environment, required development of a special transducer.

The following specifications were required:

(1) Operate in hot water up to 350°F

(2) Withstand pressures to 750 psi

(3) Measure bow or warp to within ± 0.002 inch over a range of from 0.068 to 0.225 inch

(4) Measure vibration frequencies to 10,000 cps

(5) Measure vibration amplitude from 0.001 to 0.010 inch or greater

(6) Transducer must not load the fuel plate nor protrude into the coolant channel.

A transducer to meet the stated requirements could not be found through commercial channels. It was decided, therefore, that the development of such a transducer be undertaken. Several methods were considered before choosing the eddy-current-loading method. It was quickly determined that a small induction coil in one arm of a 100 kc impedance bridge was sensitive to metals in its proximity. These metals, both ferrous and nonferrous, produced changes in the coil impedance inversely proportional to the distance between the coil and the metal object. Three problems then required solution: (a) stabilizing the inductor over a range of temperature from 70 to 350°F, (b) sealing the inductor and its associated lead wires from moisture, and (c) stabilizing the inductor over a pressure range of from atmospheric to 750 psig.

A ceramic impregnated coil proved to be more stable than coils impregnated with other encapsulating materials. However, since this did not prove completely stable with temperature, it was decided to use two coils of approximately the same size and impedance. Both coils are mounted in the same enclosure so that both are always at the same temperature. One is sensitive to metals in its proximity while the other is not. By putting these coils in opposite arms of an impedance bridge, one coil corrects the other for change due to temperature. To the extent that the coils are identical, perfect compensation can be achieved.

The coils are "potted" in a metal housing. A metal housing is used for shielding and also to concentrate the flux in the shield material. Both cold-rolled steel and magnetic stainless steel housings proved satisfactory. Magnetic

materials were chosen because these materials yielded more inductor sensitivity. A considerable effort was spent in attempting to seal the coils from the hot water environment. Many epoxy resins which were satisfactory in air up to fairly high temperatures failed to withstand the hot water environment. A good reliable seal was not obtained until a thin (0.005 inch) diaphragm of stainless steel was silver brazed over the end of the housing. The opposite ends, through which the lead wires exit, was sealed by bringing the leads out through a metal tubing which was attached to the transducer by a standard pipe fitting. The pipe threads were "doped" with Teflon cement.

The final transducer design has proven to be reliable and has maintained calibration accuracy over extended test runs in the Hydraulic Test Facility. Temperatures up to 420°F and pressures up to 1080 psig have been withstood with no catastrophic failure.

A total of six transducer channels is used in the tests. The electronic circuits block diagrams shown in Figure III-1 provide readout for only one transducer at a time. In order to record these on a strip chart recorder, a motor-driven switch is used to sequentially read transducers Nos. 1 through 6. Continuous recording of all six transducer outputs would be preferable and has been recommended.

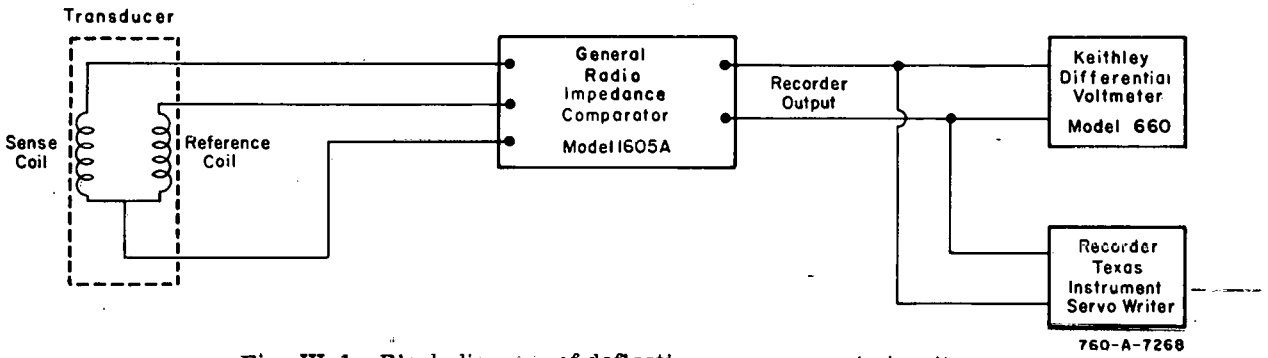

Fig. III-1 Block diagram of deflection measurement circuit.

Originally it was believed that response to vibration frequencies up to 4000 or 5000 cps would be adequate. Computation of fuel plate natural vibration frequencies, however, indicated a need to measure frequencies considerably higher. Since the available vibration spectrum analyzer covered only the range to 7500 cps, it was decided to record the information first on magnetic tape (up to 15,000 cps), then play back the tape at one half speed for analysis. Since the instrument used to measure the transducer impedance as a function of fuel plate deflection only had a frequency response of 20 cps, a different circuit was used to measure the vibration. This circuit is described elsewhere [1] in this report. This technique proved successful.

Figure III-2 shows a sketch of the transducer assembly and Figure III-3 is a plot of the output versus distance between the fuel plate and the transducer face, plotted for various temperatures. Some of the tracking error is attributable to the calibration fixture which was subject to changes with temperature and to the accuracy of reset of a given distance between transducer face and the fuel plate.

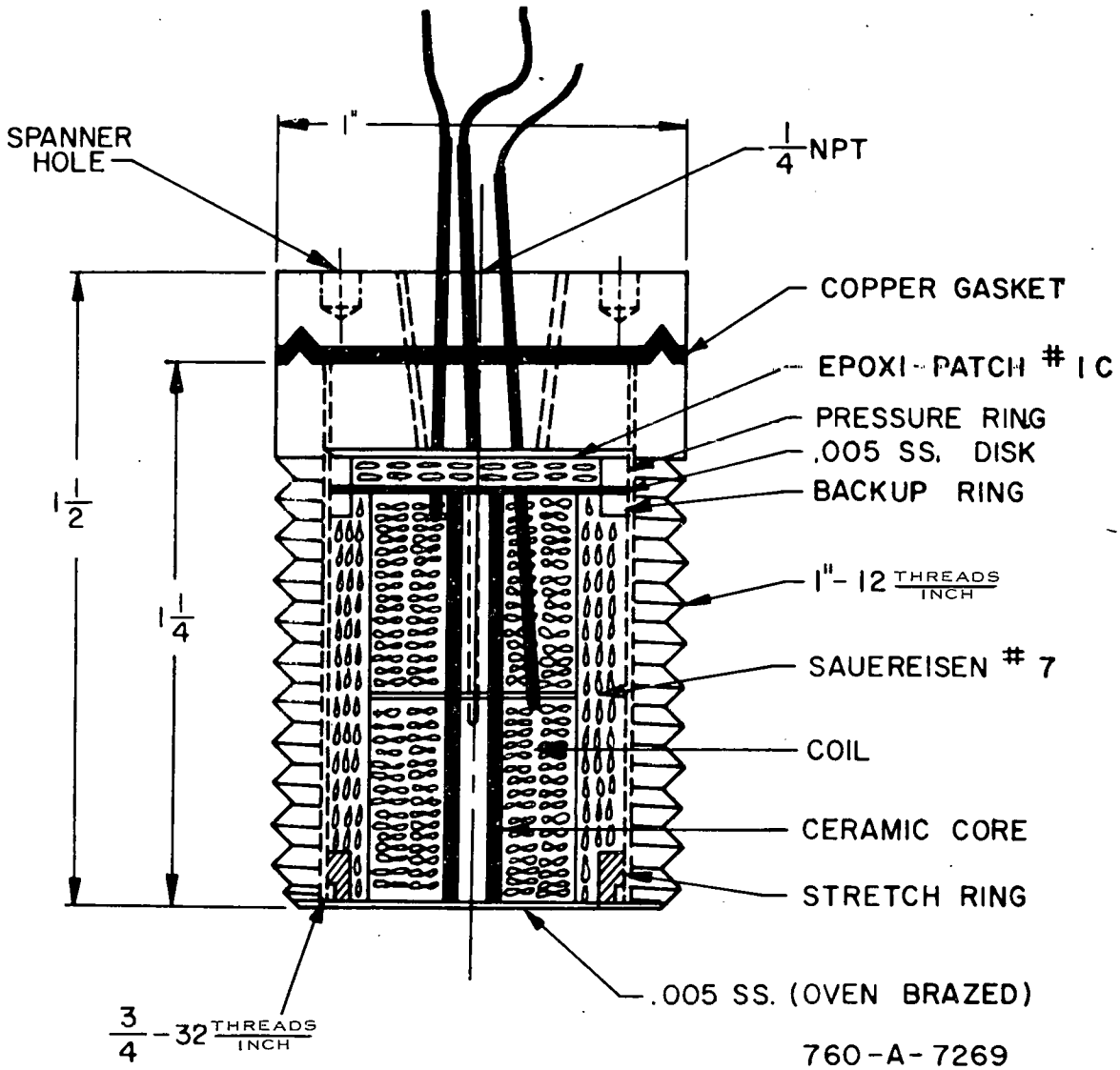

Fig. III-2 Proximity transducer assembly.

1.2 ICPP Multiplication Experiments in the Zirconium Fuel Process (J. B. Thompson, K. F. Smith)

The instrumentation for the multiplication experiment was set up and operated by Instrument Development. This system consisted of three similar counting channels, each containing a detector, preamplifier, amplifier, and count rate meter. It was necessary to develop a new preamplifier to drive the long cable between the preamplifier at the base of the dissolver in "E" cell and the amplifier on the P.M. deck at the top of the dissolver. This preamplifier, as shown in Figure III-4, uses a field effect transistor (FET) at the input where its characteristic high input impedance is used to increase the sensitivity of the preamplifier. This is followed by other transistors to form an emitter follower with a low output impedance to drive the long line. The output is a long-tailed pulse which is ideal for feeding an A-1 linear amplifier with delay line clipping.

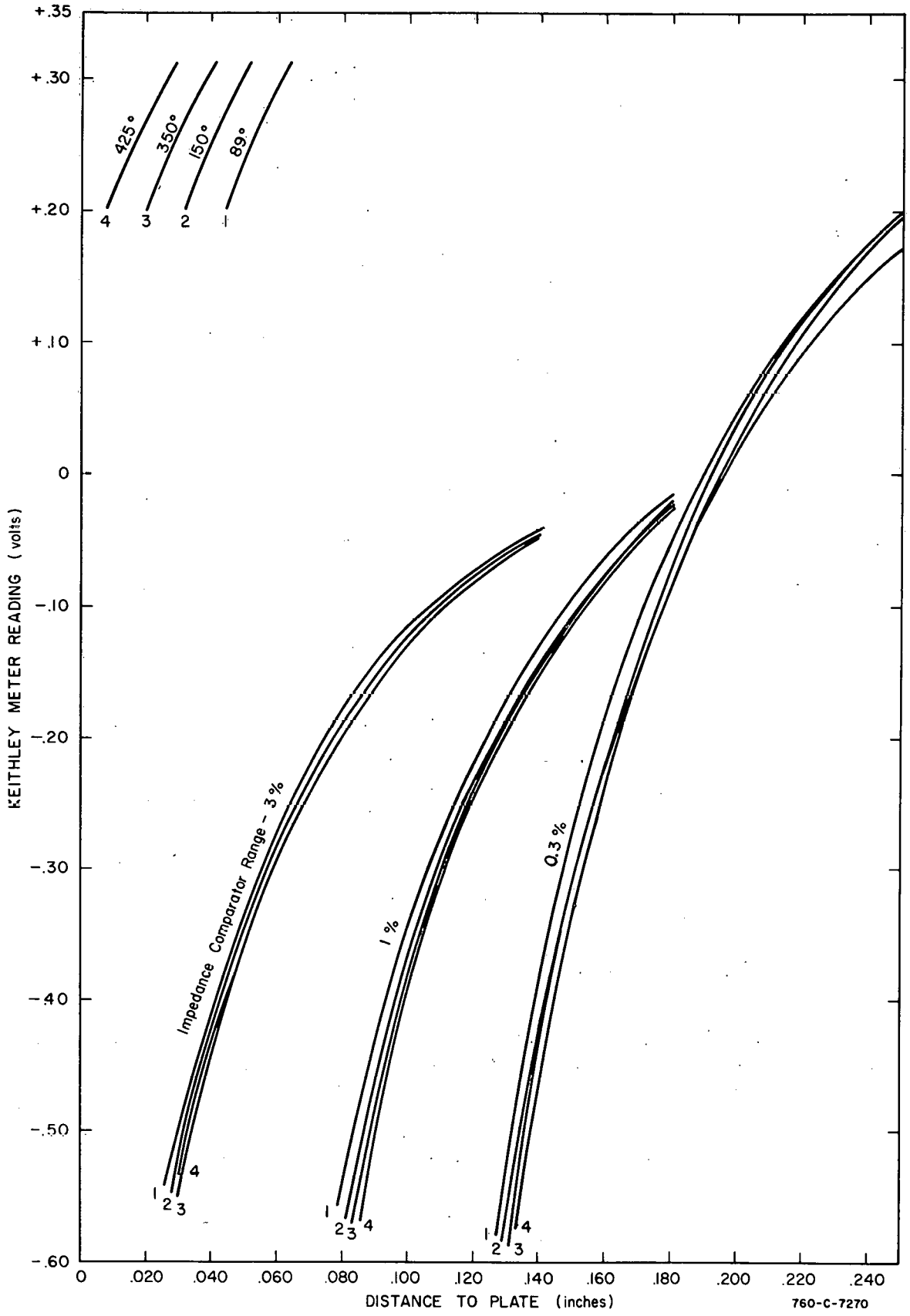

Fig. III-3 Proximity transducer calibration for typical operating temperatures.

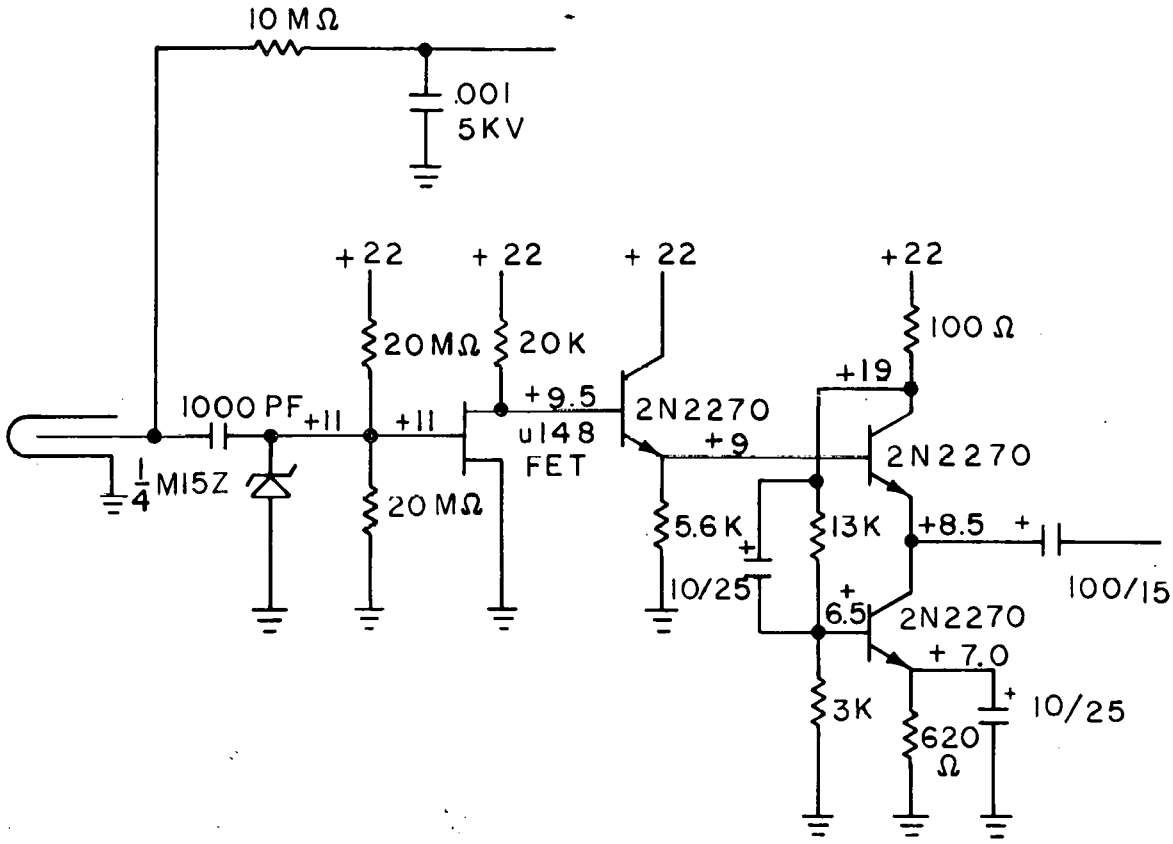

Fig. III-4 Field effect transistor preamplifier.

Another problem which had to be solved was to eliminate high frequency noise pulses which entered the equipment through the power lines. This was corrected by running in a new power source from a motor generator set.

1.3 Electrochemical Fast Data Logger (K. D. Smith)

A fast data logger has been developed for the Analytical Development Section of the Chemical Technology Branch. A block diagram of the system, wherein the fast data logger is used, is shown in Figure III-5.

The system is composed of the fast data logger, an external clock an external waveform generator, an external chemical cell, and an external current-to-voltage converter.

The purpose of the system is to interrogate the chemical cell with a potential derived from the wave form generator and to record the resulting output of the cell. When the cell is interrogated, a fast chemical reaction results requiring the use of a fast data logger.

The cell itself is a liquid uranium solution contained in a glass flask. It is interrogated by use of a potential developed across an electrode located within the cell. The cell output is a voltage derived from a third electrode. The output voltage is fed to a Bipolar Analog-to-Digital Converter (ADC) for processing by the fast data logger.

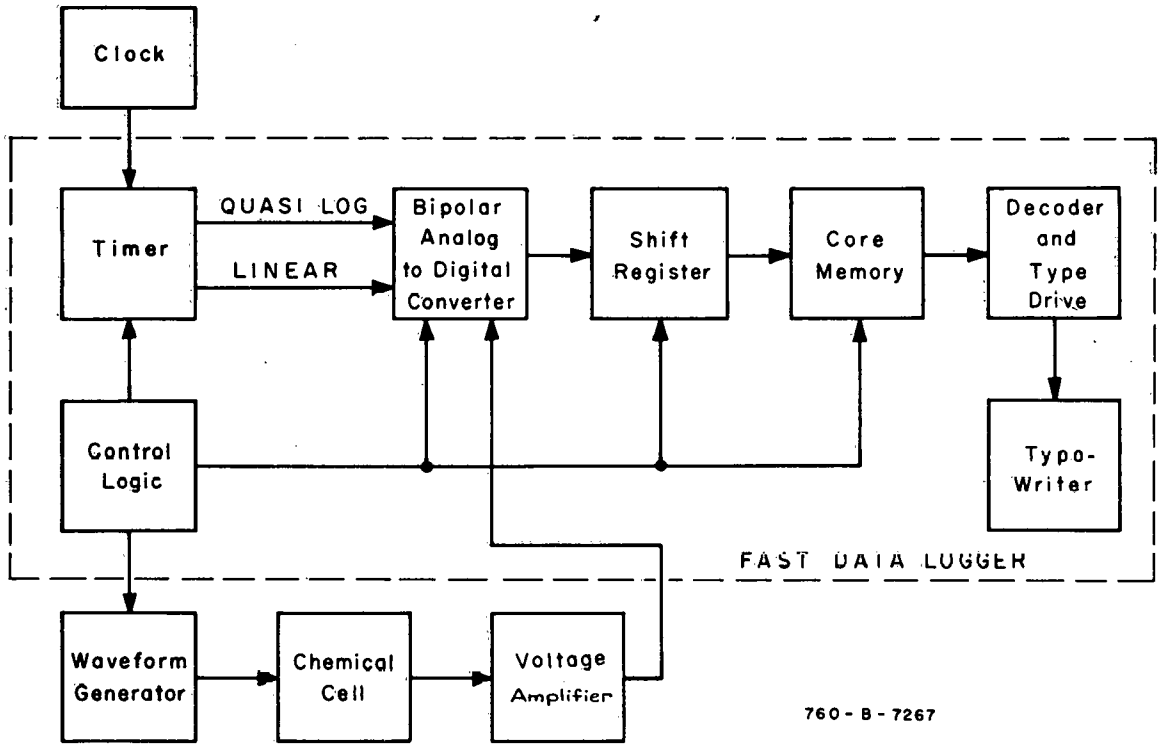

Fig. III-5 Block diagram of electrochemical fast data logger.

Operation is begun by generation of a command from the control logic which drives the external waveform generator. This generator provides the interrogation for the cell. The current output of the cell is then converted to a voltage and fed to the ADC. Conversion by the ADC is controlled by a timer operating in either a quasi-log mode or a linear mode. Certain interrogations of the chemical cell produce linear output signals while other interrogations produce exponential output signals. This required both log and linear clock control of the ADC. Log operation of a digital device is extremely difficult and costly to obtain; hence, a quasi-log clock is used in the operation. The quasi-log clock is a pulse train of X pulses separated by a time period of T, followed by X pulses separated by a time period of 2T, X pulses of period 4T, etc. The pulse period doubles for each X number of pulses generated. The number X is adjustable, by the operator, from 6 to 9. A total of 51 pulses is generated, corresponding to the word capacity of the core memory of the system. The period T of the pulses is adjustable by means of the external clock.

The output of the ADC is a four decimal digit word plus sign in a 1-2-4-8 code. However, the core memory which stores the ADC output, can load only 1 decimal digit per memory cycle. Thus, a shift register is required to interface the ADC with the core memory. This shift register shifts the ADC information a decimal digit at a time to the input of the memory for storage. The control logic initiates loading of the memory. The memory has a capacity of 51 words with a word being defined as four decimal digits plus sign. After 51 words have been loaded into the core memory, the load cycle is complete.

The sampled data from the chemical cell are read out by means of a typewriter. This unload cycle is initiated by a command from the control logic which reads a decimal digit from the memory. The decimal digit is then decoded into

a 12-inch line output and fed to a type drive which types out the character. The 12-line output provides decimal character outputs, "0" through "9", and sign outputs,"+" and "-". The unload cycle is completed when 51 five character words have been typed out on the typewriter.

1.4 Eddy Current Vibration Sensor (P. H. Hofhine, J. B. Colson)

A device was built which would use the eddy-current displacement transducers as described on page 77 of this report [2] to provide a measurement of the fuel plate vibration in the ATR fuel plate assemblies. This device uses the varying inductance of the transducer to control the frequency of a transistor oscillator. The output of the oscillator is amplified and amplitude limited and then passed into an FM detector. The detector uses the skirt of a tuned circuit to produce amplitude variations that are a function of frequency. This amplitude signal is then rectified and filtered to provide an output signal which is a function of the fuel plate vibration.

The schematic is shown in Figure III-6. The oscillator is basically a 125kc Colpitts oscillator with the sense coil of the transducer forming the major portion of the tank inductance. Thus, changes of the transducer sense coil inductance caused by changes in the fuel plate transducer spacing will change the frequency of this oscillator. The oscillator output is amplified by the following stage. The series-parallel combination of diodes serves to maintain a constant output amplitude. This signal is adjusted by the drive level potentiometer to achieve the desired input into the following stage.

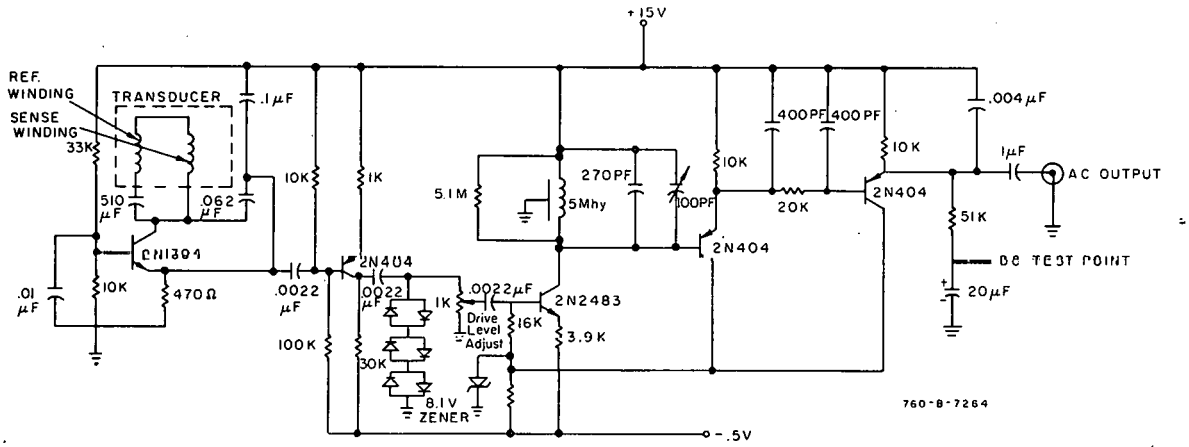

Fig. III-6 Schematic diagram of the eddy-current vibration sensor.

The heart of the detection system is the FM detector. By a trial and error process, a resonant frequency and Q were found for the tank circuit in this stage which gave the most linear output over the range of 0.02 to 0.12 inch for the transducer to fuel plate spacing. The next stage is an emitter follower used as a load isolator and half-wave rectifier. The filtered output of this detector is applied to another emitter follower. The output of this stage is dc coupled to a test point and ac coupled to the output terminal. It was found that the proper adjustment of the drive level into the FM detector and the detector center frequency would allow all the transducers, independent of their individual variations, to follow the same curve of dc test voltage versus distance. This test voltage curve is shown in Figure III-7. The proper adjustment of detector drive level and center frequency is achieved by matching the dc test voltage to this curve at two

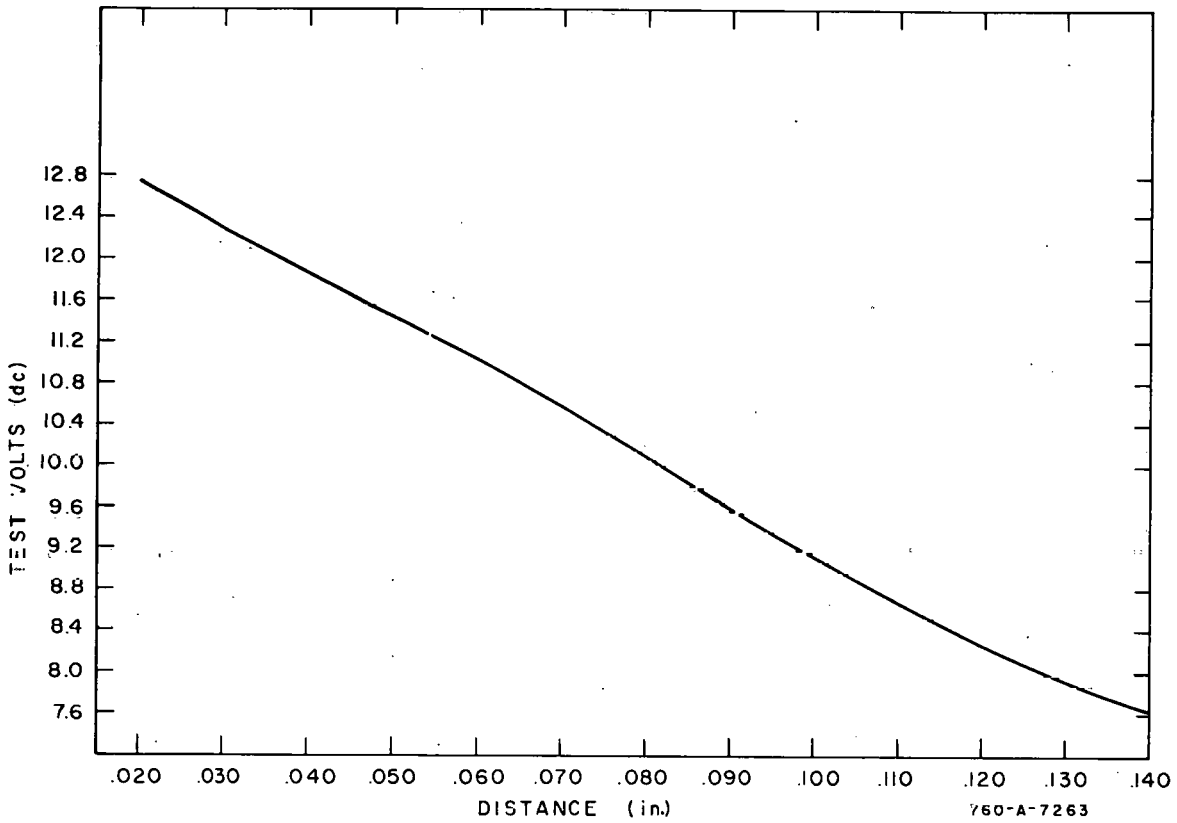

Fig. III-7 Plot of the dc voltage at the test point versus the fuel plate to transducer distance.

spacings, usually 0.040 and 0.100 inch. Shown in Figure III-8 is the slope of the curve of Figure III-7 versus distance. This is the ac transfer gain of the detector in volts per inch.

The curve of Figure III-9 shows the variation in the drive level to the FM detector as the spacing between the transducer and the fuel plate changes. When a transducer is mounted for use, the transducer-to-fuel-plate spacing is obtained and the drive signal level into the detector is set to the value given by the curve of Figure III-9 for that spacing. The FM detector center frequency is then adjusted to give the appropriate dc test voltage as shown by the curve of Figure III-7. Now the system will have the ac transfer as shown in Figure III-8.

1.5 Automatic Ultrasonic Flaw Detector Modifications for ATR Fuel Plates [3]

(B. G. Nelson, E. E. Owen)

In order to detect flaws in the ATR fuel plates, modification and/or construction of the following units for the ultrasonic flaw detector was required:

(1) Immersion tank including the fuel plate holder

(2) Longitudinal and traverse scanning methods

(3) Electronic timer for traverse motor control.

A new immersion tank with inside dimensions 1 by 1-1/2 by 6 feet was constructed. The fuel plate holder designed to accept the curved fuel plates is installed in the tank.

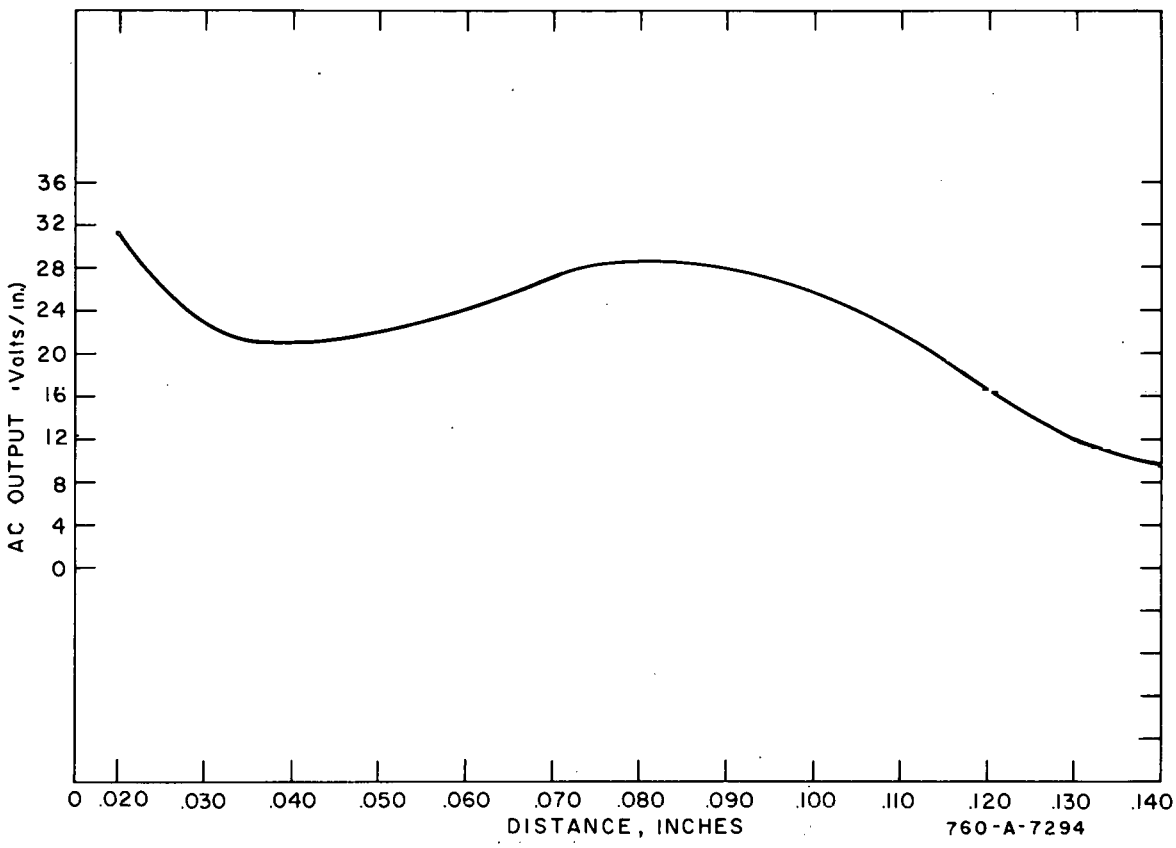

Fig. III-8 Alternating current output calibration curve versus fuel plate to transducer distance.

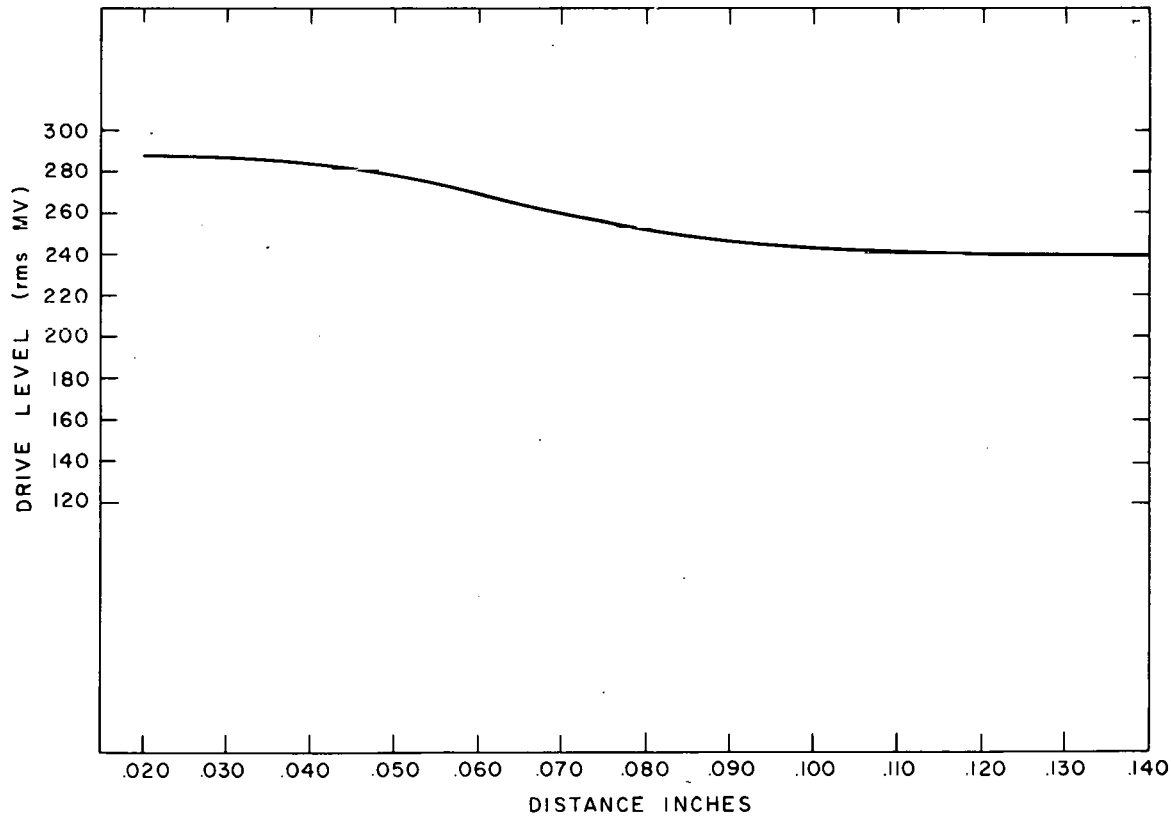

Fig. III-9 Drive signal amplitude versus fuel plate to transducer distance.

Longitudinal scanning is accomplished by moving the transducers along the fuel plate. Traverse scanning is done by rotating the fuel plate relative to the transducers. The distance through which the fuel plate is rotated is determined by the time selector switches on the electronic timer. The traverse motor is operated from the 110 V, 60-cycle line. This is a Slo Syn motor, and the shaft turns at 0.665 rpm. An additional 20:1 reduction is obtained in the coupling to the fuel plate holder. Selection of the time for which the motor is allowed to run determines the distance the fuel plate is rotated. Increments of 0.031 to 0.5 inch can be selected. The minimum increment is determined by the period of the timing oscillator.

A photograph showing the mechanical construction is shown elsewhere in this quarterly report, (Figure I-25) and is associated with the article "MTR Type Fuel Elements Containing Fuel Bearing Fiberglas", by E. C. Norman, G. W. Gibson, J. C. Read, and B. G. Carlson.

The block diagram of the electronic traverse motor control is shown in Figure III-10. The operation of the traverse motor control is as follows:

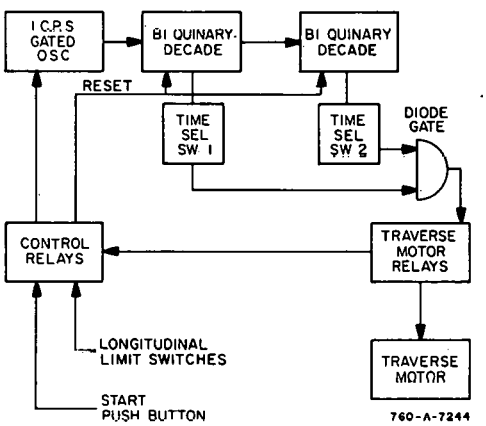

Fig. III-10 Block diagram of electronic timer for traverse motor control.

Switches, SW1 and SW2, are set to the desired time interval as determined by the distance the fuel plate is to be rotated. With the motor drive switch in the "auto" position, the reset push button is actuated. This resets the biquinary decades [4] to zero. The traverse motor and timing oscillator is started by actuating the start push button. The motor is allowed to run until an output is produced at the diode gate. The motor and timing oscillator are then stopped and the longitudinal motor started. The longitudinal scan continues until a limit switch is operated. The biquinary decades are then reset and the traverse motor and timing oscillator started. This cycle repeats until the auto-manual switch is turned to the manual position.

This traverse motor control unit has been integrated into the original automatic ultrasonic flaw detector with improved system capability.

1.6 Modified Operational Amplifier for Potentiostat (K. F. Smith)

A solid state input and output stage for a transistor operational amplifier was recently developed. The two stages are used in an electroanalytical potentiostat at the Idaho Chemical Processing Plant. The input stage consists of a field-effect transistor and three conventional transistors as shown in Figure III-11.

The input leakage current of the amplifier is less than 100 $\mu\mu$A at 25°C, and the output impedance is less than 10 ohms. The rise and fall times are approximately 0.6 and 0.1 μsec, respectively. The short and long term dc drift at the output is less than 1 MV/hr and 1 MV/24 hours, respectively, at a constant temperature of 25 °C.

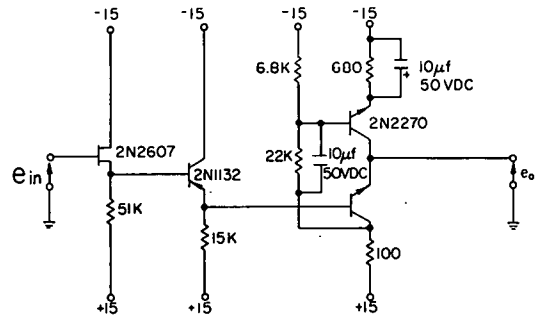

Fig. III-11 Field effect transistor input stage.

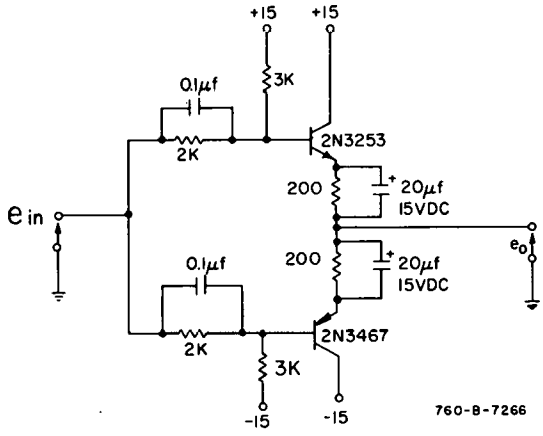

Fig. III-12 Emitter follower output stage.

The output stage is a booster amplifier which consists of a complimentary pair of emitter followers connected to operate Class A. This stage is shown in Figure III-12. The unit is capable of driving ± 1 A into a 10-ohm load with a rise and fall time of less than 20 μsec. The voltage and current gain at an output current of 1 A is approximately 0.7 and 20, respectively.

1.7 Constant Air Monitor Modification (J. B. Thompson)

The following modifications were made on the constant air monitors in order to increase the high voltage and make it variable over the range of 950 to 1200 V-dc; also included are the changes which were required in order to use the front panel meter to set the high voltage. This was done so the detector tubes could be operated in a more stable region.

1.71 Model AM-2. This model required no modifications to the high voltage circuit as it is already adjustable over this range. It was only necessary to add a 620-ohm resistor across the meter to change its range from 1000 to 2000 V full scale. (See Figure III-13.) The meter dial was relabeled to correspond to this new range.

1.72 Model CRM-10M. To increase the high voltage from 950 to 1200 volts and make it adjustable over this range required changing the voltage doubler circuit to a voltage quadrupler circuit. An adjustable resistor divider was added by which the high voltage can be adjusted over this range. The addition of a SPDT push button switch makes it possible to monitor the high voltage on the front panel meter.

These changes are all shown inside the dotted lines in Figure III-14.

1.73 Model CRM-10M-A. The circuit changes required for this instrument are the same as for the Model CRM-10M. (See Figure III-14.) There is, however, one exception and that is that on the selector switch there was an unused section. This was used instead of the push button switch that was installed in the Model CRM-10M. When this switch is set to the formerly unused position, the high voltage can be monitored on the front panel meter.

These modifications increase the performance of these instruments and makes it easier to set them up for operations.

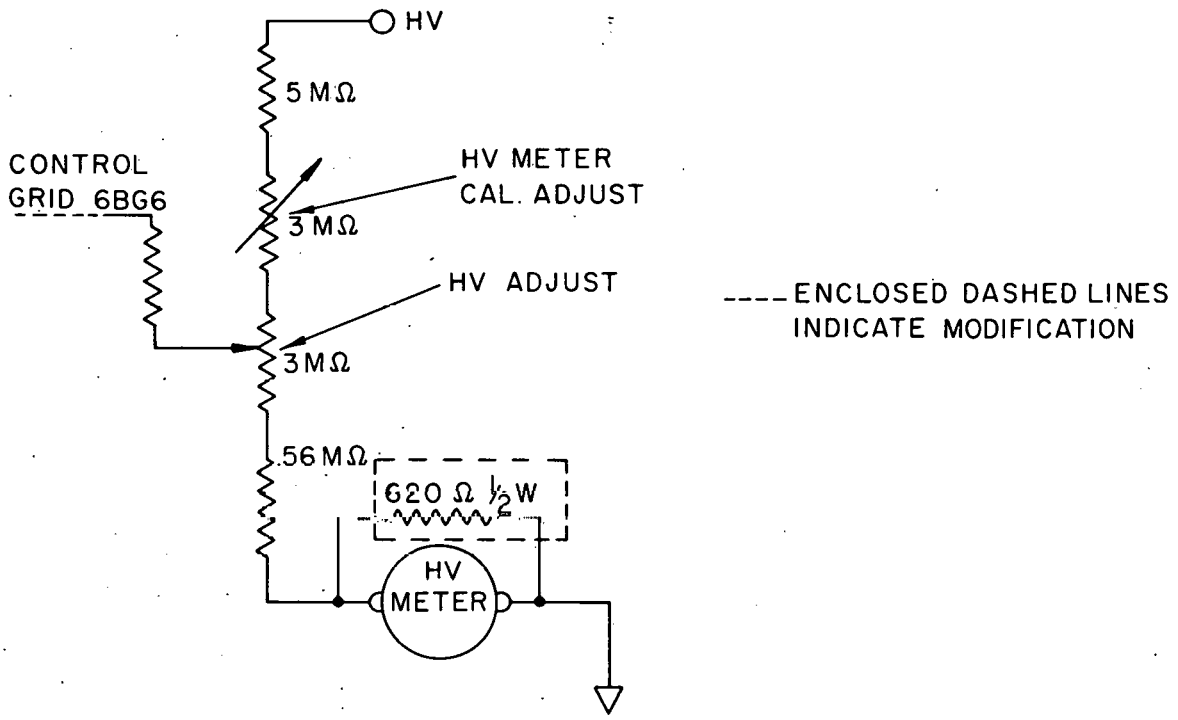

Fig. III-13 Modification made in the high voltage circuit of Model AM-2 constant air monitor.

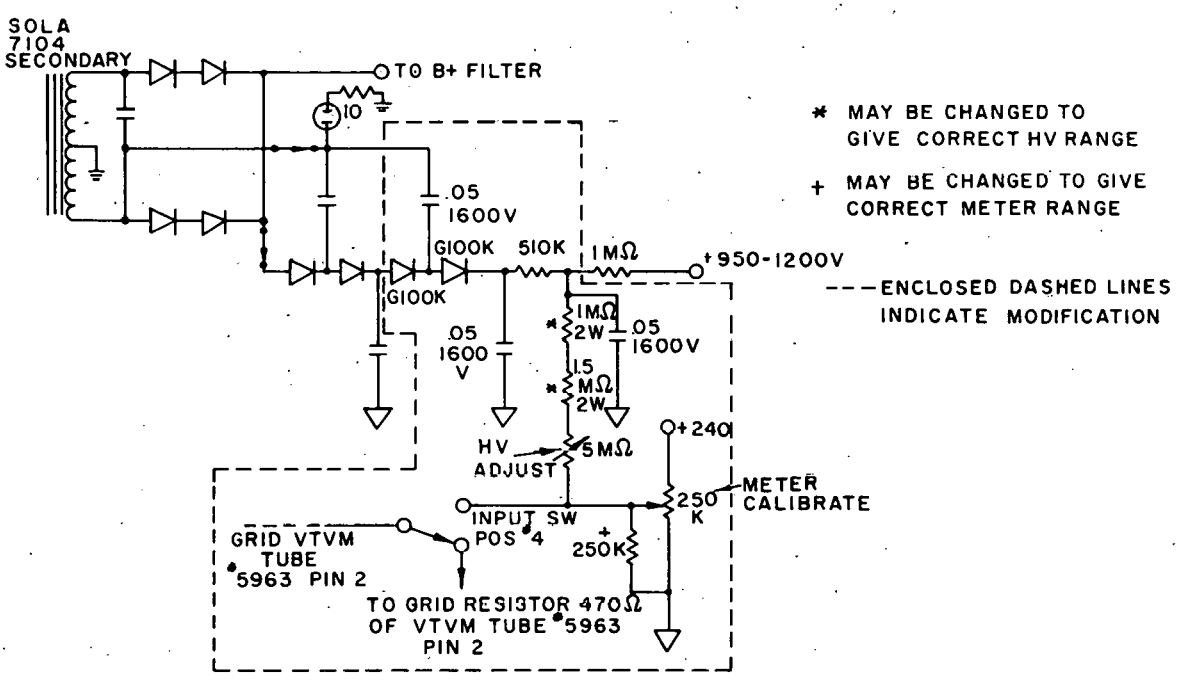

Fig. III-14 Modifications made in the high voltage circuit of Models CRM-10M and CRM-10M-A constant air monitors.

2. INSTRUMENTATION ANALYSIS
(Ned Wilde)

2.1 Simulation of PBF Transients (S. R. Gossmann)

The transient behavior of the Power Burst Facility (PBF) was studied on the analog computer in order to estimate the rod motion required for shaping the power burst under various operating conditions. Adiabatic and nonadiabatic thermal models of the reactor core were investigated. Reactor shutdown transients by means of the scram rods were also investigated. The following discussion explains the assumptions and approximations made in the mathematical formulation of the problem.

2.11 The 1-msec Transient. The first phase of the simulation examined the transient behavior of the reactor assuming that 95 percent of the total reactor power was generated in the UO_2 and heat removal from the fuel (UO_2) to the ZrO_2 by conduction was neglected. The thermal effects of the cladding and water were also neglected. Under these assumptions, 1- and 3-msec transients were obtained. The 1-msec transient was compared to the solution obtained from the IREKIN digital code as a check on the analog computer simulation. Figure III-15 shows the total power, energy release in the fuel, the core-averaged fuel temperature, and the Doppler reactivity for the last three decades of the 1-msec burst. The results from both studies at the time of peak power are listed below:

	IREKIN	Analog
Total Power, P (MW)	3.67×10^5	3.508×10^5
Energy release in fuel, E_f (MW-sec)	8.00×10^2	7.80×10^2
Fuel temperature, T_f (°C)	6.89×10^2	7.13×10^2

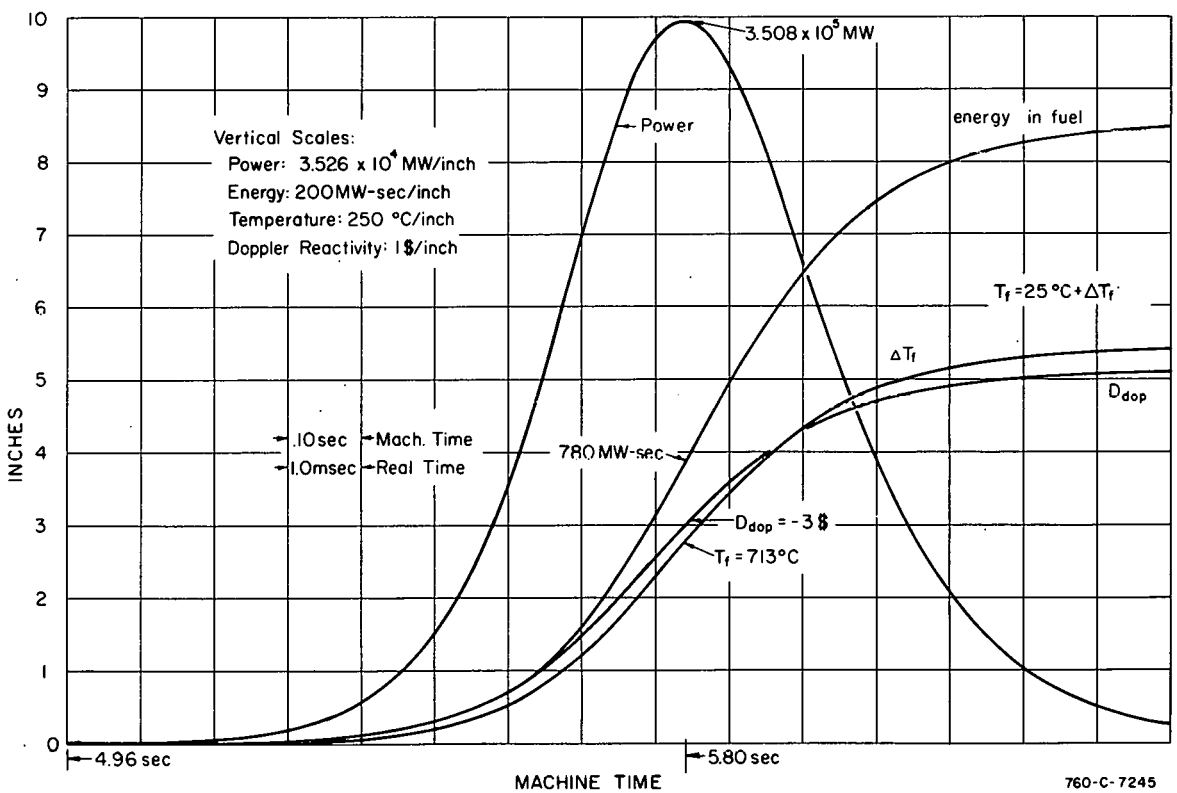

Fig. III-15 The 1-msec transient.

The Doppler reactivity was calculated according to the formula

$$D_{dop} = B - B\sqrt{1 + d\Delta T_f} \tag{1}$$

where

D_{dop} = Doppler reactivity in dollars

B = constant = 3.768 dollars

d = constant = 3.35×10^{-3}/°C

ΔT_f = change in fuel temperature in °C.

The kinetics equations solved on the analog computer were

$$\frac{\Lambda}{\beta}\frac{d\underline{P}}{dt} = D\underline{P} - \underline{P} + \sum_{i=1}^{6}\lambda_i\psi_i \tag{2}$$

$$\frac{d\psi_i}{dt} = -\lambda_i\psi_i + \frac{\beta_i}{\beta}\underline{P} \tag{3}$$

$$D = D_x + D_{dop} \tag{4}$$

where

$\underline{P}$ = total power in MW

β = total delayed neutron fraction

Λ = neutron generation time in seconds

β/Λ = 3.50×10^{2}/sec

D = net reactivity in dollars

D_x = reactivity required to initiate transient = 4$

ψ_i = delayed neutron variable

λ_i = i^{th} group decay constant in sec^{-1}

β_i/β = i^{th} group relative delayed fraction

i	λ_i	β_i/β
1	1.27×10^{-2}	3.31×10^{-2}
2	3.17×10^{-2}	1.956×10^{-1}
3	1.16×10^{-1}	1.688×10^{-1}
4	3.13×10^{-1}	4.248×10^{-1}
5	1.40	1.526×10^{-1}
6	3.88	2.51×10^{-2}

The energy released in the fuel was calculated according to the equation

$$\frac{dE_f}{dt} = \gamma_f \underline{P} \tag{5}$$

where

E_f = energy released in fuel in MW-sec

γ_f = fraction of total energy released in fuel = 0.95.

The fuel temperature was calculated from the equation

$$C_f \frac{dT_f}{dt} = \gamma_f K \underline{P} \tag{6}$$

where

C_f = heat capacity of fuel in cal/°C

K = conversion factor = 2.389×10^5 cal/MW-sec.

The heat capacity of the fuel was calculated on the basis of the following curve fit for the volumetric heat capacity of the fuel $(\rho C)_f$ supplied by PBF engineering personnel and a fuel volume of 3.951×10^5 cm^3.

$$(\rho C)_f \ (cal/°C/cm^3) = 8.126 \times 10^{-8} \ T_f^2 + 9.560 \times 10^{-6} \ T_f + 0.6573 \tag{7}$$

Attempts were made to simulate the power variation from 1 MW to the peak value of 3.508×10^5 MW on a continuous basis by a logarithmic transformation of the kinetics equations [Equations (2) and (3)]. While the transformed kinetics equations could be solved quite accurately over the extreme range in power, the linear power ($\underline{P}$) required in Equations (5) and (6) could not be computed accurately over the entire range. It was then decided to simulate the upper three decades of the power excursion only, assuming that up to the time that the power reached three decades below peak power, the energy, E_f, fuel temperature, T_f, Doppler reactivity, D_{dop}, and delayed neutron concentrations, ψ_i, had not changed significantly from the initial values at 1 MW of power. Calculations were performed that verified the validity of this assumption for the 1-, 3-, and 25-msec bursts.

In order to establish at what time following the initiation of the transient the power attained the value of 3 decades below peak power, a set of zero-power kinetics equations, logarithmically transformed, were set up on the analog computer. By comparing solutions of Equations (2) through (6) over the last 3 decades, with and without Doppler feedback, to the solution of the zero-power log-transformed equations, it was possible to determine the starting time for Equations (1) through (6).

Bandwidth limitations of the computing and recording equipment required a time scale change to be imposed on Equations (1) through (6). The time scale was expanded by a factor of 100. Figure III-15 shows the last three decades of the 1-msec transient. Note that the time scale starts at 4.96 sec machine or computer time (0.0496 sec real time).

2.12 The 3-msec Transient. The assumptions and approximations made in the simulation of the 3-msec transient were the same as those for the 1-msec transient. The total reactivity used to initiate the 3-msec transient was $D_x = 2.0\$$. The resulting period for this study was actually 2.87 msec rather than the desired 3 msec. Nevertheless, the following set of transients are identified as 3-msec transients. The peak power for this case was 3.55×10^4 MW and the energy release up to the time of peak power was 2.00×10^2 MW-sec.

2.13 Evaluation of Scram Rods. In evaluating the performance of the scram rods, it was assumed that the reactor power could be held constant at the peak value by suitable manipulation of the transient rods until 2000 MW-sec of energy had been released in the fuel. The reactor was then scrammed by insertion of the scram rods. It was assumed that the rods would move with constant acceleration. The equation of motion for the rods was

$$\frac{d^2\overline{X}}{dt^2} = a/\overline{X}_{max} \tag{8}$$

where

$\overline{X}$ = rod position normalized to 3 foot length

$\overline{X}_{max}$ = active length of rod = 3 ft

a = acceleration in ft/sec^2

The worth of the rod was related to rod position according to the equation

$$D_{sc} = D_{sc_{max}} \left[\overline{X} - \frac{1}{2\pi} \sin 2\pi \overline{X} \right] \; ; \; 0 \leq \overline{X} \leq 1 \tag{9}$$

where

D_{sc} = reactivity of scram rods in dollars

$D_{sc_{max}}$ = total worth of scram rods = 7.81\$

The following table related specified insertion times to acceleration.

T (msec)	a (ft/sec^2)
200	150.0
150	266.6
100	600.0

Case 1 of Figure III-16 shows the resulting power and energy when the scram rods are inserted from full-out in 200 msec.

Case 2 of Figure III-16 shows the resulting power and energy if the Doppler effect alone is allowed to shut down the reactor after 2000 MW-sec of energy are released in the fuel.

Figure III-17 shows the resulting power and energy for three different insertion times. The rods start from full-out or from the 36-inch position.

In Figure III-18, the scram starts with the scram rods at the 30-inch position.

In Figure III-19, the scram starts with the scram rods at the 24-inch position.

Comparison of the curves in Figures III-16 through -19 will aid in establishing the best insertion time and initial position of the scram rods for PBF.

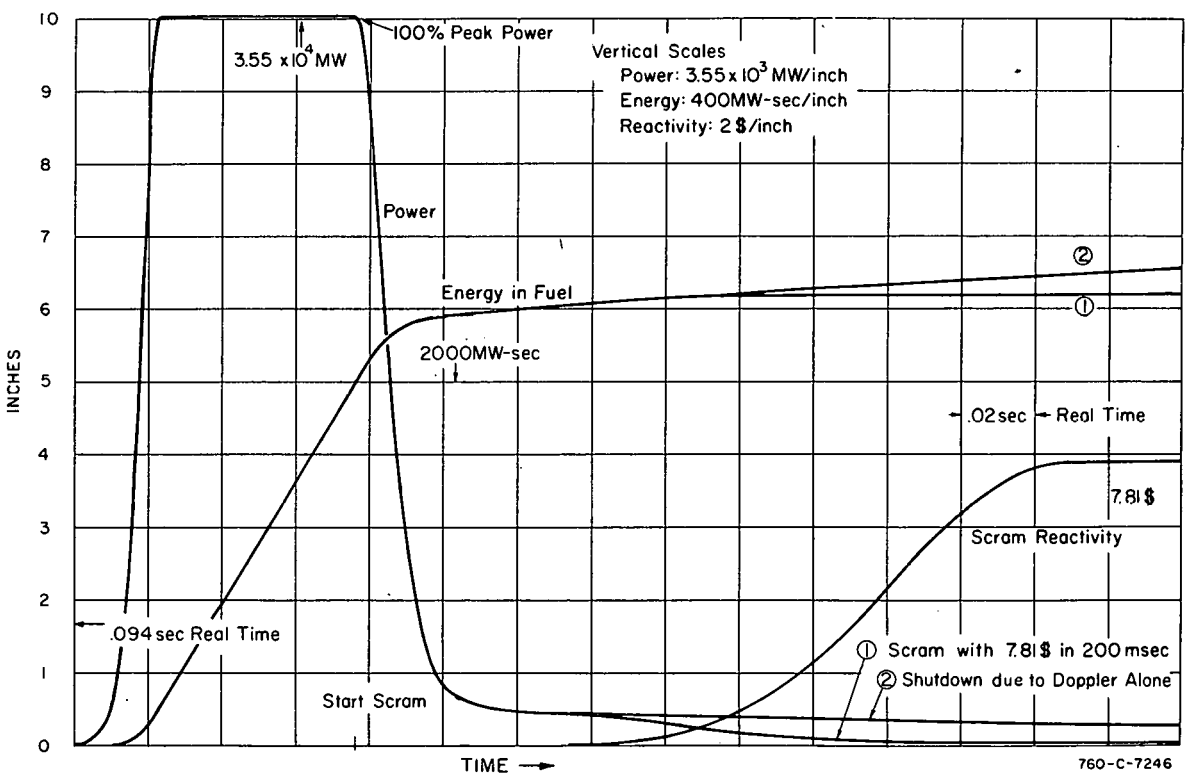

Fig. III-16 The 3-msec transient -- evaluation of scram rods.

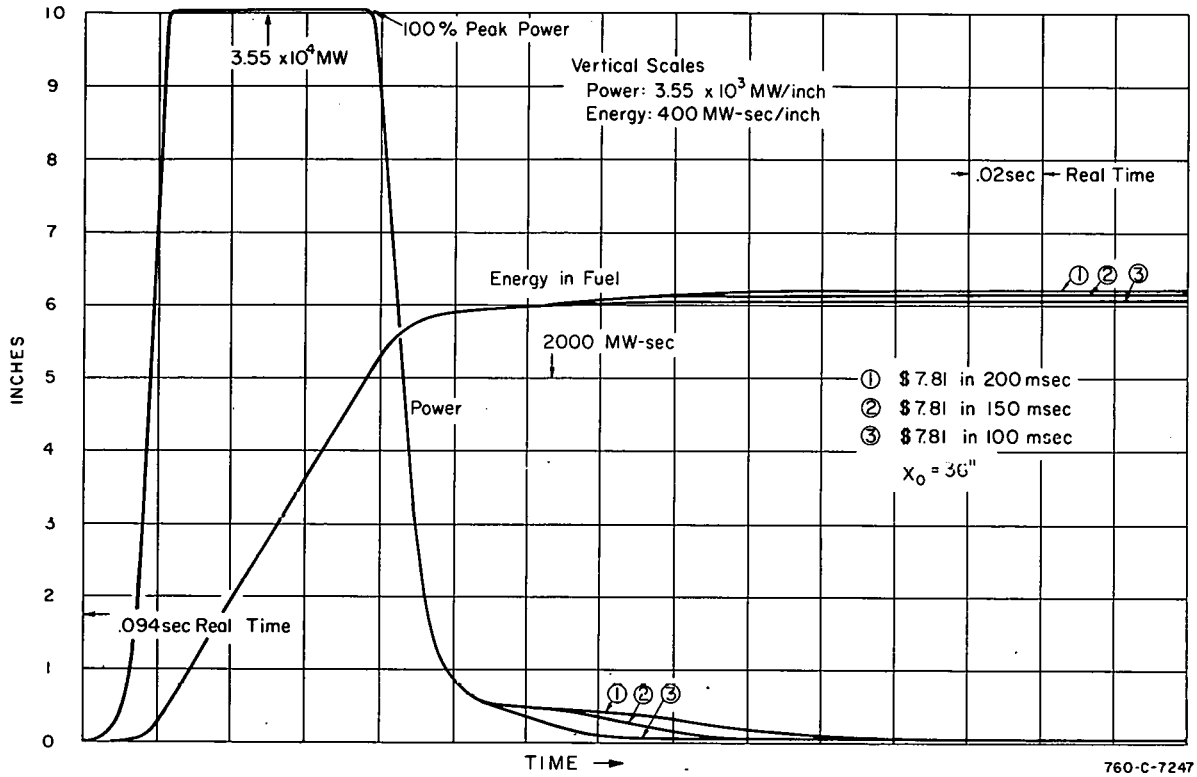

Fig. III-17 The 3-msec transient -- evaluation of scram rods.

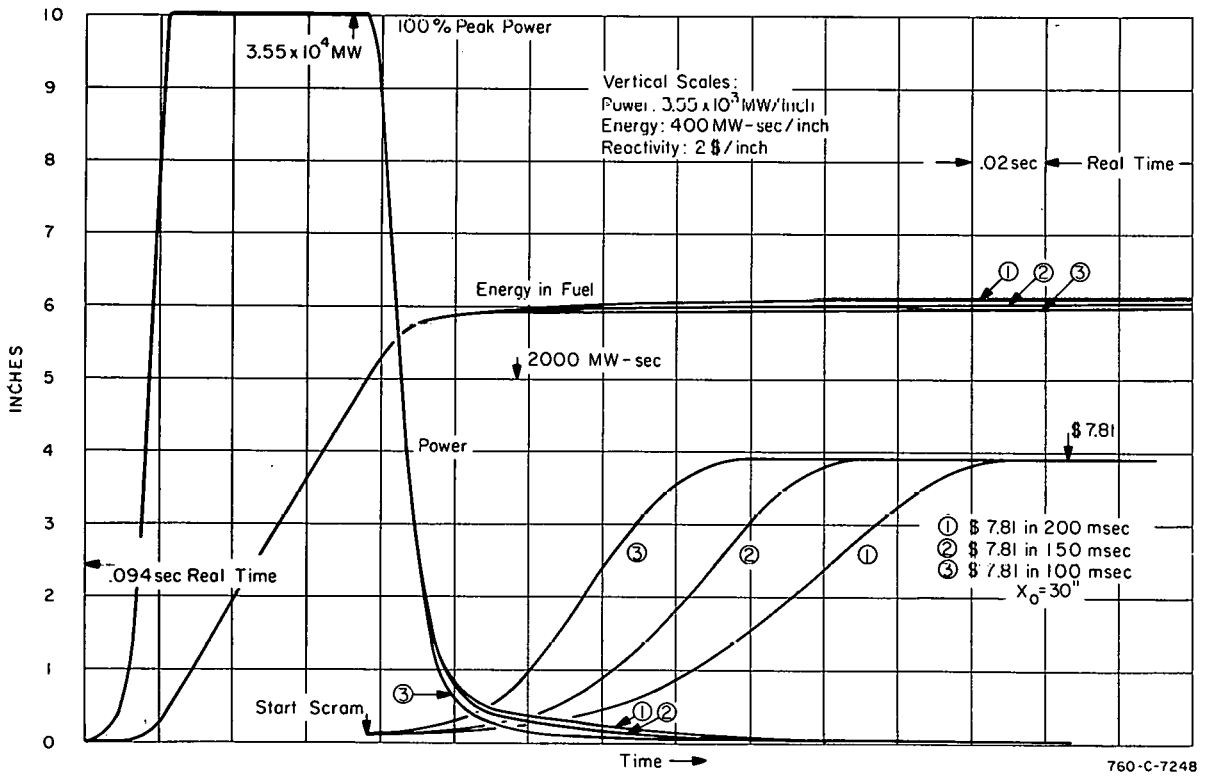

Fig. III-18 The 3-msec transient -- evaluation of scram rods.

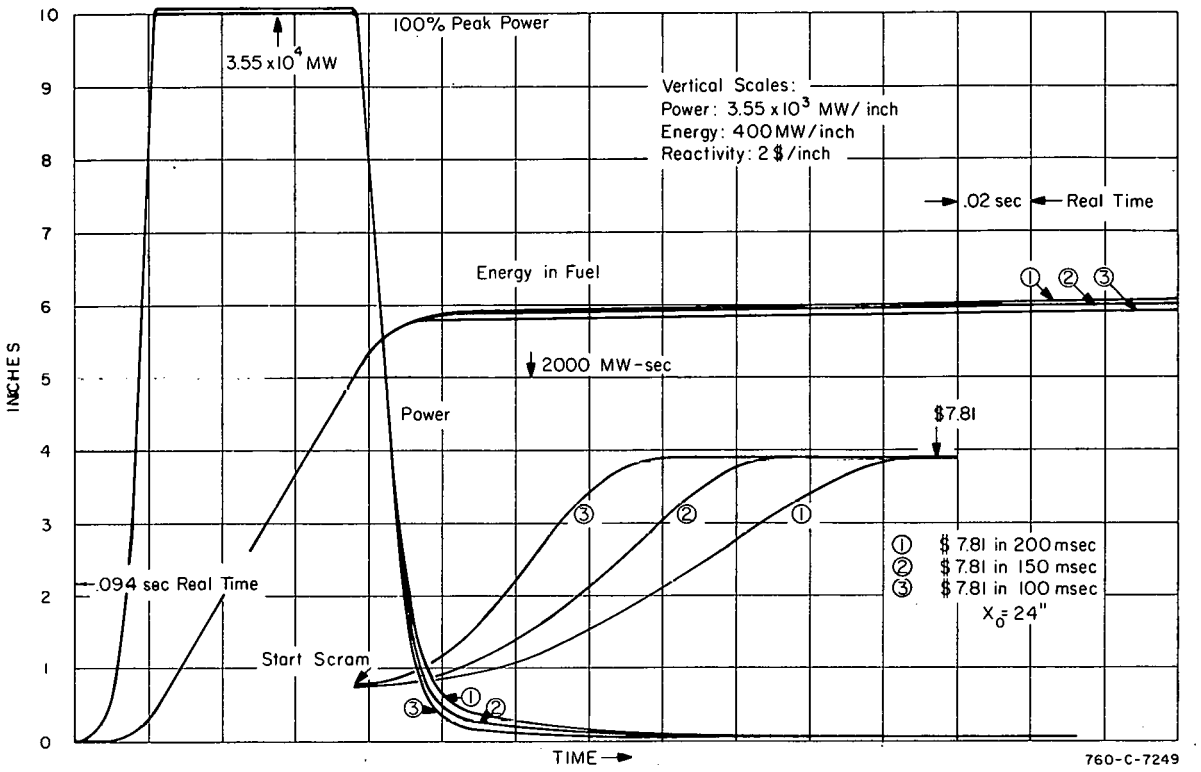

Fig. III-19 The 3-msec transient -- evaluation of scram rods.

2.14 Transient Rod Motion Required for Power Shaping. Shaping of the power burst for the 3-msec transient was studied to determine the nature of transient rod motion required to hold the power exactly at peak value long enough to release 2000 MW-sec of energy in the fuel. The rod motion shown in Figure III-20 was obtained assuming that the transient rods (worth 5$) would start moving at the instant peak power occurred. The high initial velocity (217.5 ft/sec) is required because of the low initial slope of the S-shaped rod worth curve [Equation (9)]. The high final value of velocity is required because of the low value of the rod worth curve slope at the other end of the rod. The interesting feature of the velocity curve in Figure III-20 is that the velocity never assumes a constant value. This means that transient rods fired out of the core at constant velocity at time of peak power will not be able to hold the reactor power constant. This conclusion is illustrated by Figures III-21A through -21D.

Attempts were made to hold the power constant by firing two transient rods at different times relative to the power peak. Both rods had different worths and different volocities, and both rods started from the fully inserted position. Figure III-22 shows four power transients selected from a large number of such transients to illustrate the effects of the transient rod motion. Curve 1 of Figure III-22 shows the best shaped power curve. Firing rod No. 1 before the peak causes the power to overshoot the peak attained by 10 percent with no attempts at shaping. The region of constant power is only 54 percent of the peak power attained with no shaping. As a consequence, the energy release up to the time both transient rods are out of the core is only about 1500 MW-sec. The rod worths, velocities, and firing times required to produce this transient or to improve it may not be physically realizable.

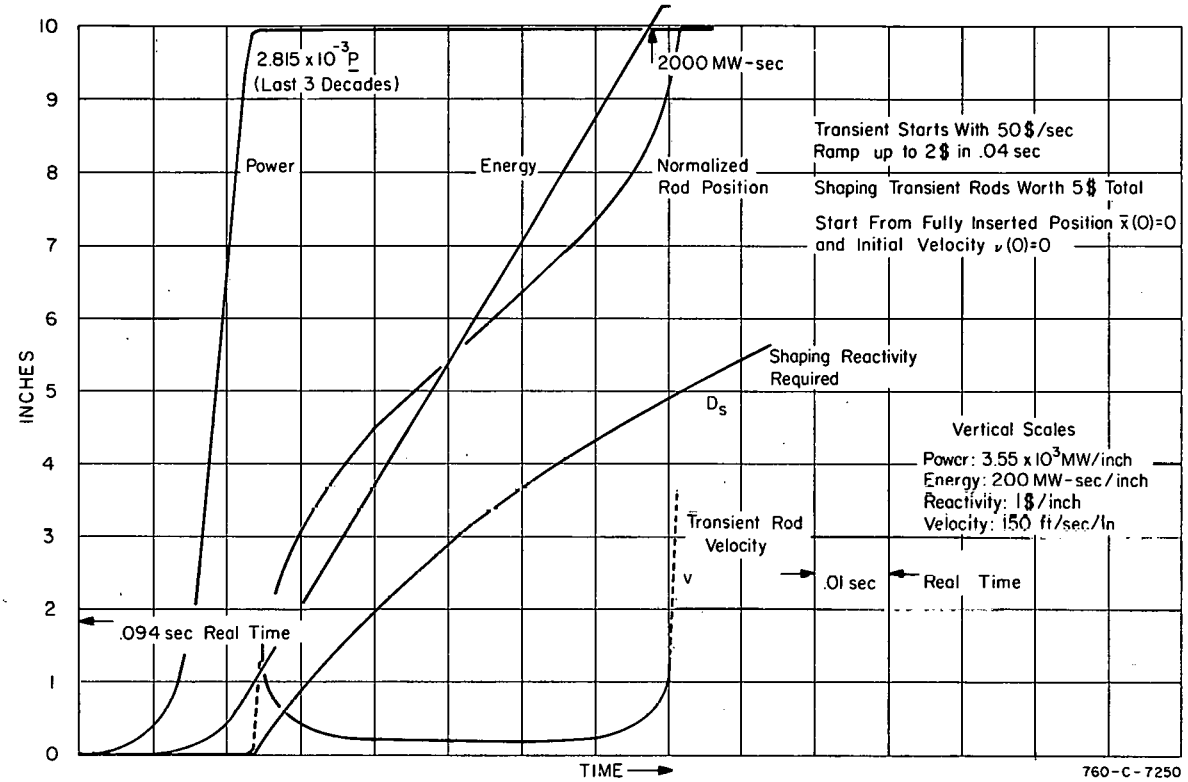

Fig. III-20 The 3-msec transient -- rod motion required for holding peak power.

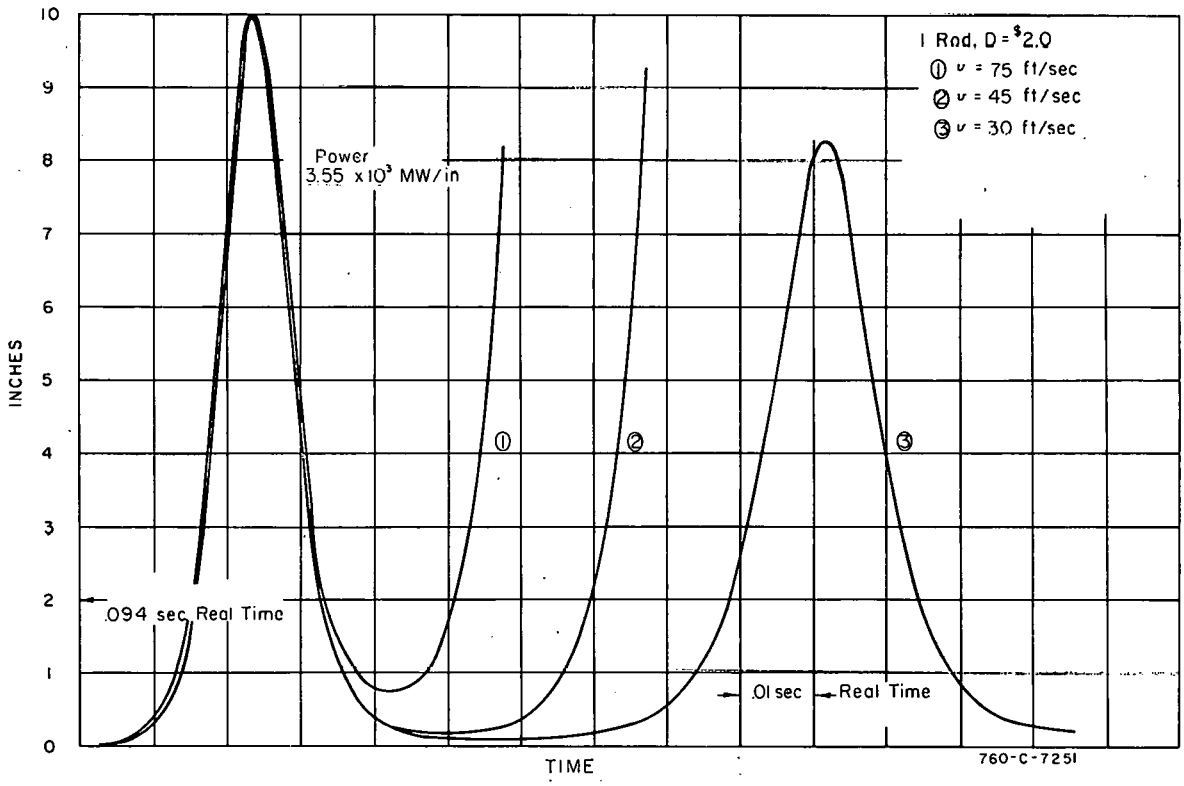

Fig. III-21A The 3-msec transient -- power shaping with constant rod velocity.

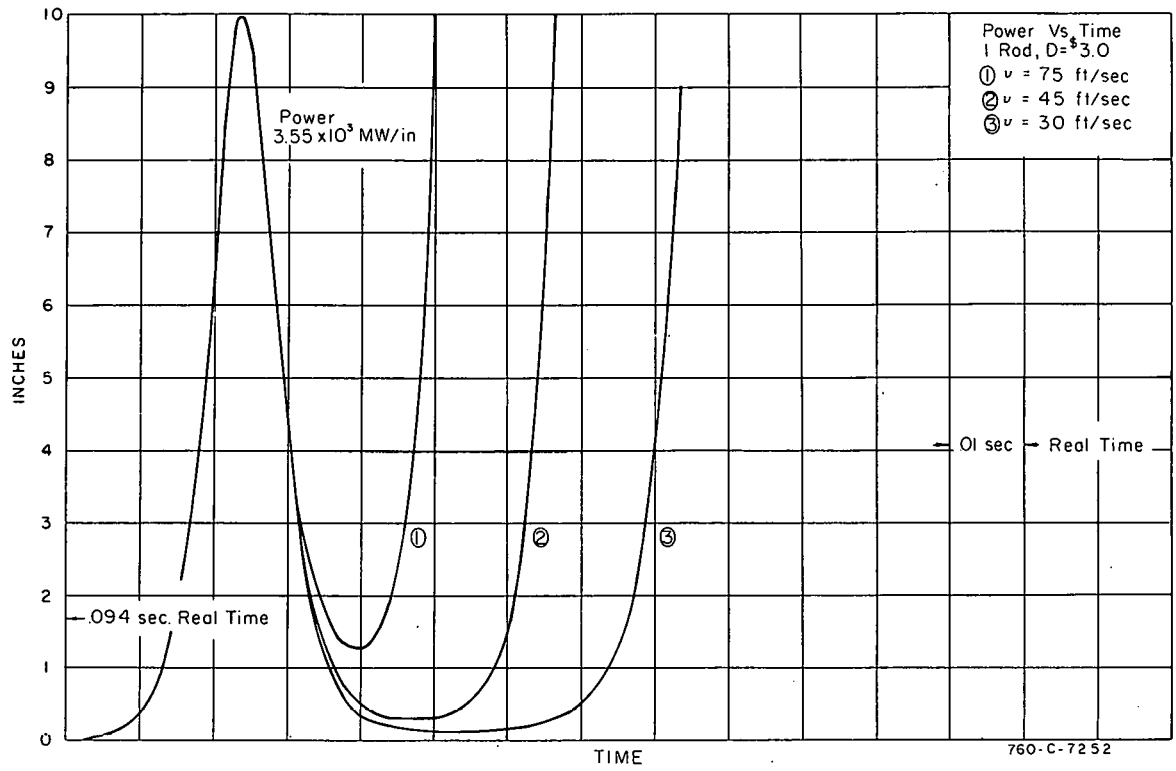

Fig. III-21B The 3-msec transient -- power shaping with constant rod velocity.

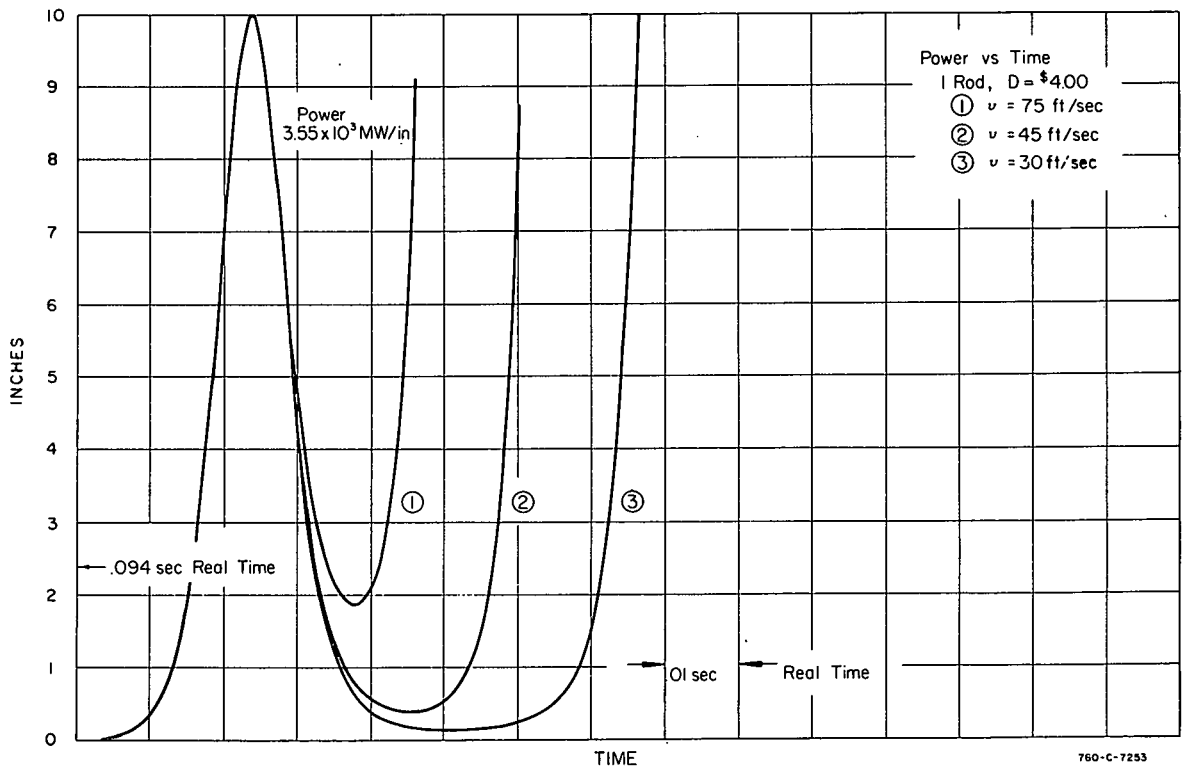

Fig. III-21C The 3-msec transient -- power shaping with constant rod velocity.

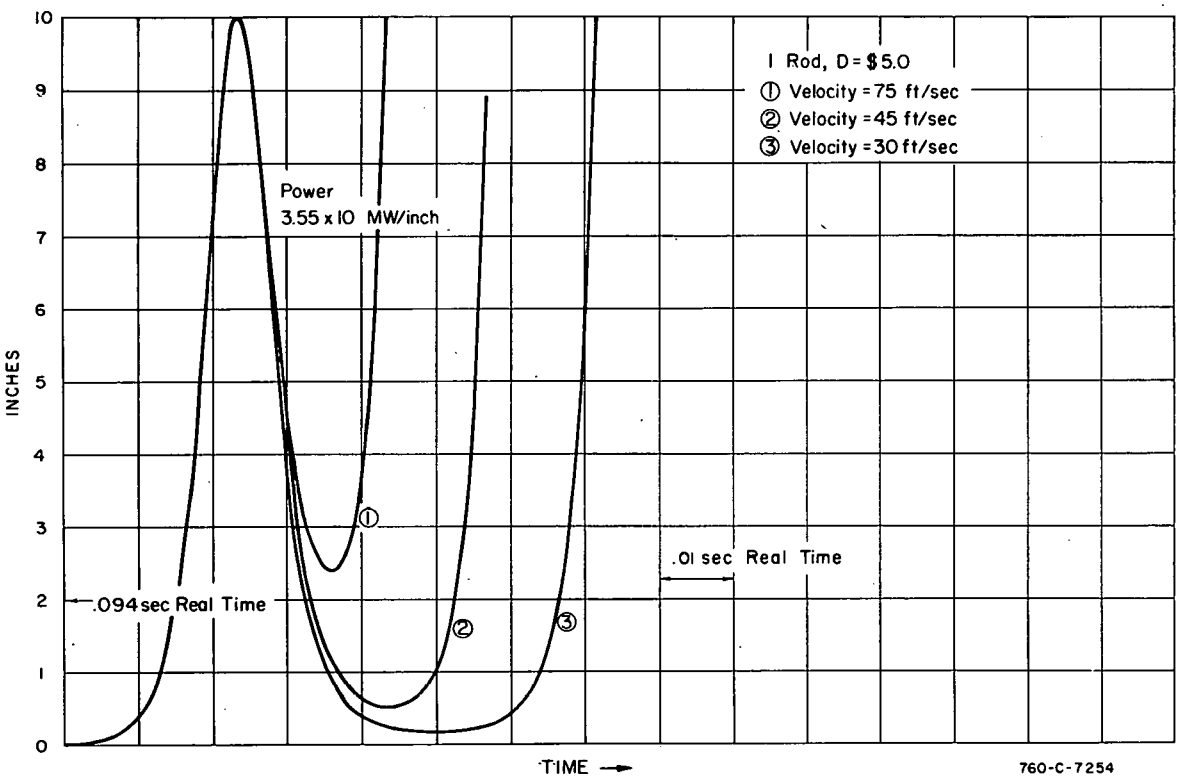

Fig. III-21D The 3-msec transient -- power shaping with constant rod velocity.

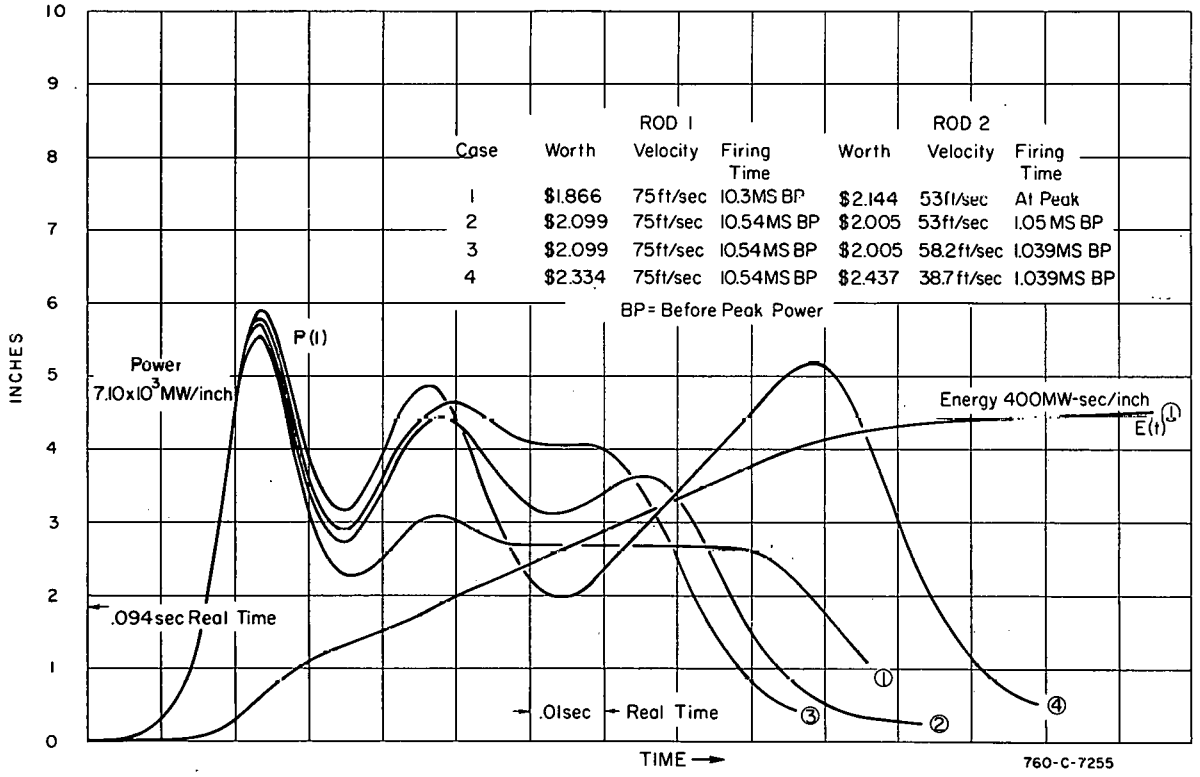

Fig. III-22 The 3-msec transient -- power shaping with two rods.

2.15 The 25-msec Transient. The simulation of the 25-msec transient on the analog computer included a simple heat transfer model for the fuel pin and water cooling. The heat transfer equations were based on the cylindrical fuel pin configuration shown in Figure III-23. The 0.0178-cm gas gap between the UO_2 and ZrO_2 was assumed to be filled with UO_2. This implies instantaneous expansion of the fuel to fill the gap as well as a reduction in the fuel density. The various dimensions, volumes, masses, etc, of the materials are given in Table III-I. The thermal model used

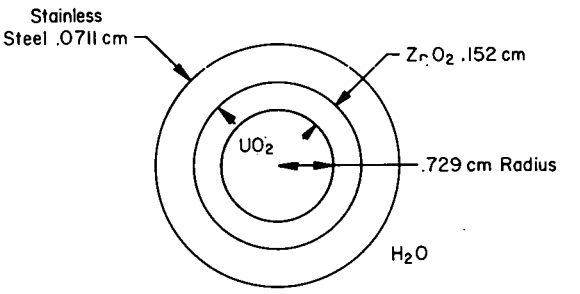

FUEL PIN CROSS SECTION

Fig. III-23 Fuel pin cross section.

TABLE III-1

THERMAL PARAMETERS

Node	Radius (cm)	Radius (cm)	Conductance Length[a] (cm)	Average Conductance[b] (cal/sec-°C)	Outer Radius (cm)	Conductance Length (cm)	Average Conductance (cal/sec-°C)	Volume (cm^3)	Average Heat Capacity (cal/°C)	Fraction of Power Generated
Fuel-1 (Center node)	0.0	0.509	----	----	0.509	----	----	1.975×10^5	----	0.447
Fuel-2	0.509	0.615	7.89×10^6	----	0.720	9.39×10^6	----	1.975×10^5	----	0.498
Zr	0.729	0.805	1.493×10^7	----	0.881	1.642×10^7	----	1.820×10^5	----	0.008
Clad	0.881	0.917	3.76×10^7	1.477×10^6	0.953	3.91×10^7	1.535×10^6	9.81×10^4	9.47×10^4	0.007
Water	----	----	----	----	----	----	----	2.83×10^5	2.74×10^5	0.040

[a] Conductance length $= \frac{2\pi Nh}{\ln \frac{r_2}{r_1}} = L_{12}$

where

N = number of fuel pins = 2588

h = length of fuel pins = 91.44 cm

r_2 = outer radius of conduction path, cm

r_1 = inner radius of conduction path, cm .

[b] Average conductance = conductance length times thermal conductivity

Water flow area = 3.10×10^3 cm^2

Water dwell time = 0.577 sec

Water temperature coefficient α_w = 0.0254 \$/°C .

describes the average core temperature, not the hot spot temperatures. Internal heat sources were assumed for the UO_2, ZrO_2, SS, and H_2O. The power generation in the fuel was taken as a hyperbolic cosine distribution according to Figure III-24. The fuel region was treated as two separate regions equal in volume and coupled by the thermal conductances of the fuel material. The heat balance equation for fuel region 1 (center of pin) was given by

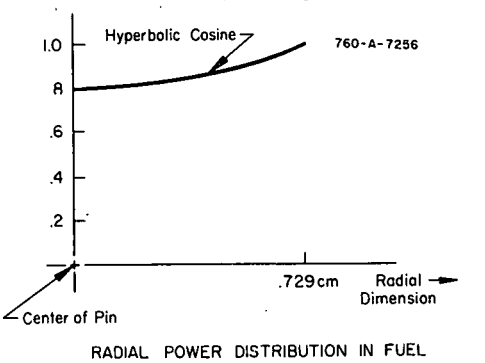

RADIAL POWER DISTRIBUTION IN FUEL

Fig. III-24 Radial power distribution in fuel.

$$C_{f1} \frac{dT_{f1}}{dt} = \gamma_f F_1 KP - K_{f1f2} (T_{f1} - T_{f2}) \qquad (10)$$

Heat balance in fuel region 2 (cylindrical shell bounded by fuel region 1 and ZrO_2)

$$C_{f2} \frac{dT_{f2}}{dt} = \gamma_f F_2 \underline{KP} + K_{f1f2} (T_{f1} - T_{f2}) - K_{f2Z} (T_{f2} - T_Z) \quad . \tag{11}$$

Heat balance in the ZrO_2 was described by

$$C_Z \frac{dT_Z}{dt} = \gamma_Z \underline{KP} + K_{f2Z} (T_{f2} - T_Z) - K_{Zc} (T_Z - T_c) \quad . \tag{12}$$

The SS cladding heat balance equation was

$$C_c \frac{dT_c}{dt} = \gamma_c \underline{KP} + K_{Zc} (T_Z - T_c) - H(T_c - T_w) \quad . \tag{13}$$

Heat balance in the water was calculated according to the equation

$$C_w \frac{dT_w}{dt} = \gamma_w \underline{KP} + H(T_c - T_w) - \frac{2Cw}{\tau_w} (T_w - T_{w\,in}) \tag{14}$$

where

T_{f1} = average temperature of fuel region 1 in °C

T_{f2} = average temperature of fuel region 2 in °C

T_Z = average temperature of ZrO_2 in °C

T_c = average temperature of SS cladding in °C

T_w = bulk water temperature in °C

$T_{w\,in}$ = inlet water temperature in °C

F_1 = power distribution factor for fuel region 1 based on cosh ar distribution

F_2 = power distribution factor for fuel region 2 based on cosh ar distribution (see Figure III-24)

C_{f1} = heat capacity of fuel region 1 in cal/°C

C_{f2} = heat capacity of fuel region 2 in cal/°C

$K_{f1f2} = L_{f1f2} k_{f2}$

k_{f2} = thermal conductivity of fuel region 2 in cal/°C-sec-cm

L_{f1f2} = conductance length, fuel region 1 to fuel region 2 in cm (see Table III-I)

$K_{f2Z} = L_{f2Z}\, k_{f2}\, L_{Z1}\, k_Z / (L_{f2Z}\, k_{f2} + L_{Z1}\, k_Z)$

L_{f2Z} = conductance length, fuel region 2 nodal point to ZrO_2 inner boundary in cm (see Table III-I)

L_{Z1} = conductance length, inner ZrO_2 boundary to ZrO_2 nodal point in cm

k_Z = thermal conductivity of ZrO_2 in cal/°C-sec-cm

C_Z = heat capacity of ZrO_2 in cal/°C

γ_Z = fraction of total power generated in ZrO_2

$K_{Zc} = L_{Z2}\, k_Z\, L_{c1}\, k_c / (L_{Z2}\, k_Z + L_{c1}\, k_c)$

L_{Z2} = conductance length, ZrO_2 nodal point to SS inner boundary in cm

L_{c1} = conductance length, SS inner boundary to SS nodal point in cm

k_c = thermal conductivity of SS in cal/°C-sec-cm

C_c = heat capacity of SS in cal/°C

γ_c = fraction of total power generated in SS

$H = L_{c2}\, k_c\, h\, A_{c2} / (L_{c2}\, k_c + h\, A_{c2})$

L_{c2} = conductance length, SS nodal point to SS outer boundary

A_{c2} = SS outer boundary heat transfer area in cm^2

h = film heat transfer coefficient in cal/°C-sec-cm^2

C_w = heat capacity of water in cal/°C

γ_w = fraction of total power generated in water

τ_w = average water dwell time in sec.

The thermal parameters (C_c, k_c, and C_w) were taken as constants because of the small change in their values over the expected temperature changes of T_c and T_w. C_c and C_w were estimated to change by about 3 percent with temperature. k_c was estimated to change about 7 percent with T_c. It was felt that because of the crudeness of the model assumed for the fuel pin, the additional small errors introduced by holding C_c, k_c, and C_w constant could be tolerated.

The other thermal conductivities and heat capacities were treated as functions of their respective temperatures according to curve fits supplied by PBF Engineering personnel (Table III-2).

The film coefficient of heat transfer, h, was treated as a function of the film temperature according to data supplied by PBF Engineering personnel. The film temperature was calculated as the arithmetic mean of the bulk water temperature and the cladding average temperature.

Bulk water temperature, T_w, was defined as the arithmetic mean of the inlet water temperature, $T_{w\,in}$, and the outlet water temperature.

TABLE III-2

HEAT CAPACITIES AND THERMAL CONDUCTIVITIES

---

k = thermal conductivity in cal/°C-sec-cm

C = heat capacity in cal/°C

V = volume in cm^3

C/V = volumetric heat capacity in cal/°C-cm^3

T = temperature in °C

$\underline{FuCl\ (UO_2)}$

$$k_f = 5.461 \times 10^{-10} (T_f + 400)^2 - 1.8645 \times 10^{-5} (T_f + 400) + 2.747 \times 10^{-3} + \frac{7.776}{T_f + 400}$$

$$C_f/V_f = 8.126 \times 10^{-8} T_f^2 + 9.56 \times 10^{-6} T_f + 0.6573$$

$\underline{ZrO_2}$

$$k_Z = 1.0 \times 10^{-6} T_Z + 4.0 \times 10^{-3}$$

$$C_Z/V_Z = -2.32 \times 10^{-7} T_Z^2 + 4.432 \times 10^{-4} T_Z + 0.575$$

The energy stored in the fuel was calculated from the equation

$$\frac{dE_f}{dt} = C_{f1} \frac{dT_{f1}}{dt} + C_{f2} \frac{dT_{f2}}{dt} \quad . \tag{15}$$

The average fuel temperature was defined as

$$\bar{T}_f = \frac{1}{2} T_{f1} + \frac{1}{2} T_{f2} \quad . \tag{16}$$

This definition is possible because of the division of the fuel region into two regions of equal volume.

The Doppler reactivity was given by

$$D_{dop} = B - B \left[1 + d\, \Delta\bar{T}_f \right]^{1/2} \tag{17}$$

where

$\Delta\overline{T}_f$ = change from initial value of $\overline{T}_f$.

The reactivity effect of the water was taken as

$$D_w = -\alpha_w \Delta T_w \tag{18}$$

where

α_w = water temperature coefficient of reactivity in dollars/°C

ΔT_w = change from iniial value of T_w.

The first 25-msec transients studied assumed the same reactor kinetics parameters as in the 1- and 3-msec transients. The reactivity used to initiate the transient was D_x = 1.107 dollars. The peak power attained was 394 MW. Figure III-25 shows the resulting energy, temperatures, and reactivities when the power is ideally held at peak power.

2.16 Transient Rod Motion Required for Power Shaping. The transient rod motion required for ideal shaping of the power is shown in Figure III-26. It is of interest to note that the required velocity is qualitatively the same as that required for shaping of the 3-msec transient. This set of curves shows that the reactivity required to hold constant power until 2000 MW-sec of energy is stored in the fuel is 5.7$ in addition to the 1.107 dollars required to initiate the transient. It is also of interest to note that if the water temperature coefficient, α_w, is set to zero, the reactivity required for shaping (at E_f = 2000 MW-sec) is 0.70$ less.

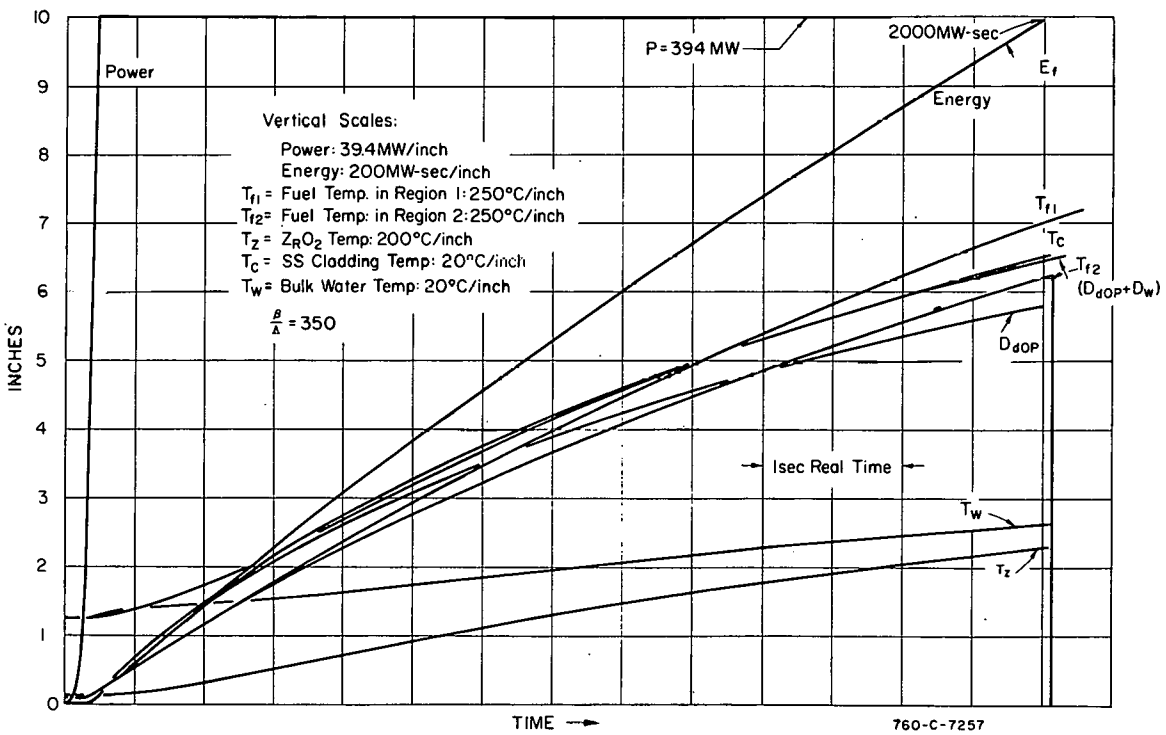

Fig. III-25 The 25-msec transient.

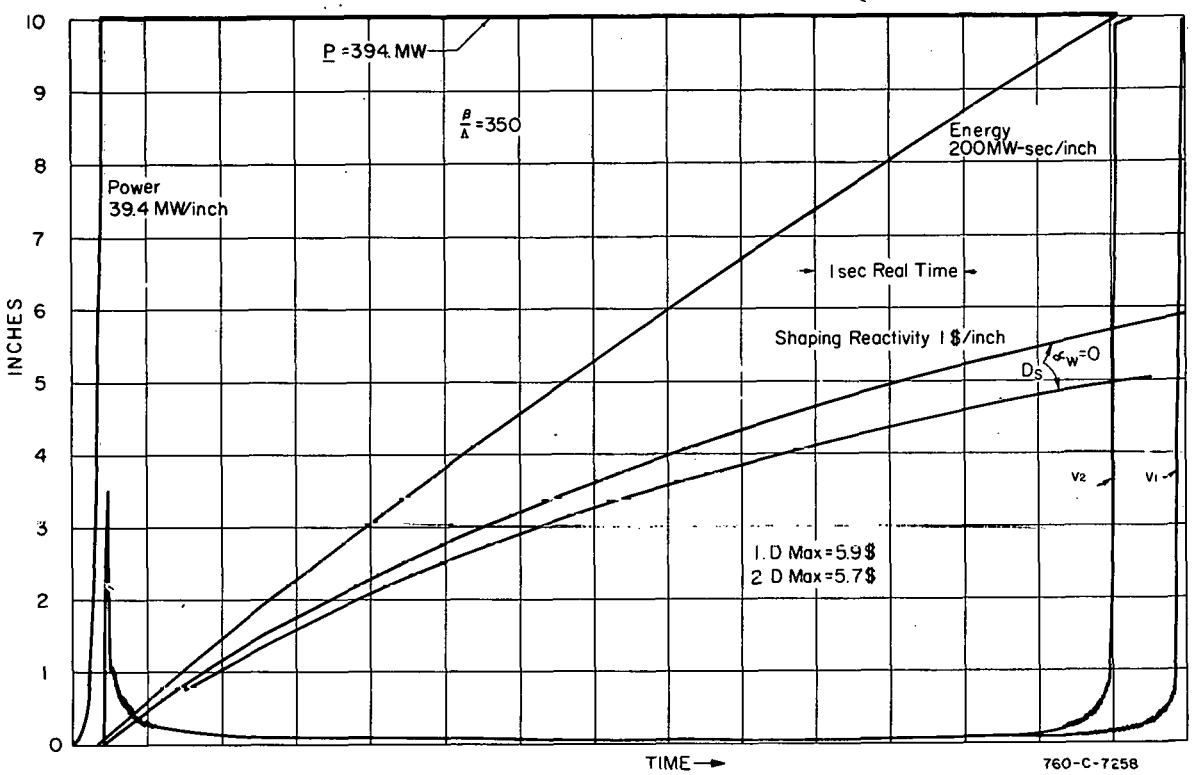

Fig. III-26 The 25-msec transient ($\beta/\Lambda = 350$).

The 25-msec transient also was studied using different estimates of some nuclear parameters. The values used next were

$$\beta/\Lambda = 500$$

$$B = 2.513 \text{ dollars}$$

$$D_x = 1.08 \text{ dollars} \quad .$$

The actual period attained for these constants was 23.2 msec. Figure III-27 shows the resulting energy and temperatures for the ideally shaped burst. The peak power attained was 462 MW.

Figure III-28 shows the transient rod motion required to hold the power at peak value (462 MW). At the time of the 2000 MW-sec energy in the fuel, the required reactivity is 3.7$ in addition to the 1.08$ used to initiate the transient. The velocity curve is essentially the same as that in Figure III-26.

Figure III-29 shows two attempts at power shaping by firing of transient rods at constant velocity. Curve 1 shows what happens when a low velocity rod (0.27 ft/sec) worth 5.25$ is fired 0.1 second ahead of the power peak. Because of the very small slope of the rod worth curve at small displacements, this rod has very little effect initially. The power is not leveled at the desired high value. Eventually the rod moves into the region where the slope of the rod worth curve is too high, and the power begins increasing. Lower rod worth for this velocity is not the answer because then there would not be enough reactivity available to hold the power constant out to the 2000 MW-sec mark. Also, lower rod worth would allow the power to drop to lower values following the peak.

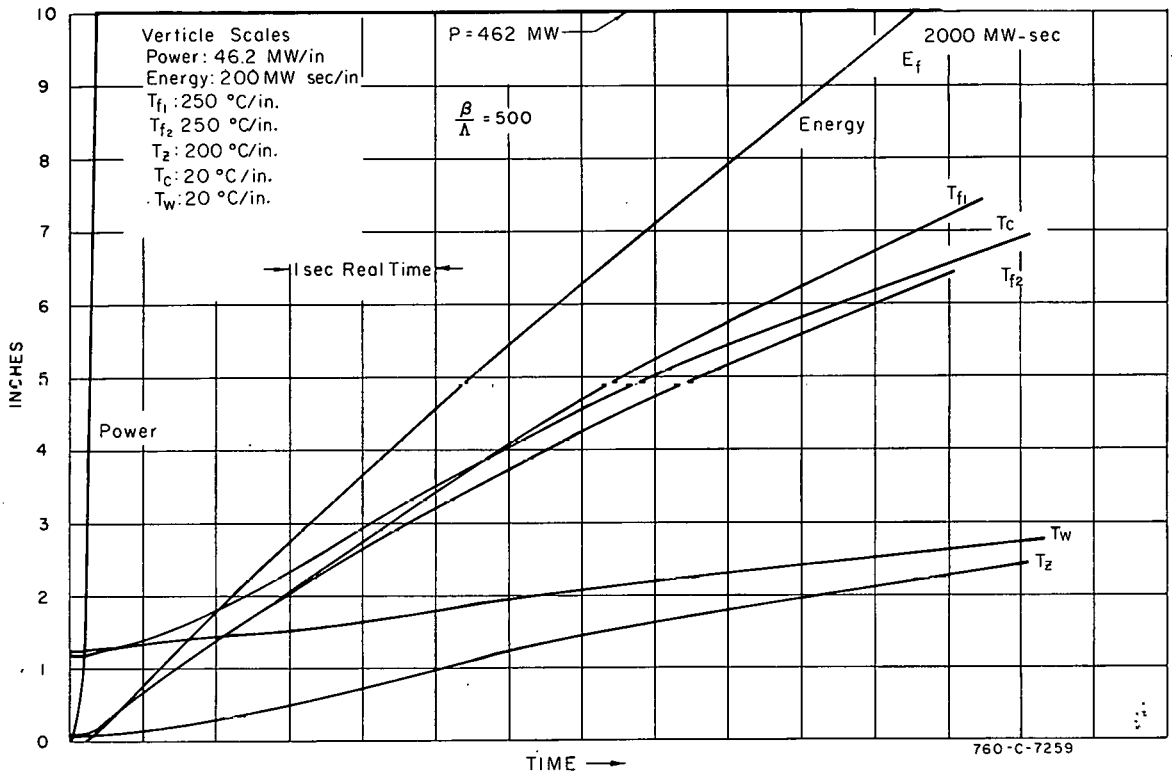

Fig. III-27 The 25-msec transient ($\beta/\Lambda = 500$).

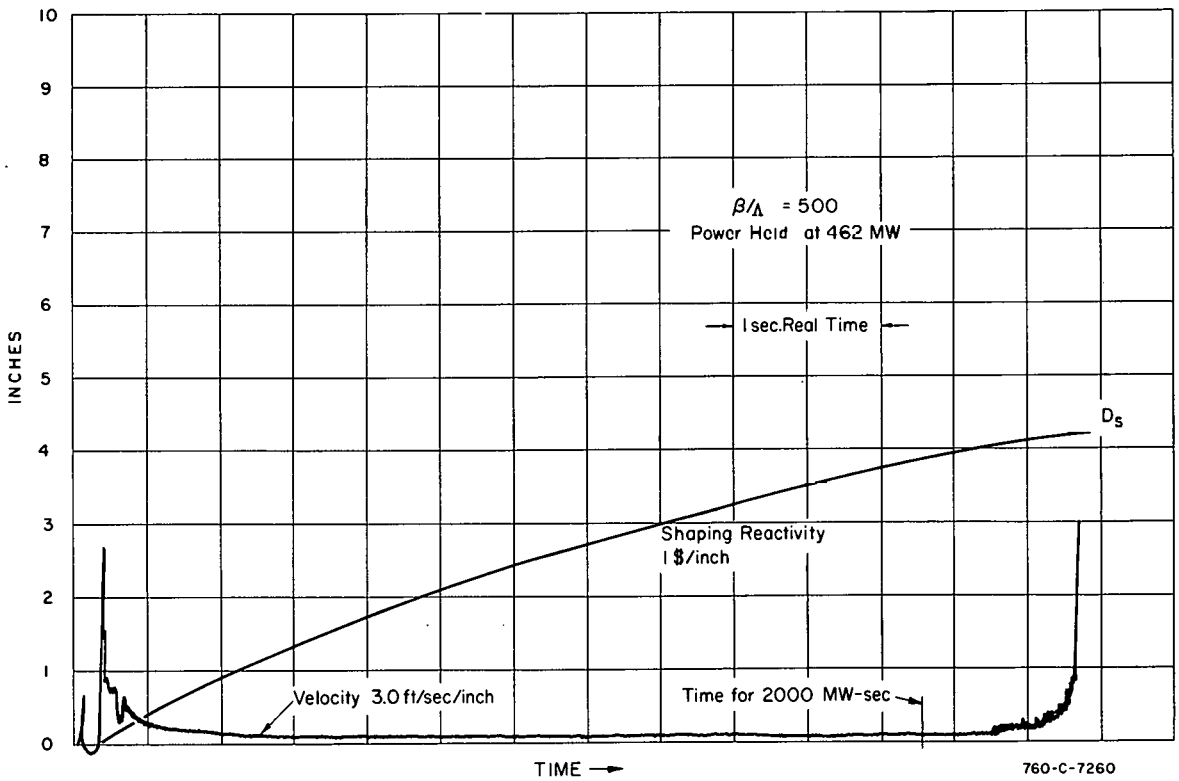

Fig. III-28 The 25-msec transient -- rod motion required for holding peak power.

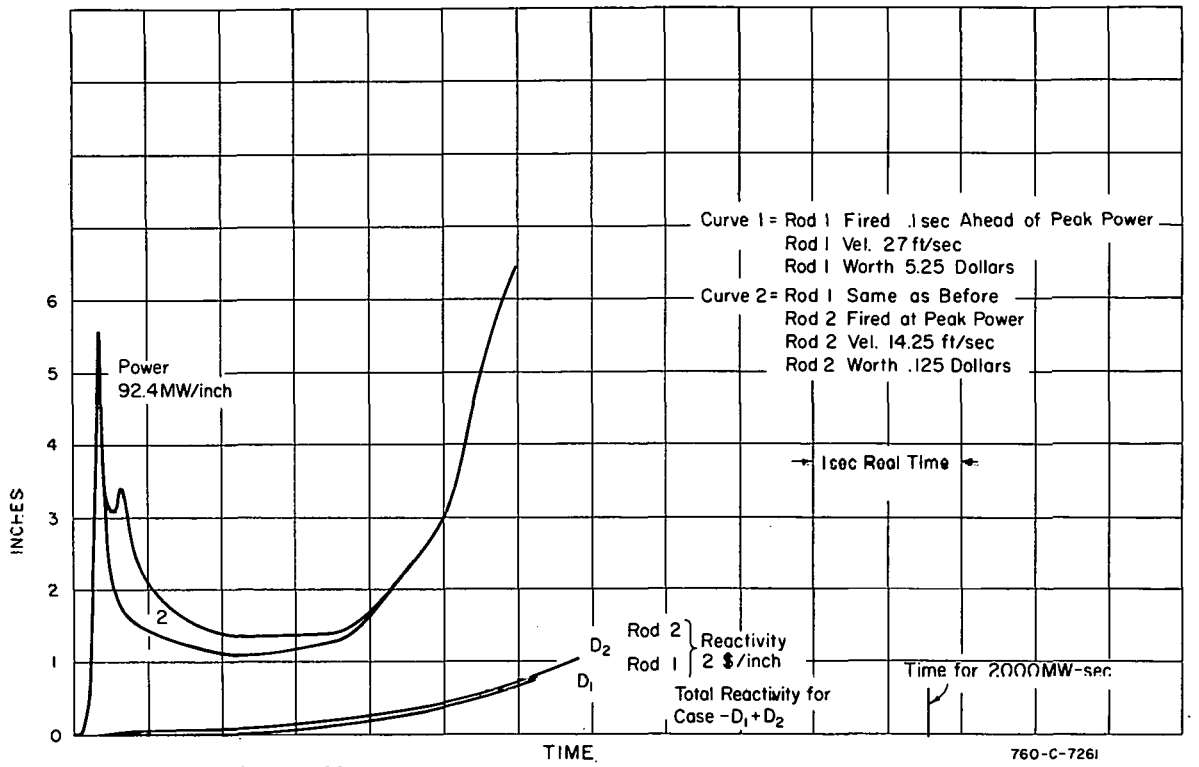

Fig. III-29 The 25-msec transient -- power shaping with two rods.

Curve 2 shows the effect of firing a second low worth (0.125$) rod at higher velocity at the time of peak power. The other rod is moved exactly as before. The effect of the second rod is to keep the power from dropping so much, but the high worth of rod 1 ultimately causes the power to go up again. Many combinations of rod worths, velocities, and firing times were tried. One set of studies considered deceleration of one rod once the rod had attained a given velocity. None of these cases resulted in a satisfactory power curve.

The most feasible solution to this problem appears to be to have a low worth rod that can be fired out of the core rapidly to keep the power from decreasing following the peak. The second rod should have a variable speed drive so that its velocity could be adjusted as the slope of the rod worth curve changes with rod withdrawl. A 5$ rod (or rods) would be withdrawn with velocities ranging down to about 0.25 ft/sec. The upper value of velocity would depend on how well the first transient rod had performed in keeping the power up.

Another possibility is to have a specially designed transient rod which when withdrawn at constant speed would have an initial slope of about 1.4$ per second. The value of the slope would have to decrease with time to a value of about 0.4$ per second.

2.2 ETR Primary Loop Transient Study (J. W. Sielinsky)

The purpose of this study was to determine the effects of a rupture in the ETR reactor vessel and the effects of a power failure to the primary coolant pumps. The results will be used by Plant Engineering in the ETR Safety Analysis review.

Four models for the analog computer simulation of the ETR primary coolant loop were developed. These models were made progressively more complex until comparison of results indicated that an adequate representation of the physical system had been obtained. The first model assumed incompressible fluid in the system; but because of the abrupt disturbances caused by a rupture, it was felt the compressibility of the fluid should be taken into account. The second model considers the compressibility of the fluid in the upper plenum of the vessel. The transients recorded from this model show that the compressibility effect of the fluid is important. The third model considers the compressibility of all the fluid in the system by lumping the fluid into 6 nodes. The transients obtained from this model show the compressibility of the fluid in the lower plenum of the vessel and in the piping is also important. The fourth model considers the compressibility of all the fluid by lumping it into 10 nodes. The transients from the 10-node model are not significantly different than those from the 6-node model. Therefore, either the 6- or 10-node model should give a good representation of the physical system.

For the 3 primary pump operation, flow and pressure transients were obtained for ruptures in the upper and lower plenum of the reactor vessel. In the upper plenum, transients were recorded for instantaneous, 10-msec time-constant and 100-msec time-constant, 36-square-inch ruptures and for an instantaneous 30-square-inch rupture. In the lower plenum, an instantaneous 36-square-inch rupture was used.

For the analysis of fluid coast-down due to a power failure, transients were obtained for 1, 2, 3, and 4 primary pump operation. For the 4 primary pump operation, the flow coast-down curve was compared to the flow coast-down curve obtained experimentally. The comparison between these curves is very good; therefore, it is felt the analog computer model is a good representation of the physical system.

2.21 Development of a Model. The ETR primary coolant system was studied to develop a mathematical model of its fluid dynamics so that an analog computer study of ruptures in the vessel and power failures to the primary coolant pumps could be performed.

Four main assumptions were made in order to simplify the sytem. The first assumption is that the reactor bypass control valve does not change during the transients. This assumption should have only a slight effect on the abrupt pressure drops following the rupture because the bypass control system is slow compared to these transients. In the coast-down study, the flow through the core will be slightly lower than if the valve had been closed. In the second assumption, the flow through the bypass demineralizer system is neglected. This should have little effect because its maximum flow is only 100 gpm. In the third assumption, the degasifier and pressurizer system is neglected. This system would have little effect on the abrupt pressure transients caused by a rupture because of the slow response of its control system. Although for the coast-down study, it would tend to keep the inlet pressure to the vessel constant, but would have little effect on the fluid coast-down because its maximum flow is about 300 gpm. The fourth assumption is that each primary pump pumps the same amount of fluid; therefore, an equivalent pump can replace the number of pumps used. The above assumptions simplified the system to a main flow loop with a bypass across the reactor vessel and a surge tank pressurizing the system (see Figure III-30).

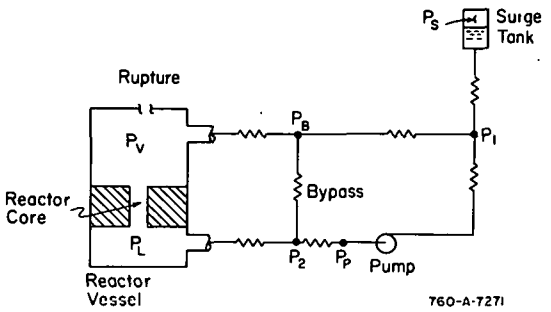

Fig. III-30 ETR primary coolant system.

The first model developed assumed incompressible fluid. The equations describing the pressure drop between nodes are of the form (see Subsection III-2.24 for definition of symbols):

$$P_1 - P_2 = RG^2 + L\dot{G} \qquad (19)$$

The assumptions made to write the equations are that steady-state pressure drops between nodes are proportional to flow squared and the fluid inertias are proportional to the length to cross-sectional area ratios of the pipes.

The equation describing the summation of the flows at a node is

$$\Sigma G_{in} = \Sigma G_{out} \quad . \qquad (20)$$

The equation describing the pressure in the surge tank, assuming isothermal expansion of the air, is

$$P_s V_s = P_o V_o \quad . \qquad (21)$$

The equation for the volume of air in the surge tank is

$$V_s = V_o + \frac{1}{60} \int_o^t G_s \, dt \quad . \qquad (22)$$

Therefore,

$$P_s = \frac{P_o V_o}{V_o + \frac{1}{60} \int_o^t G_c \, dt} \quad . \qquad (23)$$

The equation describing the pressure developed across the pump as a function of the flow through it is

$$\Delta P_p = f(G) \qquad (24)$$

where f(G) is the pump head curve (see Figure III-31) which was simulated on a function generator. The equation describing the pressure drop across an instantaneous rupture from the vessel to atmosphere is

$$P_v = R_L G_L^2 + L_L \dot{G}_L \quad . \qquad (25)$$

The assumptions made to write this equation are that the flow resistance (R_L) is constant during the flow transient and the fluid inertia (L_L) is the length to cross-sectional area of the

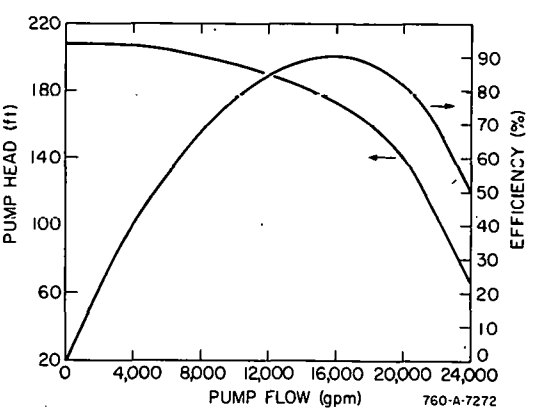

Fig. III-31 Primary pump performance curves.

rupture. The value of the fluid inertia is probably conservative because the inertia of the fluid in the vessel, affected by the rupture, is not accounted for.

The fluid dynamic equations describing the system were solved on the analog computer. Flow and pressure transients caused by the simulation of an instantaneous 36-square-inch rupture in the upper plenum of the reactor vessel were recorded (see Figure III-32). Since the upper plenum vessel pressure drops to approximately zero instantaneously after the rupture, it was felt that the compressibility of the fluid would be important.

In the second model, the compressibility of the fluid in the upper plenum was added to determine its effects. The equation used to describe the compressibility of the fluid at a node is

$$P = P(o) + \alpha \int_{o}^{t} G_n \, dt \quad . \quad (26)$$

The assumptions made in order to derive this equation are that the piping is inelastic compared to the compressibility of the fluid, that the change in density of the fluid is small compared to the magnitude of the density, and that the fluid compressibility can be separated from the fluid inertia and resistance so that the volume of the fluid can be lumped into nodes. The transients from a step rupture are shown in Figure III-33. They show the core pressure drops to a minimum of 11 psig at 90 msec.

Since this pressure transient is significantly different from the one obtained from the first model, it was felt the compressibility of all the fluid in the system should be included in the simulation. For the third model, the volume of the fluid was lumped into 6 nodes (see Figure III-34). The equations describing the 6-node model are (see Figure III-34 and Subsection III-2.24) the following:

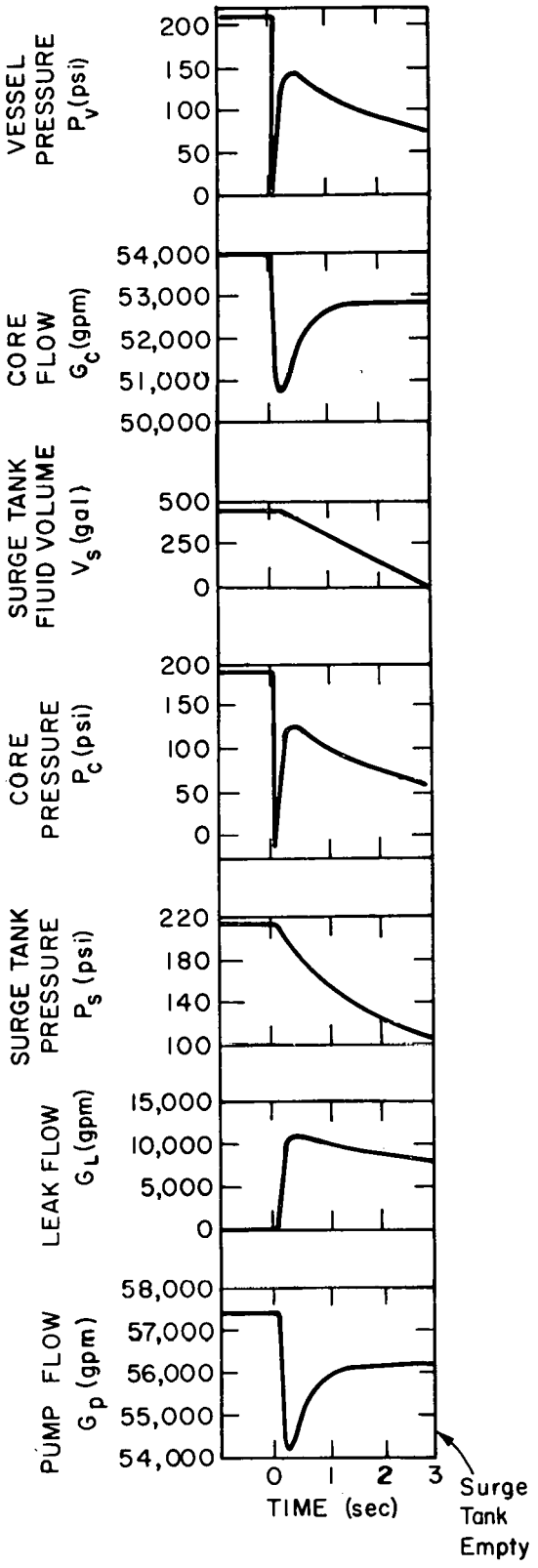

760-B-7273

Fig. III-32 Flow and pressure transients for rupture in ETR reactor vessel for surge tank initially 50 percent full (assuming incompressible fluid).

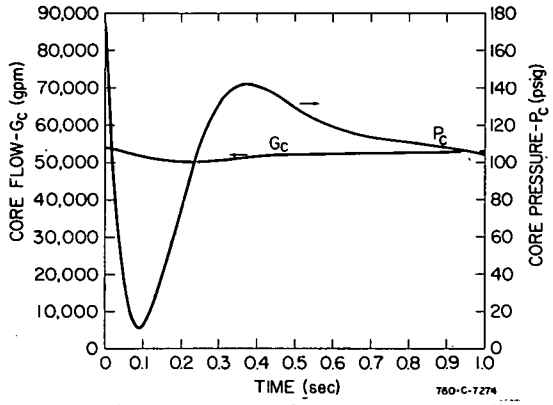

Fig. III-33 Transients for compressible fluid in upper plenum.

$$P_v - P_L = R_c G_c^2 + L_c \dot{G}_c \quad (27)$$

$$P_L - P_2 = R_H G_H^2 + L_H \dot{G}_H \quad (28)$$

$$P_2 - P_p = R_p G_p^2 + L_p \dot{G}_p \quad (29)$$

$$P_p + \Delta P_p - P_1 = R_4 G_4^2 + L_4 \dot{G}_4 \quad (30)$$

$$P_1 - P_B = R_1 G_1^2 + L_1 \dot{G}_1 \quad (31)$$

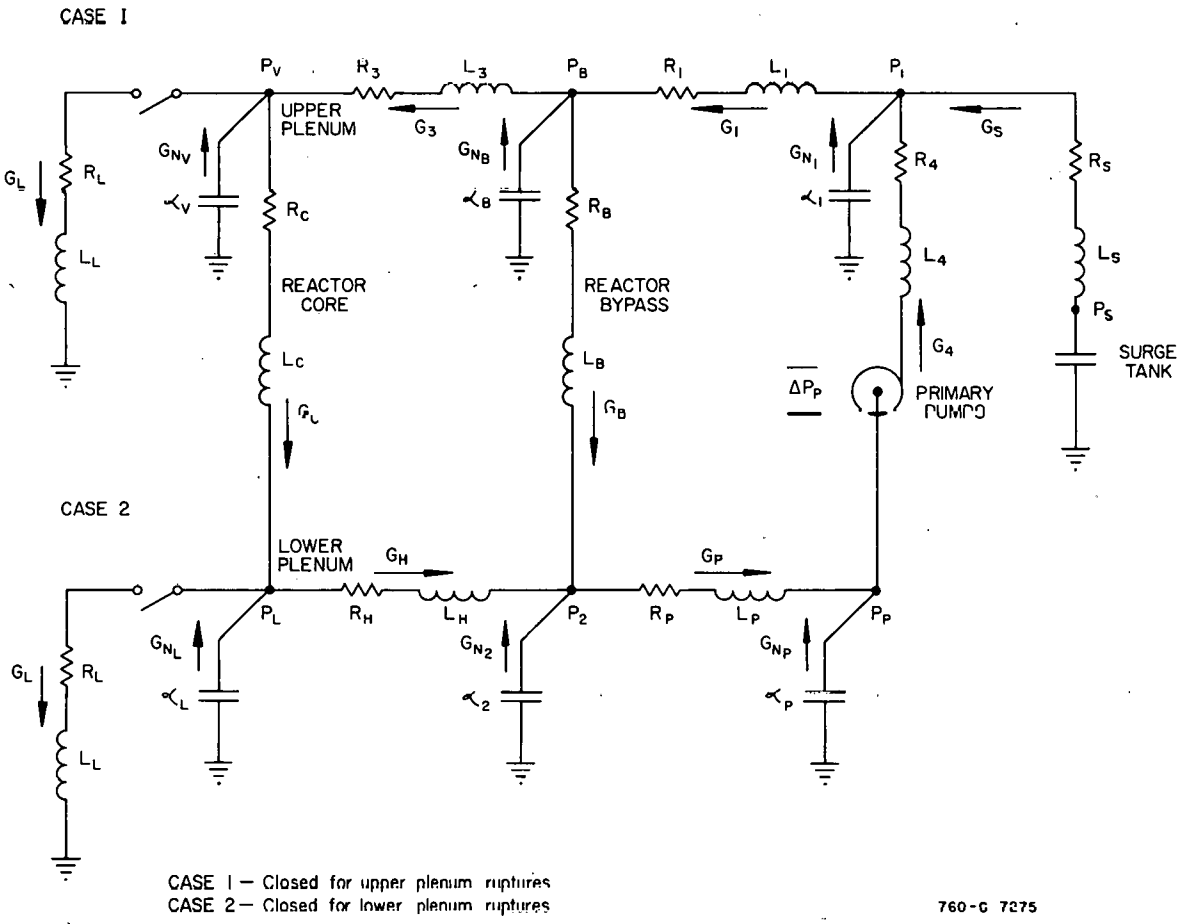

Fig. III-34 Flow diagram of six-node model.

$$P_B - P_v = R_3 G_3^2 + L_3 \dot{G}_3 \quad (32)$$

$$P_B - P_2 = R_B G_B^2 + L_B \dot{G}_B \quad (33)$$

$$P_s - P_1 = R_s G_s^2 + L_s \dot{G}_s \quad . \quad (34)$$

Pressure drop across rupture

$$P_v = R_L G_L^2 + L_L \dot{G}_L \quad . \tag{35}$$

Summation of flow at the nodes

$$G_{n_v} = G_c + G_L - G_3 \quad \text{(for upper plenum rupture)} \tag{36}$$

$$G_{n_L} = G_H - G_c \tag{37}$$

$$G_{n_2} = G_p - G_H - G_B \tag{38}$$

$$G_{n_p} = G_H - G_p \tag{39}$$

$$G_{n_1} = G_1 - G_s - G_4 \tag{40}$$

$$G_{n_B} = G_3 + G_B - G_1 \quad . \tag{41}$$

Pressure at the nodes

$$P_v = P_v(o) + \alpha_v \int_o^t G_{n_v} \, dt \tag{42}$$

$$P_L = P_L(o) + \alpha_L \int_o^t G_{n_L} \, dt \tag{43}$$

$$P_2 = P_2(o) + \alpha_2 \int_o^t G_{n_2} \, dt \tag{44}$$

$$P = P_p(o) + \alpha_p \int_o^t G_{n_p} \, dt \tag{45}$$

$$P_1 = P_1(o) + \alpha_1 \int_o^t G_{n_1} \, dt \tag{46}$$

$$P_B = P_B(o) + \alpha_B \int_o^t G_{n_B} \, dt \quad . \tag{47}$$

Pressure in core region

$$P_c = R_{c_1} G_c^2 + L_{c_1} \dot{G}_c \quad . \tag{48}$$

Pressure developed across pump

$$\Delta P_p = f(G_4) \text{ (see Figure III-31)} \quad . \tag{49}$$

Pressure in surge tank

$$P_s = \frac{P_o V_o}{V_o + \frac{1}{60}\int_o^t G_s \, dt} \quad . \tag{50}$$

The above equations were solved on the analog computer, and they show that the core pressure drops to a minimum of 46.5 psig in 190 msec (see Figure III-35).

By comparing the results from this model with the results from the model with compressible fluid in the upper plenums (see Figure III-33), it can be seen that the compressibility of the fluid in the rest of the system has a significant affect on the transients.

In order to determine the effect of lumping the fluid volumes in the pipes, a 10-node model was developed. In this model, the fluid in the piping from the outlet of the bypass around through the pumps to the junction of the main loop with the surge tank outlet pipe is lumped into five nodes instead of one node. The equations describing this model are of the same form as the ones describing the 6-node model. The results of a rupture are shown in Figure III-36. They show the core pressure drops to a minimum of 43 psig at 185 msec. By comparing Figures III-35 and -36, it can be seen that there is only a slight difference between the 6-node model and the 10-node model.

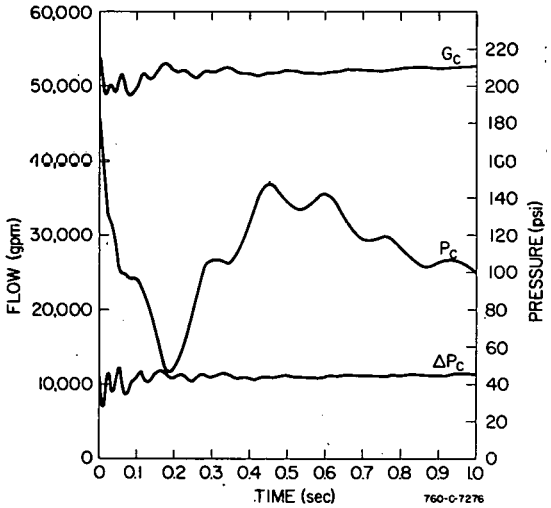

Fig. III-35 Transients for six-node model.

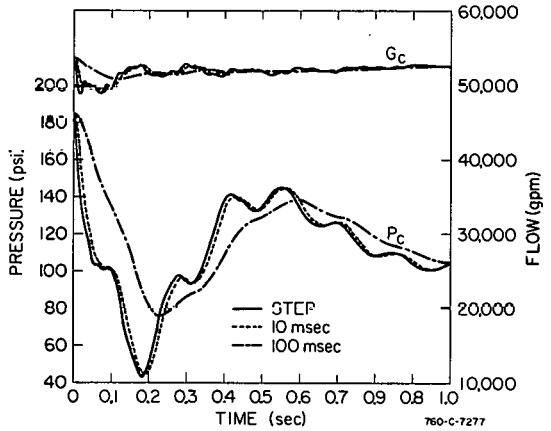

Fig. III-36 Transients from ten-node model.

For disturbances as abrupt as an instantaneous 36-square-inch rupture, the model considering incompressible fluid and the model considering compressible fluid in the upper plenum of the vessel do not give a good representation of the physical system. The reason is that the disturbance is abrupt enough to make the compressibility of all the fluid in the loop a significant factor. Although for gentle disturbances, either model would give a good representation of the system.

The results from the 6-node-compressible and the 10-node-compressible models, which consider the compressibility of all the fluid in the system, show

that lumping the fluid into more nodes does not have much effect. Therefore, it is felt that for abrupt disturbances in the system either the 6-node or the 10-node model will give a good representation of the physical system.

2.22 Types of Ruptures. An instantaneous rupture is physically impossible to obtain; therefore, different types of ruptures were tried to determine their effects. Since the configurations of a rupture in the vessel as a function of time is questionable, it is assumed the cross-sectional area of the rupture enlarges on a first-order time-constant. The equation describing this area change is

$$A(t) = A_{max}\left(1 - e^{-\frac{t}{\tau}}\right) \quad . \tag{51}$$

where τ is defined as the time-constant.

Since the flow resistance is proportional to $\frac{1}{A^2}$ and the fluid inertia is proportional to $\frac{1}{A}$, the equation describing the pressure drop across the rupture is

$$P_v = \left(\frac{k_1}{A^2}\right) G_L^2 + \left(\frac{k_2}{A}\right) \dot{G}_L \tag{52}$$

where k_1 and k_2 are constants.

Figure III-36 shows the reactor core pressure and flow transients for a step rupture, a 10-msec time-constant rupture, and a 100-msec time-constant rupture. The core pressure transients show that for a 10-msec rupture, the minimum pressure is only 1.5 psi higher than the minimum pressure for a step rupture but that the minimum pressure for the 100-msec rupture is 33.5 psi higher than for the step rupture. The reason the pressure for the 100-msec rupture does not drop as low is the 100-msec rupture is slow enough so the surge tank can keep the pressure up.

The core flow and pressure transients will be used by Plant Engineering to calculate reactor core burnout ratios; therefore, the transients from the step rupture are probably the most important because the time function of a rupture in the physical system is unknown.

For a 36-square-inch step rupture, the core pressure drops to a minimum of 43 psig which gives a burnout ratio less than one. A pressure of approximately 63 psig gives a burnout ratio of one. By reducing the area, it was determined a 30-square-inch step rupture gives a minimum pressure of approximately 63 psig (see Figure III-37).

The simulation of the rupture was changed to the lower plenum of the reactor vessel to determine its effect there. Figure III-38 shows that for the 36-square-inch rupture in the lower plenum, the minimum core pressure is 70 psig which is greater than the 63 psig calculated for a burnout ratio of one. The rupture in the lower plenum does not have as much of an effect on the core pressure as the rupture in the upper plenum because for the lower plenum rupture, the fluid has to flow through the core before it can leak out of the system.

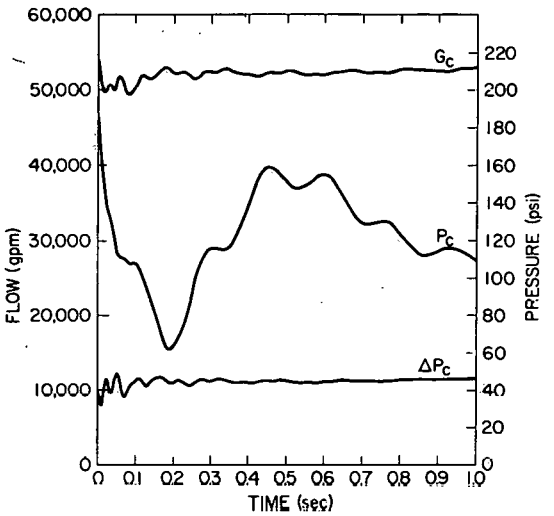

Fig. III-37 Transients for 30-square-inch rupture in upper plenum.

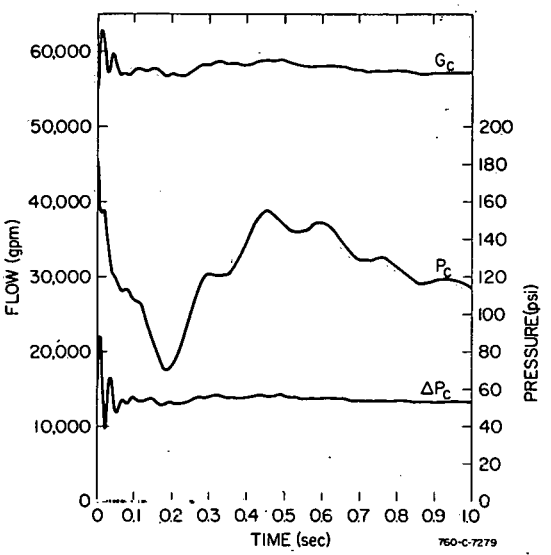

Fig. III-38 Transients for 36-square-inch rupture in lower plenum.

2.23 Flow Coast-Down. The primary-coolant pumps are connected to the commercial power bus. Since these pumps will act as generators after a power failure, the other pumping loads and resistive loads connected to this bus must be taken into account for the coast-down analysis. After the line frequency from the primary pumps drops to 58.5 cps, a relay trips which, after a constant delay of 230 msec, disconnects the primary pumps from the commercial bus. After the primary pumps are disconnected from the bus, the other loads do not have to be taken into account.

The power balance equation equates the change in kinetic energy of the rotating machinery with respect to time to the electrical power supplied minus the summation of the power losses.

$$\frac{d(\Sigma\ K.E.)}{dt} = P_e - \Sigma\ P_L \quad . \tag{53}$$

The kinetic energy of the rotating machinery is

$$\Sigma\ K.E. = \sum_{n=1}^{k} \frac{1}{2} \frac{I_n}{g} \omega_n^2 \quad . \tag{54}$$

The change in kinetic energy with respect to time is

$$\frac{d(\Sigma\ K.E.)}{dt} = \sum_{n=1}^{k} \frac{I_n}{g} \omega_n \frac{d\ \omega_n}{dt} \quad . \tag{55}$$

The power loss from the primary pumps to the primary coolant fluid is

$$P_{\text{primary pump}} = \left(k_1 \frac{\Delta p_p\ G'}{E}\right)_{\text{primary pump}} \quad ; \quad k_1\text{-constant} \quad . \tag{56}$$

The power loss to the resistive loads is proportional to the rated horsepower times the line frequency squared.

$$P_{resistive} = k_2 \, (hp)_{resistive} \left(\frac{N_L}{N_L(o)} \right)^2 \quad . \tag{57}$$

The power loss to the pumping loads is proportional to their rated horsepowers times their speed cubed.

$$P_{pumping} = \sum_{n=2}^{k} k_3 \, (hp_n)_{pumping} \left(\frac{N_{p_n}}{N_{p_n}(o)} \right)^3 \quad . \tag{58}$$

The power balance equation then becomes

$$\sum_{n=1}^{k} \frac{I_n}{g} \, \omega_n \frac{d\,\omega_n}{dt} = P_e - \left(k_1 \frac{P_p \, G}{E} \right)_1 - k_2 \, (hp)_{resistive} \left(\frac{N_L}{N_L(o)} \right)^2$$

$$- \sum_{n=2}^{k} k_3 \, (hp_n)_{pumping} \left(\frac{N_{p_n}}{N_p(o)} \right)^3 \quad . \tag{59}$$

Since the speeds of the different motors driving the pumps can be related to the line frequency by the number of poles in the motors, the power balance equation becomes

$$\Sigma I' \frac{d\,N_L}{dt} = \frac{g\,P_e}{N_L} - \left[\frac{2.939 \times 10^{-3} \, \Delta P_p \, G}{N_L \, E} \right] - \left[1.247 \times 10^{-1} \, (hp)_{resistive} (N_L) \right]$$

$$- \left[3.465 \times 10^{-5} \, \Sigma \, (hp)_{pumping} \, (N_L)^2 \right] \tag{60}$$

where

$$\Sigma I' = I_{primary\ pumps} \left(\frac{N_{primary\ pumps}(o)}{N_L(o)} \right)$$

$$+ \sum_{n=2}^{k} I_n \left(\frac{N_n(o)}{N_L(o)} \right)^2 \quad . \tag{61}$$

For a complete commercial power failure,

$$P_e = 0 \quad . \tag{62}$$

After the primary pumps are disconnected from the bus, the equation becomes

$$\Sigma \, I'_{primary\ pumps} \frac{d\,N_L}{dt} = - \frac{2.939 \times 10^{+3} \, \Delta P_p \, G}{N_L \, E} \tag{63}$$

where $\Sigma I'_{\text{primary pumps}}$ is

$$\Sigma I'_{\text{primary pumps}} = \Sigma I_{\text{primary pumps}} \left(\frac{N_{\text{primary pumps}}}{N_L(o)} \right)^2 \qquad (64)$$

Flow and pressure transients in the primary-coolant loop were then obtained from the analog computer simulation of the power balance equation, the primary pump head curve (see Figure III-31), the primary pump efficiency curve (see Figure III-31), and the 6-lump model of the primary coolant loop. Figures III-39 through -42 show the transients obtained for the 1, 2, 3, and 4 primary pump operations, respectively. Figure III-43 shows the flow coast-down data obtained experimentally for the 4 primary pump operation. By comparing the data in Figure III-43, it can be seen the experimental coast-down curve agrees with the curve obtained from the analog computer simulation. Since the results agree, it is felt the assumptions made to simulate the system on the analog computer are justifiable.

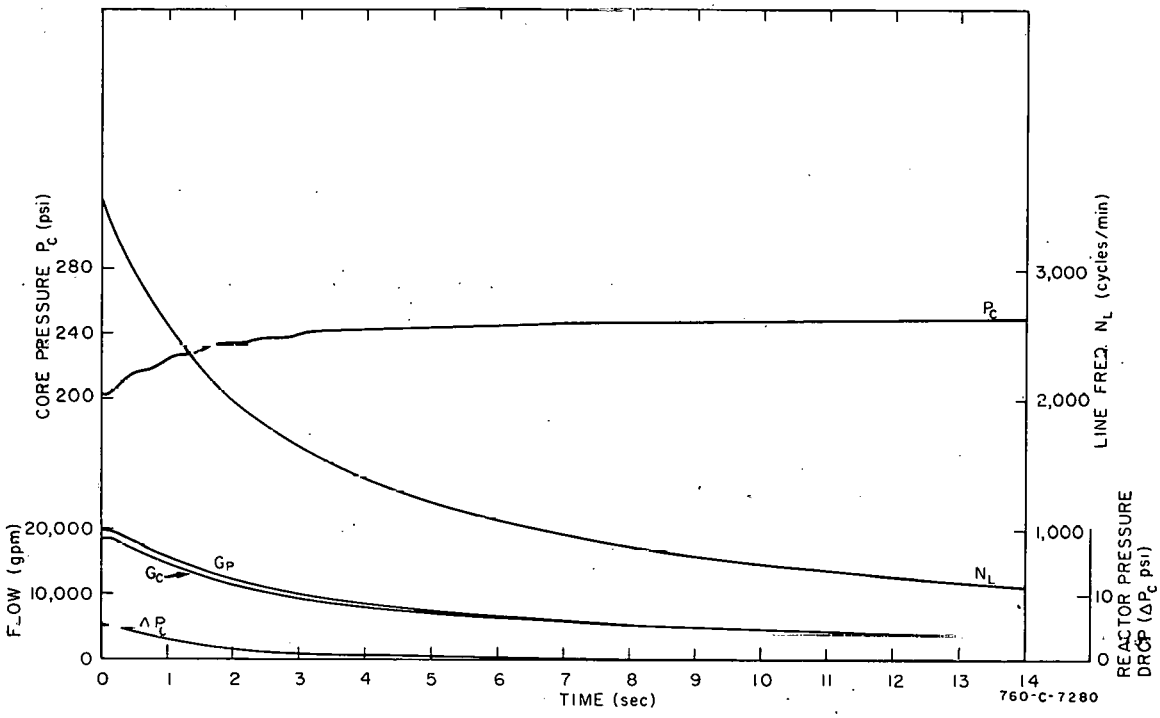

Fig. III-39 Coast-down transients for one primary pump operation.

2.24 Definition of Symbols.

(1) Definition of symbols for Equation (19)

P = pressure (psig)

R = flow resistance $\left(\frac{\text{psi}}{\text{gpm}^2}\right)$

G = fluid flow (gpm)

L = fluid inertia $\left(\frac{\text{psi min sec}}{\text{gal}}\right)$.

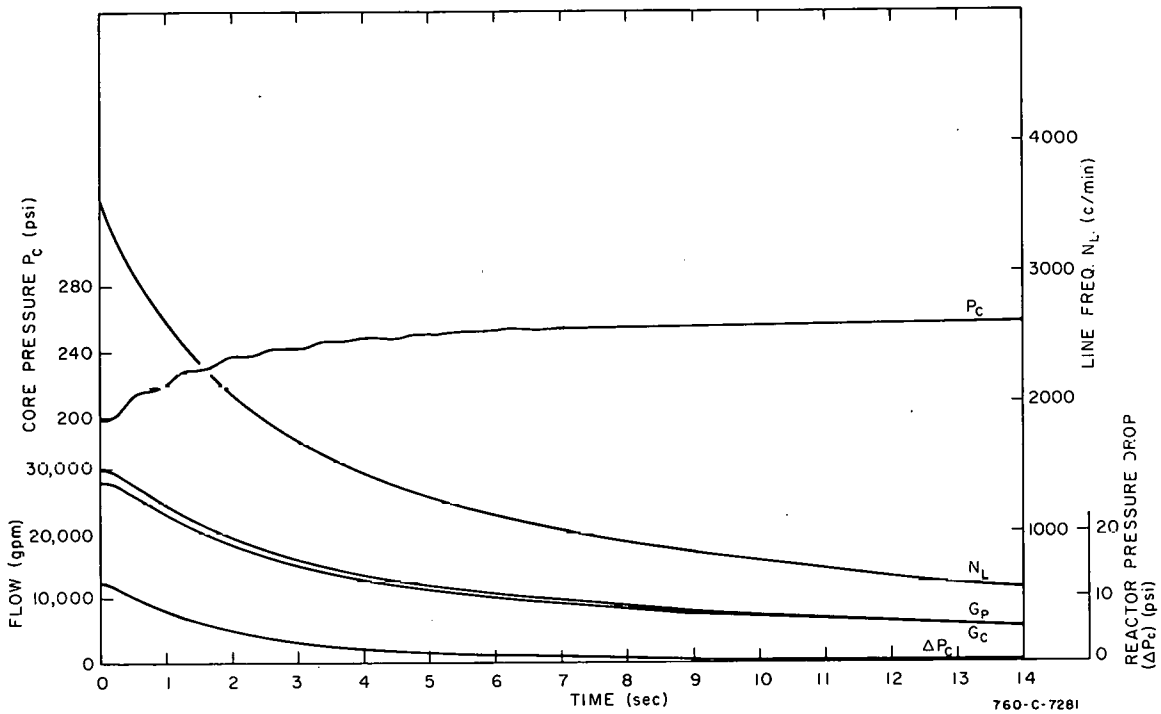

Fig. III-40 Coast-down transients for two primary pump operation.

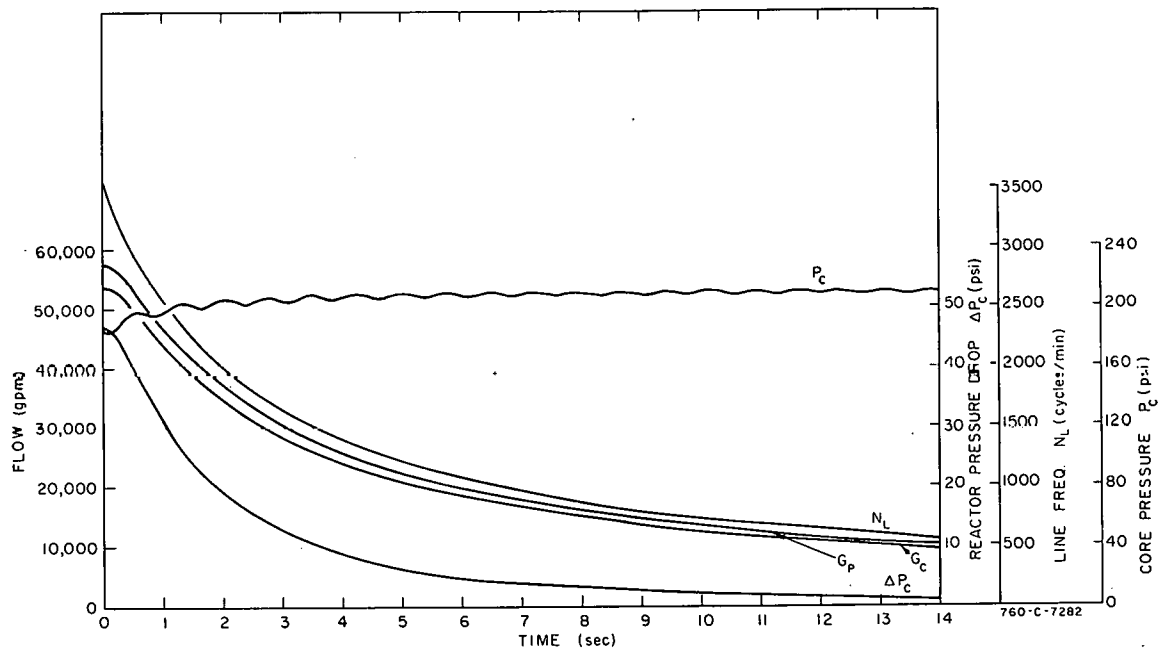

Fig. III-41 Coast-down transients for three primary pump operation.

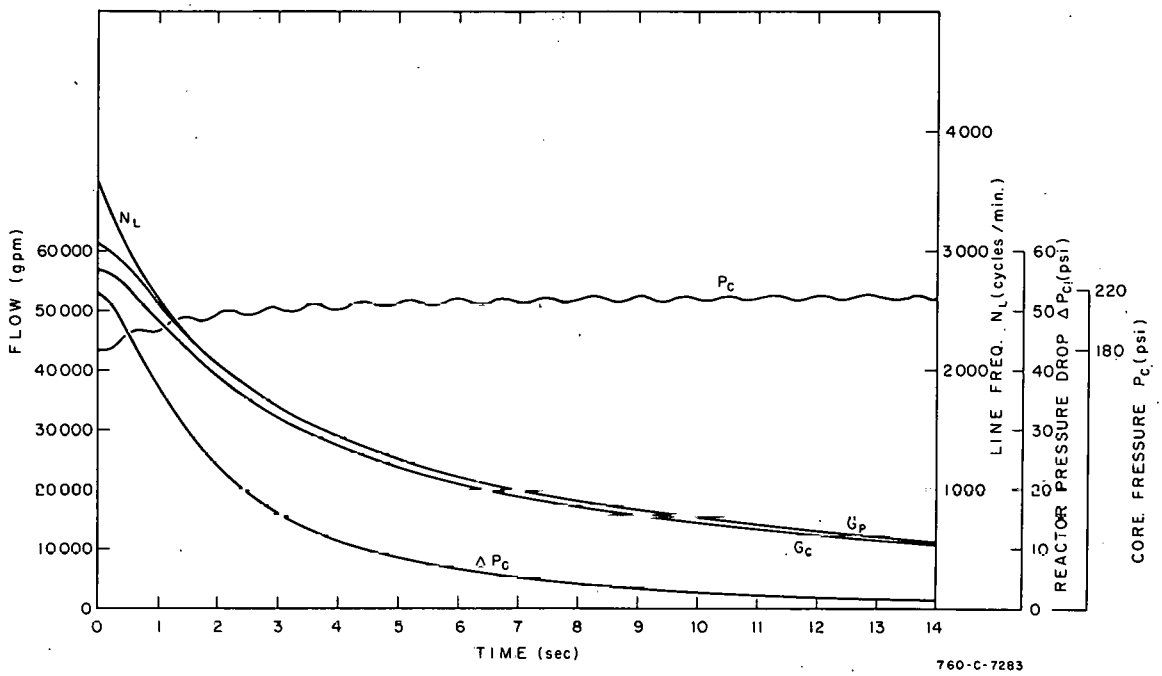

Fig. III-42 Coast-down transients for four primary pump operation.

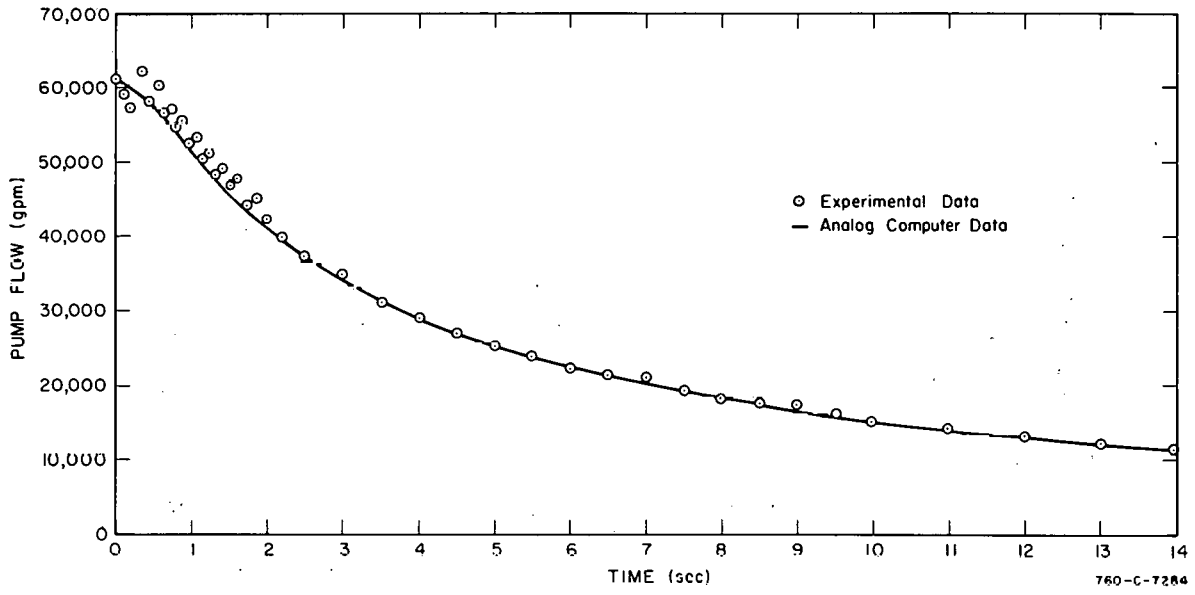

Fig. III-43 Flow coast-down transients for four primary pump operation.

(2) Definition of Symbols for Equation (26).

P = pressure at node (psig)

$P(o)$ = initial pressure at node (psig)

$\alpha = \frac{E}{60V}$ = reciprocal of the fluid capacitance, where E is the modulus of elasticity of water and V is the volume of water in the node $(\frac{\text{psi min}}{\text{gal sec}})$

G_n = net fluid flow into node (gpm)

(3) Definition of Symbols for Other Equations.

P_o = initial surge tank pressure (psig)

V_o = initial surge tank air volume (gal)

P_s = surge tank pressure at time = t (psig)

V_s = surge tank air volume at time = t (gal)

G_s = fluid flow out of surge tank (gpm)

P_v = pressure in upper plenum of vessel (psig)

P_L = pressure in lower plenum of vessel

P_2 = pressure at junction of outlet of bypass with main loop

P_p = pressure at inlet to heat exchangers

$\triangle P_p$ = pressure developed across pump

P_1 = pressure at junction of surge tank outlet with main loop

P_B = pressure at junction of inlet to bypass with main loop

P_c = pressure in reactor core region

G_c = flow through reactor core (gpm)

G_H = flow in outlet header of vessel

G_p = flow from bypass outlet to heat exchanger inlet

G_4 = flow through primary pumps

G_1 = flow from surge tank outlet to bypass inlet

G_3 = flow from bypass inlet to vessel inlet

G_B = flow through bypass

G_L = flow out of rupture

$G_{n's}$ = net flow into respective nodes

P(o)'s = initial pressure in respective nodes

R_c = resistance from upper plenum through the core to lower plenum ($1.657 \times 10^{-8} \frac{psi}{gpm^2}$)

R_H = resistance from lower plenum to bypass outlet ($1.029 \times 10^{-10} \frac{psi}{gpm^2}$)

R_p = resistance from bypass outlet to heat exchanger inlet ($6.961 \times 10^{-9} \frac{psi}{gpm^2}$, $1.884 \times 10^{-9} \frac{psi}{gpm^2}$, $9.441 \times 10^{-10} \frac{psi}{gpm^2}$, $6.150 \times 10^{-10} \frac{psi}{gpm^2}$ for the 1, 2, 3, and 4 primary pump operations, respectively)

R_4 = resistance from heat exchanger inlet to junction of surge tank outlet with main loop ($1.383 \times 10^{-8} \frac{psi}{gpm^2}$, $3.458 \times 10^{-9} \frac{psi}{gpm^2}$, $1.537 \times 10^{-9} \frac{psi}{gpm^2}$, $8.645 \times 10^{-10} \frac{psi}{gpm^2}$ for the 1, 2, 3, and 4 primary pump operations, respectively)

R_1 = resistance from junction of surge tank outlet with main loop to bypass inlet ($4.634 \times 10^{-11} \frac{psi}{gpm^2}$, $2.602 \times 10^{-11} \frac{psi}{gpm^2}$, $2.592 \times 10^{-9} \frac{psi}{gpm^2}$, $4.510 \times 10^{-11} \frac{psi}{gpm^2}$ for the 1, 2, 3, and 4 primary pump operations, respectively)

R_3 = resistance from bypass inlet to vessel inlet ($1.337 \times 10^{-9} \frac{psi}{gpm^2}$)

R_B = resistance in bypass ($3.00 \times 10^{-6} \frac{psi}{gpm^2}$)

R_s = resistance in surge tank connecting pipe ($2.980 \times 10^{-7} \frac{psi}{gpm^2}$)

R_L = resistance in rupture ($1.319 \times 10^{-6} \frac{psi}{gpm^2}$ for 36-square-inch step rupture; variable from infinity to $1.319 \times 10^{-6} \frac{psi}{gpm^2}$ for time constant ruptures; $0.916 \times 10^{-6} \frac{psi}{gpm^2}$ for 30-square-inch step rupture)

R_{c_1} = resistance from upper plenum to core region ($6.653 \times 10^{-9} \frac{psi}{gpm_2}$)

L_c = inertia from upper plenum through the core to lower plenum ($3.1362 \times 10^{-5} \frac{psi\ min\ sec}{gal}$)

L_H = inertia from lower plenum to bypass outlet ($1.486 \times 10^{-4} \frac{psi\ min\ sec}{gal}$)

L_p = inertia from bypass outlet to heat exchanger inlet ($1.336 \times 10^{-3} \frac{psi\ min\ sec}{gal}$, $0.8046 \times 10^{-3} \frac{psi\ min\ sec}{gal}$, $0.6275 \times 10^{-3} \frac{psi\ min\ sec}{gal}$, and $0.5390 \times 10^{-3} \frac{psi\ min\ sec}{gal}$, for the 1, 2, 3, and 4 primary pump operations, respectively)

L_4 = inertia from heat exchanger inlet to junction of surge tank outlet with main loop ($1.0483 \times 10^{-3} \frac{psi\ min\ sec}{gal}$, $0.5242 \times 10^{-3} \frac{psi\ min\ sec}{gal}$, $0.3494 \times 10^{-3} \frac{psi\ min\ sec}{gal}$, and $0.2621 \times 10^{-3} \frac{psi\ min\ sec}{gal}$, for the 1, 2, 3, and 4 primary pump operations, respectively)

L_1 = inertia from junction of surge tank outlet with main loop to bypass inlet ($2.7533 \times 10^{-4} \frac{psi\ min\ sec}{gal}$)

L_3 = inertia from bypass inlet to vessel inlet ($1.923 \times 10^{-4} \frac{psi\ min\ sec}{gal}$)

L_B = inertia in bypass ($1.161 \times 10^{-3} \frac{psi\ min\ sec}{gal}$)

L_s = inertia in surge tank connecting pipe ($1.424 \times 10^{-3} \frac{psi\ min\ sec}{gal}$)

L_L = inertia in rupture ($2.219 \times 10^{-5} \frac{\text{psi min sec}}{\text{gal}}$ for 36-square-inch rupture; variable from infinity to $2.919 \times 10^{-5} \frac{\text{psi min sec}}{\text{gal}}$ for the time constant rupture; 1.849×10^{-5} for 30-square-inch rupture)

L_{c_1} = inertia from upper plenum to core region ($1.894 \times 10^{-5} \frac{\text{psi min sec}}{\text{gal}}$)

α_v = reciprocal of fluid capacitance in upper plenum ($0.3141 \frac{\text{psi min}}{\text{gal sec}}$)

α_L = reciprocal of fluid capacitance in lower plenum ($0.8690 \frac{\text{psi min}}{\text{gal sec}}$)

α_2 = reciprocal of fluid capacitance in node 2 ($1.359 \frac{\text{psi min}}{\text{gal sec}}$)

α_p = reciprocal of fluid capacitance in node p ($1.1534 \frac{\text{psi min}}{\text{gal sec}}$, $0.5767 \frac{\text{psi min}}{\text{gal sec}}$, $0.3845 \frac{\text{psi min}}{\text{gal sec}}$, $0.2884 \frac{\text{psi min}}{\text{gal sec}}$ for the 1, 2, 3, and 4 primary pump operations, respectively)

α_1 = reciprocal of fluid capacitance in node 1 ($2.022 \frac{\text{psi min}}{\text{gal sec}}$, $1.427 \frac{\text{psi min}}{\text{gal sec}}$, $1.103 \frac{\text{psi min}}{\text{gal sec}}$, $0.898 \frac{\text{psi min}}{\text{gal sec}}$ for the 1, 2, 3, and 4 primary pump operations, respectively)

α_B = reciprocal of fluid capacitance in node B ($2.009 \frac{\text{psi min}}{\text{gal sec}}$)

I = moment of inertia of pump (lb-ft^2)

ω = angular velocity of pump (rad/sec)

g = acceleration of gravity (32.2 ft/sec^2)

E = pump efficiency

N_L = line frequency (cycles per min)

$\Sigma I'$ = moment of inertia of all rotating machinery normalized to line frequency (1426.5 lb-ft^2; 1794.7 lb-ft^2; and 4 primary pump operations, respectively)

$(hp)_{resistive}$ = the horsepower loss to the resistive loads (1396 hp)

$\Sigma (hp)_{pumping}$ = the horsepower loss to the pumping loads, excluding the primary pumps (2120 hp, 2530 hp, 2955 hp for the 1, 2, 3, and 4 primary pump operations, respectively).

$\Sigma I'_{primary\ pumps}$ = moment of inertia of primary pumps normalized to line frequency (802.5 lb-ft^2 per pump).

3. REFERENCES

1. P. H. Hofhine, Eddy Current Vibration Sensor (unpublished).
2. T. J. Boland et al, "Proximity Transducer" (p. 77).
3. F. A. Meichle, Private Communication (March 30, 1962).
4. K. D. Smith, A Transistorized Bidirectional Decade Counter, IDO-17059, January 1965.

THIS PAGE

WAS INTENTIONALLY

LEFT BLANK

IV. MATHEMATICAL ANALYSIS AND MACHINE COMPUTATIONS

1. MONTE CARLO PROGRAM
(R. A. Grimesey, C. W. Berner)

The input and output subroutines for the general purpose Monte Carlo program [1] are essentially complete and have been checked out with a limited number of test problems. The input for this program is complex, and considerable time was spent simplifying the input format to eliminate ambiguities for requestors.

The output includes a complete statistical analysis of the fluxes in each region obtained from a predetermined number of statistical samples. Two options are available in the input for determining the length of the samples. The sample length can be determined by a fixed number of source particles or a fixed length of machine time. The statistical analysis is based on calculating a confidence limit from a student's "t" analysis of the fluxes. In order for the student's "t" analysis to be valid, a number of conditons based on the Central Limit Theorem of Probability Theory must be satisfied. A limited number of problems have been run to test these conditions as applied to Monte Carlo. The tests are not conclusive yet but seem to indicate that the Central Limit Theorem does hold in multigroup Monte Carlo studies. Studies are presently being made with simple geometries to determine the efficiency of this program for reactor physics problems.

2. TRA MAINTENANCE EXPOSURE REPORT -- PPCo 40.0362
(A. T. Reddish)

An IBM 7040 program has been written which produces a report for TRA Maintenance. The radiation received by the men in the five trades (instrument men, mechanics, fitters, insulators, and welders) is calculated. This information is calculated for two time intervals, This Period and Year to Date. This Period is from one film badge reading to another, and Year to Date is from the first of the current year to the present film badge reading.

From the Year to Date radiation at the last badge reading and the present badge reading, all the information can be computed. The report gives the following information for each trade: number of men, number of men exchanged, highest individual exposure, average exposure to permanent men, total exposure to permanent men, total exposure to temporary men, total of all radiation for each trade, and number of men over allowable radiation.

This program is checked out and is in regular use.

3. NUMERICAL SOLUTION OF POLYNOMIAL EQUATIONS -- PPCo 40.0344

(G. A. Cazier)

An IBM 7040 program has been written which calculates the roots of the polynomial equation:

$$f(x) = a_o x^n + a_1 x^{n-1} + a_2 x^{n-2} + \ldots + a_{n-1} x + a_n = 0$$

where $a_i (i = 0, 1, \ldots, n)$ are real coefficients of the given equation.

The numerical technique employs the well-known Newton and Bairstow correction formulae for a simultaneous linear and quadratic iterated synthetic division [2].

The Newton iteration may be described with the following formula:

$$r_{i+1} = r_i - \frac{f(r_i)}{f'(r_i)}$$

where r_i is a guess for the value of a root, and r_{i+1} is the corrected guess. The value $f(r_i)$ may be computed as the remainder term in a synthetic division of $f(x)$ by $(x-r_i)$ and $f'(r_i)$ as the remainder term in a second synthetic division of the quotient by $(x-r_i)$.

The Bairstow iteration may be described as an iterated synthetic division of $f(x)$ by $(x^2 + p_i x + q_i)$, where p_i and q_i are guesses for the values of the coefficients of a quadratic factor of $f(x)$. Thus,

$$\frac{f(x)}{x^2 + p_i x + q_i} = g(x) + R$$

$$= b_o x^{n-2} + b_1 x^{n-3} + \ldots + b_{n-3} x + b_{n-2} + R$$

where

$$R = \frac{b_{n-1} x + b_n}{(x^2 + p_i x + q_i)}$$

and

$$\frac{g(x)}{x^2 + p_i x + q_i} = h(x) + S$$

$$= c_o x^{n-4} + c_1 x^{n-5} + \ldots + c_{n-5} x + c_{n-4} + S$$

with

$$S = \frac{c_{n-3}x + c_{n-2}}{(x^2 + p_i x + q_i)}$$

Then the correction formulae for the Bairstow iteration are given as

$$p_{i+1} = p_i + \frac{b_{n-1}\, c_{n-2} - b_n\, c_{n-3}}{c^2_{n-2} - \bar{c}_{n-1}\, c_{n-3}}$$

$$q_{i+1} = q_i + \frac{-b_{n-1}\, \bar{\bar{c}}_{n-1} + b_n\, c_{n-2}}{c^2_{n-2} - \bar{c}_{n-1}\, c_{n-3}}$$

where

$$\bar{c}_{n-1} = -(p_i\, c_{n-2} + q_i\, c_{n-3}) \quad .$$

The method employed will nearly always converge to the number of significant figures specified; however if it fails within a specified number of iterations, the convergence requirements will be reduced successively by one significant figure until convergence.

4. COMPUTER PROGRAM FOR CALCULATING SINGLE-ENERGY, GAMMA-RAY SHAPES -- PPCo 40.0028

(G. A. Cazier)

To facilitate the application of analytical techniques to the analysis of gamma-ray, pulse-height spectra, an IBM 7040 program has been developed for the calculation of a pulse-height response of a sodium iodide scintillation detector as a function of gamma-ray energy. This method of calculating a response function may be applied to any experimental arrangement and detector [3].

The approach used is a systematic extension of the graphical interpolation scheme which has been in use for some time. If a sufficient number of radioactive sources may be obtained which decay with the emission of a single gamma ray, then the pulse-height spectrum for a gamma ray of any energy may be determined by a suitable interpolation scheme.

First, a number of carefully measured spectra are obtained for single gamma rays. Using these pulse-height distributions, a three-dimensional model of the response of a sodium iodide scintillation detector to monoenergetic gamma rays may be constructed (see Figure IV-1). A plane perpendicular to the energy axis through a given point will intersect this surface to form a curve. This curve represents the detector response to a gamma ray of that energy.

A detailed examination of the structure of pulse-height distributions obtained from monoenergetic gamma rays shows that there are several features

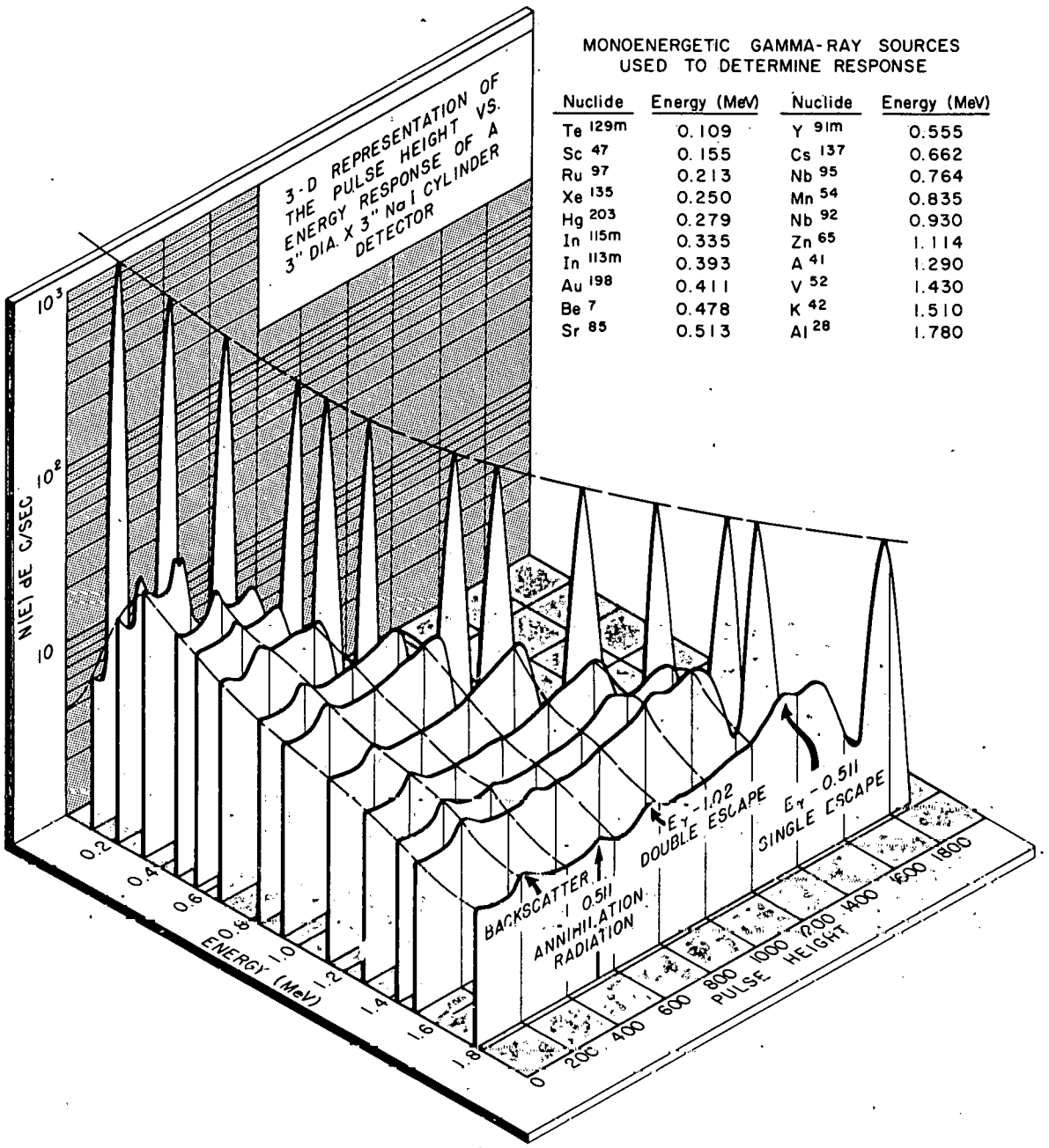

Fig. IV-1 Three-dimensional model of the response of a NaI scintillation detector to monoenergetic gamma rays.

which vary in a uniform manner with gamm-ray energy. All features of the spectra can be interpreted from a knowledge of three basic processes by which a photon interacts with the detector; ie, photoelectric, Compton, and pair-interactions.

The most prominent feature, the photopeak, is essentially Gaussian in shape with some asymmetry on the low energy side. The remaining portion of the pulse-height distribution is due largely to the Compton process, which produces a distribution of pulses from zero amplitude up to a sharp cutoff representing maximum energy transfer between the photon and a recoil electron.

This point of the spectrum is called the Compton edge (E_c). Other prominent features of the spectrum are the back-scatter peak (E_b), the single-escape peak (E_{p1}), and the double-escape (E_{p2}), all with calculable relationships to the gamma-ray energy, E_γ.

The portion of the spectrum below the photopeak is divided into five segments which are bound by O, E_b, E_{p1}, Ep2, E_c, and E_γ. Each segment is then fitted to a series of the form

$$y = a + bx + \sum_{k-1}^{Nk} bp \sin \frac{k\pi x}{L} \quad .$$

In order to ensure a smooth fit at the segment end points, a region of overlap is included in the fitting procedure. The number of terms, k, in the expansion was chosen to give a certain amount of smoothing to the data points.

The next step in the process is to evaluate the above series at a fixed number of points for each input spectrum. For a given channel, these points represent a section through the three-dimensional surface perpendicular to the pulse-height axis. These points are then fitted to a polynomial in gamma-ray energy. The number of terms in this polynomial is adjustable in order to give the most reasonable fit to the data points. Thus, a set of polynomials in energy is obtained, one for each channel on the pulse-height scale. This process is repeated for each segment of the Compton distribution.

To obtain the pulse-height distribution for a given gamma ray, channel count rate values are computed from the set of polynomials described above for each channel. Figure IV-2 shows a comparison between an experimental pulse-height distribution for a single-energy gamma ray and the calculated shape for a gamma ray of the same energy obtained from the shape-generation program. The two spectra are displaced on the vertical scale for comparison.

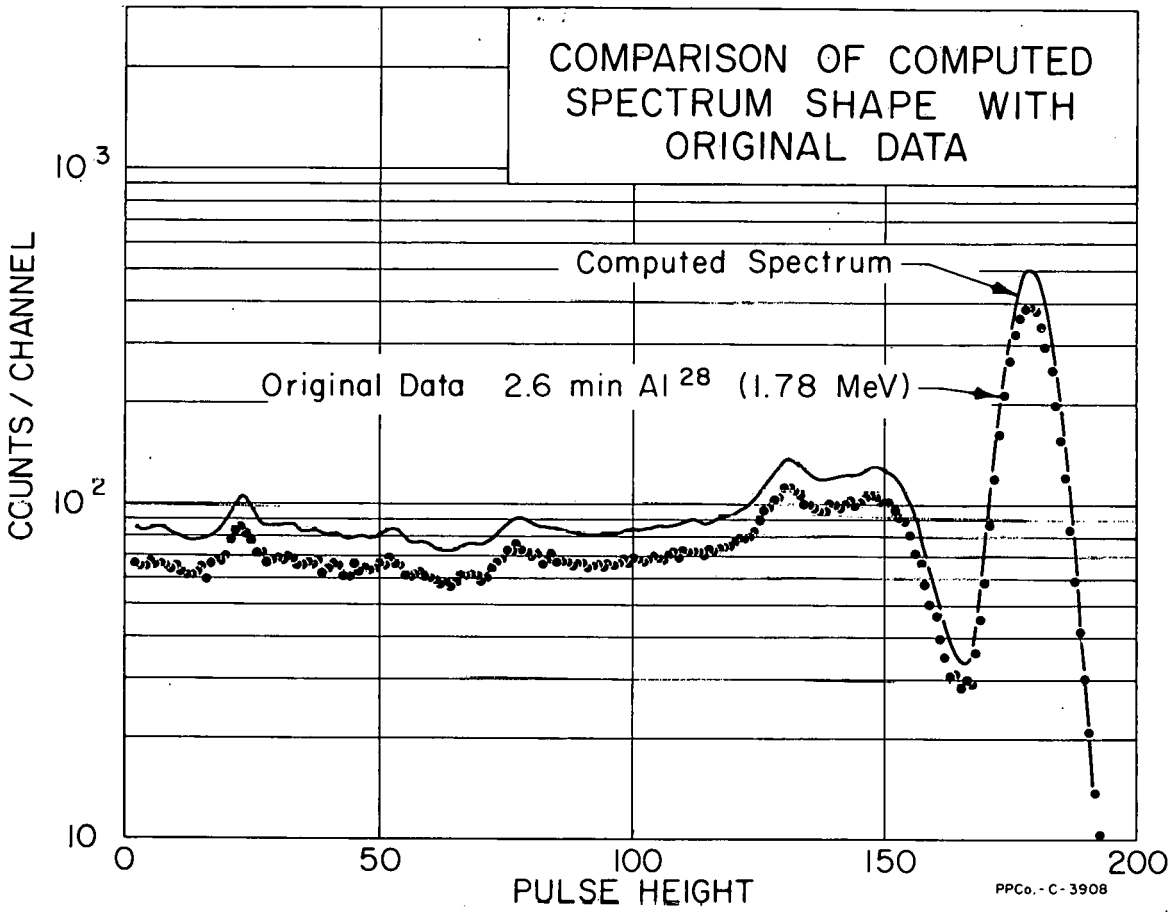

Fig. IV-2 Comparison between an experimental pulse-height distribution for a single-energy gamma ray of the same energy obtained from the shape-generation program.

5. ANALYTICAL CALCULATIONS ON WCAP-1433 WESTINGHOUSE CRITICAL EXPERIMENTS

(G. R. Poetschat)

Reactor physics calculations were made on the single-, two-, and three-region Westinghouse critical experiments described in WCAP-1433 for support of LOFT and PBF design calculations. The fuel for these experiments was UO_2 having enrichments of 1.6, 2.7, and 3.7 percent and clad in stainless steel tubes. The moderator, which was light water, was pumped into the core tank until criticality was reached. Since the total height of fuel in the axial direction was 122 cm, unmoderated dry fuel was left above the critical water height in most cores. Two lattice pitches were used, one with nonmoderator-to-moderator ratio of 1.06 and the second with nonmoderator-to-moderator ratio of 0.59. The experimental calculations for the cores with the 1.06 ratio had results from 2 to 3.5 percent high, while the cores with the 0.59 ratio had results from 1 to 2 percent high. Methods for determining reflector savings were also examined with the results generally being radially dependent. The results of the calculations are given at the end of this section.

Constants were obtained using the GAM-I, GAM-MOD, TEMPEST, and TOPIC codes. Eigenvalue calculations were obtained by the one-dimensional FOG code and the two-dimensional PDQ code. When time permits, further

calculations will be done using constants obtained by the ZUT-TUZ resonance absorption code and the Hanford Revised GAM(HRG) code.

Constants were obtained for four neutron energy groups, ie, the thermal group from TEMPEST and three fast groups from GAM. Atomic densities were obtained for a unit cell made up of the fuel pin and moderating water in the heterogeneous lattice and homogenized on a volume-fraction basis. Heterogeneity in the thermal group was accounted for by obtaining the thermal disadvantage factors for the pure materials (fuel, cladding, and moderator) with the use of the TOPIC code. Pure atomic densities were modified by the respective disadvantage factors, homogenized on a volume-fraction basis, and entered into the TEMPEST code. Atomic densities for the fast group constants were the homogenized atomic densities of the cell without disadvantage factors. Heterogeneity in the fast group constants was accounted for by the Dancoff correction factor in the resonance absorption calculation of the GAM code. A Dancoff correction of four times the ANL-5800 Dancoff correction was used since four pins in closest proximity surround every pin in the lattice.

Eigenvalues were calculated by four different methods. First, a set of one-dimensional FOG calculations was obtained using the radial description of the cores and axial bucklings, which included 15-centimeters reflector savings for each core. The second method used the FOG calculation as described above but with the Westinghouse-measured reflector savings instead of the 15 centimeters for each core. The third set of results involved an iteration method whereby first a radial calculation, then an axial calculation, and finally a second radial calculation, were obtained using the FOG code. The bucklings for the axial calculations and the second radial calculations were obtained from the results of the first radial calculations and the axial calculations, respectively. The fourth, and final set of calculations, used the two-dimensional PDQ code with radial-axial geometry for describing the core configurations. The eigenvalue results are given in Table IV-1 and -2.

FOG buckling searches for the PDQ eigenvalues were used to determine an axial reflector savings for the specific cores. From the FOG iteration method, the bucklings used in the second radial calculations were used to obtain another set of reflector savings. The measured reflector savings, the FOG iteration reflector savings, and the PDQ calculated reflector savings are plotted on Figures IV-3 and -4. Figure IV-3 has the reflector savings for the critical experiments with a nonmoderator-to-moderator ratio of 1.06, while Figure IV-4 has the reflector savings for the experiments with a nonmoderator-to-moderator ratio of 0.59. Both graphs show a radial dependency of reflector savings. Note that the reflector savings for the single region rectangular cores were not calculated, although the eigenvalues were calculated.

TABLE IV-1

CALCULATED RESULTS FOR THE
1.06 NONMODERATOR-TO-MODERATOR CORES

Core Number	Radius of Core (cm)	Critical Water Height (cm)	Lambda (λ)			
			Reflector Savings (15 cm)	Measured Reflector Savings	Iteration Method	PDQ Calculation
1A[a]	32.79	76.8	1.027	1.025	1.026	1.026
3A[a]	26.36	59.3	1.028	1.026	1.024	-----
4A[b]	61.50	55.8	1.021	1.026	1.026	-----
6A[b]	40.86	97.7	1.022	1.021	1.022	-----
7A[b]	46.36	55.9	1.023	1.024	1.025	-----
8A[c]	41.88	Maximum (150 cm)	1.020	1.020	1.020	-----
9A[c]	36.16	Maximum (150 cm)	1.020	1.019	1.019	-----
2A[d]	Solid Core	71.0	-----	-----	1.029	-----
1A[d]	Water Gap	66.0	-----	-----	1.030	-----
5A[d]	B-10-33 in Water Gap	96.2	-----	-----	-----	1.035

[a] Single fuel region.

[b] Three fuel regions: Inner-to-Outer Regions 1.6, 2.7, and 3.7 percent.

[c] Two fuel regions: 8A and 11B, 1.6 and 2.7 percent
9A and 12B, 1.6 and 3.7 percent.

[d] Rectangular cores 2.7 percent fuel.

TABLE IV-2

CALCULATED RESULTS FOR THE
0.59 NONMODERATOR-TO-MODERATOR CORES

Core Number	Radius of Core (cm)	Critical Water Height (cm)	Lambda (λ)			
			Reflector Savings (15 cm)	Measured Reflector Savings	Iteration Method	PDQ Calculation
1B[a]	25.12	83.6	1.022	1.019	1.019	-----
3B[a]	19.01	95.3	1.020	1.018	1.018	1.017
4B[b]	63.15	45.0	1.016	1.016	1.018	1.013
6B[b]	37.44	95.5	1.015	1.014	1.014	-----
7B[b]	37.58	88.9	1.013	1.013	1.012	-----
8B[b]	40.27	61.5	1.016	1.014	1.014	1.013
9B[b]	43.28	53.7	1.018	1.016	1.016	-----
10B[b]	41.83	47.4	1.017	1.016	1.015	-----
11B[c]	48.23	92.1	1.010	1.010	1.010	-----
12B[c]	44.64	91.0	1.010	1.010	1.010	-----
2B[d]	Solid Core	110.0	-----	-----	1.019	-----
IB[d]	Water Gap	90.0	-----	-----	1.019	1.020
VB[d]	B-10-SS in Water Gap	97.1	-----	-----	-----	1.021

[a] Single fuel region.

[b] Three fuel regions: Inner-to-Outer Regions 1.6, 2.7, and 3.7 percent.

[c] Two fuel regions: 8A and 11B, 1.6 and 2.7 percent
9A and 12B, 1.6 and 3.7 percent.

[d] Rectangular cores 2.7 percent fuel.

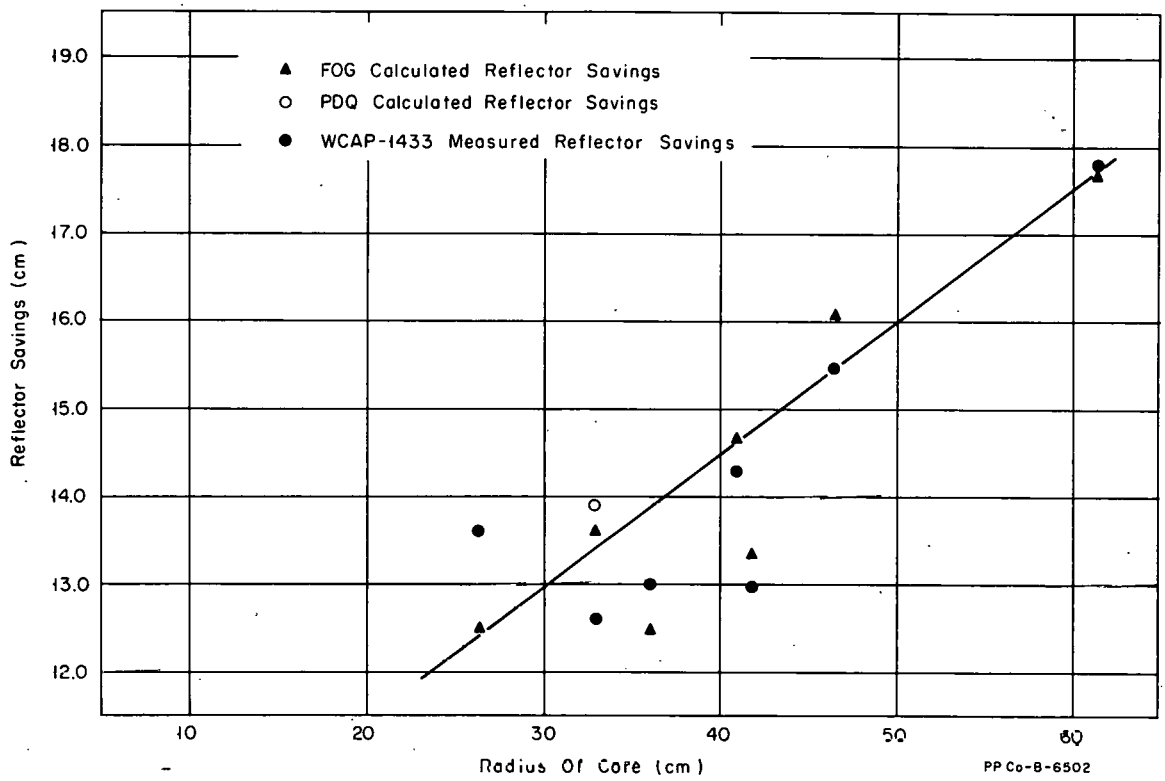

Fig. IV-3 Reflector savings versus radius for 1.06 nonmoderator-to-moderator ratio.

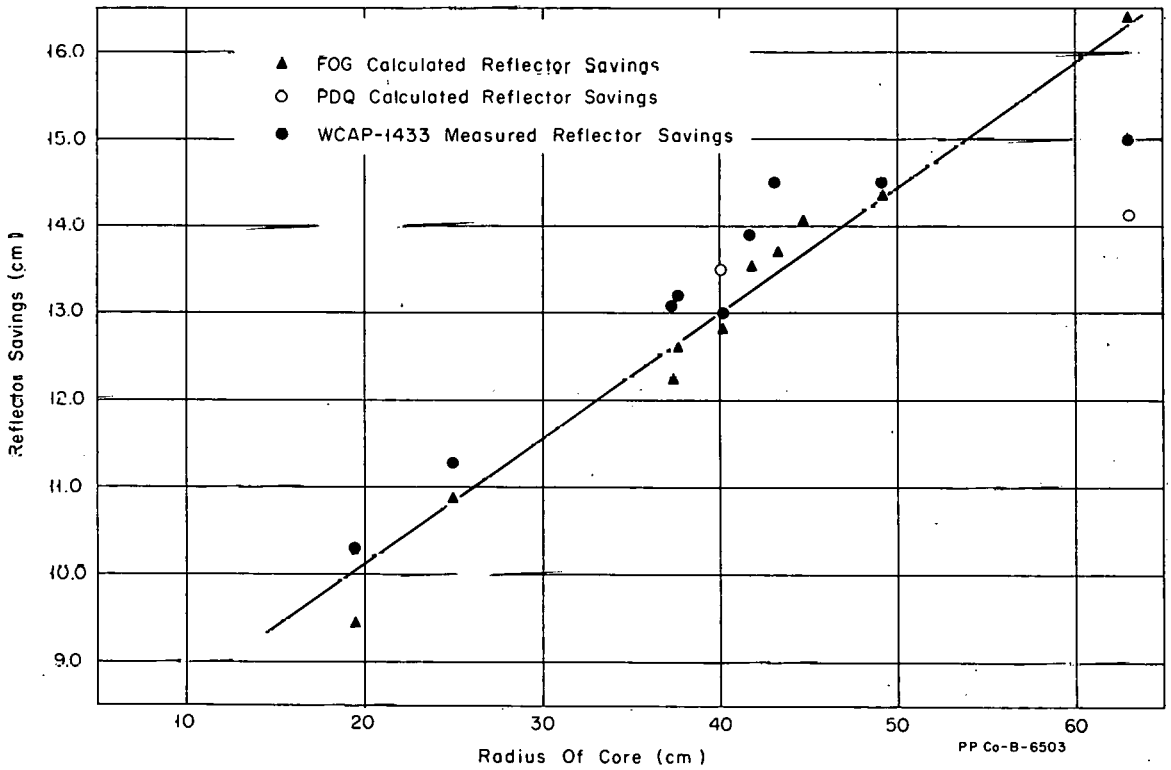

Fig. IV-4 Reflector savings versus radius for 0.59 nonmoderator-to-moderator ratio.

6. REFERENCES

1. Nuclear Technology Branches Quarterly Report 2nd Qtr 1964, IDO-17042.

2. K. W. Ellenberger, "On Programming the Numerical Solution of Polynomial Equations", Communications of the ACM, 3, No. 12 (December 1960) p 644.

3. R. L. Heath et al, The Calculation of Gamma-Ray Shapes For Sodium Iodide Scintillation Spectrometers, IDO-17017 (April 1965).

PHILLIPS
PETROLEUM
COMPANY

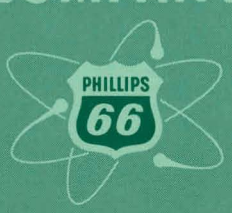

ATOMIC ENERGY DIVISION